Mitigation of Cancer Associated Effects Using Combination Therapies

by

Ismat Zerin Luna

A thesis submitted in partial fulfillment of the requirements for the degree of

Doctor of Philosophy

Department of Chemistry

University of Alberta

Abstract

Cisplatin contributes to the approximately 80% five-year survival rate for childhood cancer patients. Despite its effectiveness, cisplatin causes several toxicities, particularly ototoxicity which manifests as permanent hearing loss. To date, limited success in otoprotection without compromised anticancer effect has been observed in clinical trials. Development of effective therapies for preventing hearing loss is therefore of primary importance. Studies from the lab of Dr. Amit Bhavsar (MMI) identified a significant and biologically plausible association between cisplatin induced ototoxicity (CIO) susceptibility and expression of Toll-like receptor 4 (TLR4), an innate immune receptor protein. It is found that cisplatin treatment induces TLR4 expression and deletion of TLR4 causes decrease in CIO. From these data we identified TLR4 protein as a target to mitigate CIO. Starting with the reference hit TAK-242, we used proven synthetic methods to probe the significance of various structural motifs through selective chemical modification of the TAK-242 scaffold in order to optimize binding to TLR4 as an otoprotection strategy. Robust in vitro cisplatin "ototoxicity" platforms were developed to assess the efficacy of synthesized TLR4 inhibitors in reducing cisplatin "ototoxicity" phenotypes. Promising small molecule candidates were tested in a zebrafish CIO model in vivo. Two of the new TAK-242 based derivatives were shown to have a potent inhibitory effect on CIO in both in vitro and in vivo experiments. We carried out in silico docking studies with the synthesized inhibitors and TLR4 protein to interpret molecular interaction and refine the preferred structural features for effective inhibition.

A separate cancer-related project was focused on developing inhibitors of breast cancer (BrCa) metastasis. The most aggressive form of BrCa is the triple-negative phenotype (TNBC) which does not express estrogen receptors, progesterone receptors and human epidermal growth factor receptors. Treatment of TNBC is very difficult as it is refractory to the present BrCa treatment regimens. This highlights the lack of effective treatment strategies for TNBC and the need for innovative treatment approaches. The in vivo data from Dr. Persad lab (Department of Pediatrics) showed that the herbicide nitrofen efficiently blocks metastatic tumor growth, especially to the

liver. However, several structural properties/components of nitrofen raise concerns, including its high lipophilicity and a potential toxophore in the form of a nitroarene group. Therefore, we developed analogues of nitrofen which could allow modulation of polarity. In vitro anti-invasive activity of nitrofen analogues were evaluated which showed three of the nitrofen analogues significantly reduced invasive potential of TNBC cells. Further in vitro studies suggested that these inhibitory activities of nitrofen and its analogues are not due to cytotoxicity, but rather are due to impairment of invasive capacity of the cells.

Preface

Chapter 2 of this thesis will be published as Luna, I. Z.; Babolmorad, G.; Pollock, N. M.; Fox, A.; Khegay, A.; Allison, W. T.; West, F. G, Bhavsar, A. P. "Selective Antagonism of Toll-like Receptor 4 Mitigates Cisplatin-induced Ototoxicity" after completing few more validation studies. Bhavsar, A. P. conceived and designed the project. West, F. G.; Allison, W. T. and Bhavsar, A. P. supervised the project. I was responsible for the design, synthesis and characterization of all compounds, data collection, and manuscript composition. Khegay, A. synthesized some of the compounds under my supervision. Ghazal Babolmorad carried out cell culture and conducted all in vitro studies of the compounds and helped me in mastering some of the graphs. Pollock, N. M. and Fox, A. carried out the in vivo assays.

Chapter 3 of this thesis will be published as Luna, I. Z.; Mosa, F.; Babolmorad, G.; Bhavsar, A. P.; Barakat, K. H.; West, F. G. "Computational Insight into the Molecular Interaction between the TIR Domain of TLR4 Dimer and Its Antagonists". West, F. G., and Barakat, K. H. conceived and designed the project. Barakat, K. H. supervised the project. I was responsible for conducting the computational studies of my synthesized compounds, collecting and analyzing data as well as writing the manuscript. Mosa, F. was involved in data analysis and manuscript composition. Babolmorad, G. carried out cell culture and in vitro ELAISA assay.

Chapter 4 of this thesis has been published as Garcia, E.; Luna, I.; Persad, K. L.; Agopsowicz, K.; Jay, D. A.; West, F. G.; Hitt, M. M.; Persad, S. Inhibition of Triple Negative Breast Cancer Metastasis and Invasiveness by Novel Drugs that Target Epithelial to Mesenchymal Transition. *Sci. Rep.* **2021**, *11*, 1–15. Persad, S. conceived and designed the project. West, F. G.; Hitt, M. M. and Persad, S. supervised the project. Garcia, E. and I contributed equally to this work. I was responsible for the synthesis and characterization of all compounds. Garcia, E. and Jay, D. A. conducted the in vitro studies and Agopsowicz, K. preformed the in vivo experiments. We all contributed to manuscript design and composition.

Dedication

This thesis is dedicated to the people who have supported me throughout my education. Thanks for making me see this adventure through to the end.

Acknowledgements

At first, I would like to express my sincere gratitude to my supervisor, Dr. F. G. West, for his continuous support, guidance, as well as his endless mentorship and patience. Also, I am very thankful to you for accommodating me in your laboratory and providing the appropriate atmosphere to manage my project flexibly; the freedom you offered me in choosing a suitable project influenced the way I think and gave me the self-confidence during my PhD studies. I would not be able to defend my thesis and achieve such a milestone without your support and thoughtful advice. Thanks for being always here for me.

I am also truly grateful to my Supervisory Committee Members, Dr. Derrick Clive, and Dr. Bhavsar for their support and dedication to help aid my research with their valuable ideas and expertise during my graduate studies. I am also truly thankful to all examiners for the PhD defence exam. I would like to express my deepest sincere appreciation to them for enriching my knowledge in my discipline. Words cannot express how grateful and thankful I am to my amazing collaborators, Dr. Sujata Persad, Dr. Amit Bhavsar and Dr. William Allison for providing me with a rich multi-disciplinary environment. My chemical biology background was enriched through our usual meetings and this knowledge was broadened through the fantastic scientific community I was involved with through several symposiums organized by you. My thesis story would not be significant without your guidance and help.

I am very especially thankful to Dr. Khaled Barakat for providing me the opportunity to work in his lab to conduct my computational research during my PhD program. I am very grateful to him for his kind supervision in my computational chemistry project. I am also very thankful to Farag Mosa, the talented graduate student from Dr. Barakat lab for his continuous selfless support and assistance.

I would like to thank the past and current members of the West group for creating such an amazing environment to conduct research. I have acquired inevitable research skills from the West group, which broadened my knowledge to reach such a stage. I would like to express my deepest gratitude for Dr. Marius Constantin from whom I learnt several things in my lab and life. He was such an amazing mentor for

me throughout my graduate studies. Also, I am thankful to Dr. Nargess Hosseini, Dr. Shorena Gelozia and Dr. Ahmed Elmenoufy for their support and help in the lab. I am grateful for my friends, Natasha Rana and Ahmed Oraby for their presence beside me during my studies. I am also extremely thankful to the staff members of the NMR, IR, Mass Spectroscopy facility labs, and X-ray services. Research would not have been possible without the support you provide. I am also very grateful to Dr. Anna Jordan for editing Ch. 1, 2, & 4 of my thesis and providing me with her valuable feedback and comments, which allowed me to edit the rest of the thesis. This thesis would not be composed in such high quality without her amazing touches on it. Her dedication for lengthy hours editing my thesis is very much appreciated.

Finally, words cannot express how grateful and thankful I am to my family and relatives, especially to my mother Zayeda Begum, my father Zafar Idris, my beloved siblings Israt Zahan Ima, Iffat Zabin and Hasibul Hasan, as well as my beloved husband Monir Hossain and daughter Anisha Tabassum. I would like to thank them for their endless prayers and support to pass stressful moments throughout my studies. Indeed, I cannot thank them enough for the never-ending support, unlimited love, and care.

Table of Contents

List of Figures

Chapter 1

List of Tables

Chapter 3

List of Schemes

Abbreviations

Å	Angstrom
ACD	allergic contact dermatitis
ADR	adverse drug reaction
BINAP	(2,2′-bis(diphenylphosphino)-1,1′-binaphthyl)
BrCa	Breast Cancer
Br	broad (spectral)
CADD	computer-aided drug design
$CDCl_3$	deuterated chloroform
CDH	congenital diaphragmatic herniation (CDH)
CHS	contact hypersensitivity
CIO	Cisplatin-induced Ototoxicity
CIT	Cisplatin-induced Toxicity
cm^{-1}	reciprocal centimeter or wavenumber
CO_2	carbon dioxide
Ctr1	mammalian copper transporter 1
D	doublet (spectral)
DAMPs	damage associated molecular patterns
DASPEI	2-(4-(dimethylamino)styryl) -N-ethylpyridinium iodide
DBI	Davies-Bouldin Index
DCM	Dichloromethane
DMEM	Dulbecco's Modified Eagle's Medium
DMF	Dimethylformamide
DMSO	dimethyl sulfoxide
DMSO-d_6	deuterated dimethyl sulfoxide
Dpf	days post fertilization
ECD	extracellular domain
EDG	electron donating group
EDTA	ethylenediamine tetraacetic acid
ELISA	enzyme-linked immunosorbent assay

EMT	epithelial-mesenchymal transition
EtOAC	Ethylacetate
ESI-MS	electrospray ionization mass spectrometry
EWG	electron withdrawing group
FBS	fetal bovine serum
FTIR	fourier transform infrared
GAFF	General Amber Force Field
GBVI/WSA	Generalized Born Volume Integral/Weighted Surface Area
Gen	Generation
GMQE	Global Model Quality Estimation
GSH	Glutathione
GWAS	genome-wide association study
HA	heavy atom
HBA	hydrogen bond acceptor
HBD	hydrogen bond donor
HEI-OC1	mouse Organ of Corti outer hair cell line
HEK	human embryonic kidney
HMRS	high resolution mass spectrometry
Hz	Hertz
IC_{50}	half maximal inhibitory concentration
IL-6/8	Interleukin-6/8
IM	Immunomodulatory
in silico	computer simulation in reference to biological experiments
in vitro	referring to the studies performed in cell culture
in vivo	referring to the studies performed in living organisms
IR	ionizing radiation
J	coupling constant (in NMR)
LAR	luminal androgen receptor
LPS	lipopolysaccharide
M	moles per liter
M	multiplet (spectral)

m-CPBA	*m*-chloroperoxybenzoic acid
MD	molecular dynamics
MD2	myeloid differentiation protein 2
MET	mechano-electrical transduction
Mg	milligram
mL	Milliliter
MM/GBSA	Molecular Mechanics-Generalized Born Surface Area
MO	morpholino oligonucleotide
MOE	molecular operating environment
MS	mass spectrometry
MSL	mesenchymal stem–like
MTT	3-(4,5-dimethylthiazol-2-yl)-2,5-diphenyl-2H-tetrazolium bromide
NF-κB	nuclear factor kappa light chain enhancer of activated B cells
ng/mL	nanogram per millilitre
Nm	nanometer(s)
NMR	nuclear magnetic resonance
OCT	organic cation transporter
OHC	outer hair cells (in the Organ of Cort)
PAMPs	pathogen-associated molecular patterns
PBS	phosphate-buffered saline
PDB	protein data bank
PLL	Posterior Lateral Line
Ppm	parts per million
PME	Particle-mesh Ewald (method)
PVDF	polyvinylidene difluoride
Q	quartet (spectral)
QMEAN	Qualitative Model Energy Analysis
qRT-PCR	quantitative reverse-transcription polymerase chain reaction
R	generalized alkyl group of substituents
RMSD	root-mean-square deviation of atomic positions
RMSF	root-mean square fluctuation of individual residue flexibility

ROS	reactive oxygen species
S	singlet (spectral)
SAR	structure activity relationship
SD	standard deviation
SNAr	nucleophilic aromatic substitution
SNP	nucleotide polymorphism
STS	sodium thiosulfate
TIR	Toll/IL-1 receptor domain
TLC	thin layer chromatography
TLR4	Toll-like Receptor 4
TM	transmembrane domain
TNBC	triple-negative breast cancers
VMD	Visual Molecular Dynamics
vdW	van der Waals
WT	wild type
wt.	Weight
Δ	chemical shift in parts per million downfield from tetramethylsilane
λ	Wavelength
^{o}C	Celsius
µL	Microliter
µM	Micromolar

Chapter 1

1. Introduction

1.1 Cisplatin-induced Ototoxicity (CIO)

Cisplatin is a highly effective chemotherapeutic treatment for many solid tumours in children, such as specific brain and germ cell tumours, neuroblastomas, osteosarcomas, and lung and ovarian cancers.[1] Cisplatin use contributes to the approximately 80% five-year survival rate for childhood cancer patients. The anti-tumour activity of cisplatin is based on its formation of intra-strand and inter-strand DNA crosslinks that activate multiple signal transduction pathways leading to cell-cycle arrest and programmed cell death (Figure 1.1).[2,3] Despite its effectiveness, cisplatin use is limited by the development of several toxicities, particularly nephrotoxicity, neurotoxicity, and ototoxicity. Methods to increase diuresis, such as hydration, have been shown to reduce nephrotoxicity.[4] However, to date no effective FDA approved treatments for neurotoxicity and ototoxicity are available.

In most organs, cisplatin is eliminated within days to weeks after injection, however, inside the ear, it remains for months to years after treatment and causes ototoxicity.[5] Cisplatin-induced ototoxicity (CIO) is bilateral, permanent, and occurs frequently. It can have significant life-long consequences in children by impairing speech and language development, social-emotional development, and increasing the risk of learning difficulties.[6–8] It is estimated that >1 million patients are treated with cisplatin annually in North America and Europe,[9] with hearing loss reported for >500,000 patients per year in the USA.[10] When patients exhibit CIO, cisplatin doses are reduced, which compromises the cancer treatment efficacy.[11] Clinical risk factors for CIO include cumulative cisplatin exposure and age at treatment;[12,13] yet, incidence rates vary by 30–40% as a function of cumulative dose, suggesting a potential genetic contribution.[12,14] Currently, there are no biomarkers for CIO prediction in clinical use;[15] therefore, a pharmacogenomics-based personalized health approach could be used to guide cisplatin treatment and mitigate CIO. Given that long-term survivors all

develop cisplatin-induced ototoxicity,[16] mitigation of this adverse drug reaction (ADR) has the potential to improve children, women, and men's health by reducing immediate and late-term toxicity, respectively. Development of effective therapies for treating hearing loss is, therefore, of primary importance.

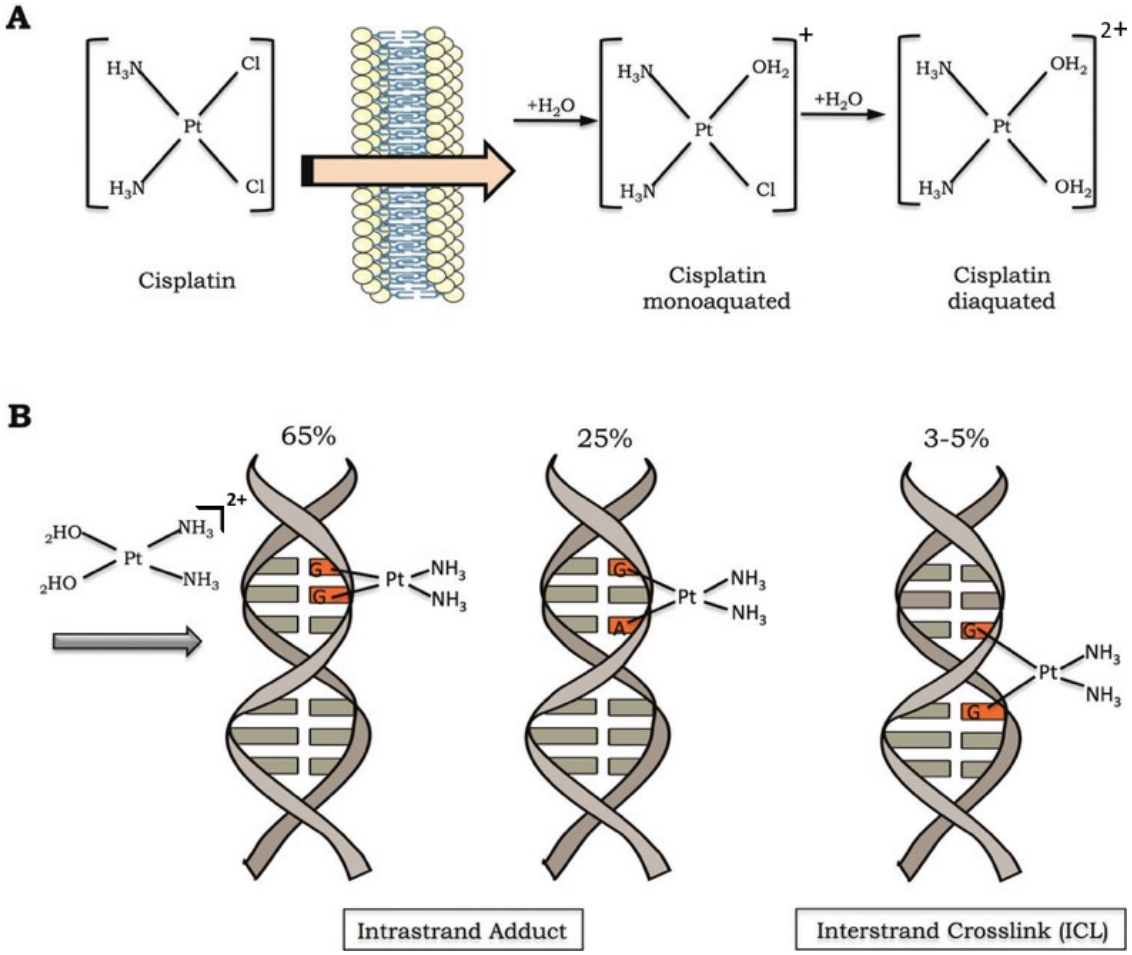

Figure 1.1. Cisplatin induced DNA damage in cancer cells. A) The cisplatin gets activated by exchanging one or two of its chlorides for water molecules (monoaquated and diaquated, respectively). B) Cisplatin can form covalent bonds with DNA. The major DNA lesions are intrastrand DNA adducts and interstrand crosslinks (ICLs). The percentages represent the frequency of each type of DNA damage induced by cisplatin. (Figure adapted from Reily et al.[3], no permission required).

1.2 Mechanisms of CIO

The anatomy of our hearing system is extremely complex but 'peripheral' and the other 'central'. The peripheral hearing system consists of three parts, the outer ear, the middle ear, and the inner ear. The hearing part of the inner ear, known as the cochlea, contains a small organ called Organ of Corti (Figure 1.2). The outer hair cells (OHC) in the Organ of Corti are critical mechano-transducers that convert mechanical stimulation into nerve signals.[18,19]

The cochlea possesses an efficient antioxidant defense system. This includes antioxidants such as vitamin C, vitamin E, and low molecular weight thiols, such as glutathione (GSH).[20] Using several distinct cellular mechanisms, cochlea defends against ototoxicity.[21–24] However, over the course of cisplatin treatment, these protective systems become overwhelmed and are no longer able to overcome the toxicity.

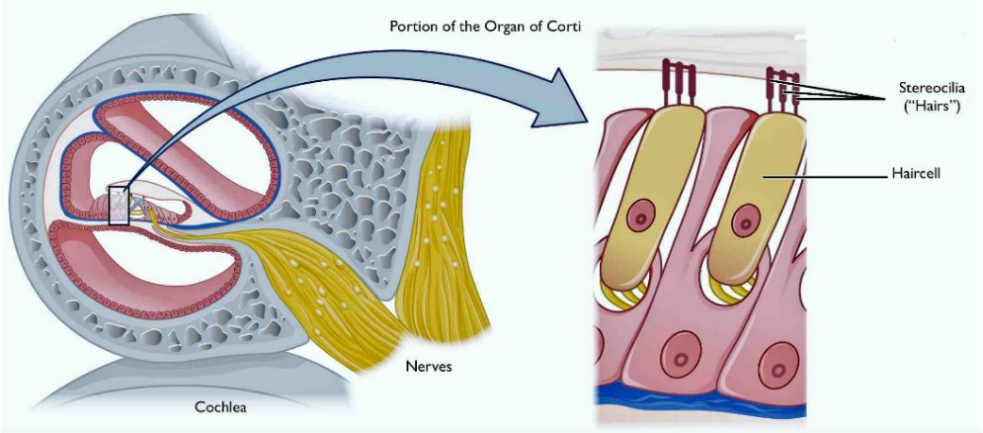

Figure 1.2. The hair cells of the Organ of Corti in the human inner ear. (Figure copied with permission from Schellack et al.[19])

CIO stems from the upregulation of reactive oxygen species (ROS) in the OHC of Organ of Corti, where cisplatin accumulates.[25,26] Cisplatin has been shown to stimulate enzyme systems linked to the ROS generation process or inactivate the antioxidant defense systems of the cochlea by reducing ROS detoxification via glutathione. The increased oxidative stress within the cochlea could increase lipid

peroxidation of membranes, inactivate essential cellular enzymes and membrane transporters, and disrupt ion channel function.[27,28]

Several studies also have shown that, upon cisplatin treatment, Organ of Corti cell lines display key in vitro cisplatin "ototoxicity" phenotypes, such as increased pro-inflammatory cytokine signalling, which can upregulate ROS generation that, in turn, can lead to morphological and functional alterations, causing apoptotic cell death.[29–32]

All these data suggest that ROS plays a critical role in cisplatin-induced ototoxicity and that its inhibition could ameliorate hearing loss. However, the mechanisms underlying how cisplatin interacts with the cell to activate these ototoxic phenotypes are still unclear.

1.3 Approaches for Otoprotection

Since there is no known mechanism of removal for the cisplatin from within the ear, patients need a treatment capable of preventing cisplatin-induced hair cell death. Presently, there are a variety of pre-clinical and clinical treatments being studied for their potential protective ability. Unfortunately, none of these treatments have been approved for use by the public.[33,34] Several approaches have been undertaken over the past two decades to boost the cochlear protective mechanism to ensure otoprotection against cisplatin treatment. Research has focused on developing antioxidant therapies that target ROS accumulation for treating hearing loss, e.g., N-acetylcysteine, sodium thiosulfate, D-methionine, and amifostine. Studies showed that N-acetyl cysteine (NAC) protected against cisplatin-ototoxicity in rats[35] and guinea pigs.[36] Sodium thiosulfate (STS) was also effective against CIO.[37] However, systemic administration of this drug led to formation of cisplatin-STS complex, which compromised the efficacy of the antitumor therapy.[38] Similarly, high doses of amifostine provided otoprotection in hamsters, but its use was associated with neurotoxicity.[39] It was also ineffective in patients with metastatic melanoma[40] and in children suffering from neuroblastoma or germ cell tumors.[41,42]

Cisplatin entry into cochlear cells is mediated by several transporters, such as mammalian copper transporter 1 (Ctr1), organic cation transporter (OCT), and mechano-electrical transduction (MET) channel. Decreasing cisplatin entry by intra-

tympanic administration of copper sulfate, a substrate of Ctr1, protects against hearing loss induced by cisplatin.[43] Inhibition of OCT with cimetidine protects against cisplatin-induced nephrotoxicity and ototoxicity.[44] Some investigators showed that inhibition of MET channels by quinine or EGTA protected against cisplatin-induced hair cell death.[33] Though most of the otoprotection approaches have been shown to reduce CIO in a clinical trial, overall survival for patients with disseminated disease also was reduced significantly.[45] This supports the critical need to examine targets upstream of ROS formation to develop an otoprotecting therapy that preserves chemotherapeutic effectiveness.

1.4 Toll-like Receptor 4 (TLR4) and Its Signaling Pathway

TLR4 is a membrane-bound pattern recognition receptor. It is a widely conserved innate immune signaling protein that detects pathogen-associated molecular patterns (PAMPs), most notably the Gram negative bacterial outer membrane component, lipopolysaccharide (LPS). TLR4 also can detect endogenous ligands, termed damage-associated molecular patterns (DAMPs), such as hyaluronan or high mobility group box 1, which serve to alert the immune system to potential danger.[57–59] LPS detection requires the TLR4 co-receptor MD-2. Structural analyses have revealed that the LPS binding pocket is comprised of both MD-2 and TLR4 on the external face of the membrane, with MD-2 making a major contribution to agonist binding.[29,60] LPS binding to the TLR4/MD-2 complex induces TLR4 dimerization and signal propagation through adapter protein recruitment on the cytoplasmic face of the membrane.[60] Two canonical signaling pathways are activated through TLR4. The TLR4 adapter protein TIRAP engages the MyD88-dependent signaling pathway that culminates in NF-κB nuclear translocation and pro-inflammatory cytokine production. TRAM, the alternate TLR4 adapter protein, engages TRIF, resulting in IRF3 translocation to the nucleus and stimulation of type I interferon response.[57] TLR4 activation initiates well-studied signaling cascades (Figure 1.3) that can elicit inflammatory cytokine production (via NF-kb), ROS formation (via NADPH oxidase and mitochondria),[61,62] and apoptosis (via Fas-associated Death Domain protein).[63]

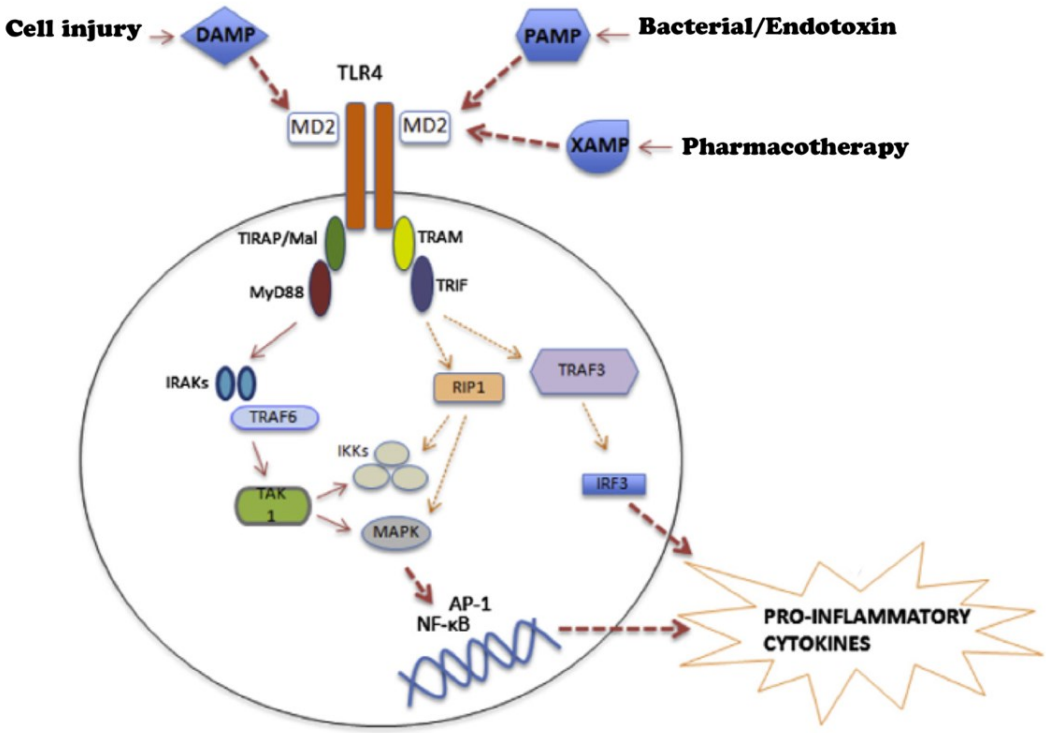

Figure 1.3. TLR4 signaling pathway: TLR4 activation by PAMPs and DAMPs leads to signaling through MyD88 or TRIF-dependent cascades, resulting in cytokine expression. (Figure adapted with permission from Jalleh et al.[64]). ROS accumulation and apoptosis induction pathways not shown.

1.5 In Vitro CIO Target Validation

A Few years ago, the research group of Dr. Amit Bhavsar (Department of Medical Microbiology and Immunology, University of Alberta) had begun examining the association between cisplatin and TLR4 in vitro. To validate TLR4 as a CIO mitigation target, Babolmorad et al. have examined its role in eliciting cisplatin ototoxic responses in an in vitro model of CIO.[56] They used HEI-OC1 cells, which are an immortalized mouse ear cell line that shows characteristic markers of Organ of Corti OHCs.[52] These are used extensively in the literature to study CIO in vitro mechanistically and have revealed key insights into cisplatin-induced cell responses.[31,65–67]

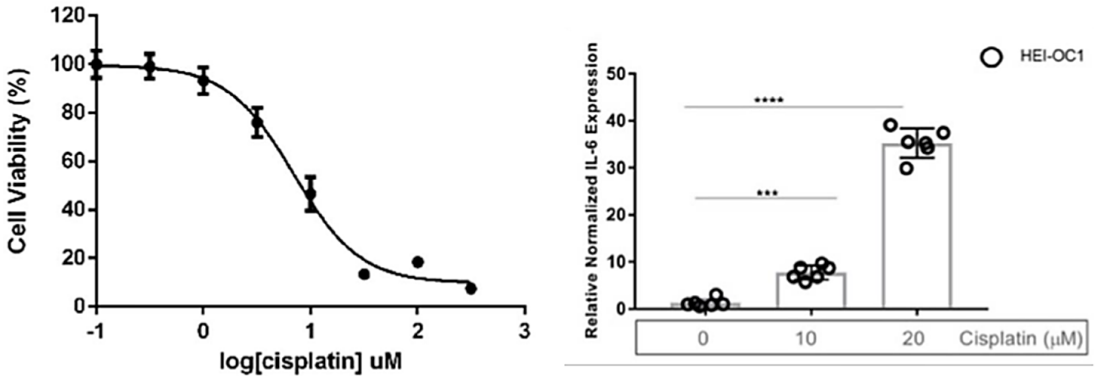

Figure 1.4. Cisplatin ototoxic phenotypes show a dose-response in an Organ of Corti cell line. HEI-OC1 cells were treated with the indicated concentrations of cisplatin and assessed for cell viability (MTT, left) and IL-6 gene expression (qRT-PCR, right). (Figures copied and adapted with permission from Babolmorad et al.[56])

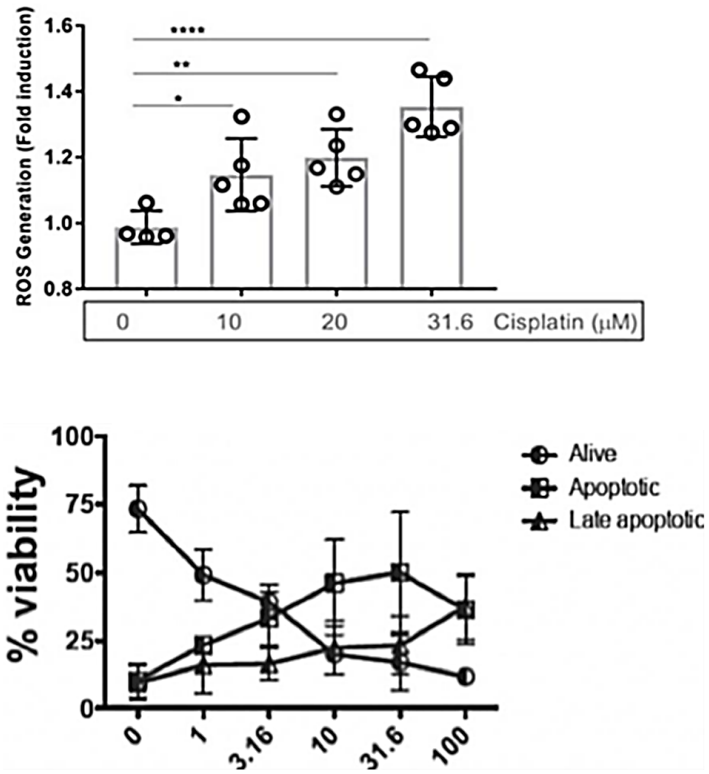

Figure 1.5. Cisplatin ototoxic phenotypes show a dose-response in an Organ of Corti cell line. HEI-OC1 cells were treated with the indicated concentrations of cisplatin and assessed for ROS formation (DCFH-DA, top); and apoptosis induction (Annexin V/PI, bottom). (Figures copied and adapted with permission from Babolmorad et al.[56])

Unfortunately, well-characterized human auditory cell lines are lacking, and inner ear cell differentiation protocols are laborious and time-consuming.[68,69] It has been shown that in the absence of LPS, cisplatin could induce robust pro-inflammatory ROS and apoptosis response in HEI-OC1 cells (Figure 1.4 and Figure 1.5).

It has been indicated that transient Tlr4 silencing (75% knockdown efficiency) significantly reduces cisplatin-induced IL-6 expression by >50% (Figure 1.6). Therefore, cisplatin treatment of murine inner ear cell lines elicits inflammatory cytokine synthesis, ROS production and apoptosis induction-phenotypes, reminiscent of those elicited by TLR4 activation. [29,31,34,66,70–73]

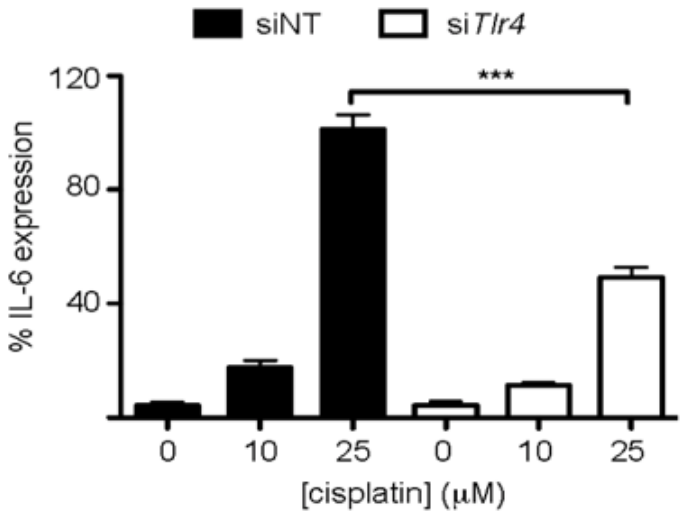

Figure 1.6. Transient Tlr4 silencing reduces cisplatin mediated cell signaling in HEI-OC1 cells. Cells were treated with non-targeting (siNT) or *Tlr4* siRNA, prior to cisplatin exposure and expression of IL-6 was determined by qRT-PCR. *** denotes $P < 0.001$ as analyzed by ANOVA; n = 9. (Figure copied and adapted with permission from Babolmorad et al.[56])

In addition, they also showed that cisplatin treatment of an HEK cell line stably expressing TLR4 induced pro-inflammatory cytokine secretion and was sensitized to cisplatin-mediated cell death compared to an isogenic cell line devoid of TLR4 expression (Figure 1.7). These data demonstrate that TLR4 is a critical mediator of CIO and validate it as a target for otoprotectant development. Therefore, our hypothesis is that TLR4 inhibition will mitigate cisplatin induced ototoxicity.

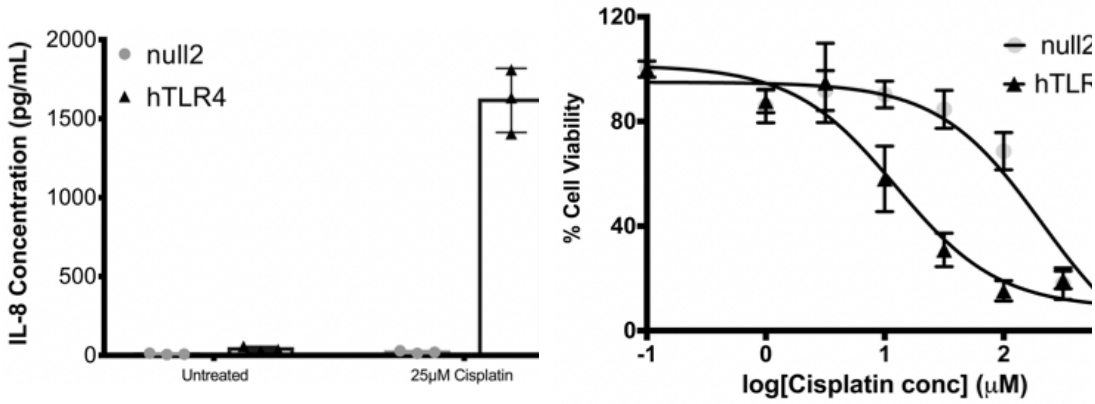

Figure 1.7. Cisplatin signals through TLR4 in vitro. Isogenic TLR4-deficient (null2) or TLR4-expressing (hTLR4) HEK cells were treated with cisplatin and assessed for IL-8 secretion (ELISA, left) or cell viability (MTT, right). (Figures copied and adapted with permission from Babolmorad et al.[56])

1.6 In Vivo CIO Target Validation

Recently, the Allison group (Department of Biological Sciences, University of Alberta) examined the role of TLR4 in an in vivo CIO model.[56] They chose to use zebrafish because it is a robust and widely accepted model of ototoxicity.[33,74–77] Using established assays, they scored the health of neuromasts, which are mechano-transducing hair cells that bear structural, cellular, and physiological similarities to Organ of Corti outer hair cells.[78] Neuromast health can be visualized using the fluorescent dye DASPEI, which accumulates in and stains viable hair cells. They used a dose-response format to establish a dose of cisplatin that robustly reduced hair cell viability in zebrafish (Figure 1.9A).

Zebrafish have two tlr4 genes, designated tlr4ba and tlr4bb, that are orphan receptors. They are not activated by LPS, but chimeric experiments showed that they are linked to the NF-κB signaling pathway.[79] Prior to a bath application of cisplatin, they knocked down the tlr4ba homolog, the tlr4bb homolog, or both tlr4ba and tlr4bb homologs, using morpholino oligonucleotide (MO), which is used widely as a gene blocking reagent.[79–81] Knockdown of either tlr4ba or tlr4bb was significantly protective against cisplatin induced toxicity (CIT). Notably, they observed that protection from this toxicity could be enhanced further by combinatorial knockdown of both tlr4ba and tlr4bb, further supporting the role of zebrafish tlr4 in CIT (Figure 1.8B). A

concentration of 15 µM was chosen for this experiment because the dose-response curve (Figure 1.8A) indicated that this concentration yielded significant but not total loss of neuromast cell viability, as determined through DASPEI staining.

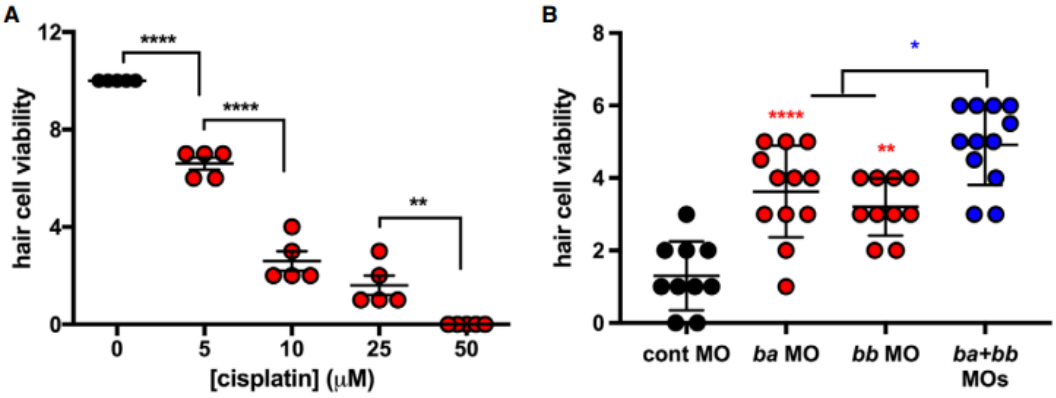

Figure 1.8. Zebrafish Tlr4 initiated cisplatin-induced cytotoxicity in vivo. (A) Hair cell viability in larval zebrafish following cisplatin treatment at the indicated concentrations. (B) Hair cell viability in larval zebrafish pre-treated with control-, tlr4ba-, and/or tlr4bb-targeting MOs, and subsequently treated with 15 µM cisplatin. Data information: In both figures, each data point represents a score of hair cell integrity in an individual animal (taken from multiple samples per animal), with lines representing the mean and standard deviation. Statistical comparisons between cisplatin concentrations (A) or to control morpholino (B, except as indicated in blue) were assessed by one-way ANOVA. *P < 0.05; **P < 0.01; ****P < 0.0001 (Tukey test). (Figures copied with permission from Babolmorad et al.[56])

1.8 Mitigating CIO through TLR4 Antagonism

In 2005, during the development of a new therapeutic agent for sepsis, Yamada and co-workers from Takeda Pharmaceuticals synthesized and identified a novel cyclohexene derivative, TAK-242 also known as Resatorvid (Figure 1.9), which is capable of inhibiting TLR4 signaling.[82] In the presence of TAK-242, there is a decrease in the secretion of pro-inflammatory cytokines, which are released during the TLR4 signaling pathway, and this effect on TLR4 results in an overall decrease of inflammation.[83]

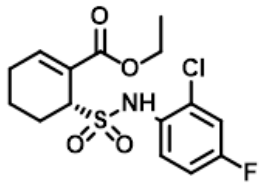

Figure 1.9. Structure of reference (hit) compound TAK-242.

While this compound was found to have no beneficial effects against sepsis in clinical trials,[84] it was shown recently to prevent bleomycin-induced organ fibrosis in animal models, and it ameliorated existing fibrosis.[85] As a result, we chose to use TAK-242 as the reference compound of our study to mitigate cisplatin induced ototoxicity by targeting TLR4. Recently our collaborators in the Bhavsar group were able to block the TLR4 signaling pathway in HEI-OC1 cells using TAK-242.[56] HEI-OC1 cells were pretreated with TAK-242 or the vehicle for 1 h and then concurrently stimulated with LPS or cisplatin. The resulting data indicated that cells treated with TAK-242 released less IL6 protein and generated less ROS after TAK-242 pre-treatment and stimulation with cisplatin or LPS (Figure 1.10A–B).

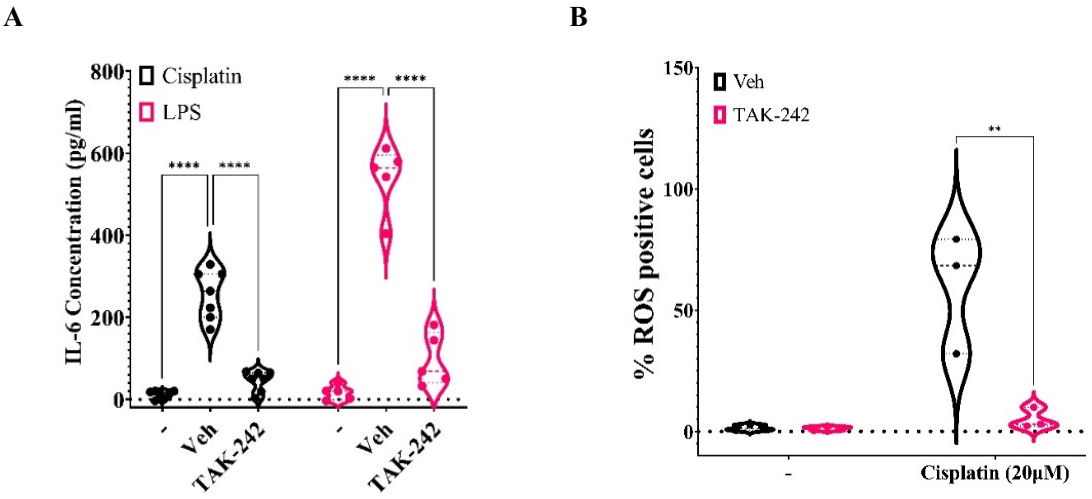

Figure 1.10. TLR4 antagonism by small molecule mitigates CIO in HEI-OC1 cells. Treatment of HEI-OC1 cells with the TLR4 inhibitor, TAK-242, reduces cisplatin-induced IL-6 production (A) and ROS generation (B). HEI-OC1 cells were pretreated with vehicle (DMF), TAK-242 (4 μM), or untreated (–) and subsequently treated with LPS (10 ng/mL) or cisplatin (20 μM) as indicated. Data are from n = 5–7 (A) or n = 3 (B) independent experiments and presented as the mean and standard deviation. The percent of ROS positive cells was determined by flow cytometry. **, $P < 0.01$; ****, $P < 0.0001$ using 2-way (A) or one-way (B) ANOVA with Dunnett's multiple comparison testing to nil treatment. (Figures adapted with permission from Babolmorad et al.[56])

Besides that, they also proved that cisplatin-induced IL-8 secretion in HEK-hTLR4 cells also can be prevented by TAK-242. Chemical inhibition of TLR4 abrogated cisplatin mediated TLR4 activation and IL8 secretion similar to LPS in HEK-hTLR4 cells (Figure 1.11A–B).[56]

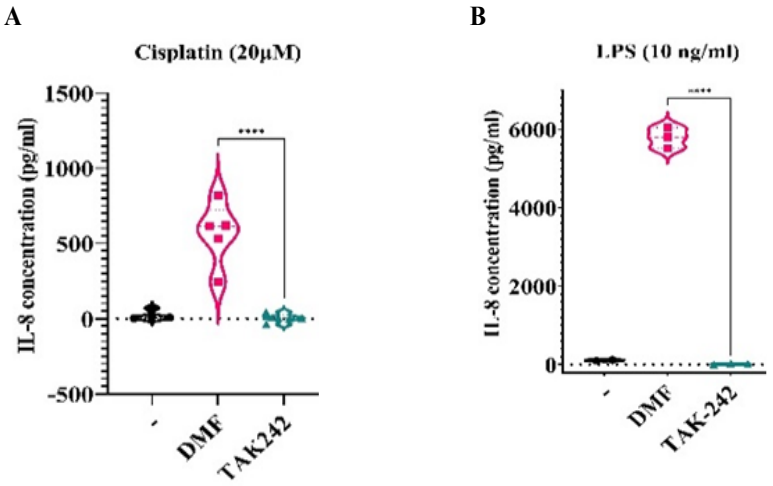

Figure 1.11. Cisplatin-induced IL-8 secretion, similar to LPS, can be prevented by a TLR4 inhibitor. HEK-hTLR4 cells were pretreated with 4 μM TAK-242 (TLR4 inhibitor) or vehicle (DMF) and then stimulated with cisplatin (20 μM) or LPS (10 ng/mL). For all panels, data are presented as a violin plot. Data are the mean of n = 3 (A and B-LPS) or n = 5 (B-Cisplatin) independent experiments. Statistical analyses were assessed by 2-way ANOVA, Fisher's LSD test (A) and one-way ANOVA, Dunnett's test (B): A) 24 h compared to 0 h; B) Comparisons between DMF and TAK-242 treatments. *, $P < 0.05$; **, $P < 0.01$; ***, $P < 0.001$; ****, $P < 0.000$. (Figures adapted with permission from Babolmorad et al.[56])

Overall, these results indicated that cisplatin responses that lead to ototoxicity can be mitigated using chemical inhibitors of TLR4 (Figure 1.12). We believe that this promising activity justifies a closer look at this molecular scaffold in order to optimize binding to TLR4 as an otoprotection strategy.

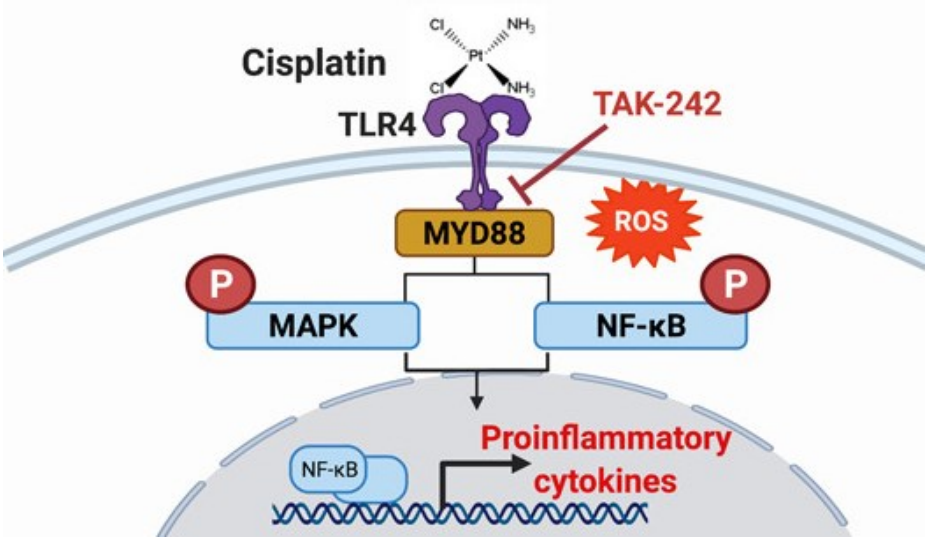

Figure 1.12. Schematic representation of cisplatin induced ototoxicity mediated by TLR4, which can be antagonized by TAK-242. (Figure adapted with permission from Babolmorad et al.[56]).

1.8 Structure of TLR4 Dimer

The human TLR4 gene encodes a 95680 Da protein containing 839 amino acids. The TLR4 protein is composed of an extracellular domain (ECD) containing 22 leucine-rich repeats (LRRs), a transmembrane (TM) domain, and the Toll/IL-1 receptor domain (TIR) that is essential for TLR signaling through homodimerization. The extracellular domain of TLR4 is composed of 608 residues, and the intracellular domain contains 187 residues. TLR4-ECD is associated tightly with a co-receptor, myeloid differentiation protein 2 (MD2), which traps agonists such as LPS in its large hydrophobic cavity and forms a right-handed superhelix that extends throughout the domain and adopts the shape of a horseshoe (Figure 1.13).[84,86,87]

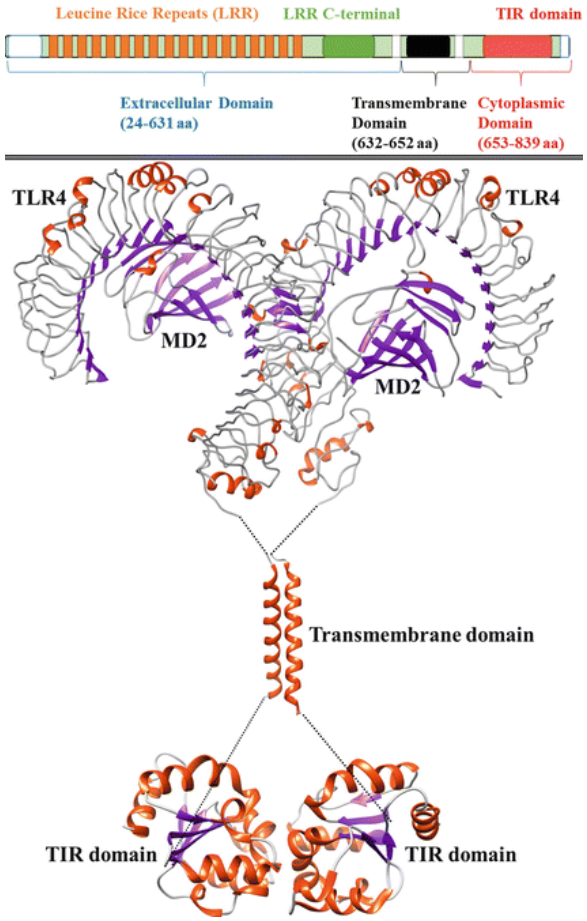

Figure 1.13. Schematic representation of the structure of TLR4 dimer as a complex with MD2. (Figure copied with permission from Krishnan et al.[87])

Several studies have been conducted to uncover the three-dimensional structures of proteins involved in this complex pathway. The extracellular domain of TLR4 has been solved through X-ray crystallography. The TM domains of TLR4 have been solved recently through NMR spectroscopy.[88,89] However, experimental studies elucidating the full-length structure of TLR4 with an intact ECD-TM-ICD organization have not been reported so far. Recently, Patra et al. proposed a full-length structural model of TLR4 using homology modeling, protein–protein docking, and molecular dynamics simulations to understand the differential domain organization of TLR4 in a membrane–aqueous environment. The structural properties of ECD, TM, and TIR domains of their intact TLR4 model are consistent with X-ray crystallography/NMR structures determined in isolated conditions.[90]

1.9 Binding Site of TLR4 with TAK-242

A study by Takashima and co-workers identified that TAK-242 selectively binds to TLR4 but not to MD-2 or adaptor molecules containing the TIR domain.[91] They examined the binding affinity of TAK-242 with TLR4 and adaptor molecules (MyD88, TIRAP/Mal, TRAM, and TRIF) using tritium-labelled TAK-242 ([^{3}H]-TAK-242). The expression levels of adaptor molecules were similar to or greater than that of TLR4. Under these conditions, [^{3}H]-TAK-242 strongly bound to TLR4 but did not bind to adaptor molecules (Figure 1.14).

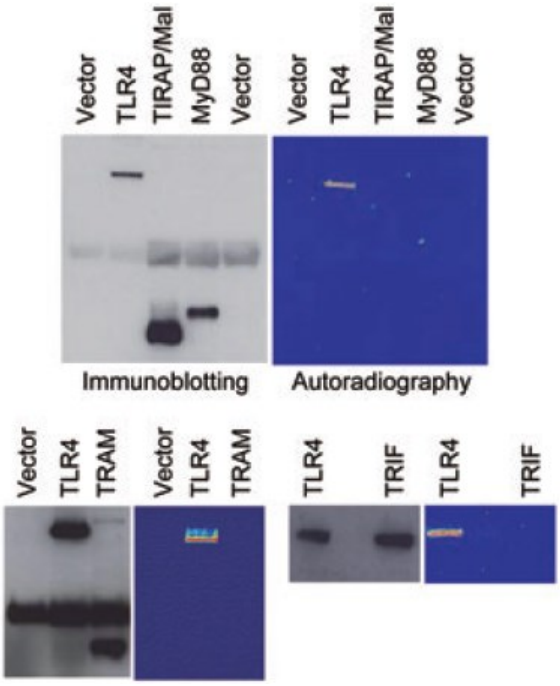

Figure 1.14. Binding of [^{3}H]-TAK-242 to TLR4-related adaptor molecules. HEK293 cells were transiently transfected with expression vector coding FLAG-TRAM, FLAG-TRIF, HA-TIRAP/Mal, HA-MyD88, and FLAG-TLR4. Empty lanes were used for a molecular weight marker. (Figure copied with permission from Takashima et al.[91])

Furthermore, considering the presence of a conjugated α,β-unsaturated ester moiety in the molecule, they speculated that TAK-242 might work as a Michael acceptor [92–94] and interact with a nucleophilic cysteine or lysine residue. To prove this hypothesis, they explored the binding of [^{3}H]-TAK-242 and TLR4 by substituting Cys and Lys residues of the TMD/ICD of TLR4 with alternative residues that lack nucleophilic groups, such as alanine (Ala) and arginine (Arg), and subsequently testing the signaling capabilities of these modified TLR4 proteins (Figure 1.15).[91]

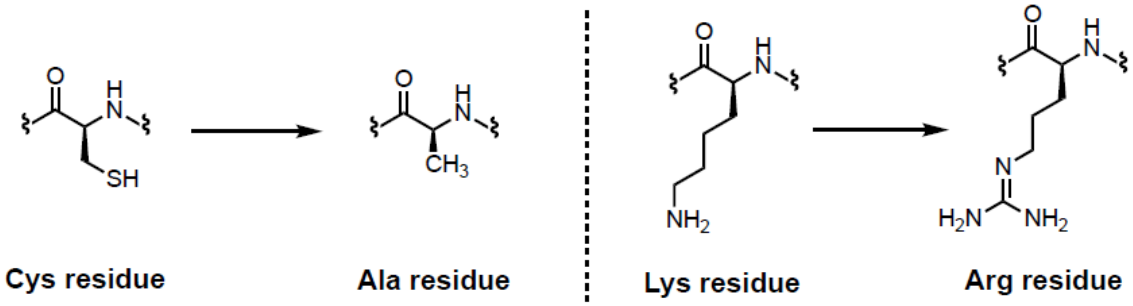

Figure 1.15. Substitution of Cys and Lys residues with Ala and Arg, respectively, by Takashima et al.[91]

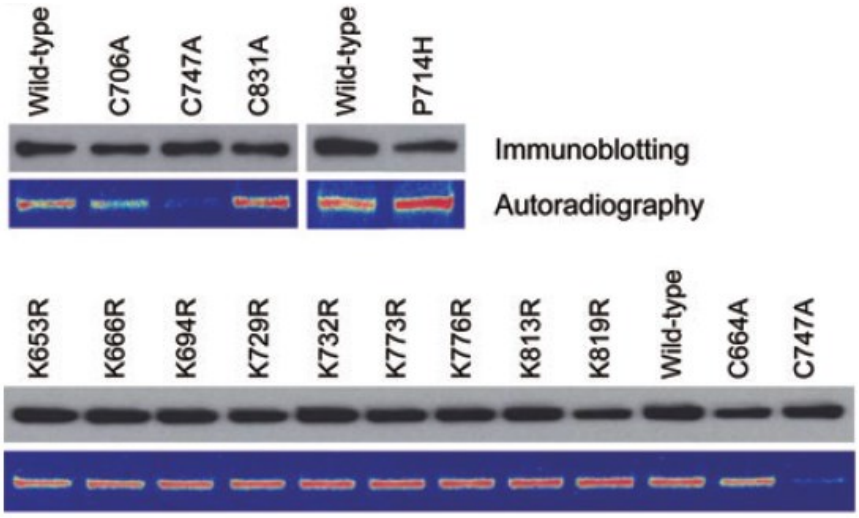

Figure 1.16. Binding of [^{3}H]-TAK-242 to TLR4 mutants with alanine substitutions at Cys residues and Arg substitutions at Lys residues in the TIR domain of TLR4. COS-7 cells were transfected transiently with expression vectors coding FLAG-TLR4 and FLAG-TLR4 with single amino acid mutations in TLR4. After 2 d of transfection, the cells were incubated with 100 nM of [^{3}H]-TAK-242 for 6 h. Cell lysates were immunoprecipitated with anti-FLAG M2 Ab, and the immunoprecipitates were subjected to SDS-PAGE and western blotting. (Copied with permission from Takashima et al.[91])

This study consisted of a control group without changes to TLR4 and experimental groups with substitution of Cys and Lys with Ala and Arg, respectively, at varying positions. All these mutants were expressed at similar levels to that of wildtype TLR4. These modified TLR4 proteins showed that substitution of Lys with Arg did not interrupt the inhibitory activity of TAK-242 on TLR4, but the C747A substitution markedly impaired the binding of [^{3}H]-TAK-242 (Figure 1.16).

Therefore, this mutational analysis indicated that TAK-242 inhibits TLR4 signalling by binding to Cys747 in the intracellular domain of TLR4. However, although these data indicate that a Cys residue interacts with TAK-242, they do not provide insight into the nature of the interaction.

Very recently, Patra et al. published their in silico studies, where they did the molecular docking of TAK-242 with their constructed full-length structural model of TLR4. TAK-242 has been reported to bind to the conserved C747, located in the helix αC of the TIR domain, while the C747 of each monomer face each other, creating a pocket for TAK-242 binding (Figure 1.17). They also showed that TAK-242 induces

conformational alterations in the residues neighboring C747 for its antagonistic interaction with TLR4.[90]

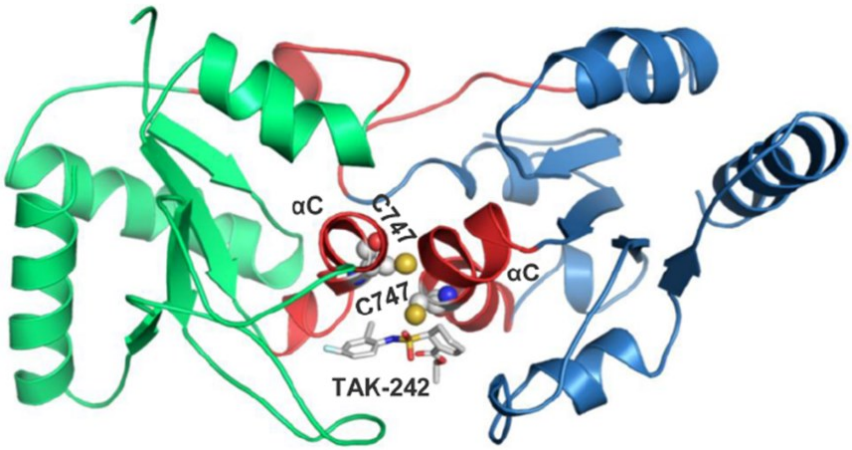

Figure 1.17. Interaction of the TAK-242 ligand with C747 in the TIR domain of TLR4 dimer. (Figure copied with permission from Patra et al.[90])

When a docked conformation TAK-242 inside the TIR domain of TLR4 dimer was visualized after 100 ns of MD simulation, they found that the TAK-242 cyclohexane ring remained ~2.5 Å away from the -SH group of C747 throughout the MD simulation (Figure 1.18).

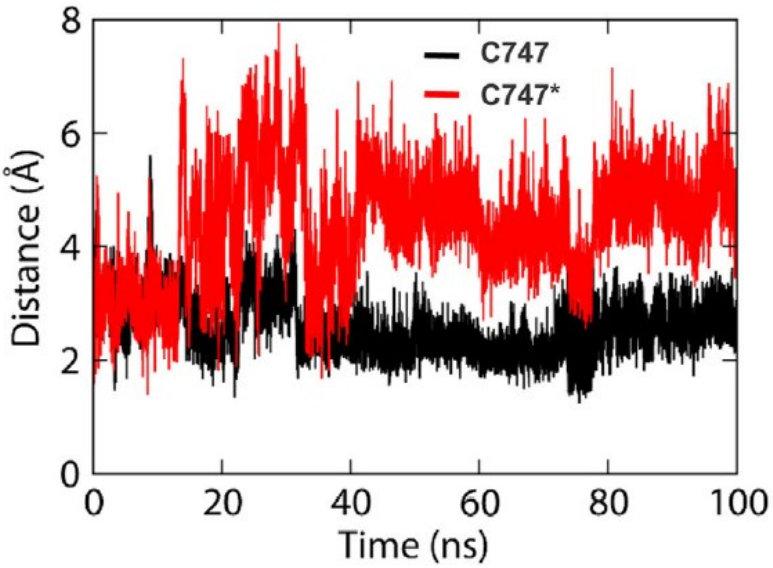

Figure 1.18. Distance between the TAK-242 cyclohexane ring and the –SH group of C747 of both TIR monomers. C747* refers to the residue of the relative monomer (Figure copied with permission from Patra et al.[90]).

1.10 Proposed Chemical Interaction between TLR4 and TAK-242

The mechanism by which TAK-242 inhibits TLR4 is unclear, but the most recent research suggests that the interaction of TAK-242 with the TIR domain of TLR4 might disrupt the subsequent stages in the TLR4 signaling pathway.[95] The affinity of TAK-242 towards the C747 residue of TLR4 suggested the occurrence of a Michael addition, also known as a conjugate addition or 1,4-addition. This is based on the presence of an α,β-unsaturated carbonyl group in TAK-242 and the nucleophilic C747 residue of TLR4.[91] The α,β-unsaturated carbonyl group is considered a electrophilic moiety since it can undergo a Michael addition, while the nucleophilic C747 residue functions as a Michael donor. In mechanistic terms, the nucleophilic thiol (–SH) group present on Cys can attack the electrophilic β-carbon of TAK-242, followed by proton transfer and loss of the C=C double bond and formation of new C–S and C–H single bonds (Figure 1.19). A similar covalent inhibition, where Cys or Lys residues undergo conjugate addition to an α,β-unsaturated carbonyl system already has been studied during the development of hepatitis C viral (HCV) protease, epidermal growth factor receptor, tyrosine kinases, fibroblast growth factor receptors (FGFR1–4), and Bruton's tyrosine kinase (Btk) inhibitors.[83,96–100]

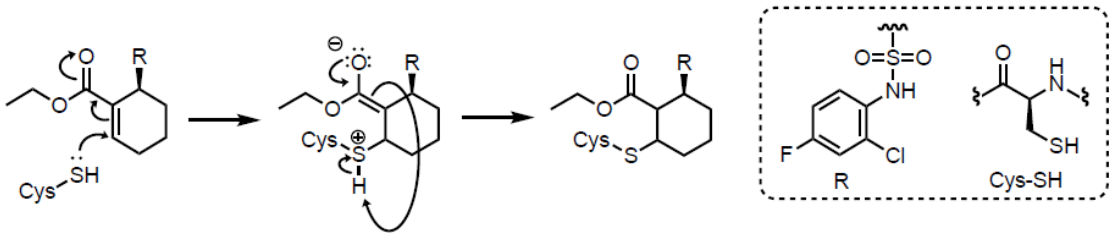

Figure 1.19. The proposed Michael addition mechanism between TAK-242 and the thiol group of C747 residue in TLR4.

1.11 Conclusion

Cisplatin is considered one of the most ototoxic pharmacologic agents, typically causing bilateral high frequency sensorineural hearing loss with progression to lower frequencies with continued exposure. Cisplatin-induced ototoxicity (CIO) can have

life-long debilitating consequences in children by impairing speech and language development, social-emotional development, and increasing the risk of learning difficulties. When childhood patients exhibit CIO, cisplatin doses are reduced, which compromises anticancer efficacy. So far it has been established that the cisplatin induced ototoxicity can be inhibited by developing TLR4 antagonists to inhibit signal propagation through adapter protein recruitment on the cytoplasmic face of the membrane. Several promising early therapies point to the possibility of developing effective otoprotectants without compromising the anticancer activity of cisplatin. However, the activities of the reported therapies to date are suboptimal in terms of clinical properties, including potency and safety. Thus, further design and development of potent inhibitors with optimized physio-chemical properties are required to inhibit inflammatory activity of TLR4. In addition, no previous in silico studies were done to analyze the molecular interactions between TLR4 and its possible antagonists.

In this thesis, synthesis, biological evaluations of TAK-242 derivatives, and in silico analysis of the binding modes between TLR4 and its inhibitors are described. Besides that, as a part of my PhD research at the beginning of my graduate studies, I worked on another anticancer project that focused on screening a library of Nitrofen (NT) analogues to investigate the invasive behavior of triple negative breast cancer (TNBC) cells, with the objective of identifying potent metastatic inhibitors that do not display teratogenicity or carcinogenicity. The details of this research project are discussed in Chapter 4.

In Chapter 2, development of three different series of generations (A, B, and C) TAK-242 derivatives by structure-based design and their synthesis through various modifications on three different sites of TAK-242 using facile, reproducible, and robust methods are discussed. The inhibitory activity of the synthesized compounds on TLR4 by using in vitro and in vivo assays is described. The structure activity relationship analysis based on biological results is presented as well. Both cell-based assays and animal studies have identified two compounds that showed improved inhibitory effect on the TLR4 inflammatory activity compared to the parent compound TAK-242.

Chapter 3 describes an in silico structure–activity relationship (SAR) analysis between TLR4 and its synthesized antagonists along with the reference compound

TAK-242. A detailed analysis of the predicted binding mode of the best inhibitor to TLR4 derived from molecular dynamics simulations is also discussed.

In Chapter 2, we used the reported TIR domain of TLR4 protein model for the computational studies. We considered C747 of TLR4 as a reference residue to perform molecular docking of our synthesised TAK-242 derivatives with it. The objectives of in silico studies are to compare the binding energy and ligand efficiency values of the TAK-242 derivatives with those of the parent compound using the TLR4 interaction domain.

Chapter 4 provides a discussion on the systematic modifications of the reference compound NT through facile synthetic routes to overcome several concerns associated with the parent compound's structure. The in vitro anti-invasiveness activity of NT derivatives is evaluated. The screening results revealed that four compounds showed significant reduction in invasive potential relative to reference compound NT, and two of them were superior to the parent scompound NT with no in vitro cytotoxic effects.

Chapter 5 provides a general summary of the findings about developing potent inhibitors for TAK-242 and the potential of improving cancer therapy. Also, this chapter addresses the future work needed for our improved inhibitors to ensure the potency, selectivity, and safety of the optimized lead compounds through in-depth biological and computational validations.

1.12 References

1. Dasari, S.; Paul, B. T. Cisplatin in Cancer Therapy: Molecular Mechanisms of Action. *Eur. J. Pharmacol.* **2014**, *740*, 364–378.
2. Siddik, Z. H. Cisplatin: Mode of Cytotoxic Action and Molecular Basis of Resistance. *Oncogene*. **2003**, *47*, 7265–7279.
3. Rocha, C. R. R.; Silva, M. M.; Quinet, A.; Cabral–Neto, J. B.; Menck, C. F. M. DNA Repair Pathways and Cisplatin Resistance: An Intimate Relationship. *Clinics.* **2018**, *73*, 1–10.
4. Khan, M. Z.; Rayaan, F. Contrast–Induced Nephropathy. *J. Med. Sci.* **2018**, *26*, 79–84.
5. Breglio, A. M.; Aaron, E. R.; Eric, D. S.; Katharine, A. F.; Katie K. S.; Katherine, M. M.; Matthew, D. H.; Lauren, A.; Lisa, L. C. Cisplatin is Retained in the Cochlea Indefinitely Following Chemotherapy. *Nat. Commun.* **2017**, *8*, 1–9.
6. Blair, J. C. The Effects of Mild Sensorineural Hearing Loss on Academic Performance of Young School–Age Children. *Volta Rev.* **1985**, *87*, 87–93.
7. Gurney, J. G.; Kevin, R. K., Nina, K. H.; Stacy, N.; Paul, C. N.; Brad, Z.; Jean, M. T.; Kirsten, K. N. Social Outcomes in the Childhood Cancer Survivor Study Cohort. *J. Clin. Oncol*. **2009**, *27*, 2390–2405.
8. Gurney, J. G.; Jean, M. T.; Kirsten, K. N.; Wendy, L.; Katherine. K. M.; Mary, L. S. Hearing Loss, Quality of Life, and Academic Problems in Long–Term Neuroblastoma Survivors: A Report from the Children's Oncology Group. *Pediatrics.* **2007**, *120*, 1229–1236.
9. Chu, Y.; Martha, S.; Jorge, O. E.; Amanda, R. P. D.; Thomas, D.; Qi, W.; Martina, R.; Peter, S. S.; Robert, M. S. Systemic Delivery and Biodistribution of Cisplatin In Vivo. *Mol. Pharm.* **2016**, *13*, 2677–2682.
10. Mukherjea, D.; Sarvesh, J.; Craig, W.; Jennifer, R. B.; Jeremy, G. T.; Leonard, P. R.; Vickram, R. Short Interfering RNA Against Transient Receptor Potential Vanilloid 1 Attenuates Cisplatin–Induced Hearing Loss in the Rat. *J. Neurosci.* **2008**, *28*, 13056–13065.
11. Chang, K. W.; Chinosornvatana, N. 2010. Practical Grading System for Evaluating Cisplatin Ototoxicity in Children. *J. Clin. Oncol*. **2010**, *28*,1788–1795.
12. Langer, T.; Zehnhoff–Dinnesen, A.; Radtke, S.; Meitert, J.; Zolk, O. Understanding Platinum–Induced Ototoxicity. *Trends Pharmacol. Sci.* **2013**, *34,* 458–469.
13. Schell, M. J.; McHaney, V. A.; Green, A. A.; Kun, L. E.; Hayes, F. A.; Horowitz, M.; Meyer, W. H. Hearing Loss in Children and Young Adults Receiving Cisplatin with or without Prior Cranial Irradiation. *J. Clin. Oncol*, **1989**, *7*, 754–760.
14. Ross, C. J.; Katzov–Eckert, H.; Dubé, M. P.; Brooks, B.; Rassekh, S. R.; Barhdadi, A.; Feroz–Zada, Y.; Visscher, H.; Brown, A. M.; Rieder, M. J.; Rogers, P. C. 2009. Genetic Variants in TPMT and COMT are Associated with Hearing Loss in Children Receiving Cisplatin Chemotherapy. *Nat. Genet.* **2009**, *41*,1345–1349.

15. Travis, L. B.; Fossa, S. D.; Sesso, H. D.; Frisina, R. D.; Herrmann, D. N.; Beard, C. J.; Feldman, D. R.; Pagliaro, L. C.; Miller, R. C.; Vaughn, D. J.; Einhorn, L. H. Chemotherapy–Induced Peripheral Neurotoxicity and Ototoxicity: New Paradigms for Translational Genomics. *J. Natl. Cancer Inst*. **2014**, *106,* 1–13.
16. Hudson, M. M.; Ness, K. K.; Gurney, J. G.; Mulrooney, D. A.; Chemaitilly, W.; Krull, K. R.; Green, D. M.; Armstrong, G. T.; Nottage, K. A.; Jones, K. E.; Sklar, C. A. Clinical Ascertainment of Health Outcomes Among Adults Treated for Childhood Cancer. *Jama*. **2013**, *309*, 2371–2381.
17. Dionne, F.; Mitton, C.; Rassekh, R.; Brooks, B.; Ross, C.; Hayden, M., Carleton, B. Economic Impact of a Genetic Test for Cisplatin–Induced Ototoxicity. *Pharmacogenomics J*. **2012**, *12*, 205–213.
18. Lim, D. J. Functional Structure of The Organ of Corti: A Review. *Hear. Res*. **1986**, *22*, 117–146.
19. Schellack, N.; Naude, A. An Overview of Pharmacotherapy–Induced Ototoxicity. *S. Afr. Fam. Pract.* **2013**, *55*, 357–366.
20. Kopke, R.; Allen, K. A., Henderson, D.; Hoffer, M.; Frenz, D.; Van De Water, T. A Radical Demise: Toxins and Trauma Share Common Pathways in Hair Cell Death. *Ann. N. Y. Acad. Sci*. **1999**, *884*, 171–191.
21. Ford, M. S.; Maggirwar, S. B.; Rybak, L. P.; Whitworth, C.; Ramkumar, V. Expression and Function of Adenosine Receptors in the Chinchilla Cochlea. *Hear. Res*. **1997**, *105*, 130–140.
22. Oh, S. H.; Yu, W. S.; Song, B. H.; Lim, D.; Koo, J. W.; Chang, S. O.; Kim, C. S. Expression of Heat Shock Protein 72 in Rat Cochlea with Cisplatin–Induced Acute Ototoxicity. *Acta Oto-laryngologica*. **2000**, *120*, 146–150.
23. Mukherjea, D.; Whitworth, C. A.; Nandish, S.; Dunaway, G. A.; Rybak, L. P.; Ramkumar, V. Expression of the Kidney Injury Molecule 1 in the Rat Cochlea and Induction by Cisplatin. *Neurosci. J.* **2006**, *139*, 733–740.
24. So, H. S.; Kim, H. J.; Lee, J. H.; Park, S. Y.; Park, C.; Kim, Y. H.; Kim, J. K.; Lee, K. M.; Kim, K. S.; Chung, S. Y.; Jang, W. C. Flunarizine Induces Nrf2–Mediated Transcriptional Activation of Heme Oxygenase–1 in Protection of Auditory Cells from Cisplatin. *Cell Death Differ*. **2006**, *13*, 1763–1775.
25. Clerici, W. J.; Yang, L. Direct Effects of Intraperilymphatic Reactive Oxygen Species Generation on Cochlear Function. *Hear. Res*. **1996**, *101*, 14–22.
26. Kopke, R. D.; Liu, W.; Gabaizadeh, R.; Jacono, A.; Feghali, J. Use of Organotypic Cultures of Corti's Organ to Study the Protective Effects of Antioxidant Molecules on Cisplatin–Induced Damage of Auditory Hair Cells. *An. J. Otol*. **1997**, *18*, 559–571.

27. Church, M. W.; Kaltenbach, J. A.; Blakley, B. W.; Burgio, D. L. The Comparative Effects of Sodium Thiosulfate, Diethyldithiocarbamate, Fosfomycin and WR–2721 on Ameliorating Cisplatin–Induced Ototoxicity. *Hear. Res*. **1995**, *86*, 195–203.
28. Rybak, L. P.; Ravi, R.; Somani, S. M. Mechanism of Protection by Diethyldithiocarbamate Against Cisplatin Ototoxicity: Antioxidant System. *Fundam. Appl. Toxicol.* **1995**, *26*, 293–300.
29. Kim, H. J.; Lee, J. H.; Kim, S. J.; Oh, G. S.; Moon, H. D.; Kwon, K. B.; Park, C.; Park, B. H.; Lee, H. K.; Chung, S. Y.; Park, R. Roles of NADPH Oxidases in Cisplatin–Induced Reactive Oxygen Species Generation and Ototoxicity. *J. Neurosci*. **2010**, *30*, 3933–3946.
30. Ravi, R.; Somani, S. M.; Rybak, L. P. Mechanism of Cisplatin Ototoxicity: Antioxidant System. *Pharmacol. Toxicol*. **1995**, *76*, 386–394.
31. So, H.; Kim, H.; Lee, J. H.; Park, C.; Kim, Y.; Kim, E.; Kim, J. K.; Yun, K. J.; Lee, K. M.; Lee, H. Y.; Moon, S. K. Cisplatin Cytotoxicity of Auditory Cells Requires Secretions of Proinflammatory Cytokines Via Activation of ERK and NF–κ B. *J. Assoc. Res. Otolaryngol*. **2007**, *8*, 338–355.
32. Ruijven, M. W.; Groot, J. C.; Smoorenburg, G. F. Time Sequence of Degeneration Pattern in the Guinea Pig Cochlea During Cisplatin Administration.: A Quantitative Histological Study. *Hear. Res*. **2004**, *197*, 44–54.
33. Thomas, A. J.; Hailey, D.W.; Stawicki, T. M.; Wu, P.; Coffin, A. B.; Rubel, E. W.; Raible, D.W.; Simon, J. A., Ou, H. C. Functional Mechanotransduction Is Required for Cisplatin–Induced Hair Cell Death in the Zebrafish Lateral Line. *J. Neurosci*. **2013**, *33*, 4405–4414.
34. Rybak, L. P.; Whitworth, C. A.; Mukherjea, D.; Ramkumar, V. Mechanisms of Cisplatin–Induced Ototoxicity and Prevention. *Hear. Res*. **2007**, *226*, 157–167.
35. Dickey, D. T.; Muldoon, L. L.; Doolittle, N. D.; Peterson, D. R.; Kraemer, D. F.; Neuwelt, E. A. Effect of N–acetylcysteine Route of Administration on Chemoprotection Against Cisplatin–Induced Toxicity in Rat Models. *Cancer Chemother. Pharmacol.* **2008**, *62*, 235–241.
36. Choe, W. T.; Chinosornvatana, N.; Chang, K. W. Prevention of Cisplatin Ototoxicity Using Transtympanic N–Acetylcysteine and Lactate. *Otol. Neurotol.* **2004**, *25*, 910–915.
37. Otto, W. C.; Brown, R. D.; Gage–White, L.; Kupetz, S.; Anniko, M.; Penny, J. E.; Henley, C. M. Effects of Cisplatin and Thiosulfate Upon Auditory Brainstem Responses of Guinea Pigs. *Hear. Res*, **1988**, *35*, 79–85.
38. Wimmer, C.; Mees, K.; Stumpf, P.; Welsch, U.; Reichel, O.; Suckfüll, M. Round Window Application of D–methionine, Sodium Thiosulfate, Brain–Derived Neurotrophic Factor, and Fibroblast Growth Factor–2 in Cisplatin–Induced Ototoxicity. *Otol. Neurotol.* **2004**, *25*, 33–40.
39. Church, M. W.; Blakley, B. W.; Burgio, D. L.; Gupta, A. K. WR–2721 (Amifostine) Ameliorates Cisplatin–Induced Hearing Loss but Causes Neurotoxicity in Hamsters: Dose–Dependent Effects. *J. Assoc. Res. Otolaryngol*. **2004**, *5*, 227–237.

40. Ekborn, A.; Laurell, G.; Johnström, P.; Wallin, I.; Eksborg, S.; Ehrsson, H. D–Methionine and Cisplatin Ototoxicity in the Guinea Pig: D–Methionine Influences Cisplatin Pharmacokinetics. *Hear. Res*. **2002**, *165,* 53–61.
41. Marina, N.; Chang, K. W.; Malogolowkin, M.; London, W. B.; Frazier, A. L.; Womer, R. B.; Rescorla, F.; Billmire, D. F.; Davis, M. M.; Perlman, E. J.; Giller, R. Amifostine Does Not Protect Against the Ototoxicity of High-Dose Cisplatin Combined with Etoposide and Bleomycin in Pediatric Germ-Cell Tumors: A Children's Oncology Group Study. *Cancer*. **2005**, *104*, 841–847
42. Sastry, J.; Kellie, S. J. Severe Neurotoxicity, Ototoxicity and Nephrotoxicity Following High–Dose Cisplatin and Amifostine. *Pediatr. Hematol. Oncol.* **2005***, 22*, 441–445.
43. More, S. S.; Akil, O.; Ianculescu, A. G.; Geier, E. G.; Lustig, L. R.; Giacomini, K. M. Role of the Copper Transporter, CTR1, in Platinum–Induced Ototoxicity. *J. Neurosci*. **2010**, *30*, 9500–9509.
44. Lanvers–Kaminsky, C.; Sprowl, J. A.; Malath, I.; Deuster, D.; Eveslage, M.; Schlatter, E.; Mathijssen, R. H.; Boos, J.; Jürgens, H.; am Zehnhoff–Dinnesen, A. G.; Sparreboom, A. Human OCT2 Variant c.808G> T Confers Protection Effect Against Cisplatin–Induced Ototoxicity. *Pharmacogenomics J*. **2015**, *16*, 323–332.
45. Freyer, D. R.; Chen, L.; Krailo, M. D.; Knight, K.; Villaluna, D.; Bliss, B.; Pollock, B. H.; Ramdas, J.; Lange, B.; Van Hoff, D.; VanSoelen, M. L. Effects of Sodium Thiosulfate Versus Observation on Development of Cisplatin–Induced Hearing Loss in Children with Cancer (ACCL0431): A Multicentre, Randomised, Controlled, Open–Label, Phase 3 Trial. *Lancet Oncol.* **2017**, *18*, 63–74.
46. Mukherjea, D.; Rybak, L. P. Pharmacogenomics of Cisplatin–Induced Ototoxicity. *Pharmacogenomics J*. **2011**, *12*, 1039–1050.
47. Lee, J. W.; Pussegoda, K.; Rassekh, S. R.; Monzon, J. G.; Liu, G.; Hwang, S.; Bhavsar, A. P.; Pritchard, S.; Ross, C. J.; Amstutz, U.; Carleton, B. C. Clinical Practice Recommendations for the Management and Prevention of Cisplatin–Induced Hearing Loss Using Pharmacogenetic Markers. *Ther. Drug Monit.* **2016**, *38*, 423–431.
48. Pussegoda, K.; Ross, C. J.; Visscher, H.; Yazdanpanah, M.; Brooks, B.; Rassekh, S. R.; Zada, Y. F.; Dubé, M. P.; Carleton, B. C.; Hayden, M. R. Replication of TPMT and ABCC3 Genetic Variants Highly Associated with Cisplatin-Induced Hearing Loss in Children. *Clin. Pharm. Therap.* **2013**, *94*, 243–251.
49. Maranville, J. C.; Cox, N. J. Pharmacogenomic Variants have Larger Effect Sizes Than Genetic Variants Associated with Other Dichotomous Complex Traits. *Pharmacogenomics J*. **2016**, *16*, 388–392.

50. Bhavsar, A. P.; Gunaretnam, E. P.; Li, Y.; Hasbullah, J. S.; Carleton, B. C.; Ross, C. J. Pharmacogenetic Variants in TPMT Alter Cellular Responses to Cisplatin in Inner Ear Cell Lines. *PloS one*. **2017**, *12*, 711–727.
51. Oh, G. S.; Kim, H. J.; Choi, J. H.; Shen, A.; Kim, C. H.; Kim, S. J.; Shin, S. R.; Hong, S. H.; Kim, Y.; Park, C.; Lee, S. J. Activation of Lipopolysaccharide–TLR4 Signaling Accelerates the Ototoxic Potential of Cisplatin in Mice. *J. Immunol.* **2011**, *186*, 1140–1150.
52. Kalinec, G. M.; Webster, P.; Lim, D. J.; Kalinec, F. A Cochlear Cell Line as an In Vitro System for Drug Ototoxicity Screening. *Audiol. Neurootol.* **2003**, *8*, 177–189.
53. Ragnarsdottir, B.; Jönsson, K.; Urbano, A.; Grönberg–Hernandez, J.; Lutay, N.; Tammi, M.; Gustafsson, M.; Lundstedt, A. C.; Leijonhufvud, I.; Karpman, D.; Wullt, B. Toll–Like Receptor 4 Promoter Polymorphisms: Common TLR4 Variants May Protect Against Severe Urinary Tract Infection. *PloS one*. **2010**, *5*, 10734–10751.
54. Faure, E.; Thomas, L.; Xu, H.; Medvedev, A. E.; Equils, O.; Arditi, M. Bacterial Lipopolysaccharide and IFN–α Induce Toll–Like Receptor 2 and Toll–Like Receptor 4 Expression in Human Endothelial Cells: Role Of NF–κB Activation. *J. Immunol.* **2001**, *166*, 2018–2024.
55. Muzio, M.; Bosisio, D.; Polentarutti, N.; D'amico, G.; Stoppacciaro, A.; Mancinelli, R.; van't Veer, C.; Penton–Rol, G.; Ruco, L. P.; Allavena, P.; Mantovani, A. Differential Expression and Regulation of Toll–Like Receptors (TLR) in Human Leukocytes: Selective Expression of TLR3 in Dendritic Cells. *J. Immunol.* **2000**, *164*, 5998–6004.
56. Babolmorad, G.; Latif, A.; Domingo, I. K.; Pollock, N. M.; Delyea, C.; Rieger, A. M.; Allison, W. T.; Bhavsar, A. P. Toll-Like Receptor 4 is Activated by Platinum and Contributes to Cisplatin-Induced Ototoxicity. *EMBO Rep*. **2021**, *22*, 51280–51298.
57. Kawasaki, T.; Kawai, T. Toll–Like Receptor Signaling Pathways. *Front. Immunol.* **2014**, *5*, 461–478.
58. Salaun, B.; Romero, P.; Lebecque, S. Toll-Like Receptors' Two-Edged Sword: When Immunity Meets Apoptosis. *Eur. J. Immunol*. **2007***, 37*, 3311–3318.
59. Wardill, H. R.; Van Sebille, Y. Z.; Mander, K. A.; Gibson, R. J.; Logan, R. M.; Bowen, J. M.; Sonis, S. T. Toll–Like Receptor 4 Signaling: A Common Biological Mechanism of Regimen–Related Toxicities: An Emerging Hypothesis for Neuropathy and Gastrointestinal Toxicity. *Cancer Treat. Rev.* **2005**, *41*, 122–128.
60. Park, B. S.; Lee, J. O. Recognition of Lipopolysaccharide Pattern by TLR4 Complexes. *Exp. Mol. Med.* **2013**, *45*, 66–76.
61. Singh, A.; Singh, V.; Tiwari, R. L.; Chandra, T.; Kumar, A.; Dikshit, M.; Barthwal, M. K. The IRAK–ERK–P67phox–Nox–2 Axis Mediates TLR4, 2–Induced ROS Production For IL–1 B Transcription and Processing in Monocytes. *Cell. Mol. Immunol.* **2016**, *13*, 745–763.

62. West, A. P.; Brodsky, I. E.; Rahner, C.; Woo, D. K.; Erdjument–Bromage, H.; Tempst, P.; Walsh, M. C.; Choi, Y.; Shadel, G. S.; Ghosh, S. TLR Signalling Augments Macrophage Bactericidal Activity Through Mitochondrial ROS. *Nature*, **2011**, *472*, 476–480.
63. Haase, R.; Kirschning, C. J.; Sing, A.; Schröttner, P.; Fukase, K.; Kusumoto, S.; Wagner, H.; Heesemann, J.; Ruckdeschel, K. A Dominant Role of Toll–Like Receptor 4 in the Signaling of Apoptosis in Bacteria–Faced Macrophages. *J. Immunol.* **2003**, *171*, 4294–4303.
64. Jalleh, R.; Koh, K.; Choi, B.; Liu, E.; Maddison, J.; Hutchinson, M. R. Role of Microglia and Toll–Like Receptor 4 in the Pathophysiology of Delirium. *Med. Hypotheses.* **2012**, *79*, 735–739.
65. Kalinec, G.; Thein, P.; Park, C.; Kalinec, F. HEI–OC1 Cells as a Model for Investigating Drug Cytotoxicity. *Hear. Res*. **2016**, *335*, 105–117.
66. Kaur, T.; Mukherjea, D.; Sheehan, K.; Jajoo, S.; Rybak, L. P.; Ramkumar, V. Short Interfering RNA Against STAT1 Attenuates Cisplatin–Induced Ototoxicity in The Rat by Suppressing Inflammation. *Cell Death Dis.* **2011**, *2*, 180–190.
67. Rivolta, M. N.; Holley, M. C. Cell Lines in Inner Ear Research. *J. Neurobiol.* **2002**, *53*, 306–318.
68. Ohnishi, H.; Skerleva, D.; Kitajiri, S. I.; Sakamoto, T.; Yamamoto, N.; Ito, J.; Nakagawa, T. Limited Hair Cell Induction from Human Induced Pluripotent Stem Cells Using a Simple Stepwise Method. *Neurosci. J. Letters*. **2015**, *599*, 49–54.
69. Oshima, K.; Shin, K.; Diensthuber, M.; Peng, A. W.; Ricci, A. J., Heller, S. Mechanosensitive Hair Cell–Like Cells from Embryonic and Induced Pluripotent Stem Cells. *Cell*. **2010**, *141*, 704–716.
70. Devarajan, P.; Savoca, M.; Castaneda, M. P.; Park, M. S.; Esteban-Cruciani, N.; Kalinec, G.; Kalinec, F. Cisplatin-Induced Apoptosis in Auditory Cells: Role of Death Receptor and Mitochondrial Pathways. *Hear. Res*. **2002**, *174*, 45–54.
71. Kalinec, F.; Kalinec, G.; Boukhvalova, M., Kachar, B. Establishment and Characterization of Conditionally Immortalized Organ of Corti Cell Lines. *Cell Biol. Int.* **1999***, 23*, 175–184.
72. So, H.; Kim, H.; Kim, Y.; Kim, E.; Pae, H. O.; Chung, H. T.; Kim, H. J.; Kwon, K. B.; Lee, K. M.; Lee, H. Y.; Moon, S. K. Evidence that Cisplatin–Induced Auditory Damage is Attenuated by Downregulation of Pro–Inflammatory Cytokines via Nrf2/HO–1. *J. Assoc. Res. Otolaryngol*, **2008**, *9*, 290–306.
73. Yin, H.; Sun, G.; Yang, Q.; Chen, C.; Qi, Q.; Wang, H.; Li, J. NLRX1 Accelerates Cisplatin–Induced Ototoxity in HEI–OC1 Cells via Promoting Generation of ROS and Activation of JNK Signaling Pathway. *Sci. Rep*. **2017**, *7*, 1–14.
74. Ton, C.; Parng, C. The Use of Zebrafish for Assessing Ototoxic and Otoprotective Agents. *Hear. Res*. **2005**, *208*, 79–88.

75. Kari, G.; Rodeck, U.; Dicker, A. P. Zebrafish: An Emerging Model System for Human Disease and Drug Discovery. *Clin. Pharm. Therap.* **2007**, *82*, 70–80.
76. Ou, H. C.; Raible, D. W.; Rubel, E. W. Cisplatin–Induced Hair Cell Loss in Zebrafish (Danio Rerio) Lateral Line. *Hear. Res*. **2007**, *233*, 46–53.
77. Uribe, P. M.; Mueller, M. A.; Gleichman, J. S.; Kramer, M. D.; Wang, Q.; Sibrian–Vazquez, M.; Strongin, R. M.; Steyger, P. S.; Cotanche, D. A.; Matsui, J. I. Dimethyl Sulfoxide (DMSO) Exacerbates Cisplatin–Induced Sensory Hair Cell Death in Zebrafish (Danio Rerio). *PLoS One*. **2013**, *8*, 55359–55370.
78. Coffin, A. B.; Ramcharitar, J. Chemical Ototoxicity of the Fish Inner Ear and Lateral Line. *Fish Hearing and Bioacoustics*. **2016**, 419–437.
79. Sepulcre, M. P.; Alcaraz–Pérez, F.; López–Muñoz, A.; Roca, F. J.; Meseguer, J.; Cayuela, M. L.; Mulero, V. Evolution of Lipopolysaccharide (LPS) Recognition and Signaling: Fish TLR4 Does Not Recognize LPS and Negatively Regulates NF–κB Activation. *J. Immunol.* **2009**, *182*, 1836–1845.
80. He, Q.; Zhang, C.; Wang, L.; Zhang, P.; Ma, D.; Lv, J.; Liu, F. Inflammatory Signaling Regulates Hematopoietic Stem and Progenitor Cell Emergence in Vertebrates. *Am. J. Hematol*. **2015**, *125*, 1098–1106.
81. Chang, M. Y.; Cheng, Y. C.; Hsu, S. H.; Ma, T. L.; Chou, L. F.; Hsu, H. H.; Tian, Y. C.; Chen, Y. C.; Sun, Y. J.; Hung, C. C.; Pan, R. L. Leptospiral Outer Membrane Protein Lipl32 Induces Inflammation and Kidney Injury in Zebrafish Larvae. *Sci. Rep.* **2016**. *6*, 1–12.
82. Yamada, M.; Ichikawa, T.; Ii, M.; Sunamoto, M.; Itoh, K.; Tamura, N.; Kitazaki, T. Discovery of Novel and Potent Small–Molecule Inhibitors of NO And Cytokine Production as Antisepsis Agents: Synthesis and Biological Activity of Alkyl 6– (N–Substituted Sulfamoyl) Cyclohex–1–Ene–1–Carboxylate. *J. Med. Chem.* **2005**, *48*, 7457–7467.
83. Jackson, P. A.; Widen, J. C.; Harki, D. A.; Brummond, K. M. 2017. Covalent Modifiers: A Chemical Perspective on the Reactivity of α, β–unsaturated Carbonyls with Thiols via Hetero–Michael Addition Reactions. *J. Med. Chem.* **2017**, *60*, 839–885.
84. Patra, M. C.; Choi, S. Recent Progress in The Development of Toll–Like Receptor (TLR) Antagonists. *Expert. Opin. Ther. Pat*. **2016**, *26*, 719–730.
85. Bhattacharyya, S.; Wang, W.; Tamaki, Z.; Shi, B.; Yeldandi, A.; Tsukimi, Y.; Yamasaki, M.; Varga, J. Pharmacological Inhibition of Toll–Like Receptor–4 Signaling by TAK242 Prevents and Induces Regression of Experimental Organ Fibrosis. *Front. Immunol.* **2018**, *9*, 2434–2448.
86. Medzhitov, R.; Preston–Hurlburt, P.; Janeway, C. A. A Human Homologue of The Drosophila Toll Protein Signals Activation of Adaptive Immunity. *Nature*. **2018**, *388*, 394–397.
87. Krishnan, J.; Anwar, M. A.; Choi, S. TLR4 (Toll–Like Receptor 4). *Journal: Encyclopedia of Signaling Molecules*. **2018**, 5472–5483.

88. Mineev, K. S.; Goncharuk, S. A.; Goncharuk, M. V.; Volynsky, P. E.; Novikova, E. V.; Aresinev, A. S., 2017. Spatial Structure of TLR4 Transmembrane Domain in Bicelles Provides the Insight into the Receptor Activation Mechanism. *Sci. Rep.* **2017**, *7*, 1–12.
89. Park, B. S.; Song, D. H.; Kim, H. M.; Choi, B. S.; Lee, H.; Lee, J. O. The Structural Basis of Lipopolysaccharide Recognition by the TLR4–MD–2 Complex. *Nature*. **2009**, *458*, 1191–1195.
90. Patra, M. C.; Kwon, H. K.; Batool, M.; Choi, S. Computational Insight into the Structural Organization of Full–Length Toll–Like Receptor 4 Dimer in a Model Phospholipid Bilayer. *Front. Immunol.* **2018***, 9*, 489–502.
91. Takashima, K.; Matsunaga, N.; Yoshimatsu, M.; Hazeki, K.; Kaisho, T.; Uekata, M.; Hazeki, O.; Akira, S.; Iizawa, Y.; Ii, M. Analysis of Binding Site for the Novel Small-Molecule TLR4 Signal Transduction Inhibitor TAK-242 and Its Therapeutic Effect on Mouse Sepsis Model. *Br. J. Pharmacol*. **2009**, *157*, 1250–1262.
92. Dragovich, P. S.; Webber, S. E.; Babine, R. E.; Fuhrman, S. A.; Patick, A. K.; Matthews, D. A.; Reich, S. H.; Marakovits, J. T.; Prins, T. J.; Zhou, R.; Tikhe, J. Structure–Based Design, Synthesis, and Biological Evaluation of Irreversible Human Rhinovirus 3C Protease Inhibitors. 2. Peptide Structure− Activity Studies. *J. Med. Chem.* **1998**, *41*, 2819–2834.
93. Zhu, S.; Hudson, T. H.; Kyle, D. E.; Lin, A. J. Synthesis and In Vitro Studies of Novel Pyrimidinyl Peptidomimetics as Potential Antimalarial Therapeutic Agents. *J. Med. Chem.* **2002**, *45*, 3491–3496.
94. Matthews, D. A.; Dragovich, P. S.; Webber, S. E.; Fuhrman, S. A.; Patick, A. K.; Zalman, L. S.; Hendrickson, T. F.; Love, R. A.; Prins, T. J.; Marakovits, J. T.; Zhou, R. Structure–Assisted Design of Mechanism–Based Irreversible Inhibitors of Human Rhinovirus 3C Protease with Potent Antiviral Activity Against Multiple Rhinovirus Serotypes. *Proc. Natl. Acad. Sci*. **1999**, *96*, 11000–11007.
95. Kong, W., Merino, E. and Nevado, C., 2014. Arylphosphonylation and arylazidation of activated alkenes. *Angewandte Chemie International Edition*, *53*(20), pp.5078–5082.
96. Liu, R.; Yue, Z.; Tsai, C. C.; Shen, J. Assessing Lysine and Cysteine Reactivities for Designing Targeted Covalent Kinase Inhibitors. *J. Am. Chem. Soc.* **2019**, *141*, 6553–6560.
97. Pettinger, J.; Carter, M.; Jones, K.; Cheeseman, M. D. Kinetic Optimization of Lysine–Targeting Covalent Inhibitors of HSP72. *J. Med. Chem.* **2019**, *62*, 11383–11398.
98. Zhang, T.; Hatcher, J. M.; Teng, M.; Gray, N. S.; Kostic, M. Recent Advances in Selective and Irreversible Covalent Ligand Development and Validation. *Cell Chem. Biol*. **2019**, *26*, 1486–1500.
99. Cheng, S. S.; Yang, G. J.; Wang, W.; Leung, C. H.; Ma, D. L. The Design and Development of Covalent Protein–Protein Interaction Inhibitors for Cancer Treatment. *J. Hematol. Oncol.* **2020**, *13*, 1–14.

100. Butler, K.V.; Ma, A.; Yu, W.; Li, F.; Tempel, W.; Babault, N.; Pittella–Silva, F.; Shao, J.; Wang, J.; Luo, M.; Vedadi, M. Structure–Based Design of a Covalent Inhibitor of the SET Domain–Containing Protein 8 (SETD8) Lysine Methyltransferase. *J. Med. Chem.* **2016**, *59*, 9881–9889.

Chapter 2

Design, Synthesis, and Biological Evaluations of TLR4 Antagonists to Mitigate Cisplatin-induced Ototoxicity

2.1 Introduction

While being a highly effective chemotherapeutic agent for treating pediatric malignancies, cisplatin can cause sensorineural hearing loss in children, which is known as cisplatin-induced ototoxicity (CIO).[1] This resultant hearing loss affects patients' ability to learn, their language development, and social life. When patients exhibit CIO, cisplatin doses are reduced, which compromises the anti-cancer efficacy. To date, limited success in otoprotection without compromised anticancer effect has been observed in clinical trials.[1–10]

Toll Like Receptor 4 (TLR4), a family of type I transmembrane glycoproteins, recognizes highly conserved patterns on gram-negative bacteria lipopolysaccharide (LPS) and viruses (viral proteins). It also can recognize damage-associated molecular patterns (DAMPs) and transition metals, such as nickel, cobalt, and palladium.[11,12] The binding of the ligand to the extracellular domain of the TLR4 leads to the conformational changes of the receptor and subsequent TLR4 homodimerization required for TLR4 activation.[13] TLR4 TIR domain dimerization causes the recruitment of adaptor proteins and initiation of either TLR4/MyD88/NF-κB or TLR4/TRIF/IRF3 signaling pathways that trigger pro-inflammatory cytokine/chemokine and interferon secretion.[14] Recently, the association of TLR4 with CIO also was validated through in vitro and in vivo experiments.[17]

In 2005, during development of new therapeutic agent for sepsis, Yamada and co-workers synthesized and identified a novel cyclohexene derivative called TAK-242, which is capable of selectively-inhibiting TLR4 signaling.[2] In the presence of TAK-242, there is a decrease in the secretion of pro-inflammatory cytokines, which are released during the TLR4 signaling pathway, and this effect on TLR4 results in an overall decrease of inflammation.[18] The mechanism by which TAK-242 inhibits TLR4 is unclear, but the most recent research by Takashima and co-workers suggests that the

Cys747 residue on TLR4 plays a critical role in the TAK-242 inhibition mechanism.[19] Although these data do not provide insight into the nature of the interaction, it is believed TAK-242 can bind to Cys747 of TLR4 as a Michael acceptor, disrupting subsequent stages in the TLR4 signaling pathway (Figure 2.1).

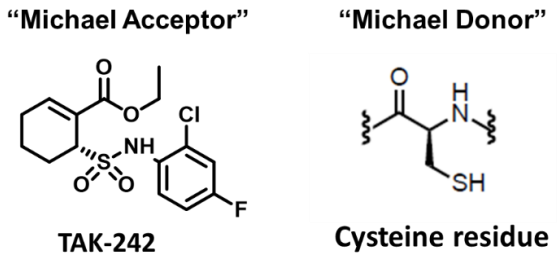

Figure 2.1. Structure of TAK-242, a Michael acceptor, and the Michael donor cysteine.

To determine if Michael addition is occurring, certain modifications to the structure of TAK-242 can be made that will prevent 1,4-addition. For instance, replacement of the TAK-242 cyclohexene moiety with an aromatic ring would render Michael addition unlikely due to the need to disrupt aromaticity. Therefore, it would be beneficial to explore the interaction between TAK-242 and TLR4 by altering the structure of TAK-242 to remove its Michael acceptor reactivity and to test how these changes affect TLR4 activation. Ideally, this will allow for the design of TAK-242 derivatives with varying control over TLR4 activity, which potentially can be used as chemotherapeutic agents to treat cisplatin induced ototoxicity (CIO).

While to date there has been no co-crystallization of TLR4 with TAK-242 or NMR structural work, recent computational studies have refined the model for TAK-242 binding to TLR4 dimer.[20] This work suggested that a cavity at the dimeric interface can accommodate TAK-242, with close contacts to the Cys747 of both monomers, a hydrogen bonding interaction with a nearby glutamine sidechain, and a hydrophobic pocket into which the aromatic ring can insert. This nonpolar region appears to have enough space to accommodate additional steric bulk in the region of the aromatic ring. Therefore, this part of the molecule can be modified to capture additional energetically favorable van der Waals interactions with the nearby side chains.

The aim of this project is to develop new TLR4 antagonists that prevent CIO without interfering with the normal function of TLR4 in bacterial responsiveness; this could be an important step in mitigating cisplatin side effects in childhood cancer treatment. In this study, we have conducted a structure activity relationship analysis through synthesis of different series of compounds, based on modification of specific sites of TAK-242. We synthesized a library of non-Michael acceptor derivatives of TAK-242 to test the hypothesis of involvement of the thiol group of Cys747 in protein-ligand interaction. A list of TAK-242 derivatives with various amine groups was synthesized to explore if the inhibition of TLR4 signaling depends solely on Michael addition or if additional interactions, such as hydrophobic or hydrogen bonding interactions, also play important roles in TAK-242 inhibitory activity.

Syntheses of all compounds were carried out according to the reported procedures with minor modifications, following straightforward and convergent routes and characterized with ^{1}H and ^{13}C nuclear magnetic resonance (NMR), mass spectrometry (MS), and Fourier-transform infrared spectroscopy (FTIR). Then, the compounds were screened to find potent inhibitors in vitro and in vivo.

2.2 Results and Discussion

2.2.1 Selective Modifications of TAK-242 Scaffold

In this study, we have conducted a structure activity relationship analysis based around the hit compound, ethyl (6R)-6-[N-(2-chloro-4-fluorophenyl)sulfamoyl]cyclohex-1-ene-1-carboxylate (TAK-242) **(1)**, as a reference compound, as shown in Figure 2.1. Three different series of compounds (Gen A, B, and C) have been designed and synthesized successfully through various modifications on three different sites of TAK-242.

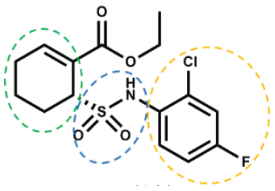

Figure 2.2. The potential modification sites of TAK-242 for hit to lead optimization.

For the first generation **(Gen A1-A5)** (Figure 2.3), the aniline moiety of TAK-242 was modified with different substituted anilines and cyclohexylamine. General synthesis of the **Gen A** compounds (Scheme 2.1) was carried out according to the literature method.[21] The chlorination reaction of compound **1** was carried out with thionyl chloride ($SOCl_2$), and the resulting intermediate compound **2** was coupled with different amine substrates in the presence of triethylamine (Et_3N) to obtain five TAK-242 analogues **(A1-A5)**. Analogues **A1** and **A2** were obtained with concomitant double bond migration.

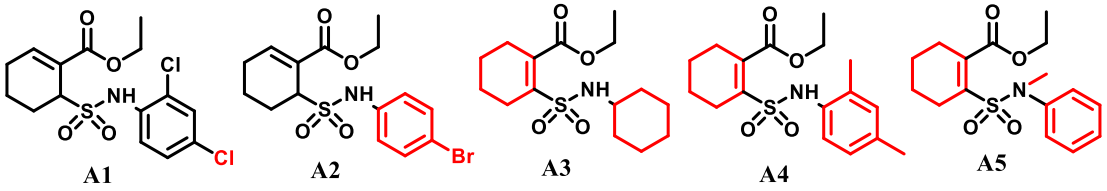

Figure 2.3. Chemical structures of **Gen A** analogues.

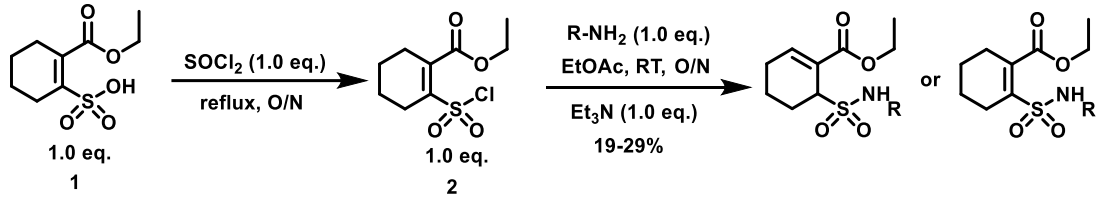

Scheme 2.1. General synthetic route of **Gen A** compounds.

For the second-generation series **(Gen B1-B4)** (Figure 2.4), we focused on replacing the cyclohexenyl moiety of the TAK-242 scaffold with an aromatic ring to gain more insight into the role of this group on the activity of TLR4 protein. While the aromatic ring would be expected to display a similar steric demand to the cyclohexene and to position the ester and sulfonamide substituents with similar orientations, it was not expected to react as a Michael acceptor. The **Gen B** compounds were prepared via coupling of compound **4** and different anilines and cyclohexylamine in the presence of triethylamine as depicted in Scheme 2.2.[2,19]

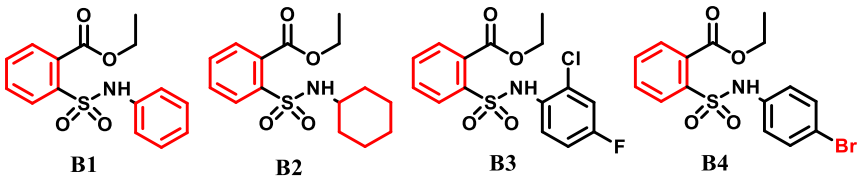

Figure 2.4. Chemical structures of **Gen B** analogues.

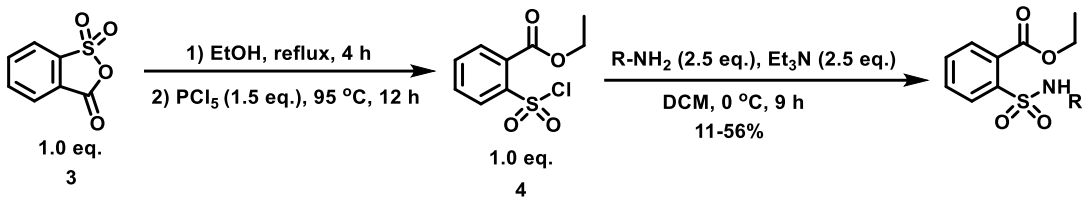

Scheme 2.2. General synthetic route of **Gen B** compounds.

To examine the effect of the sulfonamide linker of the TAK-242 scaffold on the inhibition of TLR4 protein, we replaced this linker with sulfide and sulfonyl functional groups to make third generation **(Gen C)** compounds (Figure 2.5). Sulfides **(C1-C3)** were prepared by a coupling reaction of thiol and bromide precursors. Subsequently, the sulfide analogue **C1** was oxidised with *m*-chloroperoxybenzoic acid *(m*-CPBA) to yield the corresponding sulfone compound **C4,** as shown in Scheme 2.3.[21]

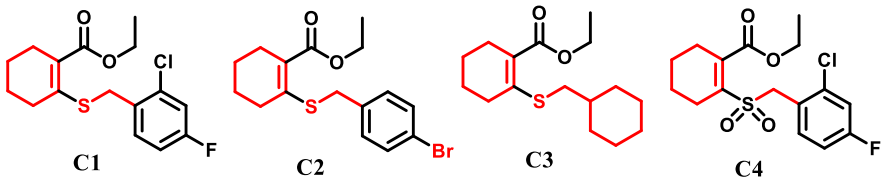

Figure 2.5. Chemical structures of **Gen C** analogues.

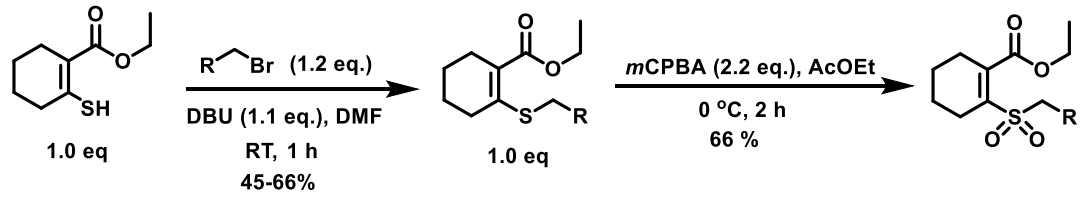

Scheme 2.3. General synthetic route of **Gen C** compounds.

2.2.2 In Vitro Inhibition of Cisplatin-induced TLR4 Activity

Recently published studies showed that the reference inhibitor, TAK-242, reduces both cisplatin and LPS induced proinflammatory cytokine secretions in vitro.[17] The TLR4

signaling pathway was blocked successfully in both HEI-OC1 and HEK-hTLR4 cells by pre-treating them with TAK-242 prior to treatment with LPS or cisplatin. Results of these experiments indicated that cells treated with TAK-242 released significantly less proinflammatory cytokines (IL-6 and IL-8) in comparison to the vehicle control in response to both cisplatin and LPS. These assays have been described in Chapter 1. Therefore, TAK-242 was used as a reference compound for otoprotection experiments using all synthesized TAK-242 analogues. In contrast to TAK-242, which was designed to inhibit LPS signaling through the TLR4, the ideal synthetic inhibitors should inhibit cisplatin signalling specifically. Cisplatin mediated responses were tested in the presence of synthetic inhibitors or vehicle (DMF) in both HEI-OC1 (mTLR4) and HEK-hTLR4 cells.

2.2.2.1 Inhibitory Effects of Gen A Compounds on in Vitro Mouse Model

Synthesis and evaluation of **Gen A** compounds was envisioned as a feasibility study to explore whether structural changes in the TAK-242 scaffold could result in differences in activity against TLR4 relative to the initial hit TAK-242. Preliminary results indicate that all **Gen A** compounds can block cisplatin-mediated proinflammatory cytokine (IL-6) secretion in HEI-OC1 cells (Figure 2.6A) and four of them (**A2-A5**) do not interfere with the LPS-induced signaling (Figure 2.6B). Due to the structural similarity between TAK-242 and compound **A1**, both show the same inhibitory activity upon cisplatin and LPS treatment. Compound **A2** did not suppress LPS mediated IL-6 secretion, regardless of having an olefinic proton at 2-position of the cyclohexene ring in analogy to the reference compound TAK-242.

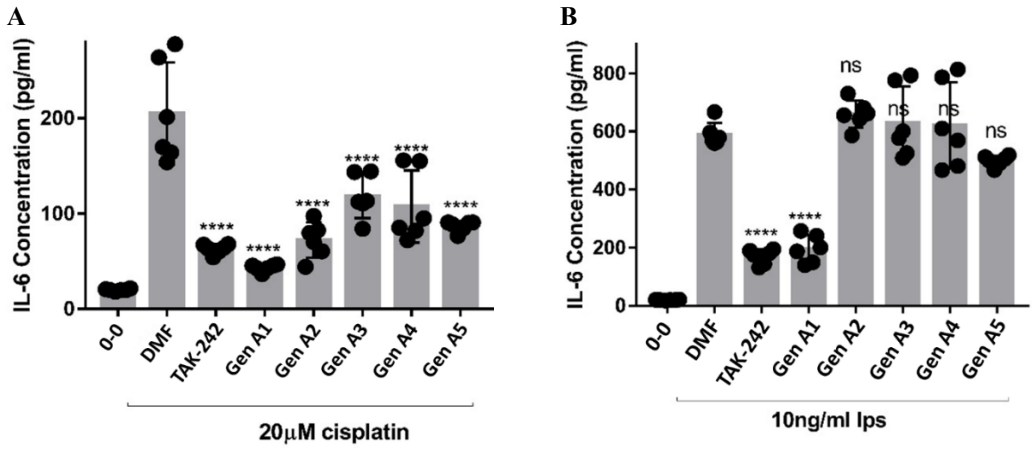

Figure 2.6. Effects of **Gen A** compounds on cisplatin and LPS induced IL-6 secretion in HEI-OC1 cells (A and B). Cells were seeded in 24 well plates (2.5 x 10^5 cells/well) and incubated at 33 °C, 10% CO_2. Compounds were dissolved in vehicle (DMF) and stored at –20 °C prior to use. Cells were left untreated (-), pretreated with DMF or 4 μM of inhibitors for 1 h and then stimulated with 20 μM cisplatin or 10 ng/mL LPS 24 h after seeding in fresh media. Supernatants were collected to measure IL-6 secretion 48 h post-treatment using ELISA kit. Data are from 6 independent experiments and presented as mean and standard deviation. **, $P < 0.01$; ****, $P < 0.0001$ using one-way ANOVA with Dunnett's multiple comparison testing to DMF treatment and ns refers to nonsignificant.

2.2.2.2 Inhibitory Effects of Gen B Compounds on in Vitro Mouse Model

None of the second-generation derivatives (**B1-B4**) had any significant suppressive effect on cisplatin induced IL-6 production though they showed marked inhibitory effects on LPS signalling (Figure 2.7A, B). Replacement of the cyclohexene ring with a benzene ring caused a marked decrease of potency. It can be concluded that the cyclohexene moiety is crucial to the compound's inhibitory activity.

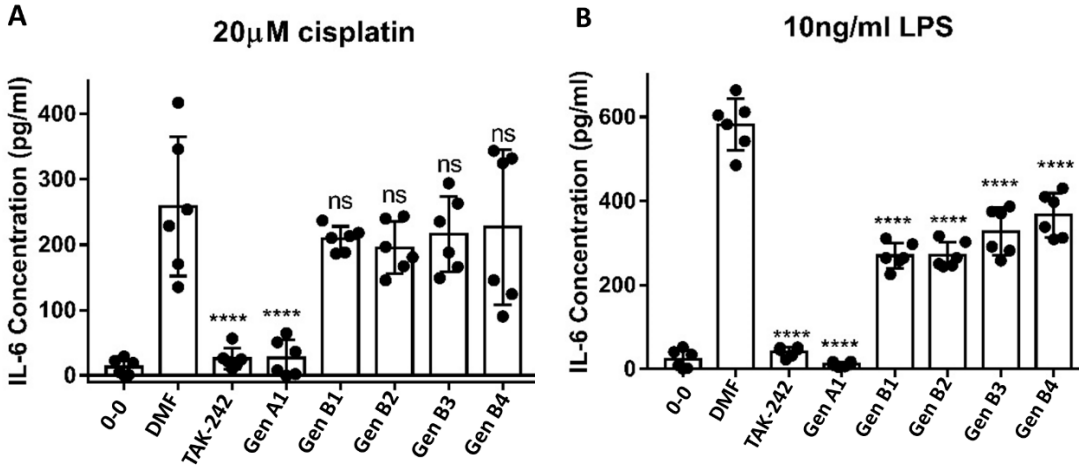

Figure 2.7. Effects of **Gen B** compounds on cisplatin (A) and LPS (B) induced IL-6 secretion in HEI-OC1 cells. These assays are done under the same conditions applied for **Gen A** compounds.

2.2.2.3 Inhibitory Effects of Gen C Compounds on in Vitro Mouse CIO Model

Unfortunately, the inhibitory effects of **Gen C** compounds on cisplatin induced inflammatory response decreased relative to reference compound TAK-242, as depicted in Figure 2.8A. The only structural difference between Gen A and Gen C compounds is the sulfonamide moiety. These results support the idea that the presence of the sulfonamide linker is critical for maintaining inhibitory activity, regardless of the modifications on the aniline moiety of the TAK-242 scaffold. These compounds have no significant effect on LPS-induced IL-6 secretion either (Figure 2.8B).

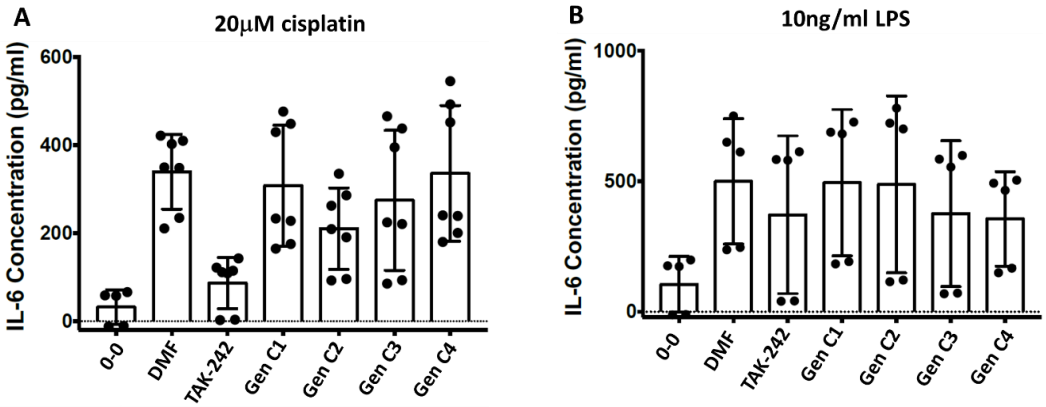

Figure 2.8. Effects of **Gen C** compounds on cisplatin (A) and LPS (B) induced IL-6 secretion in HEI-OC1 cells. These assays are done under the same conditions applied for **Gen A** compounds.

2.2.2.4 Inhibitory Effects of All Compounds on in Vitro Human Model

TLR4 is distributed widely in both immune and other body cells. It has been found that the TLR4-induced intracellular signaling pathways are similar for all types of cells.[22,23] Therefore, we used hTLR4 expressing human embryonic kidney (HEK-hTLR4) cells to investigate the inhibitory effects of our synthesized compounds via an in vitro human CIO model.

Preliminary results indicate that the **Gen A** and **Gen C** significantly block cisplatin-mediated IL-8 secretion in HEK-hTLR4 cells compared to **Gen B** compounds (Figure 2.9). These results are similar to that of the in vitro mouse CIO model. Since **Gen A** compounds displayed the most effective proinflammatory cytokine production inhibition in both mouse and human CIO models, they were subjected to further analysis.

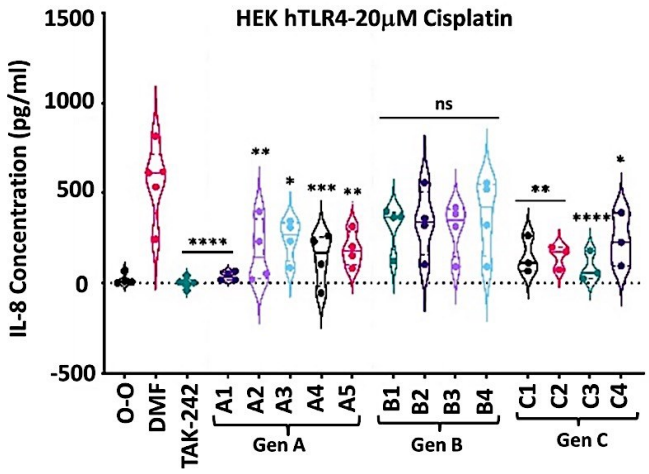

Figure 2.9. Effects of all compounds on cisplatin induced IL-8 secretion in HEK-hTLR4 cells. These assays are done under the same conditions applied for in vitro mouse CIO model.

2.2.2.5 Inhibitory Effects of Gen A Compounds on ROS Generation

In ROS generation studies, it was found that all **Gen A** compounds were able to inhibit ROS production in cisplatin stimulated HEI-OC1 cells. However, compounds **A3**, **A4**, and **A5** showed more significant suppressive effects compared to the parent compound TAK-242. (Figure 2.10).

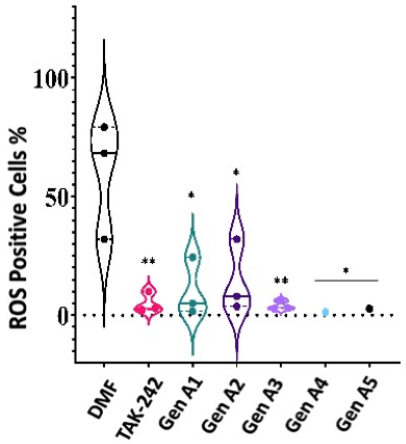

Figure 2.10. Effects of **Gen A** compounds on cisplatin induced ROS generation in HEI-OC1 cells. These assays are done under the same conditions applied for IL-6 secretion assays. ROS generation assay was carried out using redox-sensitive reagents (DCFH-DA and ROS-Glo). The percent ROS positive cells were determined by flow cytometric analysis. **, $P < 0.01$; ****, $P < 0.0001$ using one-way ANOVA with Dunnett's multiple comparison testing to DMF treatment.

2.2.3 In Vivo Inhibition of Cisplatin-induced TLR4 Activity

The zebrafish lateral line is a well studied, high-throughput animal model for screening otoprotective substances.[24–29] Recently, the role of TLR4 in cisplatin-induced ototoxicity was examined via an in vivo zebrafish CIO model. It has been found that zebrafish TLR4 mediates cisplatin-induced ototoxicity.[17] Findings of this experiment were discussed in Chapter 1.

As it has been identified that **Gen A** and **Gen C** compounds have inhibitory effects in cisplatin induced ototoxicity responses in vitro, we sought to examine the ability of these compounds to block cisplatin-induced hair cell death in zebrafish. Using established assays, we scored the health of neuromasts, which are mechanotransducing hair cells that bear structural, cellular, and physiological similarities to Organ of Corti outer hair cells.[30] The working concentration of cisplatin was chosen in such a way as to yield significant, but not total, loss of neuromast cell viability as determined through DASPEI staining, which accumulates and stains viable hair cells. DMF was used as a vehicle for antagonists that did not affect the hair cells in comparison to the no-treatment group.

2.2.3.1 Inhibitory Effects of Gen A Compounds on in Vivo Zebrafish Model

The following graphs (Figure 2.11) represent PLL (Posterior Lateral Line) neuromast scores after cisplatin and/or TLR4 antagonists' treatment in 6–7 dpf (days post fertilization) fish. Treatment with cisplatin alone was used as a negative control, and no treatment was applied as a positive control. DMF was used as a vehicle for the compounds in all experiments, as it has no toxic effects when applied alone. Neither TAK-242, **A1**, nor **A2** inhibited cisplatin-induced neuromast toxicity. Moreover, inclusion of these three compounds appear to exacerbate the effects of cisplatin. However, there was a small but significant increase in neuromast score in **A3** injected zebrafish at 5 μM cisplatin compared to other compounds (Figure 2.11A).

Even at higher concentration (7.5 μM) of cisplatin, compound **A3** provided significant protection against toxicity at the same concentration (5 μM) (Figure 2.11B). Compound **A4** at 5 μM concentration also showed a significant inhibitory effect compared to fish being treated with 7.5 μM cisplatin alone in two different

experiments. (Figure 2.11B, C). However, compound **A5** showed no protective effect on the neuromasts and causes similar or decreased DASPEI fluorescence intensity as the 7.5 µM cisplatin group (Figure 2.11C).

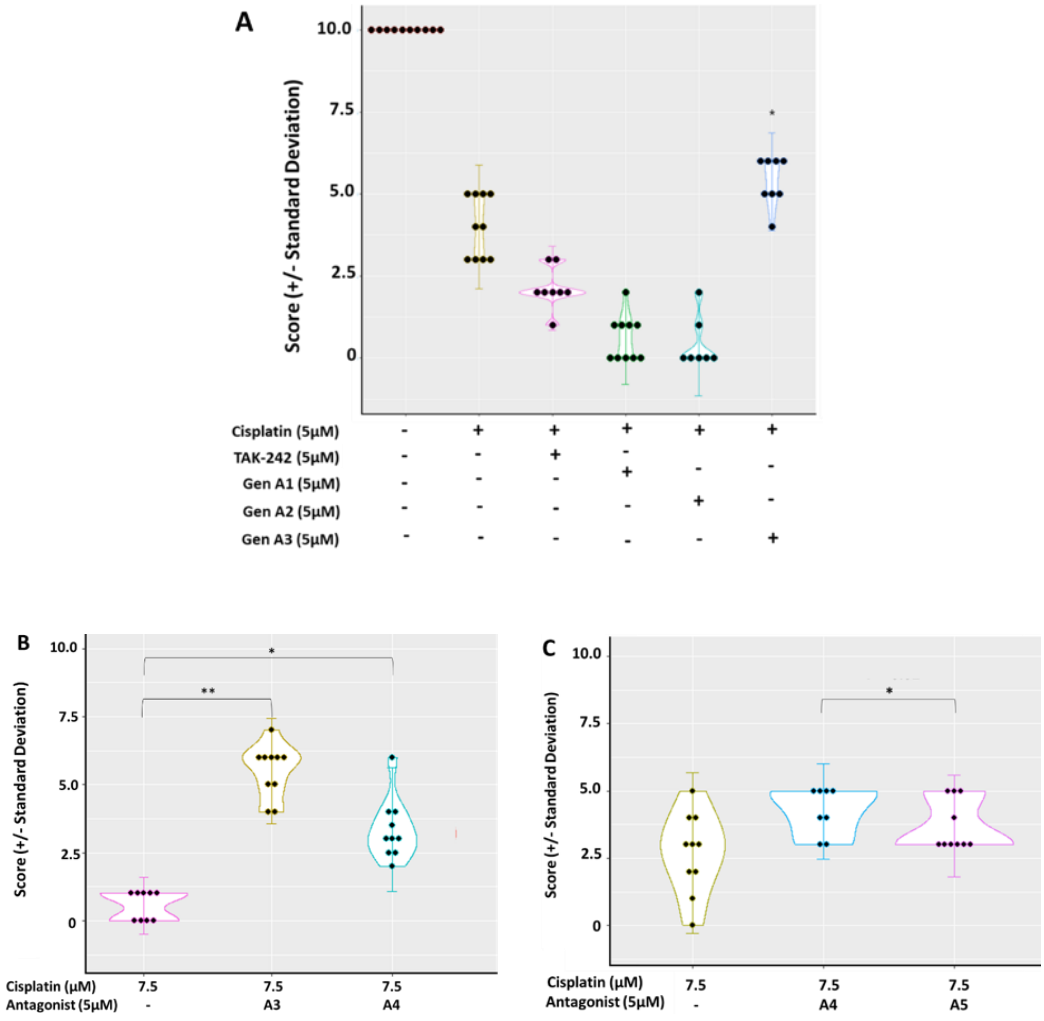

Figure 2.11(A-C). The effects of antagonists TAK-242 and **Gen A** compounds **(A1-A5)** on cisplatin-induced hair cell death in 6 dpf zebrafish neuromasts along the posterior lateral line. 8–0 fishes were subjected to bath application of cisplatin and/or antagonists for 20 h at 28 °C. Neuromasts were stained with DASPEI before applying 4% MS-222 and visualised under a fluorescent microscope. Data were collected based on the DASPEI fluorescent intensity of the neuromast. The individual dots represent a single fish. Neuromast scores were analyzed using one-way ANOVA with Tukey's multiple comparisons test.

Overall, antagonists **A3** and **A4** showed promising inhibitory activities towards cisplatin toxicity compared to TAK-242 and other **Gen A** derivatives and may prevent total hair-cell death.

2.2.3.2 Inhibitory Effects of Gen C Compounds on in Vivo Zebrafish Model

Among all **Gen C** compounds, **C1** and **C2** both at either 5 or 10 μM concentrations demonstrated no significant protection from cisplatin toxicity (Figure 2.12A).

Similarly, compound **C4** also lacked otoprotective effects, and neuromast cells showed complete loss of fluorescence when co-treated with cisplatin (Figure 2.12C). However, **C3** showed significant improvement of neuromast fluorescence in comparison to the control (Figure 2.12B).

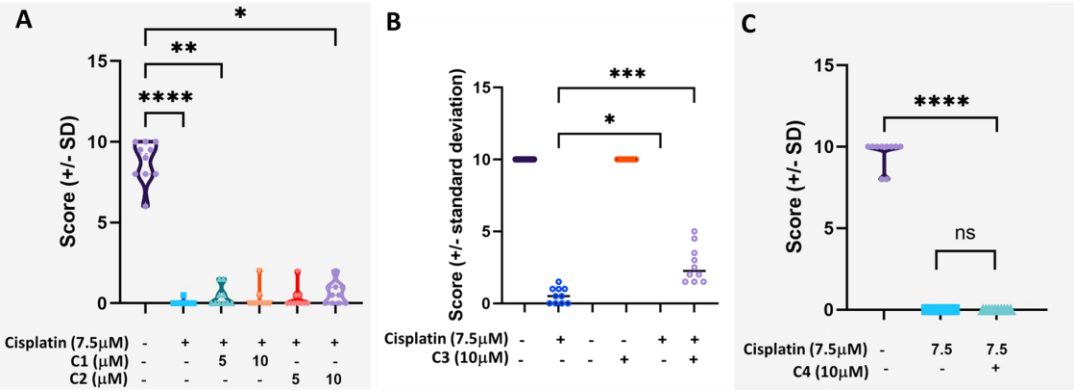

Figure 2.12. The effects of **Gen C** compounds on cisplatin-induced hair cell death in 6–7dpf zebrafish neuromasts along the posterior lateral line. 10–15 fish were subject to bath application of cisplatin and/or antagonists at different concentrations for 20 h at 28 °C. Collection and statistical analysis of data were performed in the same way as in the previous experiment (Figure 2.11A). The individual dots represent a single fish and the summed score of five neuromasts chosen on the pLL.

2.2.4 Inhibition of TLR4 Mediated Immune Hypersensitivity

Metals are one of the most notorious clinically known contact sensitizers, particularly transition metals. Around 65 million people in Europe are sensitized to Ni^{2+} and develop allergic contact dermatitis (ACD) upon contact with Ni^{2+}-releasing metal alloys, such as costume jewelry, body piercings, and coins. ACD is based on a contact hypersensitivity (CHS) reaction that contributes to the development of inflammatory response by the immune cells. Activation of the immune cells results in increased endothelial adhesion proteins allowing for leukocyte recruitment to the contacted area.[31–36]

TLR4 was found to mediate immune hypersensitivity reactions to the Group 9/10 transition metals.[33] Ni^{2+} is known to bind directly to human TLR4,

facilitating activation of the NF-κB pathway in human endothelial cells. Mechanistically, Ni^{2+} binding to TLR4 induces receptor dimerization to activate downstream signaling of the immune cells.[12,17,37,38] Given that cisplatin is a transition metal, platinum based chemotherapeutic agent, we speculated that our synthesized TAK-242 derivatives may inhibit Ni^{2+} mediated TLR4 activation in a manner analogous to that of cisplatin.

Unpublished studies from the Allison lab found that Ni^{2+} causes zebrafish hair cell death in a dose dependant manner, which is also consistent with the findings by Babolmorad et al. on murine inner ear cell studies in vitro.[17] Seven of our synthesized TAK-242 derivatives were selected to probe Ni^{2+} induced hair cell toxicity on zebrafish. It is found that when exposed to nickel (II) chloride, compounds **C2**, **C3**, and **C4** had a significant increase in fluorescence and protection against Ni^{2+} induced hair cell death (Figure 2.13B). However, compounds **A3**, **A4**, **A5**, and **C1** have no beneficial protective effects on the Ni^{2+} treatment group (Figure 2.13A, B).

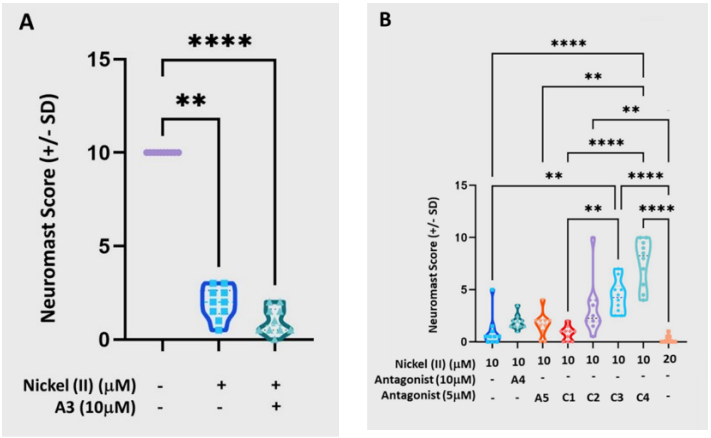

Figure 2.13. The effects of compounds **A3**, **A4**, **A5**, **C1**, **C2**, **C3**, and **C4** on nickel (II) chloride-induced hair cell death in 6-7dpf wildtype larval zebrafish along the posterior lateral line. This experiment was performed under the same condition indicated in Figure 2.11A.

Therefore, the effects of **Gen A** and **Gen C** compounds on the Ni^{2+} treatment group are quite reverse compared to that of the cisplatin treatment group. These reversal effects may have occurred due to their distinct TLR4 activation pathways.[17,37,38] Although these effects need increased replications to produce a solid conclusion, these observations can be implicated to treat different diseases, such as hypersensitivity allergies, joint replacement, cancer, chemotherapy, and more.[4,12,37]

2.4 Conclusion

Cisplatin is an indispensable chemotherapeutic that contributes to a 5-year survival rate nearing 80% in children with pediatric malignancies who are treated with it. Unfortunately, ototoxicity continues to be a prominent issue, inducing permanent bilateral hearing loss in up to 90% of patients treated. This study was done to develop new synthetic TLR4 antagonists in order to mitigate cisplatin induced ototoxicity. In the current study, mouse inner hair cell line and zebrafish neuromasts were used as in vitro and in vivo CIO models to identify compounds potentially capable of mediating protection from cisplatin and to facilitate the development of potential CIO therapies.

Only two first-generation derivatives, **A3** and **A4**, were shown to have a significant antagonizing effect on TLR4 activation and may provide partial protection from total hair cell death. Data obtained from both in vitro and in vivo studies provide sufficient evidence to conclude that there is a significant difference in hair cell death between a CIO model co-treated with cisplatin and **A3** or **A4** and those only treated with cisplatin alone. On the other hand, one of the third-generation compounds, **C3**, also provided partial protection against cisplatin-induced toxicity in both assays. However, its inhibitory effect was not as potent as compound **A3** and **A4** may be due to the absence of sulfonamide linkage in its structural moiety. These results strongly suggest that a sulfonamide linkage is important for the antagonist to have better molecular interaction with the TLR4 receptor. Four other TAK-242 derivatives **A1, A2**, **A5**, and **C2** in this study appear to provide beneficial effects in vitro; however, when they were applied in the zebrafish CIO model, they no longer provided any protection against cisplatin induced toxicity.

In summary, the analysis of the conducted SAR studies identified compounds **A3** and **A4** for otoprotection against cisplatin. Further validation studies are required to consider these two compounds as potential TLR4 antagonists to inhibit CIO. Although none of the synthesized derivatives appear to cause in vivo cellular toxicity on their own, we will examine cell viability using MTT assay and determine cisplatin IC_{50} values in the presence of vehicle or antagonists. In the near future, human TLR4 transgenic zebrafish will be used for further in vivo validation studies that will provide

a more accurate model for cisplatin toxicity on human hair cells. In the long run, we will examine the impact of compound **A3** and **A4** on cisplatin anti-cancer effectiveness by co-administering selected inhibitors with cisplatin to lung cancer cell lines as models for solid tumors.

2.5 Materials and Methods

2.5.1 Experimental Procedures for Synthesis of TAK-242 Analogues

All starting materials and solvents were purchased from commercial suppliers and were used without further purification. Reactions were carried out in flame-dried glassware under nitrogen atmosphere using standard Schlenk techniques, unless otherwise stated. Transfer of anhydrous solvents and reagents was accomplished with oven-dried syringes. Thin layer chromatography was performed on glass plates precoated with 0.25 mm silica gel. Column chromatography was performed using 230−400 mesh silica gel. Samples were dissolved in either $CDCl_3$ or DMSO-d_6 to obtain nuclear magnetic resonance (NMR) spectra. Proton nuclear magnetic resonance spectra (^{1}H NMR) were recorded at 500 or 700 MHz in the solvent indicated. Chemical shifts are given in ppm (parts per million) relative to residual $CHCl_3$ (7.26 ppm) or DMSO (2.50 ppm) and coupling constants (*J*) are reported in hertz (Hz). Standard notation was used to describe the multiplicity of signals observed in ^{1}H NMR spectra: broad (br), multiplet (m), singlet (s), doublet (d), triplet (t), etc. Carbon nuclear magnetic resonance spectra (^{13}C NMR) were recorded at 176 MHz and are reported (ppm) relative to the center line of the triplet from $CDCl_3$ (77.0 ppm) or to the center line of the quintet from DMSO-d_6 (39.5 ppm). Infrared (IR) spectra were measured with a Thermo Nicolet 8700 FTIR Spectrometer and Continuum FTIR Microscope. Mass spectra were determined on a high-resolution electrospray positive ion mode spectrometer using Agilent 6220 spectrometer and Kratos Analytical MS-50G system.

2.5.1.1 Synthesis and Characterization of Gen A Compounds

Ethyl 2-(chlorosulfonyl)cyclohex-1-ene-1-carboxylate (2)

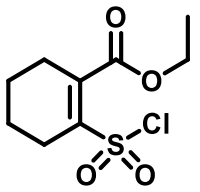

2-(Ethoxycarbonyl)cyclohex-1-ene-1-sulfonic acid (**1**) (58.4 mg, 0.25 mmol) was stirred with $SOCl_2$ (0.16 mL, 0.25 mmol) under reflux for 14 h. The reaction mixture was evaporated under reduced pressure evaporation to dryness. Then, the residue was subjected three times to a procedure involving an addition of hexane (0.25 mL), followed by evaporation to dryness to yield ethyl 2-(chlorosulfonyl)cyclohex-1-ene-1-carboxylate intermediate as a clear yellow semisolid (46.2 mg). The synthesized reaction intermediate **2** was used in the subsequent step without further purification and was characterized only partially; IR (cast film), ν_{max} = 2945, 2939, 2868, 1735, 1449, 1374, 1253, 1173, 1049, 846, 742 cm^{-1}; ^1H NMR (500 MHz, $CDCl_3$) 4.22 (q, J = 7.0 Hz, 2H), 2.45–2.25 (m, 4H), 1.65–1.58 (m, 4H), 1.31(t, J = 7.0 Hz, 3H).

Ethyl 6-[N-(2,4-dichlorophenyl)sulfamoyl]cyclohex-1-ene-1-carboxylate (A1)

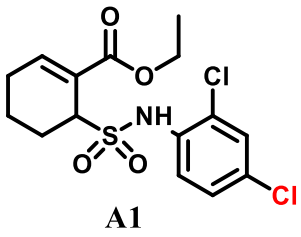

A1

The synthesized reaction intermediate **1,** ethyl 2-(chlorosulfonyl)cyclohex-1-ene-1-carboxylate (34.7 mg, 0.14 mmol) was dissolved in EtOAc (0.2 mL), and the resultant mixture was then added to a solution of 2,4-dichloroaniline (21.3 mg, 0.13 mmol), triethylamine (0.02 mL, 0.13 mmol), and EtOAc (0.4 mL). The reaction mixture was then stirred for 18 h at room temperature. Then, the reaction mixture was dissolved in 5.0 mL EtOAc and extracted with water (3 x 5.0 mL). The organic layers were combined, washed with brine, dried with Na_2SO_4, filtered, and concentrated. The crude material was purified by column chromatography (gradient elution with 10% to 15%

EtOAc/hexanes) to obtain compound **A1** as a light brown solid (12.3 mg) in 25% yield; IR (cast film), ν_{max} = 3255, 3062, 2982, 2940, 2870, 1716, 1646, 1604, 1494, 1446, 1329, 1250, 1147, 1061, 894, 762 ; ^{1}H NMR (500 MHz, DMSO-d_6) δ 9.77 (s, 1H), 7.66 (d, J = 2.4 Hz, 1H), 7.51 (d, J = 8.8 Hz, 1H), 7.42 (dd, J = 8.7, 2.5 Hz, 1H), 7.09 (t, J = 3.9 Hz, 1H), 4.30 (app d, J = 5.7 Hz, 1H), 3.99 (q, J = 7.1 Hz, 2H), 2.45–1.70 (m, 6H), 1.06 (t, J = 7.1 Hz, 3H); ^{13}C NMR (176 MHz, DMSO-d_6) δ 166.9, 145.6, 144.6, 134.5, 134.2 129.8, 127.4, 126.5, 63.4, 60.6, 24.0, 23.7, 17.0, 14.6; HRMS (ESI) *m/z* calcd for $C_{15}H_{16}Cl_2NO_4S$ $[M - H]^-$ 376.0182; found 376.0180.

Ethyl 6-[(4-bromophenyl)sulfamoyl]cyclohex-1-ene-1-carboxylate (A2)

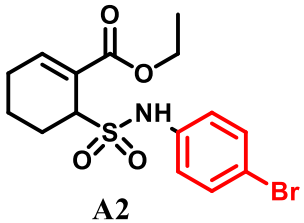

A2

The method used above in the preparation of **A1** was employed to synthesize compound **A2** with the following stoichiometric amounts: ethyl 2-(chlorosulfonyl)cyclohex-1-ene-1-carboxylate (60.4 mg, 0.25 mmol), 4-bromoaniline (40.2 mg, 0.23 mmol), Et_3N (0.03 mL, 0.23 mmol) and EtOAc (0.8 mL) to obtain **A2** as a brownish solid (21.3 mg, 22%); IR (cast film), ν_{max} = 3272, 3024, 2985, 2812, 1727, 1600, 1519, 1508, 1464, 1217, 1033, 808, 750; ^{1}H NMR (500 MHz, $CDCl_3$) δ 7.47 (dd, J = 9.2, 2.5 Hz, 2H), 7.38 (t, J = 3.9 Hz, 1H), 7.27 (dd, J = 9.2, 2.5 Hz, 2H), 7.09 (s, 1H), 4.29–4.22 (m, 3H), 2.52–2.41 (m, 3H), 2.31–2.21 (m, 1H), 2.02–1.90 (m, 1H), 1.70–1.61 (m, 1H), 1.33 (t, J = 7.1 Hz, 3H); ^{13}C NMR (126 MHz, $CDCl_3$) δ 167.4, 147.2, 136.9, 132.5 (2C), 125.3, 123.4 (2C), 118.5, 61.6, 56.5, 25.6, 24.8, 17.4, 14.3; HRMS (ESI) *m/z* calcd for $C_{15}H_{19}BrNO_4S$ $[M + H]^+$ 388.0213; found 388.0217.

Ethyl 2-(cyclohexylsulfamoyl)cyclohex-1-ene-1-carboxylate (A3)

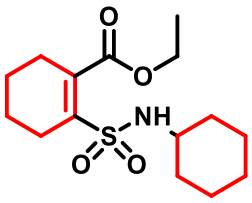

A3

The method used above for **A1** was employed to synthesize compound **A3** with the following stoichiometric amounts: ethyl 2-(chlorosulfonyl)cyclohex-1-ene-1-carboxylate (42.1 mg, 0.18 mmol), cyclohexanamine (0.02 mL, 0.18 mmol), Et_3N (0.025 mL, 0.18 mmol), and EtOAc (0.7 mL) to obtain a brownish solid (16.4 mg, 29%); IR (cast film), ν_{max} = 3280, 2938, 2857, 1718, 1455, 1316, 1289, 1176, 991, 846; ^{1}H NMR (500 MHz, DMSO-*d*$_6$) δ 3.94–3.89 (m, 1H), 3.38 (q, *J* = 7.0 Hz, 2H), 2.47–2.45 (m, 2H), 2.34–2.31 (m, 2H), 1.93–1.60 (m, 11H), 1.35–1.28 (m, 2H), 1.16–1.11 (m, 1H), 1.09 (t, *J* = 7.0 Hz, 3H), sulfonyl NH proton not detected; ^{13}C NMR (176 MHz, DMSO-*d*$_6$) δ 159.8, 145.4, 135.9, 64.9, 53.6, 30.0 (2C), 25.3 (2C), 24.7, 20.3, 20.0, 19.8, 18.0, 15.2; HRMS (ESI) *m/z* calcd for $C_{15}H_{25}NNaO_4S$ $[M + Na]^+$ 338.1397; found 338.1398.

Ethyl 2-[(2,4)-dimethylphenyl)sulfamoyl]cyclohex-1-ene-1-carboxylate (A4)

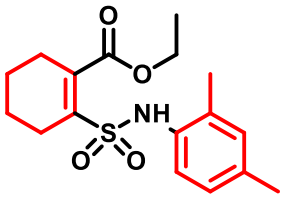

A4

The method used above for **A1** was employed to synthesize compound **A4** with the following stoichiometric amounts: ethyl 2-(chlorosulfonyl)cyclohex-1-ene-1-carboxylate (40 mg, 0.17 mmol), 2,4-dimethylaniline (0.02 mL, 0.18 mmol), Et_3N (0.025 mL, 0.18 mmol) and EtOAc (0.7 mL) to obtain a light brown solid (11.5 mg, 19%); IR (cast film), ν_{max} = 3388, 2978, 2934, 2858, 1726, 1682, 1572, 1500, 1367, 1250, 1174, 1056, 813, 738 cm^{-1}; ^{1}H NMR (700 MHz, $CDCl_3$) δ 8.10 (s, 1H), 7.55 (d, *J* = 8.1 Hz, 1H), 7.14 (d, *J* = 2.2 Hz, 1H), 7.05 (dd, *J* = 8.1, 1.9 Hz, 1H), 4.27 (q, *J* = 7.5 Hz, 2Hß), 2.69 (s, 3H), 2.38 (s, 3H), 1.50–1.31 (m, 8H), 0.96 (t, *J* = 7.5 Hz, 3H); ^{13}C NMR (176 MHz, $CDCl_3$) δ 166.1, 149.4, 140.9, 138.0, 136.9, 134.4, 131.9, 127.3, 115.9, 67.9, 30.7, 29.1, 24.2, 23.1, 21.5, 17.7, 14.2; HRMS (ESI) *m/z* calcd for $C_{17}H_{23}NNaO_4S$ $[M + Na]^+$ 360.1240; found 360.1244.

Ethyl 2-[methyl-(phenyl)sulfamoyl]cyclohex-1-ene-1-carboxylate (A5)

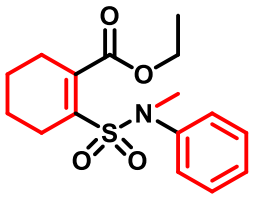

A5

The method used above for **A1** was employed to synthesize compound **A5** with the following stoichiometric amounts: ethyl 2-(chlorosulfonyl)cyclohex-1-ene-1-carboxylate (40 mg, 0.17 mmol), N-methylaniline (0.02 mL, 0.18 mmol), Et_3N (0.25 mL, 0.18 mmol) and EtOAc (0.7 mL) to obtain a brownish solid (25 mg, 45%); IR (cast film), ν_{max} = 2980, 2961, 2890, 1713, 1612, 1587, 1495, 1250, 1154, 1026, 891, 763 cm^{-1}; ^1H NMR (700 MHz, $CDCl_3$) δ; 7.33–7.03 (m, 5H), 4.16 (q, *J* = 7.0 Hz, 2H), 3.48 (s, 3H), 2.68–2.66 (m, 2H), 2.24–2.44 (m, 2H), 1.80–1.75 (m, 4H), 1.19 (t, *J* = 7.0 Hz, 3H); ^{13}C NMR (176 MHz, $CDCl_3$) δ 169.3, 143.9, 141.4, 139.1, 130.6 (2C), 127.3 (2C), 126.5, 60.9, 36.7, 27.3, 24.4, 21.6, 21.0, 14.2; HRMS (ESI) *m/z* calcd for $C_{16}H_{21}NNaO_4S$ $[M + Na]^+$ 323.1188; found 323.1190.

2.3.1.2 Synthesis and Characterization of Gen B Compounds

Ethyl 2-(chlorosulfonyl)benzoate (4)

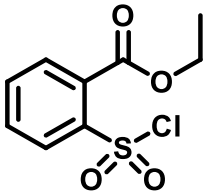

Synthesis of reaction intermediate **4** was achieved through a one pot sequential addition reaction in two steps. A solution of 2-sulfobenzoic acid cyclic anhydride (**3**) (0.309 g, 1.7 mmol) in ethanol (5 mL) was heated at refluxed for 1 h. The solution was cooled to room temperature, and the solvent was removed under reduced pressure and high vacuum overnight, yielding a clear pale-yellow oil. Phosphorus pentachloride (0.496 g, 2.4 mmol) was added slowly to the sulfonic acid intermediate, and the reaction mixture was stirred at 95 °C for 2 h. The residue was dissolved in 10 mL CH_2Cl_2, extracted with ice-cold distilled water (3 x 10 mL), and dried with $MgSO_4$. After gravity filtration, the solvent was removed under reduced pressure and high vacuum,

yielding a clear yellow oil (0.241 g) and was characterized only partially ; IR (cast film), ν_{max} = 3100, 2987, 1736, 1377, 1295, 1185, 1053 cm^{-1}; ^1H NMR (700 MHz, $CDCl_3$) δ 8.15 (m, 1H), 7.78 –7.70 (m, 3H), 4.46 (q, *J* = 7.0 Hz, 2H), 1.42 (t, *J* = 7.0 Hz, 3H).

Ethyl 2-(phenylsulfamoyl)benzoate (B1)

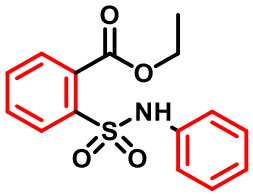

B1

To ethyl 2-(chlorosulfonyl)benzoate (58 mg, 0.2 mmol) in 5 mL of CH_2Cl_2 were added triethylamine (0.11 mL, 0.70 mmol) and aniline (0.11 mL, 1.11 mmol) at 0 °C under nitrogen. The reaction mixture was stirred overnight at room temperature. Then, the mixture was diluted with 10 mL of CH_2Cl_2, followed by extraction of the organic layer from 2M HCl (3 x 10 mL). The organic layer was washed with brine (15 mL) and dried over Na_2SO_4. The crude material was purified by column chromatography (gradient elution with 5% to 10% EtOAc/hexanes), yielding compound B1 as a dark red viscous oil (39.7 mg, 56%); IR (cast film) ν_{max} = 3280, 3073, 2983, 1711, 1599, 1496, 1282, 1169, 756 cm^{-1}; ^1H NMR (700 MHz, $CDCl_3$) δ 8.02 (s, 1H), 7.80 (app t, *J* = 7.6 Hz, 2H), 7.56 (td, *J* = 7.6, 1.3 Hz, 1H), 7.46 (dd, *J* = 7.7, 1.3 Hz, 1H), 7.23–7.20 (m, 2H), 7.17–7.15 (m, 2H), 7.11 (app d, *J* = 7.3 Hz, 1H), 4.51 (q, *J* = 7.2 Hz, 2H), 1.47 (t, *J* = 7.2 Hz, 3H); ^{13}C NMR (176 MHz, $CDCl_3$) δ 168.0, 137.9, 136.7, 132.5, 131.3, 131.0, 130.5, 130.3, 129.1 (2C), 125.8, 122.9 (2C), 62.8, 14.1; HRMS (ESI) *m/z* calcd for $C_{15}H_{15}NNaO_4S$ $[M+Na]^+$: 328.0614; found: 328.0619.

Ethyl 2-[N-(cyclohexyl)sulfamoyl]benzoate (B2)

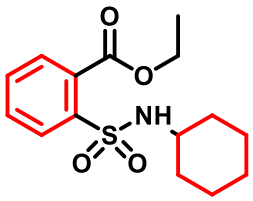

B2

The method used above for **B1** was employed to synthesize compound **B2** with the following stoichiometric amounts: ethyl 2-(chlorosulfonyl)benzoate (55 mg, 0.2 mmol), DCM (5 mL), triethylamine (0.1 mL, 0.7 mmol) and cyclohexylamine (0.1 mL, 0.9 mmol) to obtain a clear yellow oil (7.3 mg, 11%); IR (cast film), ν_{max} = 3292, 2930, 2853, 1714, 1450, 1336, 1295, 1189, 1115, 887, 759 cm^{-1}; ^{1}H NMR (500 MHz, $CDCl_3$) δ 8.11–8.09 (m, 1H), 7.81–7.79 (m, 1H), 7.61 (ddd, *J* = 6.4, 3.9, 1.8 Hz, 2H), 5.92 (d, *J* = 7.3 Hz, 1H), 4.44 (q, *J* = 7.1 Hz, 2H), 3.26–3.24 (m, 1H), 1.74–1.71 (m, 2H), 1.64–1.61 (m, 2H), 1.51–1.47 (m, 1H), 1.42 (t, *J* = 7.1 Hz, 3H), 1.25–1.19 (m, 5H); ^{13}C NMR (176 MHz, $CDCl_3$) δ 168.1, 141.2, 132.3, 131.8, 131.0, 130.9, 129.5, 62.9, 52.9, 34.0 (2C), 25.6 (2C), 24.8, 14.4; HRMS (ESI) *m/z* calcd for $C_{15}H_{21}NNaO_4S$ $[M+Na]^+$: 334.1083, found: 334.1087.

Ethyl 2-[N-(2-chloro-4-fluorophenyl)sulfamoyl]benzoate (B3)

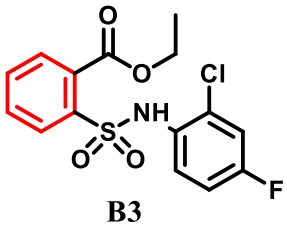

B3

The method used above for B1 was employed to synthesize compound 166 with the following stoichiometric amounts: ethyl 2-(chlorosulfonyl)benzoate (58 mg, 0.2 mmol), DCM (5 mL), triethylamine (0.1 mL, 0.7 mmol) and 2-chloro-4-fluoroaniline (0.1 mL, 0.8 mmol) to obtain a clear viscous brown oil (11 mg, 15%); IR (cast film), ν_{max} = 3259, 3057, 2940, 1758, 1494, 1437, 1238, 1150, 1012, 824, 736 cm^{-1}; ^{1}H NMR (700 MHz, $CDCl_3$) δ 8.51 (s, 1H), 7.89 (dd, *J* = 7.7, 1.3 Hz, 1H), 7.84 (dd, *J* = 7.8, 1.4 Hz, 1H), 7.63–7.58 (m, 2H), 7.53 (td, *J* = 7.7, 1.4 Hz, 1H), 7.10 (app d, *J* = 8.8 Hz, 1H), 6.96 (dd, *J* = 9.9, 2.3 Hz, 1H), 4.51 (d, *J* = 7.2 Hz, 2H), 1.46 (t, *J* = 7.1 Hz, 3H); ^{13}C NMR (176 MHz, $CDCl_3$) δ 167.4, 155.4, 154.0, 138.5, 133.1, 131.7, 131.3, 130.9, 129.9, 126.3, 125.1, 123.7, 116.5, 63.0, 14.2; HRMS (ESI) *m/z* calcd for $C_{15}H_{13}ClFNNaO_4S$ $[M+Na]^+$: 380.0130; found: 380.0129.

Ethyl 2-[N-(4-bromophenyl)sulfamoyl]benzoate (B4)

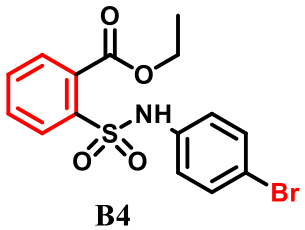

B4

The method used above for B1 was employed to synthesize compound B4 with the following stoichiometric amounts: ethyl 2-(chlorosulfonyl)benzoate (52 mg, 0.2 mmol), DCM (5 mL), triethylamine (0.1 mL, 0.7 mmol) and 4-bromoaniline (0.1 mL, 0.9 mmol) to obtain a clear viscous brown oil (40.9 mg, 46%); IR (cast film), ν_{max} = 3270, 3095, 2983, 1711, 1489, 1461, 1282, 1170, 1011, 903, 708 cm^{-1}; ^{1}H NMR (700 MHz, $CDCl_3$) δ 8.08 (s, 1H), 7.82–7.79 (m, 2H), 7.59 (td, *J* = 7.6, 1.3 Hz, 1H), 7.49 (td, *J* = 7.7, 1.3 Hz, 1H), 7.34–7.32 (m, 2H), 7.06–7.04 (m, 2H), 4.51 (q, *J* = 7.1 Hz, 2H), 1.47 (t, *J* = 7.2 Hz, 3H); ^{13}C NMR (176 MHz, $CDCl_3$) δ 168.2, 137.8, 136.0, 132.9, 132.4 (2C), 131.6, 131.1, 130.7, 130.5, 124.6 (2C), 119.3, 63.1, 14.2; HRMS (ESI) *m/z* calcd for $C_{15}H_{14}BrNNaO_4S$ $[M+Na]^+$: 405.9719, found: 405.9721.

2.3.1.3 Synthesis and Characterization of Gen C Compounds

Ethyl 2-[(2-chloro-4-fluorobenzyl)thio]cyclohex-1-ene-1-carboxylate (C1)

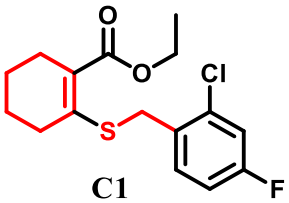

C1

1-(Bromomethyl)-2-chloro-4-fluorobenzene (58 mg, 0.26 mmol) and DBU (0.04 mL, 0.26 mmol) were added to a solution of ethyl 2-mercaptocyclohex-1-ene-1-carboxylate (0.04 mL, 0.21 mmol) in DMF (1.0 mL). The reaction mixture was stirred at room temperature for 1 h. Then, the reaction mixture was partitioned between EtOAc and water. The organic layer was collected, and the aqueous layer was extracted with EtOAc (2 x 10 mL). The organic layers were combined, washed with water, brine, dried with Na_2SO_4, filtered, and concentrated. The crude material was purified by column chromatography (gradient elution with 5% to 10% EtOAc/hexanes) to obtain compound **C1** as an off-white solid (30.9 mg) in 45% yield; IR (cast film) ν_{max} = 3067, 2979, 2861, 1691, 1600, 1579, 1477, 1278, 1156, 907, 857 cm^{-1}; ^{1}H NMR (700 MHz,

$CDCl_3$) δ 7.43 (dd, *J* = 8.6, 6.1 Hz, 1H), 7.11 (dd, *J* = 8.4, 2.7 Hz, 1H), 6.94 (td, *J* = 8.3, 2.7 Hz, 1H), 4.19 (q, *J* = 7.1 Hz, 2H), 4.08 (s, 2H), 2.48–2.45 (m, 2H), 2.37–2.35 (m, 2H), 1.70–1.60 (m, 4H), 1.28 (t, *J* = 7.1 Hz, 3H); ^{13}C NMR (176 MHz, $CDCl_3$) δ 168.0, 162.7, 161.3, 147.6, 135.0, 132.3, 124.1, 117.3, 114.6, 60.6, 32.6, 30.8, 27.4, 23.4, 22.0, 14.6; HRMS (ESI) *m/z* calcd for $C_{16}H_{18}ClFNaO_2S$ $[M + Na]^+$ 351.0592; found 351.0594.

Ethyl 2-[(4-bromobenzyl)thio]cyclohex-1-ene-1-carboxylate (C2)

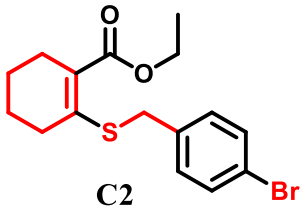

C2

The method used above for **C1** was employed to synthesize compound **C2** with the following stoichiometric amounts: 1-bromo-4-(bromomethyl)benzene (65 mg, 0.26 mmol), DBU (0.04 mL, 0.26 mmol), ethyl 2-mercaptocyclohex-1-ene-1-carboxylate (0.04 mL, 0.21 mmol) and DMF (1.0 mL) to afford compound **C2** as a brownish solid (37.3 mg) in 50% yield; IR (cast film) ν_{max} = 3070, 2978, 2860, 1690, 1568, 1468, 1447, 1277, 1070, 1054, 836, 766 cm^{-1}; ^{1}H NMR (500 MHz, $CDCl_3$) δ 7.42 (app d, *J* = 8.4 Hz, 2H), 7.22 (app d, *J* = 8.5 Hz, 2H), 4.19 (q, *J* = 7.1 Hz, 2H), 3.94 (s, 2H), 2.45–2.41 (m, 2H), 2.36–2.33 (m, 2H), 1.69–1.57 (m, 4H), 1.28 (t, *J* = 7.2 Hz, 3H); ^{13}C NMR (176 MHz,$CDCl_3$) δ 168.0, 147.6, 136.7, 132.0 (2C), 131.0 (2C), 123.9, 121.3, 60.6, 35.3, 30.9, 27.4, 23.3, 22.0, 14.6; HRMS (ESI) *m/z* calcd for $C_{16}H_{19}BrNaO_2S$ $[M + Na]^+$ 377.0181; found 377.0180.

Ethyl 2-[(cyclohexylmethyl)thio]cyclohex-1-ene-1-carboxylate. (C3)

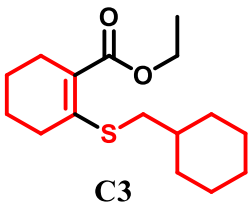

C3

The method used above for **C1** was employed to synthesize compound **C3** with the following stoichiometric amounts: (bromomethyl)cyclohexane (0.05 mL, 0.26 mmol),

DBU (0.04 mL, 0.26 mmol), ethyl 2-mercaptocyclohex-1-ene-1-carboxylate (0.04 mL, 0.21 mmol) and DMF (1.0 mL) to afford compound **C3** as a light brown solid (39.5 mg) in 66% yield; IR (cast film) ν_{max} = 3072, 2979, 2854, 1693, 1600, 1566, 1490, 1239, 1174, 1055, 857, 767 cm^{-1}; ^1H NMR (500 MHz, $CDCl_3$) δ 4.21 (q, *J* = 7.1 Hz, 2H), 2.63 (d, *J* = 6.7 Hz, 2H), 2.46–2.35 (m, 4H), 1.72–1.59 (m, 9H), 1.29–1.12 (m, 4H), 1.28 (t, *J* = 7.2 Hz, 3H), 1.01–0.93 (m, 2H); ^{13}C NMR (126 MHz, $CDCl_3$) δ 168.1, 147.7, 123.0, 60.7, 38.3, 38.0, 33.4 (2C), 32.6, 30.9, 27.5, 26.5 (2C), 23.4, 22.0, 14.8; HRMS (ESI) *m/z* calcd for $C_{16}H_{26}NaO_2S$ $[M + Na]^+$ 305.1546; found 305.1547.

Ethyl 2-[(2-chloro-4-fluorobenzyl)sulfonyl]cyclohex-1-ene-1-carboxylate (C4)

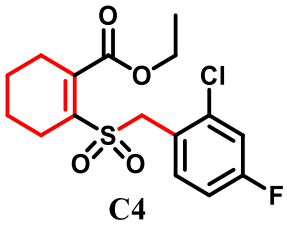

C4

To a solution of ethyl 2-mercaptocyclohex-1-ene-1-carboxylate (13.3 mg, 0.04 mmol) in AcOEt (0.5 mL) was added *m*CPBA (15.5 mg, 0.09 mmol). The reaction mixture was stirred at 0 °C for 2 h, then partitioned between EtOAc and saturated $NaHCO_3$. The organic layer was collected, and the aqueous layer was extracted with EtOAc (2 x 20 mL). The organic layers were combined, washed with aqueous $NaHCO_3$, brine, dried with Na_2SO_4, filtered, and concentrated. The crude material was purified by column chromatography (gradient elution with 5% to 10% EtOAc/hexanes) to obtain compound **C4** as white power (9.3 mg) in 65% yield; IR (cast film) ν_{max} = 3073, 2982, 2877, 1702, 1597, 1575, 1493, 1436, 1262, 1140, 913, 898, 721 cm^{-1}; ^1H NMR (700 MHz, $CDCl_3$) δ 7.53 (dd, *J* = 8.7, 5.9 Hz, 1H), 7.18 (dd, *J* = 8.2, 2.7 Hz, 1H), 7.03 (td, *J* = 8.3, 2.7 Hz, 1H), 4.58 (s, 2H), 4.29 (q, *J* = 7.2 Hz, 2H), 2.46–1.62 (m, 8H), 1.34 (t, *J* = 7.1 Hz, 3H); ^{13}C NMR (176 MHz, $CDCl_3$) δ 168.8, 163.8, 162.3, 145.4, 136.5, 134.9, 122.8, 117.7, 115.1, 62.3, 57.4, 29.4, 25.9, 22.0, 20.8, 14.3; HRMS (ESI) *m/z* calcd for $C_{16}H_{18}ClFNaO_4S$ $[M + Na]^+$ 383.0491; found 383.0494.

2.5.2 Cell Culture and Treatments

The murine inner ear cell line HEI-OC1 cells (a kind gift from Dr. Federico Kalinec, UCLA) were grown in DMEM supplemented with 10% FBS (Gibco, 123483-020) and 5% penicillin–streptomycin (1 unit penicillin/ml and 0.1 mg streptomycin/mL, Sigma, P4333). HEI-OC1 cells were grown at 33 °C in the presence of 10% CO_2. HEK (human embryonic kidney)-hTLR4 cells (cat# hkbhtlr4, Invivogen) were grown in DMEM supplemented with 10% FBS, 5% penicillin–streptomycin, and 100 µg/mL Normocin (Invivogen) at 37 °C and 5% CO_2. Cells were routinely seeded in 96-well plates (5×10^3 cells/well), 24-well plates (7.0×10^4 cells/well), 12-well plates (1.1×10^5 cells/well), or 6-well plates ($1.5–2.5 \times 10^5$ cells/ well). Cisplatin (Teva, 02402188), LPS (Invitrogen, L23351) were added to cells 48 h after seeding in fresh media. Vehicle (DMF; Fisher Scientific, D1331) or TAK242 (Cayman, 243984-11-4) and its analogues (**Gen A-C**) (synthesis described above) were added to the cell culture in fresh media 1 h prior to treatments. Following a 1 h pre-treatment, the media was aspirated, and vehicle or TAK242 or its analogues were added to cells in combination with cisplatin or LPS treatments for 24 or 48 h. All reagents were assessed for endotoxin contamination > 0.125 ƐU using Pyrotell Gel Clot Formulation kit for bacterial endotoxin testing (Pyrotell, GS125-5). LPS and low endotoxin water (<0.005 ƐU; HyClone, SH30529.02) were used as positive and negative controls, respectively.

2.5.3 Enzyme-Linked Immunosorbent Assays (ELISA)

As an alternate method of assessing TLR4 activation, IL-6 secretion was quantified in HEI-OC1 because this cytokine is a key mediator of cisplatin toxicity in HEI-OC1 cells.[39] IL-8 secretion was reported previously as a marker of TLR4 activation in HEKhTLR4 cells and was chosen for our experiments using related cell lines.[40] In addition, both IL-6 and IL-8 have been reported to be upregulated by cisplatin in human cells,[41] while mice do not contain a true gene ortholog for IL8 precluding its direct characterization. Colorimetric protein assays were conducted using commercial human IL-8 ELISA and mouse IL-6 ELISA kits (Invitrogen; 88-8086, 88-7064), according to the manufacturer's protocol. Supernatants were collected from 12-well plates or 24-well plates 0, 0.25, 0.5, 1, 2, 3, 24, or 48 h post-treatment (leaving half the volume in

the well for subsequent MTT assays). Protein secretion was normalized to the number of viable cells to account for agonist toxicity.

2.5.4 In Vitro Cell Viability Assays

MTT reagent (ACROS, 158990010) was added to 1 mg/mL to seeded cells, 24 or 48 h post-treatment. When required, aliquots of the supernatant were collected for ELISAs before the addition of MTT. Plates were incubated at 33 °C at 10% CO_2 (HEI-OC1) or 37 °C at 5% CO_2 (HEK) for 4 h in the dark. Next, the supernatants were replaced with DMSO (Sigma, D109) and incubated with shaking at room temperature for 20 min. Absorbance at 590 nm was collected in a plate reader (SpectraMax i3x, Molecular Devices). For the purposes of cell viability dose–response curves, the mean absorbance for a no-treatment control was considered 100% cell viability so that cell viability (%) of treatment = (absorbance treatment/absorbance control) × 100.

2.5.5 ROS Detection Assays

ROS generation was monitored as a hallmark response of cisplatin treatment in vitro using the Total ROS-ID detection kit (Enzo Life Sciences, ENZ-51011). HEI-OC1 or control cells were seeded in 96-well plates. Cell density was approximately 70–80% on the day of the cisplatin (20 μM) treatment. Then, the cells were stained following the manufacturers' protocol. In brief, the supernatants were removed, the cells were washed with 1X ROS Wash Buffer, and the cells were stained with 100 μL/well of ROS Detection Solution for 60 min at 37 °C in the dark. No washing was required prior to sample analysis using the SpectraMax i3x fluorescence plate reader. Excitation and emission were monitored at 488 and 520 nm, respectively. For total ROS measurements of HEI-OC1 cells in response to TAK242 treatment, the cells were pre-treated with 4 μM TAK242 or its analogues or DMF for 1 h before cisplatin stimulation for 24 h. One million cells were trypsinized and then washed with 1× ROS Wash Buffer. Then, the cells were stained following the manufacturers' protocol. In brief, the cells were re-suspended in 500 μL of the ROS Detection Solution for 30 min. No washing was required prior to sample analysis using an Attune NxT flow cytometer (Thermo Fisher

Scientific). A minimum of 10,000 events were acquired for each sample. Following acquisition, samples were analyzed using FlowJo (BD Biosciences)

2.5.6 Animal Ethics and Zebrafish Husbandry

Zebrafish were kept at the University of Alberta following a 14:10 light/dark cycle at 28 °C, according to a well established method.[42] They were raised, bred, and maintained following an institutional Animal Care and Use Committee approved protocol AUP00000077, operating under guidelines set by the Canadian Council of Animal Care.

2.5.7 Zebrafish Breeding

Wildtype (AB strain) zebrafish were bred using either a single male and two females or a single male and a single female. Fish were placed in tanks where the genders were separated by a plastic divider. The fish remained in a 28 °C room overnight, and the following morning the water was replaced, and the dividers were removed. In the afternoon, the tanks were drained and, if embryos were present, they were collected using a wide-bore plastic Pasteur pipette. Embryos were placed in a petri dish and 25 mL of standard E3 embryo media was poured overtop. No more than approximately 100 embryos were placed in each petri dish. All the petri dishes were placed in a 28 °C incubator overnight. The following day, dead or unfertilized embryos were placed in the waste.

2.5.8 Neuromasts Quantification Assays

Wild-type (AB strain) zebrafish were grown to either 2–3 or 6–7-days postfertilization (dpf) in standard E3 embryo media [42] and were treated with DMF or cisplatin and/or TLR4 antagonists (in 95% ethanol) at different concentrations in 6-well plates, with 10–15 zebrafish larvae per well. After every 20 h incubation at 28 °C, the wells were washed with embryo media before the fish were incubated in media containing 0.01% 2-[4-(dimethylamino) styryl]-1-ethylpyridinium iodide (DASPEI, Sigma-Aldrich) to stain for neuromast mitochondrial activity for 20 min. The wells were washed again in embryo media, and the zebrafish larvae anesthetized with 4% tricaine. Neuromasts were imaged under a Leica M165 FC dissecting microscope equipped with a

fluorescent filter. A standard scoring method for zebrafish hair cell viability was used.[43] Five posterior lateral line (PLL) neuromasts for each fish were assigned a score representing cell viability based on DASPEI fluorescent intensity (2 for no noticeable decline, 1.5 for minor decline, 1 for moderate decline, 0.5 for severe decline, and 0 for complete loss of fluorescent intensity). These five scores were summed for each individual (10 = all hair cells appear normal and viable; 0 = intense ototoxicity).

2.5.9 Statistical Analyses

TLR4 activation across multiple cell lines was analyzed by 2-way ANOVA with Bonferroni multiple comparison test between samples and Dunnett's multiple comparison test against a control sample (nil or vehicle). TLR4 activation in a single cell line was analyzed by a one-way ANOVA using Dunnett's multiple comparison test to a control sample (nil or siNT). Cisplatin responses tested in HEI-OC1 were analyzed by a 2-way ANOVA at multiple concentrations, or a one way ANOVA at a single concentration of cisplatin, using Bonferroni multiple comparison test. Neuromast scores were analyzed via one-way ANOVA with Tukey's multiple comparison test. All statistical analyses were performed using Prism 7.2.

2.6. References

1. Takashima, K.; Matsunaga, N.; Yoshimatsu, M.; Hazeki, K.; Kaisho, T.; Uekata, M.; Hazeki, O.; Akira, S.; Iizawa, Y.; Ii, M. Analysis of Binding Site for the Novel Small-Molecule TLR4 Signal Transduction Inhibitor TAK-242 and Its Therapeutic Effect on Mouse Sepsis Ebner Model. *Br. J. Pharmacol.* **2009**, *157*, 1250–1262.
2. Yamada, M.; Ichikawa, T.; Ii, M.; Itoh, K.; Tamura, N.; Kitazaki, T. Novel Cyclohexene Derivatives as Anti-Sepsis Agents: Synthetic Studies and Inhibition of NO and Cytokine Production. *Bioorg. Med. Chem.* **2008**, *16*, 3941–3958.
3. Blair, J. C. The Effects of Mild Sensorineural Hearing Loss on Academic Performance of Young School-Age Children. *Volta Rev.* **1985**, *87*, 87–93.
4. Gurney, J. G.; Tersak, J. M.; Ness, K. K.; Landier, W.; Matthay, K. K.; Schmidt, M. L. Hearing Loss, Quality of Life, and Academic Problems in Long-Term Neuroblastoma Survivors: A Report from The Children's Oncology Group. *Pediatrics*. **2007**, *120*, 1229–1236.
5. Lee, E. H.; Choi, S. E. The Effects of Music Therapy by Self-Selected Music Listening on Terminal Cancer Patients' Affect and Stress by Pain Level. *Korean J. Hospice Palliat. Care.* **2012**, *15*, 77–87.
6. Brock, P. R.; Bellman, S. C.; Yeomans, E. C.; Pinkerton, C. R.; Pritchard, J. Cisplatin Ototoxicity in Children: A Practical Grading System. *Med. Pediatr. Oncol.* **1991**, *19*, 295–300.
7. Li, Y.; Womer, R. B.; Silber, J. H. Predicting Cisplatin Ototoxicity in Children: The Influence of Age and The Cumulative Dose. *Eur. J. Cancer.* **2004**, *40*, 2445–2451.
8. Blakley, B. W.; Myers, S. F. Patterns of Hearing Loss Resulting from Cis-Platinum Therapy. *Otolaryngol. Head Neck Surg.* **1993**, *109*, 385–391.
9. Skinner, R.; Pearson, A. D. J.; Amineddine, H. A.; Mathias, D. B.; Craft, A. W. Ototoxicity of Cisplatinum in Children and Adolescents. *Br. J. Cancer.* **1990**, *61*, 927–931.
10. Siddk, Z. H. Cisplatin: Mode of Cytotoxic Action and Molecular Basis of Resistence. *Oncogene*. **2003**, *22*, 7265–7279.
11. Yu, M.; Wang, H.; Ding, A.; Golenbock, D. T.; Latz, E.; Czura, C. J.; Fenton, M. J.; Tracey, K. J.; Yang, H. HMGB1 Signals Through Toll-Like Receptor (TLR) 4 and TLR2. *Shock*. **2006**, *26*, 174-179.
12. Ho, J. K. K. Formulation of a Systemic PEST Analysis for Strategic Analysis. *Eur. J. Acad. Res.* **2014**, *2*, 6478–6492.
13. Bovijn, C.; Ulrichts, P.; De Smet, A. S.; Catteeuw, D.; Beyaert, R.; Tavernier, J.; Peelman, F. Identification of Interaction Sites for Dimerization and Adapter Recruitment in

Toll/Interleukin-1 Receptor (TIR) Domain of Toll-Like Receptor 4. *J. Biol. Chem.* **2012**, *287*, 4088–4098.

14. Park, B. S.; Lee, J. O. Recognition of Lipopolysaccharide Pattern by TLR4 Complexes. *Exp. Mol. Med.* **2013**, *45*, 66–76.
15. Pussegoda, K.; Ross, C. J.; Visscher, H.; Yazdanpanah, M.; Brooks, B.; Rassekh, S. R.; Zada, Y. F.; Dubé, M. P.; Carleton, B. C.; Hayden, M. R. Replication of and ABCC3 Genetic Variants Highly Associated with Cisplatin-Induced Hearing Loss in Children. *Clin. Pharmacol. Ther.* **2013**, *94*, 243–251.
16. Maranville, J. C.; Cox, N. J. Pharmacogenomic Variants have Larger Effect Sizes than Genetic Variants Associated with Other Dichotomous Complex Traits. *Pharmacogenomics J.* **2016**, *16*, 388–392.
17. Babolmorad, G.; Latif, A.; Domingo, I. K.; Pollock, N. M.; Delyea, C.; Rieger, A. M.; Allison, W. T.; Bhavsar, A. P. Toll-Like Receptor 4 is Activated by Platinum and Contributes to Cisplatin-Induced Ototoxicity. *EMBO reports*. **2011**, *22*, 51280–51293.
18. Lee, S.; Phuan, P. W.; Felix, C. M.; Tan, J. A.; Levin, M. H.; Verkman, A. S. Nanomolar-Potency Aminophenyl-1, 3, 5-Triazine Activators of the Cystic Fibrosis Transmembrane Conductance Regulator (CFTR) Chloride Channel for Prosecretory Therapy of Dry Eye Diseases. *J. Med. Chem.* **2017**, *60*, 1210–1218.
19. Kuang, Y.; Shi, J.; Li, J.; Yuan, D.; Alberti, K. A.; Xu, Q.; Xu, B. Pericellular Hydrogel/Nanonets Inhibit Cancer Cells. *Angew. Chem.* **2014**, *126*, 8242–8245.
20. Patra, M. C.; Kwon, H. K.; Batool, M.; Choi, S. Computational Insight into the Structural Organization of Full-Length Toll-Like Receptor 4 Dimer in a Model Phospholipid Bilayer. *Front. Immunol.***2018**, *9*, 489-511.
21. Yamada, M.; Ichikawa, T.; Ii, M.; Sunamoto, M.; Itoh, K.; Tamura, N.; Kitazaki, T. Discovery of Novel and Potent Small-Molecule Inhibitors of NO And Cytokine Production as Antisepsis Agents: Synthesis and Biological Activity of Alkyl 6-(N-Substituted Sulfamoyl) Cyclohex-1-Ene-1-Carboxylate. *J. Med. Chem.* **2005**, *48*, 7457–7467.
22. Molteni, M.; Gemma, S.; Rossetti, C. The Role of Toll-like Receptor 4 in Infectious and Noninfectious Inflammation. *Mediators Inflamm*. **2016**, *16*, 1–9.
23. El-Zayat, S. R.; Sibaii, H.; Mannaa, F. A. Toll-like Receptors Activation, Signaling, and Targeting: An Overview. *Doc. Bull. Natl. Res. Cent.* **2019**, *43*, 1–12.
24. Chiu, L. L.; Cunningham, L. L.; Raible, D. W.; Rubel, E. W.; Ou, H. C. Using The Zebrafish Lateral Line to Screen for Ototoxicity. *J. Assoc. Res. Otolaryngol.* **2008**, *9*, 178–190.
25. Domarecka, E.; Skarzynska, M.; Szczepek, A. J.; Hatzopoulos, S. Use of Zebrafish Larvae Lateral Line to Study Protection Against Cisplatin-induced Ototoxicity: A Scoping Review. *Int. J. Immunopathol. Pharmacol.* **2020**, *34*, 1–19.

26. Pickett, S. B.; Raible, D. W. Water waves to sound waves: Using Zebrafish to Explore Hair Cell Biology. *J. Assoc. Res. Otolaryngol.* **2019**, *20*, 1–19.

27. Suli, A.; Watson, G. M.; Rubel, E. W.; Raible, D. W. Rheotaxis in Larval Zebrafish Is Mediated by Lateral Line Mechanosensory Hair Cells. *PloS one*. **2012**, *7*, 29727–29749.

28. Loes, A. N.; Hinman, M. N.; Farnsworth, D. R.; Miller, A. C.; Guillemin, K.; Harms, M. J. Identification and Characterization of Zebrafish Tlr4 Coreceptor Md-2. *J. Immunol. Res.***2021**, *206*, 1046–1057.

29. Zhu, S.; Hudson, T. H.; Kyle, D. E.; Lin, A. J. Synthesis and In Vitro Studies of Novel Pyrimidinyl Peptidomimetics as Potential Antimalarial Therapeutic Agents. *J. Med. Chem.* **2002**, *45*, 3491–3496.

30. Coffin, A. B.; Ramcharitar, J. Chemical Ototoxicity of The Fish Inner Ear and Lateral Line. *Fish Hear. Bioacoustics*. **2016**; 419–437.

31. Mattila, L.; Kilpeläinen, M.; Terho, E. O.; Koskenvuo, M.; Helenius, H.; Kalimo, K. Prevalence of Nickel Allergy Among Finnish University Students In 1995. *Contact Derm.* **2001**, *44*, 218–223.

32. Lidén, C.; Skare, L.; Vahter, M. Release of Nickel from Coins and Deposition onto Skin from Coin Handling–Comparing Euro Coins and SEK. *Contact Derm.* **2008**, *59*, 31–37.

33. Nestle, F. O.; Speidel, H.; Speidel, M. O. High Nickel Release From 1-And 2-Euro Coins. *Nature*. **2002**, *419*, 132–132.

34. Spiewak, R.; Pietowska, J.; Curzytek, K. Nickel: A Unique Allergen–From Molecular Structure to European Legislation. *Expert Rev. Clin. Immunol.* **2007**, *3*, 851–859.

35. Grabbe, S.; Schwarz, T. Immunoregulatory Mechanisms Involved in Elicitation of Allergic Contact Hypersensitivity. *Immunol. Today.* **1998**, *19*, 37–44.

36. Martin, S. F.; Jakob, T. From Innate to Adaptive Immune Responses in Contact Hypersensitivity. *Curr. Opin. Allergy Clin. Immunol.* **2008**, *8*, 289–293.

37. Schmidt, M.; Raghavan, B.; Müller, V.; Vogl, T.; Fejer, G.; Tchaptchet, S.; Keck, S.; Kalis, C.; Nielsen, P. J.; Galanos, C.; Roth, J. Crucial Role for Human Toll-Like Receptor 4 in the Development of Contact Allergy to Nickel. *Nat. Immunol.***2010**, *11*, 814–819.

38. Rachmawati, D.; Bontkes, H. J.; Verstege, M. I.; Muris, J.; von Blomberg, B. M. E.; Scheper, R. J.; van Hoogstraten, I. M. Transition Metal Sensing by Toll-Like Receptor-4: Next to Nickel, Cobalt and Palladium are Potent Human Dendritic Cell Stimulators. *Contact Derm.* **2013**, *68*, 331–338.

39. So, H.; Kim, H.; Lee, J. H.; Park, C.; Kim, Y.; Kim, E.; Kim, J. K.; Yun, K. J.; Lee, K. M.; Lee, H. Y.; Moon, S. K. Cisplatin Cytotoxicity of Auditory Cells Requires Secretions of Proinflammatory Cytokines Via Activation of ERK and NF-K B. *J. Assoc. Res. Otolaryngol.* **2007**, *8*, 338–355.

40. Schmidt, M.; Raghavan, B.; Müller, V.; Vogl, T.; Fejer, G.; Tchaptchet, S.; Keck, S.; Kalis, C.; Nielsen, P. J.; Galanos, C.; Roth, J. Crucial Role for Human Toll-Like Receptor 4 in the Development of Contact Allergy to Nickel. *Nat. Immunol.***2010**, *11*, 814–819.

41. Kiss, E.; Abdelwahab, E. H. M. M.; Steib, A.; Papp, E.; Torok, Z.; Jakab, L.; Smuk, G.; Sarosi, V.; Pongracz, J. E. Cisplatin Treatment Induced Interleukin 6 and 8 Production Alters Lung Adenocarcinoma Cell Migration in an Oncogenic Mutation Dependent Manner. *Respir. Res.***2020**, *21*, 1–13.

42. Westerfield, M. A Guide for the Laboratory Use of Zebrafish Danio (Brachydanio) Rerio. *University of Oregon*. **2007**.

43. Chowdhury, S.; Owens, K. N.; Herr, R. J.; Jiang, Q.; Chen, X.; Johnson, G.; Groppi, V. E.; Raible, D. W.; Rubel, E. W.; Simon, J. A. Phenotypic Optimization of Urea–Thiophene Carboxamides to Yield Potent, Well Tolerated, and Orally Active Protective Agents Against Aminoglycoside-Induced Hearing Loss. *J. Med. Chem.* **2018**, *61*, 84–97.

Chapter 3

Computational Insight into the Molecular Interaction between the TIR Domain of TLR4 and its Antagonists

3.1 Introduction

Toll-like receptors (TLRs) are a class of membrane glycoproteins that play a key role in the induction and regulation of immune/inflammatory responses. They are single-spanning protein receptors expressed on the membranes of different immune cells and several non-immune cells that recognize structurally conserved molecules present on microbes.[1] TLR4 is one of the most studied TLRs. TLR4 is a widely conserved innate immune signaling molecule that detects pathogen-associated molecular patterns (PAMPs), most notably the Gram negative bacterial outer membrane component, lipopolysaccharide (LPS). It can also detect endogenous ligands termed damage-associated molecular patterns (DAMPs), such as hyaluronan or high mobility group box 1 (HMGB1) and some Group 9/10 transition metals such as nickel, cobalt, and palladium, which is believed to mediate immune hypersensitivity reactions. [2,3]

The binding of the ligand at the cell surface causes the homodimerization of TLR4 receptors through interactions between their intracellular toll/interleukin-1 receptor (TIR) domains, resulting in conformational changes in the molecule. Thus, TLR4 initiates subsequent intracellular signaling via two canonical signaling pathways: myeloid differentiation factor 88 (MyD88) dependent pathway and TIR-domain-containing adapter inducing interferon-β (TRIF) dependent pathway. TLR4 requires several adapter proteins to mediate a comprehensive immune response. TIR-domain-containing adapter protein or TIRAP engages the MyD88 that culminates in nuclear factor kappa B (NF-κB) nuclear translocation and pro-inflammatory cytokine production. TRIF-related adapter protein or TRAM engages TRIF resulting in IRF3 translocation to the nucleus and stimulation of type I interferon response.[4] The TRIF dependent pathway is also responsible for the late phase NF-κB activation through IRF3 and tumor necrosis factor alpha (TNF-α) secretion (Figure 3.1). Besides inflammatory cytokine production (via NF-κB), TLR4 activation initiates reactive

oxygen species (ROS) formation (via NADPH oxidase and mitochondria),[5,6] and apoptosis (via Fas-associated Death Domain protein). ROS accumulation and apoptosis induction pathways are not shown in Figure 3.1.[7] Thus, the TIR domain plays a central role in TLR4 mediated immune responses.

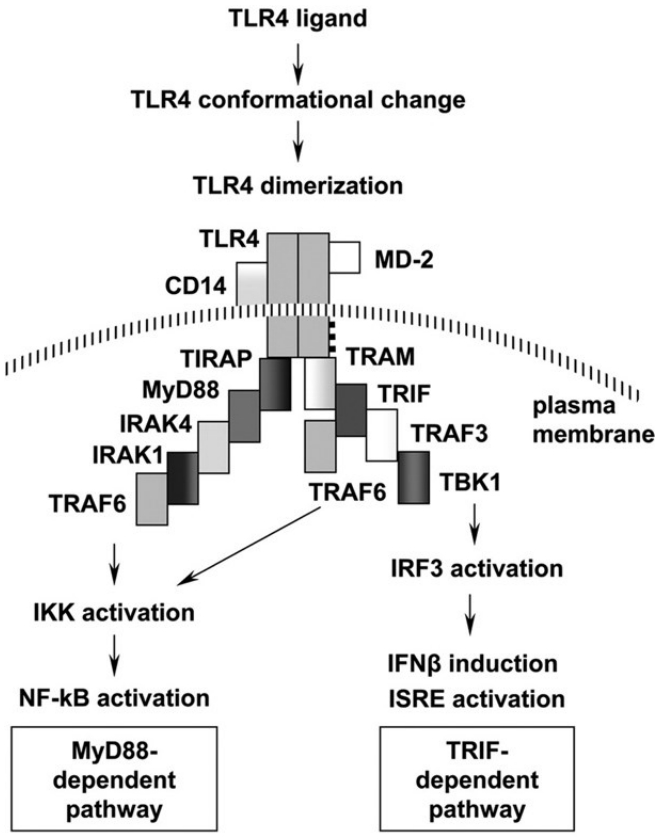

Figure 3.1. TLR4 signaling pathway: TLR4 signaling can be divided into two distinct signaling pathways, namely MyD88- and TRIF-dependent pathways. (Copied with permission from Matsunaga et al.[8])

TLR4 is believed to be involved in several pathologies such as sepsis, septic shock, lung inflammation, cardiac diseases, and ischemia/reperfusion (I/R) injury. It has been established as an excellent therapeutic target for different inflammatory diseases.[9–13] Several exogenous synthetic TLR4 antagonists have been developed to block TLR4 signaling cascades.[14] In particular, TAK-242 (Figure 3.2), a small molecule TLR4 antagonist shows inhibitory effects on LPS mediated inflammatory cytokine production though TRIF-dependent signaling pathway.[15] According to mutational

analysis, TAK-242 is proven to bind selectively to the TIR domain of TLR4 near Cys747 and inhibits TLR4 signal transduction and its downstream signaling events.[16,17]

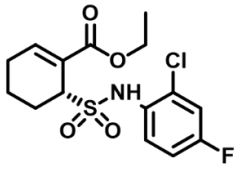

Figure 3.2. Chemical structure of TAK-242.

Sequence alignment predicts that in TLR4, Cys747 corresponds to a location in helix αC′ in the TIR domain which forms a part of the dimer interface. [18,19] Therefore, the cysteine residue in the TIR domain is predicted to be involved in the dimeric interface and is functionally relevant.[20] From a protein fragment complementation assay, it has been found that binding TAK-242 in the TIR domain did not affect the dimerization of TLR4.[16] Recent biochemical studies suggested that TAK-242 inhibits TLR4 signaling by interfering with interactions between TLR4 and the adaptor molecules TIRAP and TRAM (Figure 3.3).[15,21] However, the precise mode of action by which TAK-242 inhibits TLR4 signaling after binding to the receptor has remained uncertain.

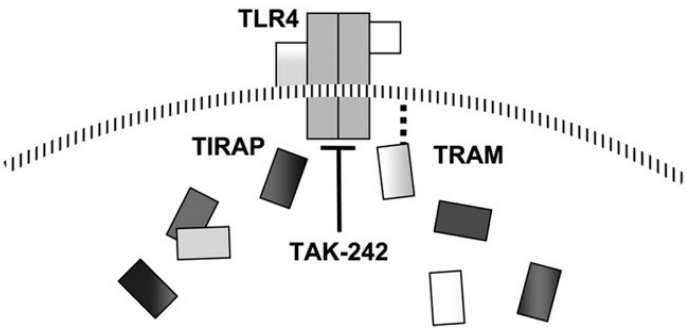

Figure 3.3. TAK-242 interferes with interactions between TLR4 and its adaptor molecules, TIRAP and TRAM (copied with permission from Matsunaga et al.[8]).

Recent biochemical studies done by Babolmorad et al. have identified the association of cisplatin with TLR4 activation.[22] They demonstrated that cisplatin activates pathways downstream of TLR4 to a similar extent as the canonical TLR4 agonist LPS. TLR4 plays a critical role mediating cisplatin induced ototoxicity (CIO) response in vitro which can be inhibited by TAK-242 which was discussed in detail in Chapter 1.

Cisplatin induced ROS generation and apoptosis induction in the inner ear cells cause the death of these critical mechanotransducing cells; however, it is poorly understood how these responses are elicited.[22] These findings revealed TLR4 as a potential druggable therapeutic target for CIO mitigation.

This chapter describes the computational studies we performed to investigate the molecular interaction of some synthetic small molecule inhibitors with TLR4 for inhibiting its downstream signal transduction. The in silico structure activity relationship analyses are also discussed here based on previous published and unpublished biological results.

Several studies have been conducted to uncover the three-dimensional structure of TLR4. The extracellular domain of TLR4 has been solved through X-ray crystallography. The transmembrane domains of TLR4 have been solved recently through NMR spectroscopy.[23,24] However, no crystal or NMR structure of the intracellular (TIR) domain of TLR4 has been reported so far. As TAK-242 is known to bind in the TIR domain of TLR4, we used the three-dimensional model of this domain in both monomer and dimer forms to conduct our in silico studies. The TIR domains were subjected to molecular dynamics (MD) simulations in an explicit solvent environment. The refined structures obtained from the MD simulations were subjected to clustering analysis to extract the dominant protein conformations. The obtained dominant conformations were then used in molecular docking studies with some selected inhibitors. The subsequent MD simulations of protein-ligand complexes were performed to characterize the structural changes introduced by small molecule inhibitors binding to TLR4 compared to free TLR4 form. We also evaluated the hydrogen bond network of all compounds with TLR4 in order to probe potential modes of binding.

3.2. Materials and Methods

3.2.1. Receptor Structures Preparation

The current study employs the equilibrated TIR domains (residues 661–839) of both TLR4 monomer and dimer to understand protein-ligand interactions. We prepared the

TIR monomer model by homology modeling and obtained the individual TIR dimer constructed using protein-protein docking approach by Patra et al.[25].

To generate the structure for TIR monomer, the amino acid sequence of this domain was retrieved from the UniProt database (UniProt ID: O00206-1).[26] Ten top models were obtained using SWISS-MODEL web server,[27] with acceptable sequence identity, QMEAN (Qualitative Model Energy Analysis) and GMQE (Global Model Quality Estimation). All the models were then ranked by their packing quality function and Ramachandran plots. The model was then validated from ERRAT score [28] and PROCHECK results.[29] The best model was then selected as a preliminary structure for TIR monomer.

Prior to molecular docking, both TLR4-TIR (monomer and dimer) models were subjected to extensive MD simulations and conformational analyses to achieve lower energy conformations by removing of structural clashes that can otherwise lead to further imprecisions in the desired results. The protocols for MD simulations and conformational analyses are described in sections **3.2.3** and **3.2.5**.

3.2.2. Ligand Preparation and Molecular Docking Protocol

We selected seven small molecule compounds for docking, comprising TAK-242 as hit compound, its enantiomer and six synthesized derivatives of TAK-242 as Figure 3.4. The chemical structures of the compounds were designed using ChemDraw.[30] Molecular docking simulations were run with the molecular operating environment (MOE) program.[31] Prior to docking, all compounds were protonated at physiological pH (pH 7) using MOE Protonate3D[32] and energy minimized. The refined and optimized receptor structures were used for the docking. The binding zone of receptors was determined as lying around residue Cys747 based on previous studies.[8,15,16] Docking studies were performed using MMFF94x force field optimization. The placement method was chosen as Triangle Matcher,[33] returning three thousand poses based on the London dG scoring.[34] The receptor was kept flexible for the refinement step, where thirty poses were retained based on the GBVI/WSA scoring function.[34] All thirty poses were visually inspected, and redundant and symmetrical poses were filtered out

manually, and the remaining five poses were taken for subsequent molecular dynamics (MD) simulations based on the binding affinity (*S*) scores and ligand orientations.

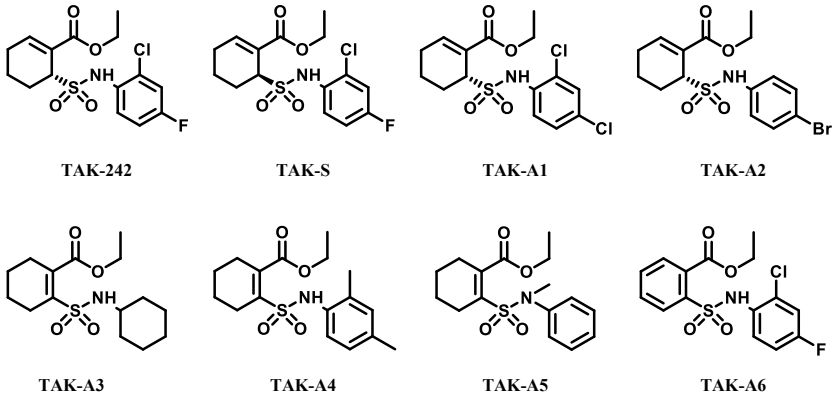

Figure 3.4. Chemical structures of selected small molecule TLR4 antagonists

3.2.3. Classical MD Simulations: Parameters and Protocol

For all generated structures, MD simulations were carried out under physiological conditions using the NAMD program on the CEDAR supercomputer from Compute Canada.[35]. We ran 2 initial MD simulations on the TIR monomer and dimer structures using the all-hydrogen Amber ff14SB force field using AmberTools18 tleap.[36] The protonation states of all ionizable residues were assigned using MOE Protonate3D[32] at pH 7 and then visualized and inspected carefully to ensure their correct protonation states. The protonated system was solvated with octahedral boxes of TIP3P explicit water molecules with 12 Å of buffer between any atom of the system and the edge of the box. The overall charge of the system was neutralized, and a 0.15 M physiological ionic concentration was established by adding the required numbers of Na^+ and Cl^- ions.[37] All solvated-ionized systems were initially minimized in 100,000 iterative steps using conjugate gradient algorithm as implemented in NAMD software. Using SHAKE algorithm[38] a restraint of 50 kcal/mol/Å^2 was imposed to the protein backbones and on the small molecules during this step under constant volume (NVT) conditions. This step allows the relaxation of the systems and the removal of structural clashes that can otherwise lead to further imprecisions in the desired results. Under the same restraint, the systems were then heated up to 310 K in a time of 100 ps. Following heating, the

systems were equilibrated in two successive NVT and NPT steps for 250ps, each with a gradual removal of the restraints. The systems were then continued for the production NPT simulation to generate reasonably long trajectories (200 ns for dimer and 30 ns for monomer) in order to explore their conformational dynamics.

All MD simulations were performed using an integration time step of 2 fs, under periodic boundary conditions. The Langevin dynamics were adopted for temperature (310 K) and non-isotropic pressure control (1 bar).[39] Bonded interactions computed every one-time step, short-range non-bonded interactions every two timesteps, and long-range electrostatic interactions every four-time steps. A cut-off of 12 Å was used for the van der Waals interactions and short-range electrostatic interactions, with a switching function starting at 10 Å for van der Waals interactions to ensure a smooth cut-off. The simulations performed under periodic boundary conditions; long-range electrostatic interactions calculated by using the particle-mesh Ewald (PME) method.[40] The unit cells were large enough that adjacent copies of the protein are never close enough for shortrange interactions to apply.

Following the same protocol, we carried out 50 ns MD simulation on each of the selected 8 compounds from docking simulations with TIR dimer as a post-processing to the docked protein-ligand complexes. The General Amber Force Field (GAFF)[41] parameters were assigned to the small molecule ligands using Antechamber[42] for the simulation of complexes.

To assess the equilibration of the system, the mass-weighted root-mean-square deviations (RMSD) of the heavy atoms of protein backbone and ligand were calculated over the duration of the simulation using CPPTRAJ utility from AmberTools18.[43]

To assess the flexibility of the different residues, beta factors for each residue in the proteins using the whole trajectory were calculated as well. All plots were generated using Gnuplot.[44] In addition, the trajectory was visually analyzed using Visual Molecular Dynamics (VMD) program.[45]

3.2.4. Binding Energy Analysis using MM-GBSA Method

The binding energy (or free energy) is one of the most important measurable quantities in structure activity relationship (SAR) studies, as it demonstrates the affinity between

the ligand and the target; the lower the value for this energy the better is the affinity between the ligand and the target. In our work, we used the Molecular Mechanics Generalized Born Solvation Area (MM/GBSA) method[46] implemented in the MMPBSA.py script[47] to calculate relative binding free energies of protein-ligand complex. Using MM/GBSA allows the establishment of a good balance between the speed of the calculations and the correctness of the rank between the investigated compounds. In MM/GBSA, the binding free energy of a ligand-receptor complex was calculated as[48]

$$\Delta G_{bind,solv} = \Delta G_{MM,vac} + \Delta G_{solv,complex} - (\Delta G_{solv,ligand} + \Delta G_{solv,protein}) - T\Delta S \quad (3.1)$$

where $\Delta G_{MM,vac}$ includes averaged non-bonded molecular mechanics terms (electrostatic and van der Waals) occurring between protein and ligand. The $T\Delta S$ term defines the change in conformational entropy due to the binding, which was neglected in our study because calculating $T\Delta S$ is quite expensive in terms of computational cost and it is not necessary as the goal of this study is to estimate binding affinities of ligands with a common target, where the entropic contribution can be considered as constant. When using the MM/GBSA method, the solvation terms are given by the equation[38]

$$\Delta G_{solv} = \Delta G_{solv,polar} + \Delta G_{solv,npolar} \quad (3.2)$$

We performed all the energy calculations considering the last 1000 frames of production MD simulation of the system at regular intervals of 20 ps from the trajectory. Using the same utility, the binding energy decompositions were carried out among the different residues involving in the binding reaction.

3.2.5. Clustering Analysis Protocol

The MD simulations of the two proteins, i.e., TIR-monomer and TIR-dimer, resulted in quite long trajectories that contained massive amounts of structural data, and selecting true representative conformations from these trajectories is crucial. Clustering MD trajectories is an efficient way of grouping the dynamic conformations in a meaningful way in order to obtain dominant structural representatives from the whole trajectory. To analyze the conformational dynamics of the active-site residues of the apo receptor proteins, we carried out RMSD conformational clustering for the whole

MD trajectories. In this work, we adopted a well validated clustering algorithm called average-linkage algorithm as implemented in the CPPTRAJ utility of AMBER using cluster counts ranging from 2 to 100 clusters.[49] First, we carried out an RMSD fitting of all Cα-atoms of the equilibrated proteins to their minimized initial structures in order to remove overall rotation and translation. These atoms were then clustered into groups of similar conformations and the optimal numbers of clusters were predicted after evaluation of the Davies-Bouldin index (DBI)[50] and the 'elbow criterion'[49]. A high-quality clustering scheme is expected when a local minimum in the DBI values coincides with a plateau in the percentage of variance explained by the data (SSR/SST), while varying the number of clusters.[49] The centroid of each cluster, the structure having the smallest RMSD to all members of the cluster, was then selected as the cluster representative structure and the dominant structures, representing the dominant clusters, were then used for further analysis.

Using the same clustering protocol, we clustered the conformations of ligands of the ligand-bound systems from the whole MD trajectories to extract the dominant mode(s) of binding of the ligands within the active site of the receptor.

3.2.6. Hydrogen Bond Analysis

Hydrogen bond analyses were performed on the whole trajectory of each of the seven MD systems using the CPPTRAJ tool as implemented in AMBER 18[43] by computing the average distance between donor and acceptor atoms. A hydrogen bond was defined by a cut-off distance of 3.5 Å between a donor and acceptor atom and an absolute angular deviation below 60^{o} from linearity. Hydrogen bond analyses evaluated every potential H-bond based on their bond length and angle during the MD simulation. Neighboring water molecules within 5 Å of the bound compounds were also evaluated for their ability to bridge any H-bond interactions with the surrounding residues and visualized using the VMD software for the final conformation. Hydrogen bond analysis plots were generated using Gnuplot[44] and visualization of the hydrogen bonds were performed using VMD[45].

3.3. Results and Discussion

3.3.1. Homology Modeling of TLR4-TIR Monomer

A plausible three-dimensional structure of the protein is very crucial for receptor-inhibitor interaction studies. As the experimental structure for human TLR4-TIR protein is not currently available we used in silico homology modeling tools to model TLR4-TIR monomer, which rely on the sequence similarity of the target protein to related proteins of known structure. After retrieving the sequence of the TLR4-TIR monomer from the UniProt database (UniProt ID: O00206-1), we used SWISS-MODEL web server to obtain models with acceptable protein quality evaluation parameters. Eventually, among ten top models, the 7NUW[51] PDB entry (human TLR1 monomer) was chosen as the template to be used for the homology modeling because of a higher sequence similarity and other relevant comparative parameters shown in **Table 3.1**. The TIR domain of human TLR4 monomer consists of 179 residues for each monomer. **Figure 3.5** shows the sequence alignment results of both receptor fragments. The modeling of the receptor resulted in 153 residues. The new TLR4 monomer model is reported in **Figure 3.6(a)**.

Table 3.1. The results of template search.

Crystal Structure	X-ray Resolution	Sequence Similarity	QMEAN Z-score	GMQE
7NUW	1.9 A˚	37.33%	-1.51	0.60

QMEAN Z-score around 0.0 indicates a "native-like" structure and below -4.0 indicates a model with low quality. GMQE is a quality estimate which combines properties from the target-template alignment and the template structure.

```
TLR4_HUMAN      1   LAGCIKYGRGENIYDAFVIYSSQDEDWVRNELVKNLEEGVPPFQLCLHYRDFIPGVAIAA   60
TLR1_HUMAN      1   -----------LQFHAFISYSGHDSFWVKNELLPNLEKE--GMQICLHERNFVPGKSIVE   47
                              :.**: **.:*. **:***: ***:    :*:*** *:*:** :*.

TLR4_HUMAN     61   NIIHEGFHKSRKVIVVVSQHFIQSRWCIFEYEIAQTWQFLSSRAGIIFIVLQKVEKTLL-  119
TLR1_HUMAN     48   NIIT-CIEKSYKSIFVLSPNFVQSEWCHYELYFAHHNLFHEGSNSLILILLEPIPQYSIP  106
                    ***   :.** * *.*:* :*:**.** :*  :*:   * ..  .:*:*:*: : :  :

TLR4_HUMAN    120   RQQVELYRLLSRNTYLEWEDSVLGRHIFWRRLRKALLDGKSWNPEGTVGTGCNWQEATSI  179
TLR1_HUMAN    107   SSYHKLKSLMARRTYLEWPKEKSKRGLFWANLRAAINIKLTEQAKK--------------  152
                     .  :*  *::*.***** ..   * :** .** *:    : : :
```

Figure 3.5. Structure of the monomeric model of human TLR4-TIR domain obtained from homology modelling from the human TLR1 template.

The model was then validated from ERRAT score[28] and PROCHECK results[29].The results from the structural evaluation are reported in **Table 3.2**. The PROCHECK

results indicate a small number of amino acids that present a wrong value for the Ψ and Φ angles (0.7%), and a large number of residues with torsion values in the theoretically correct part of the Ramachandran plot as shown in **Figure 3.6(b)** as well.

Table 3.2. Structural evaluations performed for the human TLR1 crystallographic structure, the human TLR4-TIR monomer model obtained with homology modeling.

Structure	ERRAT Quality Factor	PROCHECK			
		Core	Additional	Generously	Disallowed
TLR1	96.026	91.7	7.6	0.7	0.0
TLR4 model	96.454	90.8	7.8	0.7	0.7

ERRAT results refer to the percentage of the protein for which the calculated error value falls below the 95% rejection limit. PROCHECK results refer to the percentage of angles lying in the relative zones of Ramachandran plot.

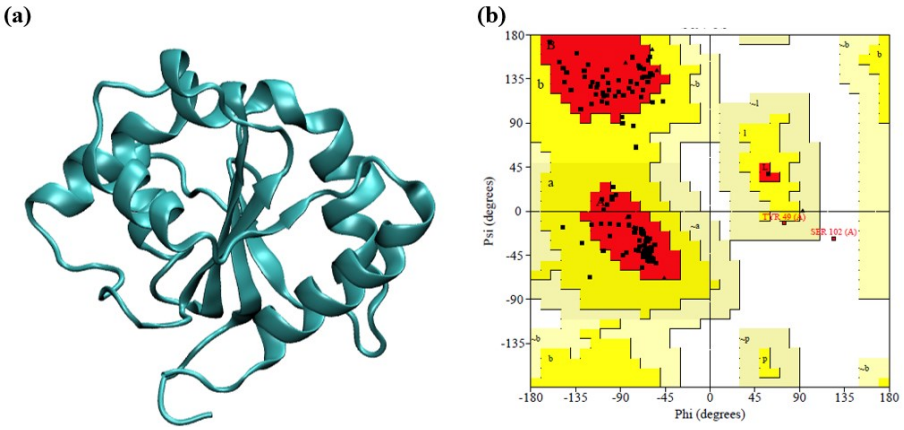

Figure 3.6: (a) The model for the human TLR4-TIR monomer obtained with homology modeling, using the crystallographic structure of human TLR1-TIR as template. **(b)** Ramachandran plot of the protein model.

3.3.2 MD Simulation and Clustering Analyses of Apo Structures

TLR4-TIR monomer model derived from the 7NUW template 51 and TLR4-TIR dimer obtained from previous work[25] were simulated with classical molecular dynamics (MD) for 20 ns and 200 ns respectively. The root-mean-square deviation (RMSD) graphs shown in **Figure 3.7 (a)** and **(b)** confirm that both proteins had reached equilibrium, which is an indication of structural and energetic relaxation of the systems. RMSD of the backbone atoms of the modeled monomeric and dimeric domains reached

a plateau after about 3 ns and 100 ns, with stable fluctuations around 2.5 Å and 5 Å, respectively, for the remaining simulation time.

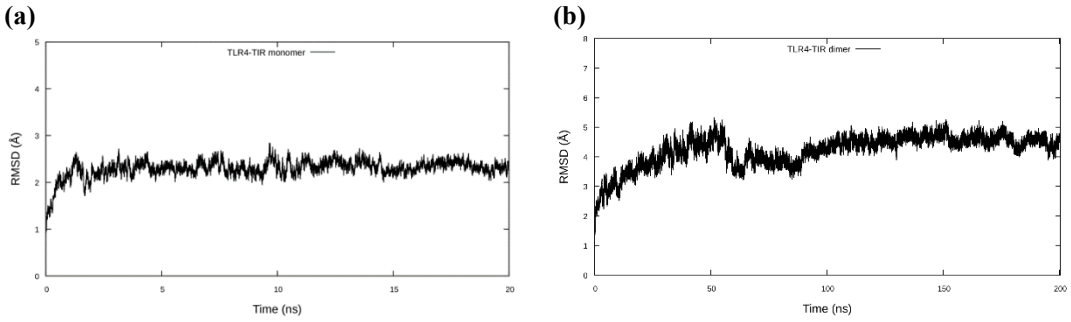

Figure 3.7. Root-mean-square deviations (RMSD) from the initial MD simulations for apo TLR4-TIR monomer **(a)** and dimer **(b)**.

Our next step was to identify and to study the dominant conformations from the two MD trajectories of monomer and dimer within the ligand binding sites. To extract all useful information from the MD trajectories we ran the RMSD conformational clustering analysis for a wide range of clusters. **Figure 3.8** shows clustering analysis of TLR4-TIR monomer and dimer. For the monomer **(Figure 3.8a)** a local minimum in the DBI parameter is observed at a cluster count of 10, which coincides with a plateau in the percentage of variance explained by the data (SSR/SST), indicative of 10 clusters as the optimal number of clusters for monomer conformations. The largest cluster of those includes around 38% of the whole trajectory, and the sizes of the first and second clusters are significantly smaller than the largest cluster, indicating the presence of a single dominant conformation for monomer **(Figure 3.8b)**. On the other hand, 16 clusters are predicted to be the optimal number of clustering for the dimer MD trajectories, the dominant cluster in this case includes around 45% of the whole dimer trajectory, indicating the existence of a main dominant conformation **(Figure 3.8c,d)**. The dominant representative conformations obtained from the clustering analyses were then used in the subsequent protein–ligand docking simulations.

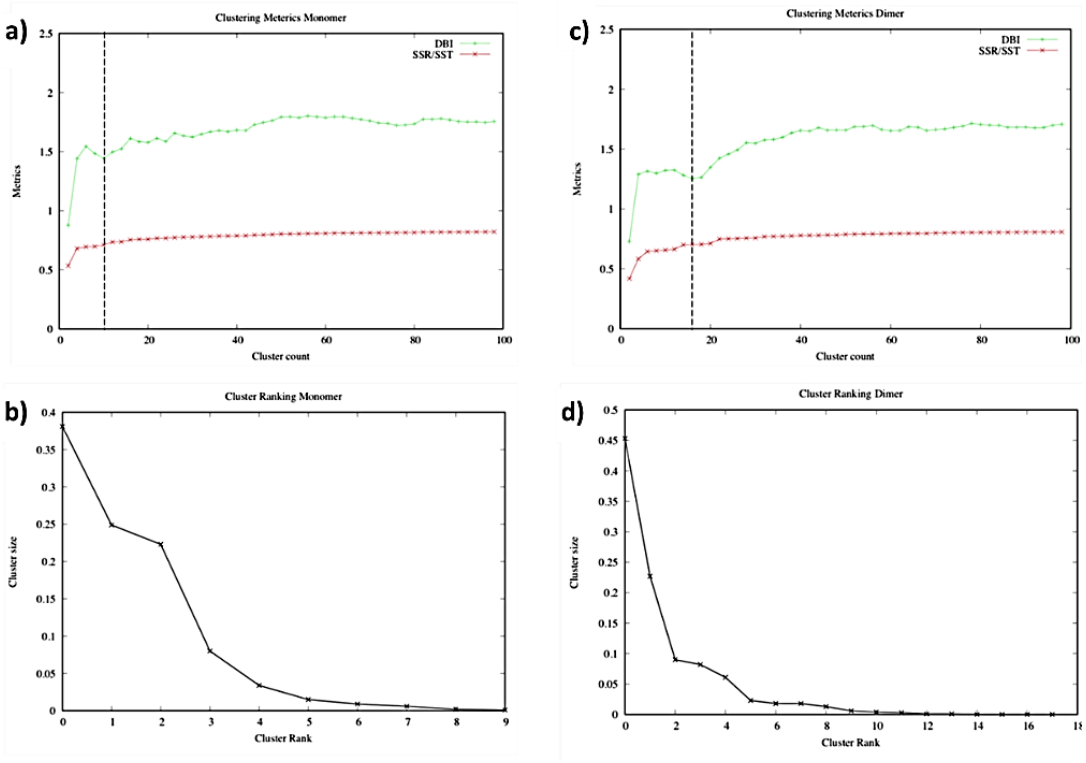

Figure 3.8. Conformational clustering of the MD trajectories of TLR4-TIR monomer and dimer. **(a, c)** Clustering metrics of monomer and dimer for different cluster counts, **(b, d)** Clusters' sizes at the predicted optimal number of clusters for monomer and dimer.

3.3.3. Molecular Docking

It has been found that **TAK-242** inhibited TLR4 signaling by binding near **Cys747** residue in the intracellular domain (ICD) of TLR4.[16] The residue **Cys747** resides in the dimeric interface of this receptor and a cleft is present at the interface of the two TLR4-TIR monomers around this residue. However, in the previous cell-based studies there is no clear indication of whether **TAK-242** binds with the receptor monomer or dimer to inhibit the cell signaling. To investigate this phenomenon computationally we carried out the docking simulations of the hit compound **TAK-242** with both the TLR4-TIR monomer and dimer near **Cys747**. Accordingly, we performed the docking of the **TAK-242** enantiomer and six **TAK-242** derivatives with TLR4-TIR dimer. The protocols of docking studies are described in the Materials and Methods section.

3.3.4. MD Simulation Analyses of Complex Structures

After performing the docking simulations, the complexes were subjected to classical explicit solvent MD simulations. Employing explicit solvent MD simulations helps in resolving two prime issues of docking, i.e., accounting for all-atom protein and ligand flexibility and including the effects of explicit waters, as well as also improves the accuracy of the predictions. To remove any redundant information from docking simulations, for each compound, five best-scoring docked poses that differed in their positions, orientations, and the number and types of interactions with the key residues present in the binding site were selected to perform subsequent MD simulations followed by RMSD and MM-GBSA-based re-scoring.

3.3.3.1. RMSD and MM-GBSA-based Ranking

For each compound, the selected the five poses from docking simulations were subjected to 5ns MD simulations. The RMSDs calculated for each protein-ligand complex system stabilized mostly at around 2 Å (**Figure 3.9**).

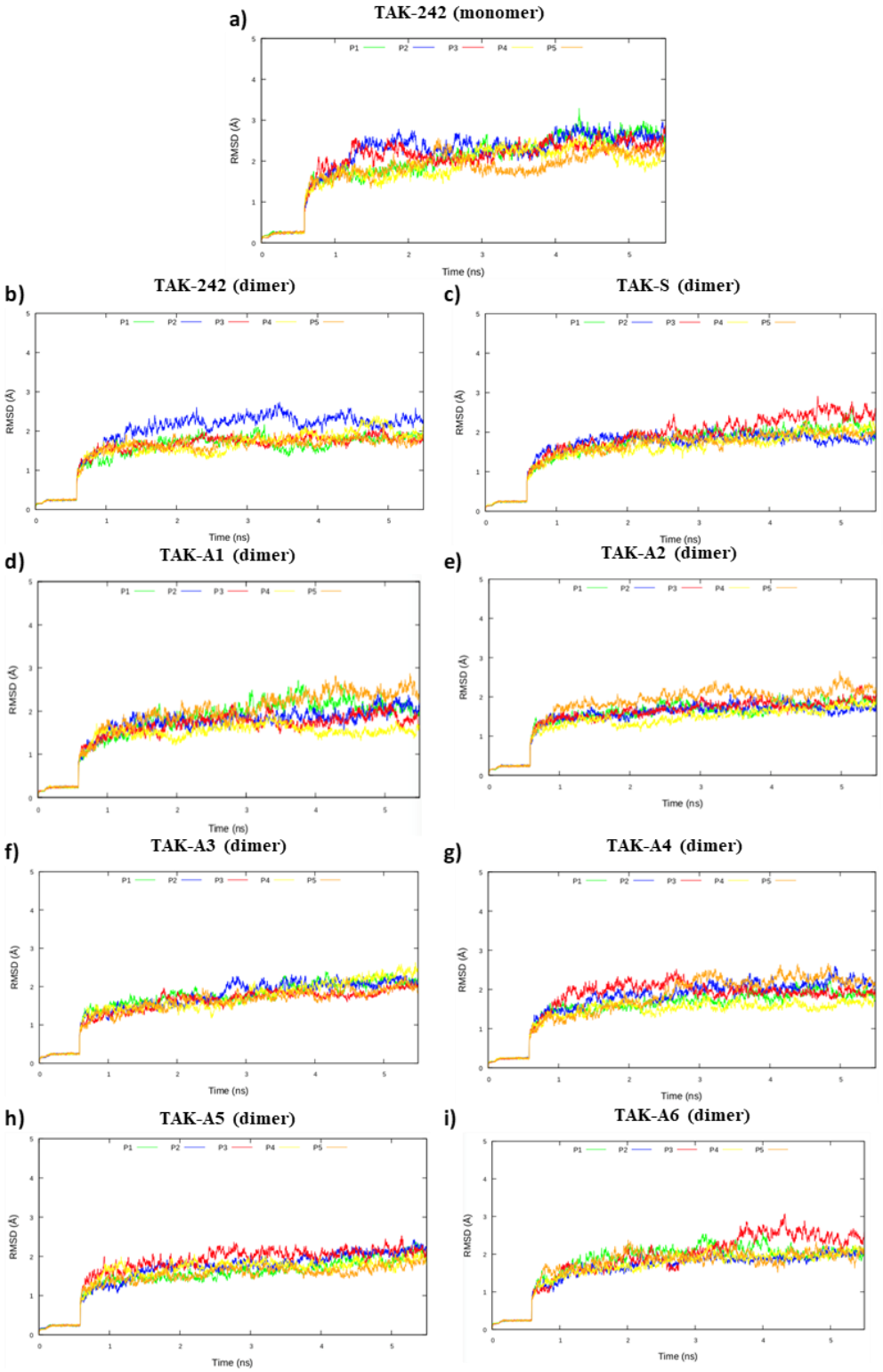

Figure 3.9. RMSDs of all five poses of the complexes observed in the 5 ns classical MD equilibration protocol.

However, the RMSDs for ligands stabilized (**Figure 3.10**) at variable distance ranging from 0.5 to 3 Å and ligands of some poses were unstable in the binding pocket throughout the simulation.

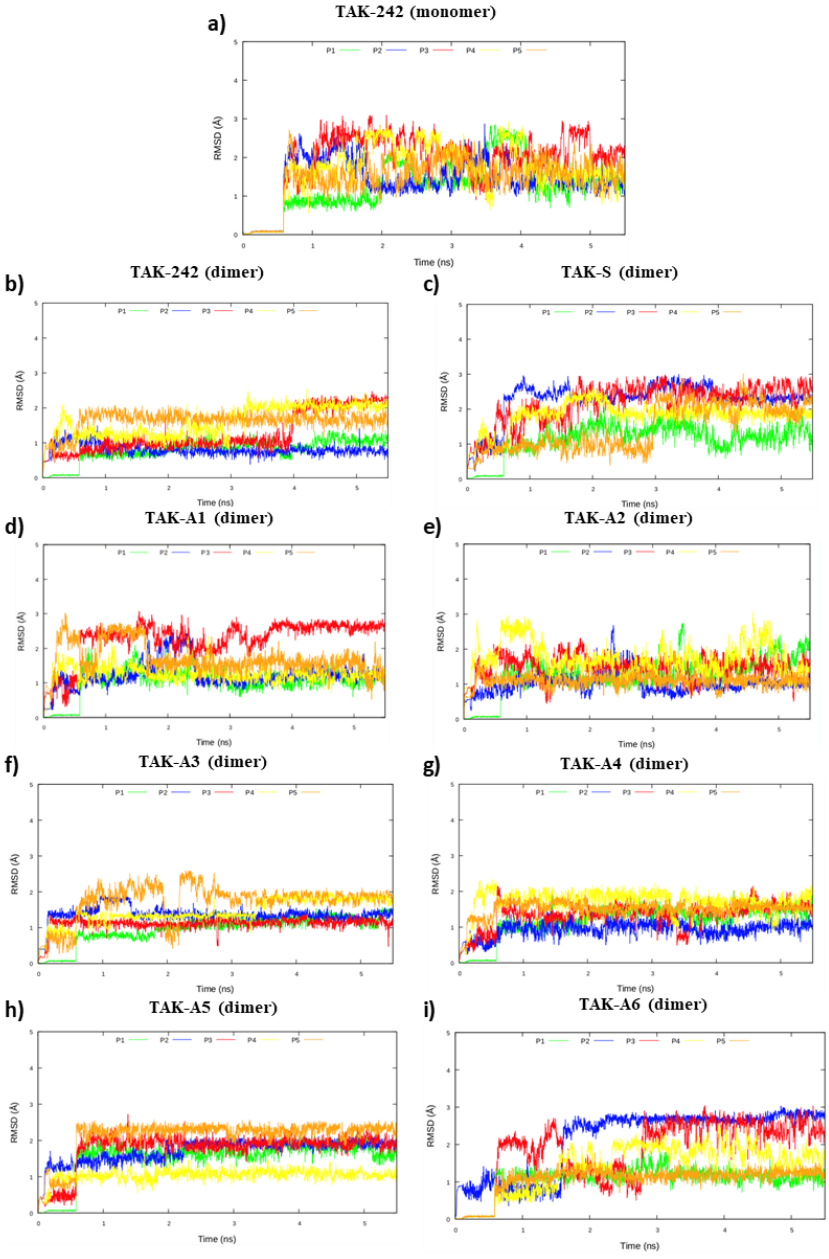

Figure 3.10. RMSDs of all five poses of all the ligands observed in the 5 ns classical MD equilibration protocol.

Later, MM-GBSA was used to estimate the binding free energies for each pose (**Figure 3.11**) using snapshots that were sampled at equal intervals from the respective equilibration trajectories.

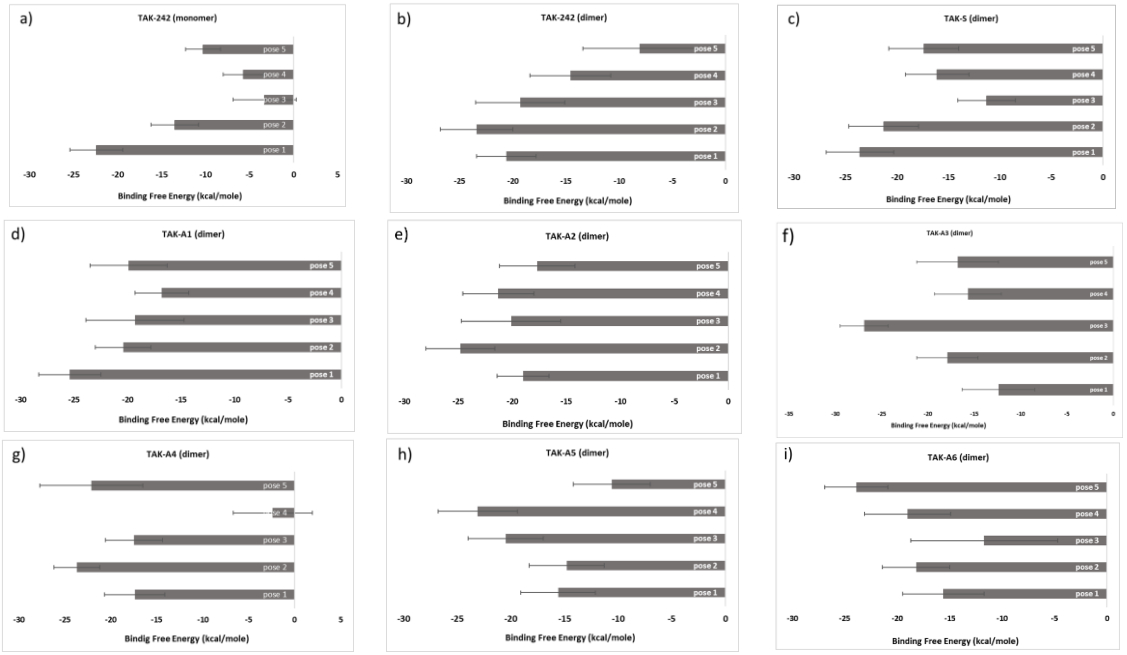

Figure 3.11. MM-GBSA binding free energies (kcal/mol) for all five poses of all the ligands in complex with the receptor.

For each compound, the best pose for each compound was selected based on the stability of the ligand inside the binding pocket with lower RMSD and best MM-GBSA score (i.e., the lowest negative energy).

Our initial MM-GBSA rescores of all selected best poses are almost the same. The overall relative ranking of the compounds was not possible at this stage. To predict the relative order of the compounds more accurately we need to continue the simulation for reasonable amount of time. To efficiently use our computational resources, we decided to focus on the best pose for each compound obtained from the initial MD-based ranking.

3.3.3.2. MD Simulation Analysis of Selected Complexes

MD simulation was continued till 30 ns for the best pose of TAK-242 and monomer complex. The root-mean-square-deviations (RMSDs) were calculated for the complex, and the ligand alone to ensure the equilibration of the system.

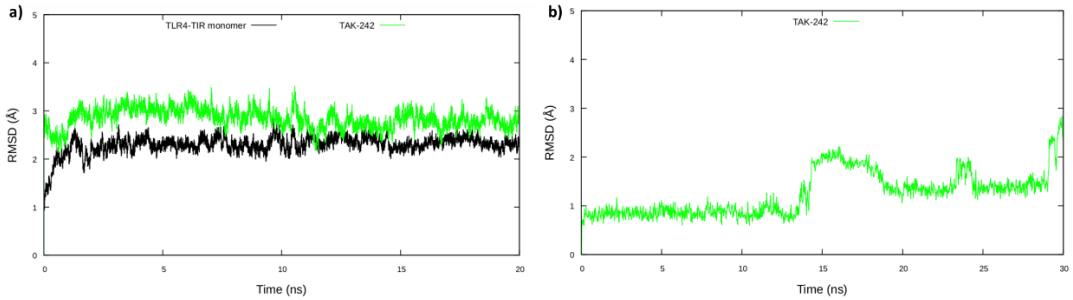

Figure 3.12. RMSDs analysis of TAK-242 and TLR4-TIR-monomer. **a)** RMSD of monomeric complex (last 20 ns of MD) along with that of the apo monomer as reference; **b)** RMSD of TAK-242 bound with monomer observed in the 30 ns classical MD equilibration protocol

From **Figure 3.12a** we see that RMSD of TAK-242 and monomer complex shows a similar trend as that of monomer alone. More interestingly, RMSD of the ligand TAK-242 showed a plateau till ~10 ns and after that it started fluctuating between 1 and 2.5 Å (**Figure 3.12b**). When we visualized the complex we saw that the ligand was totally out of the binding pocket of the monomer. Furthermore, the MM-GBSA score of the complex was only -0.62±2.49 kcal/mole after 30 ns of MD simulation. Therefore, we can conclude that TAK-242 has very negligible affinity towards the TIR domain of TLR4 monomer. For this reason, we did not carry out the in silico studies of the monomer complex with other ligands.

As the dimeric complex structure is bigger than the monomeric complex, therefore we decided to continue the MD simulation of the dimeric complex till 50 ns to ensure the equilibration of the system. The RMSDs graph in **Figure 3.13a**, suggests that all the complex structures have reached the acceptable equilibria, fluctuating at around 2-3Å indicating the stabilizing effects upon binding of the ligands (**TAK-242, TAK-A1, TAK-A2, TAK-A3, TAK-A4, TAK-A5,** and **TAK-A6**) to the TLR4-TIR dimeric interface. All the complex systems reached plateaus after ~40 ns of simulations in explicit solvent. The MD simulation of the ligand-bound forms of the dimer complexes revealed significant changes from the unbound structure of dimer, with

1.0~2.5 Å of differences in RMSDs (**Figure 3.13a**). The observed flexibility in RMSDs can be mainly attributed to the presence of many loops within the receptor. From the RMSDs graph (**Figure 3.13b**) of the ligands we can see that all ligands except **TAK-A6** and **TAK-S** maintained a stable pose within the binding pocket of the dimer, with the average displacements of ~0.5-1.5 Å from the starting structures.

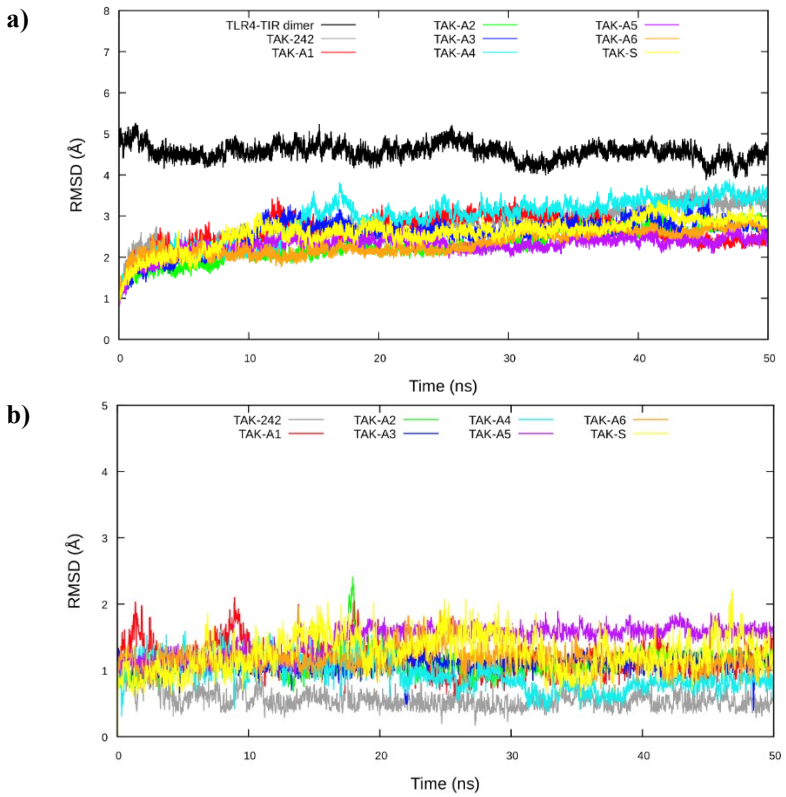

Figure 3.13. RMSDs analysis of compounds and TLR4-TIR-dimer observed in the 50 ns classical MD equilibration protocol. **a)** RMSDs of the dimeric complexes along with the last 50 ns apo dimer as reference; **b)** RMSDs of ligands bound with dimer.

In previous biochemical studies, the activities of the two enantiomers, (*R*)-(+)-**TAK-242** and (*S*)-(-)-**TAK-S**, were evaluated in order to investigate the stereochemical requirement for inhibition. A significant difference was observed between the enantiomers, and **TAK-242** exhibited 350-fold more activity than **TAK-S**.[53] In our in silico study, we observed a similar result in terms for the RMSD trends of these two ligands. As expected, **TAK-242** stabilized around 0.5 Å of RMSD value after about 4 ns of production simulation and maintained the same fluctuation trend for the

remaining simulated time, whereas RMSD of **TAK-S** showed an unstable trend in complex with the receptor dimer as shown in **Figure 3.14**.

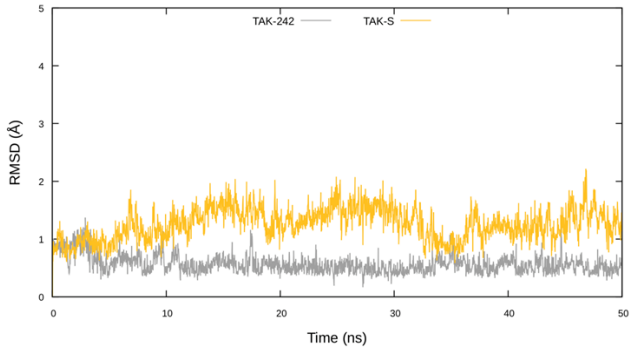

Figure 3.14. RMSDs analysis of TAK-242 and TAK-S in complex with the receptor dimer observed in the 50 ns classical MD equilibration protocol.

To evaluate the effects of each compound on the flexibility of the different parts of the TLR4-TIR dimer, we used the 50 ns from each simulation to calculate the atomic fluctuations values (i.e., beta factors) for each residue in the presence of a compound relative to the free protein. The atomic fluctuation graphs for apo and ligand-bound systems are shown in **Figure 3.15**. In the graph, the residues of one monomer are defined as 684–839 and for the other monomer is as 684*–839*. The atomic fluctuations for both apo and ligand-bound systems show several regions with variable flexibility. The main fluctuations in the structure belong to the several loops and linkers that connect the helical segments of the protein that give these protein regions additional freedom to move. For the apo-protein, mostly six regions containing residues 697–708, 813–821, 698*–719*, 750*–765*, and 827*–839* showed highest motional variability, whereas the region ranging 713–770 showed the highest atomic rigidity. According to **Figure 3.15**, all compounds affected almost the same regions of the protein; however, their effects were not identical. For example, while **TAK-242**, **TAK-A1**, **TAK-A4**, **TAK-A6** significantly enhanced the flexibility of residues 697–708, **TAK-A3** and **TAK-S** seemed to decrease the flexibility of the same region, whereas **TAK-A2** and **TAK-A5** did not affect the conformations of these residues. Furthermore, all compounds increased the flexibility of residues 813–839, especially, **TAK-A2**, **TAK-A4** and **TAK-A6,** which caused exceptionally increase in the flexibility of residues 830–839. In contrast, all compounds reduced the flexibility of residues 698*–719* and 750*–765*. On the other hand, **TAK-A1, TAK-A3** and **TAK-A5**

increased the flexibility of residues 827*–839*, whereas the remaining compounds deceased the flexibility of these residues. It's worth mentioning that **TAK-S** caused exceptional flexibility in 705–733 region compared to other compounds though this region was quite rigid on the apo protein.

Findings from beta factor calculations suggest that subtle variations in ligand structure result in higher differences in the relative motions of the receptor backbone.

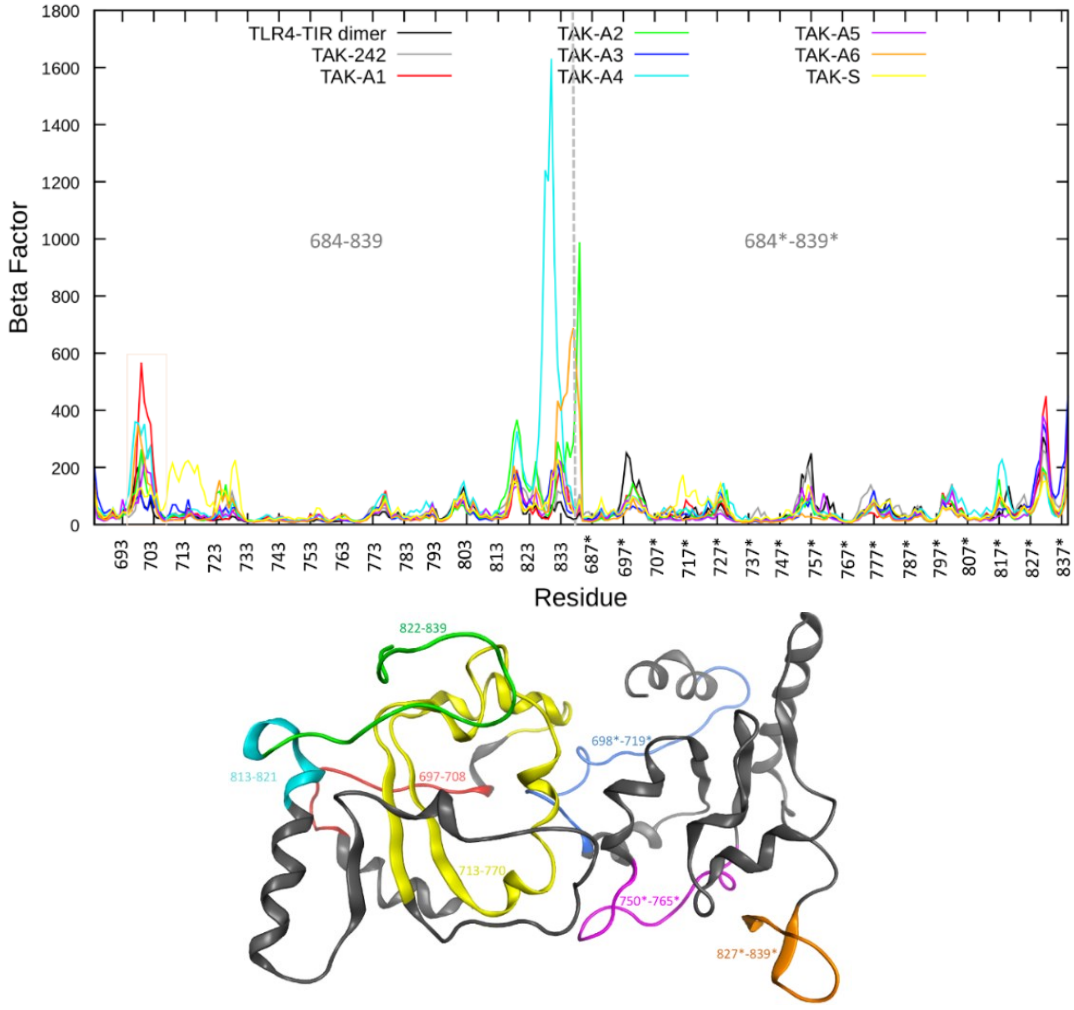

Figure 3.15. Atomic fluctuations (beta factors) of the backbone atoms of the TLR4-TIR dimer in the free and ligand-bound systems observed in the 50 ns classical MD equilibration protocol.

3.3.3.3. Binding Free Energy Estimates

The results of the molecular mechanics-generalized Born surface area (MM/GBSA) calculations for ligand-receptor complexes after 50 ns MD simulations are reported in **Figure 3.16a.** Our data show that the MM-GBSA rescoring predicted the relative order

of the drugs quite accurately. For example, **TAK-A1**, the strongest TLR4 inhibitor amongst all compounds in our recent in vitro study (**Figure 3.16b)**, was predicted with the lowest (most negative) binding free energy score of~−39 kcal/mol. Similarly, **TAK-242** is the second most active inhibitor which has the second highest MM-GBSA score (~−34 kcal/mol). Further, based on the binding free energies predicted for TAK-A6 (~−15.6 kcal/mol), (TAK-S (~−15.2 kcal/mol), these molecules can be classified as the ligands with lowest-affinity to the TLR4, which is consistent with both our experimental results and literature data.[52]

Notably, the MM-GBSA rescoring struggled when comparing the compounds that showed mid-range and closer affinities. For example, the MM-GBSA score of **TAK-A2** (~−25.1 kcal/mole)**, TAK-A4** (~−25.2 kcal/mole) **and TAK-A5** (~−25.6 kcal/mole) showed the energy differences of ~3 kcal/mol from that of **TAK-A3** (~−28.3 kcal/mole)**,** however, the standard deviation estimate for **TAK-A3** was over ±3 kcal/mol, thereby placing all of them at almost same footing.

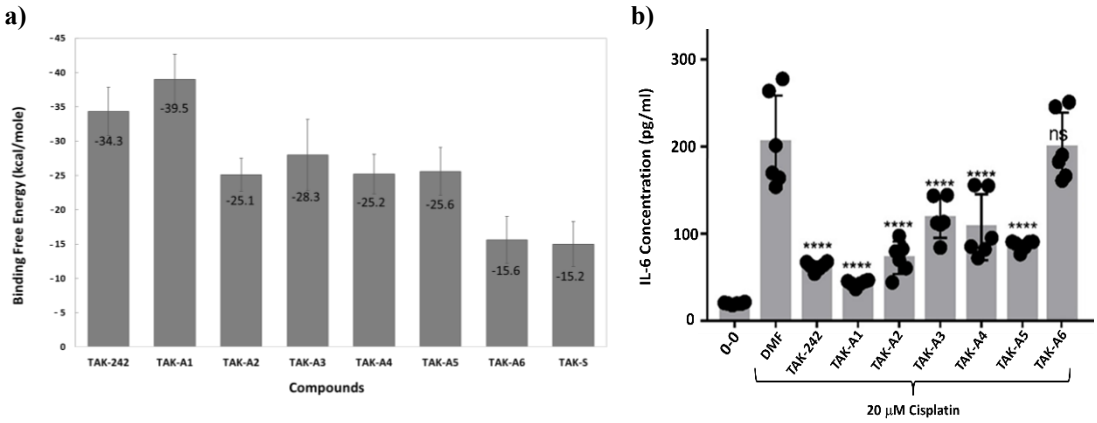

Figure 3.16. a) Binding free energies of ligand-dimer complexes estimated using the MMGBSA method on snapshots sampled from the MD trajectories in the 50 ns classical MD equilibration protocol. Error bars represent standard deviation, **b)** Effects of small molecule inhibitors on cisplatin induced IL-6 secretion in HEI-OC1 cells. Cells were seeded in 24 well plates (2.5 x 10^5 cells/well) and incubated at 33°C, 10% CO_2. Compounds were dissolved in vehicle (DMF) and stored at -20°C prior to use. Cells were left untreated (-), pretreated with DMF or 4μM of inhibitors for 1 hours and then stimulated with 20μM cisplatin 24 hours after seeding in fresh media. Supernatants were collected to measure IL-6 secretion 48 hours post-treatment using ELISA kit.

3.3.3.5. Clustering Analysis of the Complexes

Figure 3.17 and **Figure 3.18** show the clustering metrics observed for different cluster counts and the clusters' sizes, respectively, at the predicted optimal number of clusters using DBI and SSR/SST statistics for the dimer complexes after MD equilibration. **TAK-A4** (**Figure 3.17e** and **Figure 3.18e**) has shown a local minimum in the DBI parameter with cluster count of 10, with more than 95% of the MD trajectory included in its largest cluster. Next higher cluster counts were observed for **TAK-242**, **TAK-A1**, **TAK-A2** and **TAK-A3** (**Figure 3.17a-d** and **Figure 3.18a-d**) with a single confirmation for each compound representing ~80% of the whole trajectory, with cluster counts of 8, 12, 6, and 16, respectively. **TAK-A5, TAK-A6** and **TAK-S** (**Figure 3.17f-h** and **Figure 3.18f-h**) have shown ~55% of trajectory in its dominant clusters with cluster counts of 14, 14 and 12, respectively. The extracted dominant modes (largest cluster centroids) were used for further hydrogen bond analysis.

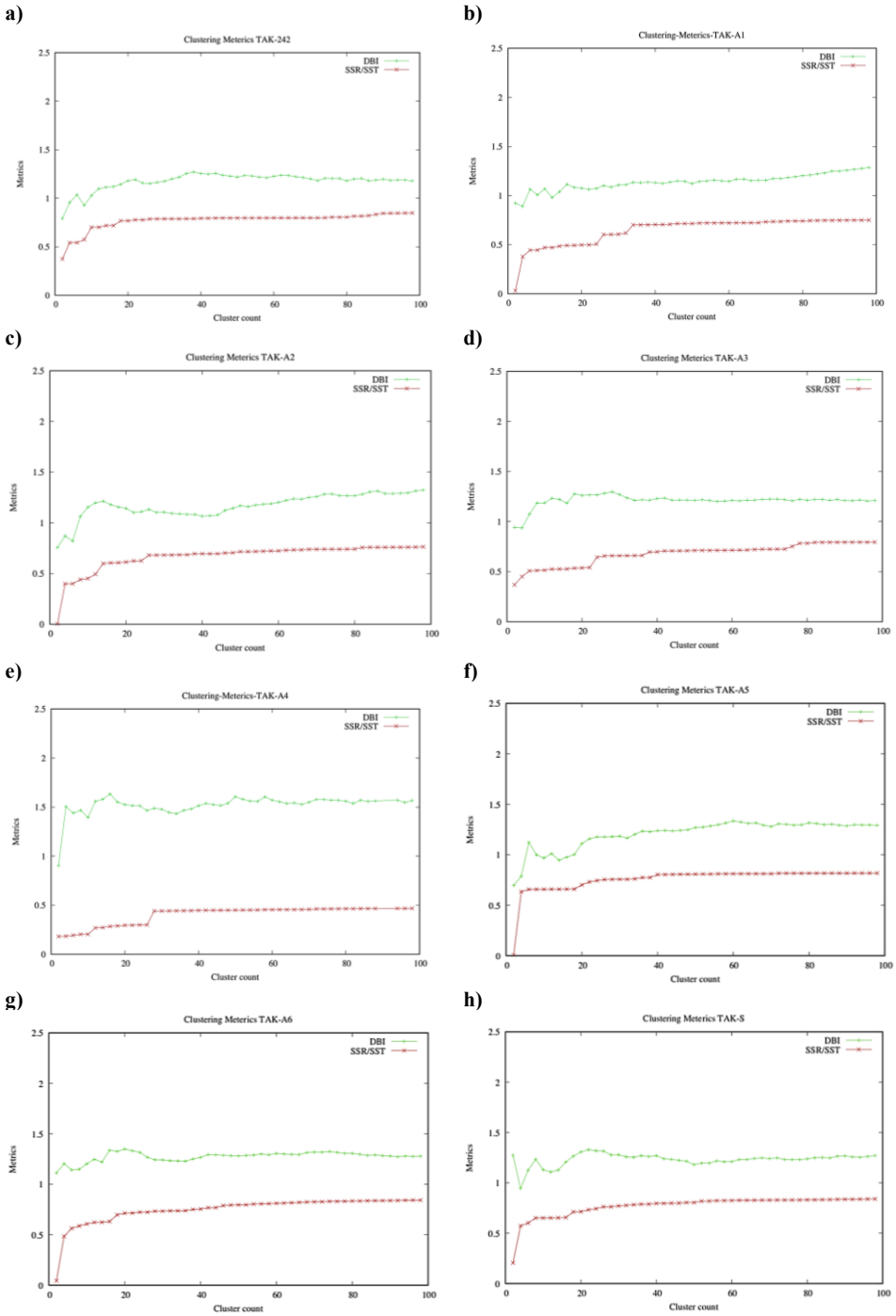

Figure 3.17. Clustering analysis MD trajectories for TLR4-TIR dimeric receptor-bound compounds after 50 ns MD simulations.

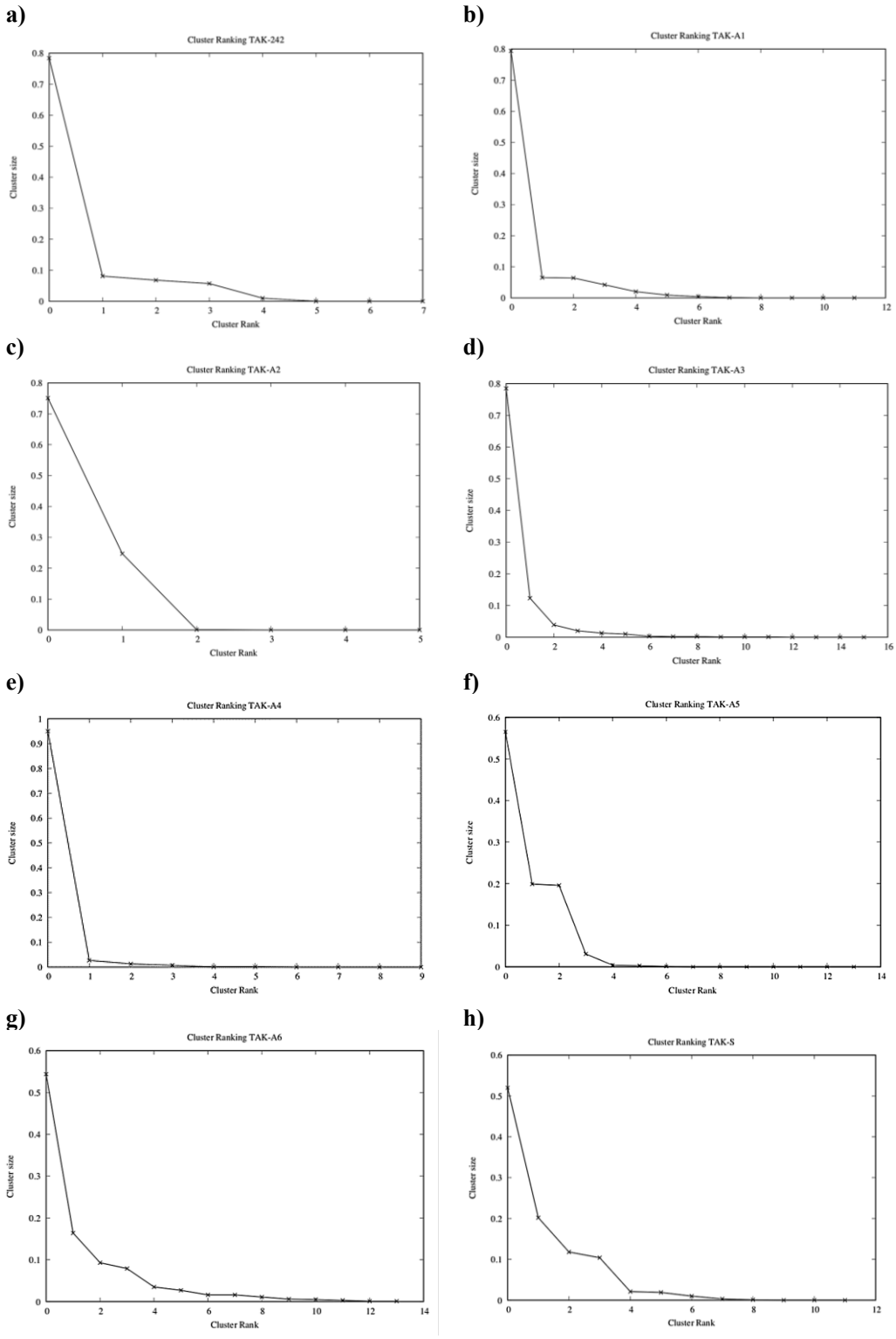

Figure 3.18. Cluster ranking for ligand-bound TLR4-TIR dimeric receptor complexes after clustering.

3.3.3.6. Binding Mode Analysis

To understand the molecular interactions of the ligand-receptor complex, we performed energetic evaluation as well as structural analysis. Energetic evaluation was done by calculating the decomposition of the MM/GBSA energies among the residues constituting the binding site of the receptor, in order to quantitatively assess the pattern of intermolecular interactions established between compounds and the receptor. Calculation of the per-residue binding energy allowed us to understand the contributing energies, e.g., vdW, electrostatic interactions, etc. **Figure 3.19** shows decompositions of the total binding energies of the complexes after 50 ns MD simulations. From the figure we see that, **Arg780*** is the largest electrostatic contributor (>6 kcal/mole) for **TAK-242**, **TAK-A1** and **TAK-A2**, as expected by the similarities in their chemical structures. Regarding **TAK-A4**, the energetic contribution from **Arg780*** is negligible. Leu779* show significant vdW interactions with the top two strongest inhibitors **TAK-242** and **TAK-A1**. **Gln743*** have significant interactions with all the compounds regardless the structural differences.

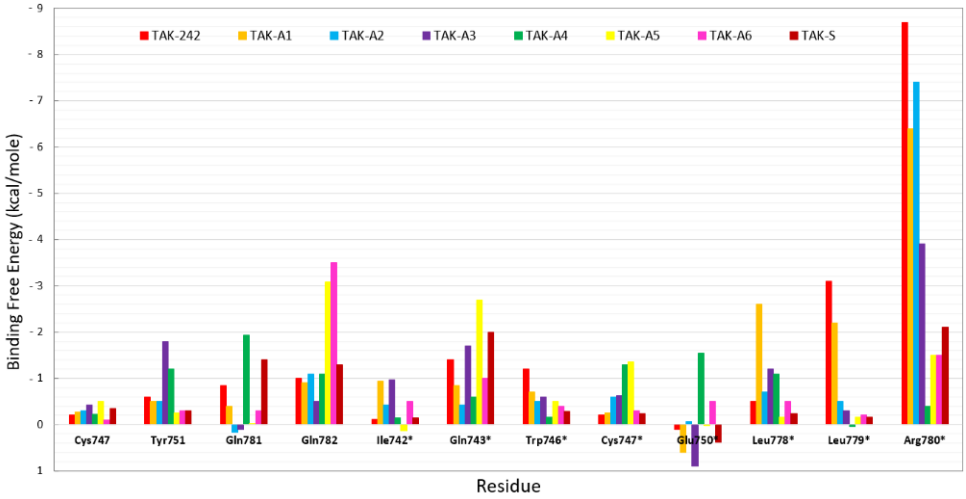

Figure 3.19. Decomposition of total energies between the residues of the TLR4 binding pocket and the eight compounds. *Residue suffix refers to the relative TLR4 monomer.

Residues from the other chain also played an important role in receptor-ligand interactions, especially **Cys747**, **Tyr751** and **Gln782** were able to establish van der Waals (vdW) interactions with all the ligands. However, the energetic contribution of **Cys747*** is more prominent than **Cys747**. It is worth mentioning that all residues in the

binding site are more or less interacting with all the compounds which indicates that all the ligands bind in the same site of the TLR4 receptor to different extents.

On the other hand, structural analysis provided insights into the specific binding between ligand-receptor interfaces. **Figure 3.20** and **Figure 3.21** show the predicted binding modes and the hydrogen bonds' analysis graph for each complex using the representative conformation extracted from the clustering analysis. The H-bond occupancies were measured with a distance cut-off of 3.5 Å and a cut-off angle of 60° for last 5 ns of the MD trajectory for each complex. As shown in **Figure 3.20** and **Figure 3.21**, all compounds except **TAK-A4** form hydrogen bonds with the same residue **Arg780*** and **TAK-242** is the strongest hydrogen bond mediator. These hydrogen bonds were formed between the oxygens of the sulfonamide group and/or carboxylate group of the compounds and the nitrogen of the **Arg780*** residue where this residue acted as an H-bond donor. Hydrophobic interactions of the compounds with **Tyr751, Ile742***, **Trp746*, Leu778*** and **Leu779* (Figure 3.19- 3.21)** help in maintaining the hydrogen bonds by properly carrying the compounds to the right position. Even though **Trp746*** made hydrophobic interactions with all the compounds, it formed very weak trackable hydrogen bonds with **TAK-242** and **TAK-A2 (Figure 3.19a, c)**.

TAK-A3 is the most flexible among all the compounds because of having the cyclohexane moiety unlike the rest of the compounds, which allowed the compound to get its way into the deep binding pocket where it made the strongest hydrophobic interaction with **Tyr751**. **TAK-A3** mediates hydrogen bonds with **Arg780*** and **Leu778*** similar to **TAK-A1 (Figure 3.19b, d)**. Although our energy decomposition analysis suggests the presence of weak electrostatic interactions between **TAK-A4** and **Arg780***, the final mode of binding didn't show any interaction between these entities (**Figure 3.21a**). However, **TAK-A4** having the dimethyl aromatic moiety, showed the strongest van der Waals (vdW) interactions with side chains of **Gln781** and **Gln750*** (**Figure 3.19**) which seem to be dominating its binding to the receptor.

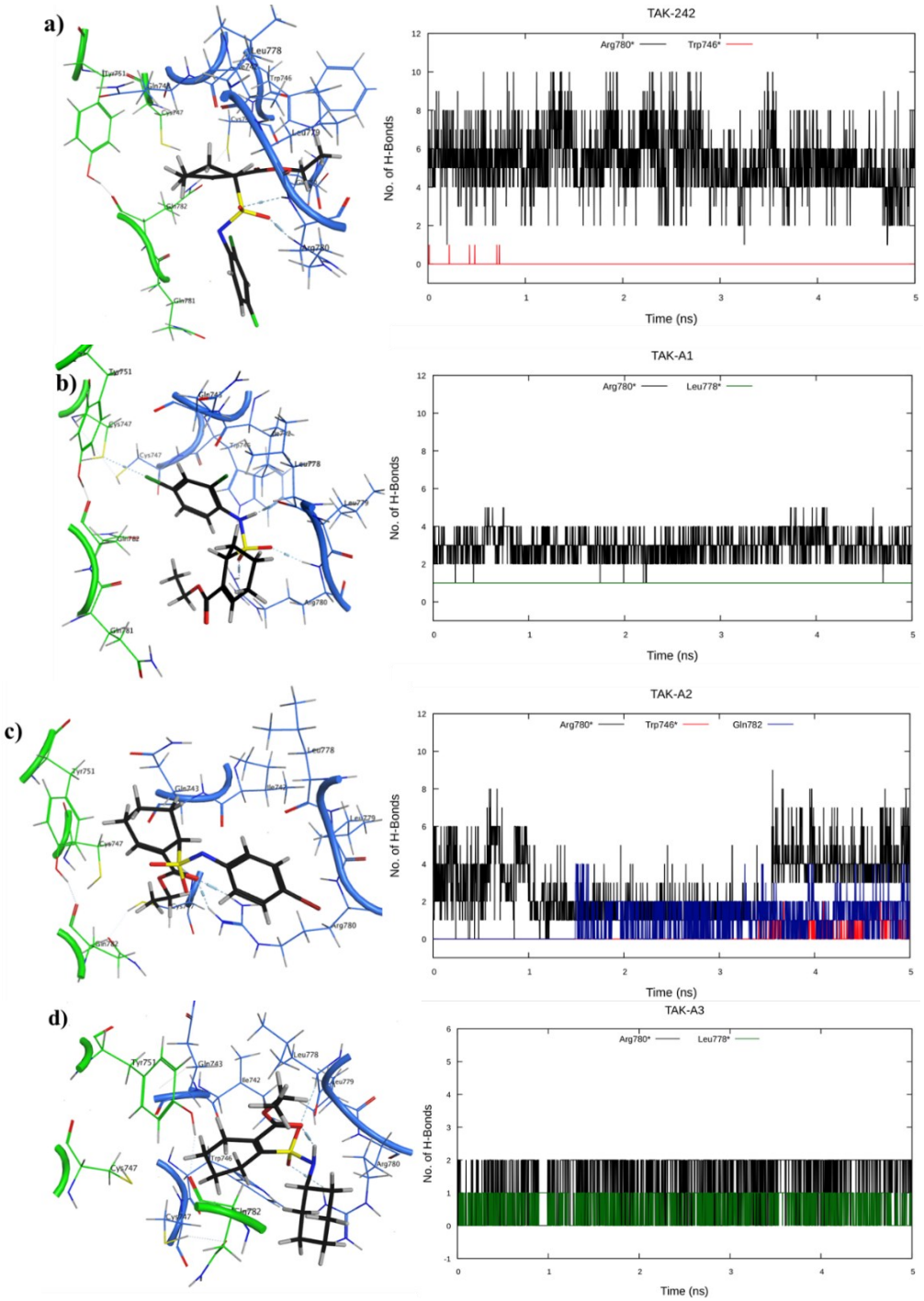

Figure 3.20. Predicted binding modes of the complexes with **a) TAK-242, b) TAK-A1, c) TAK-A2, d) TAK-A3** obtained from clustering analysis (left) and H-bond analysis and their distance over the last 5 ns simulation time (right) between residues and ligand in each complex. Nitrogens are depicted in blue. Hydrogens are depicted in white. Oxygens are depicted in red. Sulfurs are depicted in yellow.

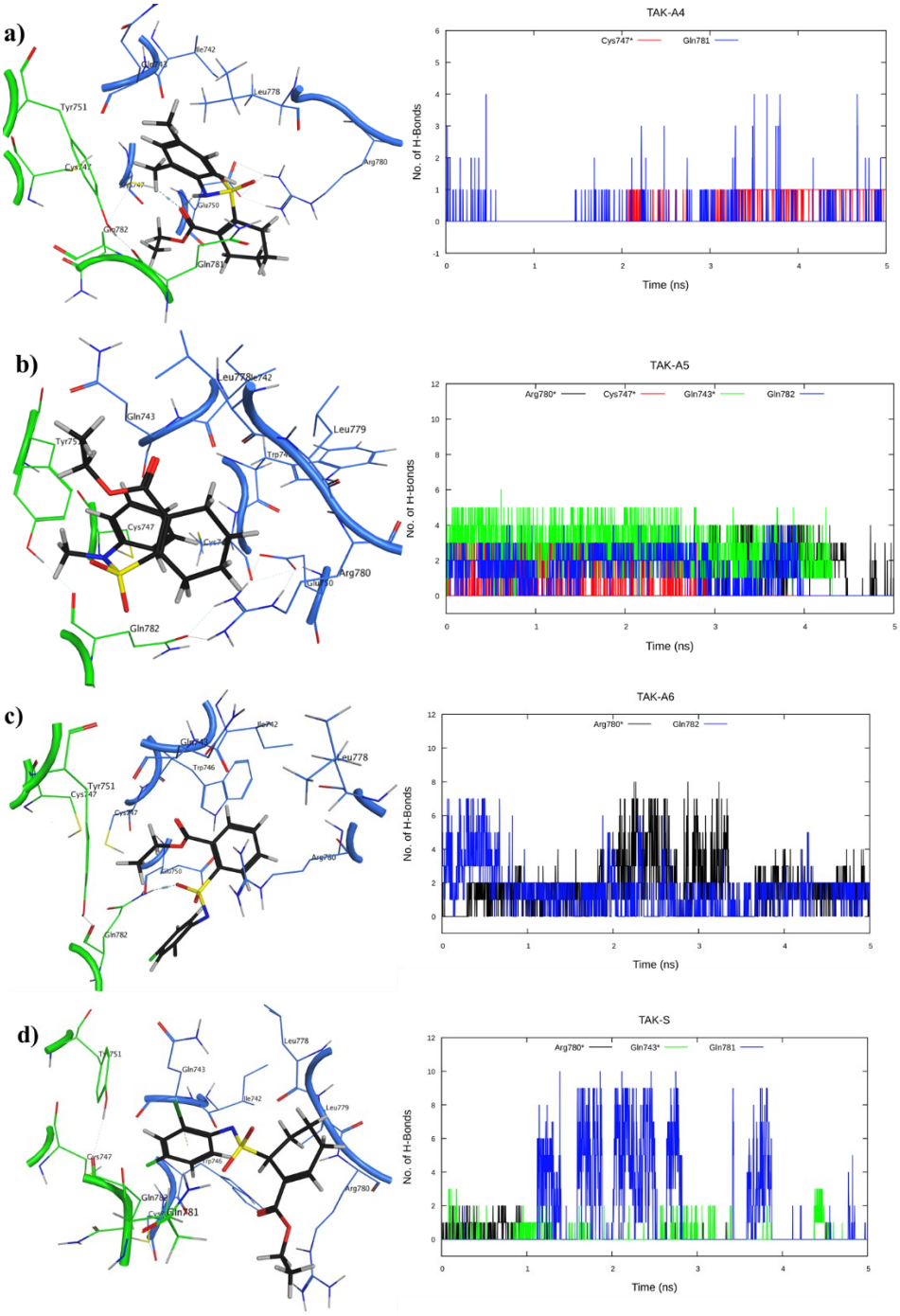

Figure 3.21. Predicted binding modes of the complexes with **a) TAK-A4, b) TAK-A5, c) TAK-A6, d) TAK-S** obtained from clustering analysis (left) and H-bond analysis and their distance over the last 5 ns simulation time (right) between residues and ligand in each complex. Nitrogens are depicted in blue. Hydrogens are depicted in white. Oxygens are depicted in red. Sulfurs are depicted in yellow.

From **Figure 3.20** and **Figure 3.21** we see that both **Cys747** and **Cys747*** are within 5 Å of the binding site for all compounds. Of all compounds, **TAK-A4** and **TAK-A5** are the main two compounds that formed hydrogen bonds with **Cys747*** within 3.5 Å distance; however, they were not persistent throughout the simulation.

Although **TAK-A5** possesses middle range MM-GBSA score (~25 Kcal/mole from **Figure 3.16a**), unlike other active compounds, its activity doesn't mainly come from the electrostatic interaction with **Arg780***. Moreover, it is the only compound which forms hydrogen bonds with maximum number of residues namely **Arg780***, **Cys474***, **Gln743*** and **Gln782***. Interestingly it is the compound which has the lowest vdW interactions with its surrounding residues.

TAK-A6 and **TAK-S** form strong hydrogen bonds with **Gln782** and **Gln781** respectively; however, they are deficient from any stable hydrogen bonds with **Arg780*** throughout the simulation time (**Figure 3.21c,d**) which seems to be the reason for their weak binding affinity towards the binding site. **TAK-A2, TAK-A5** and **TAK-A6** exhibit strong hydrogen bond interactions with **Gln782** where the MM-GBSA scores of **TAK-A5** and **TAK-A6** are quite low compared to **TAK-A2** (**Figure 3.16a**) which indicates **Gln782** is not selective for the strong antagonists.

The data obtained from the energy decomposition analysis together with the structural analysis indicates **TAK-A1** has the strongest interactions with the binding site. These interactions are mediated by hydrogen bonds and vdW interactions.

3.4. Conclusion

The work presented in this paper is a computational study focused on investigating the molecular interactions between TLR4 dimer and several small molecule antagonists. The inhibition TLR4-mediated cell signalling pathways has been previously investigated but no details of molecular action on the target have been given before. This is not intended to be a virtual screening effort since we knew which compounds already showed the desired activity. Our work elucidated the detailed mode of action of some synthetic antagonists at an atomistic level. The lack of an experimental three-dimensional structure constituted an obstacle for using computational tools in order to accurately investigate the behavior of ligands within the protein. In this work, we used

a published model for the dimeric form of TLR4 and a series of known and novel ligands were docked in the putative binding pocket around residue Cys747.

In our study, we used the powerful molecular docking technique implemented in MOE in order to rapidly and efficiently place a ligand in the best possible conformation within the protein binding site; however, this technique suffers from several issues, mainly related with the rigidity of the receptor and the cheapness of the scoring function during the simulation, that in fact limits the power of the software in distinguishing between real and false positive results; our workflow permits us to overcome these limits by post-processing the binding poses using MD simulations and using more sophisticated scoring functions, respectively.

RMSD and atomic fluctuations data showed a clear difference between the bound and free states for the stability and dynamicity of the TLR4 receptor. Binding affinities calculated over the simulations allowed us to obtain a relative rank between compounds which was fairly consistent with the experimental data about the activities. The results from the MMGBSA calculations showed a notable difference in binding energies between antagonists and inactive compounds, as **TAK-A2**, **TAK-A3**, **TAK-A4**, and **TAK-A5** have relative unfavorable binding energies compared to **TAK-242** and **TAK-A1**; specifically, **TAK-A1** showed the best binding energy toward the set. Furthermore, considering the less favorable binding energies of the **TAK-A6** and **TAK-S** compounds observed in silico, we could hypothesize an extremely reduced affinity and incapability to bind with the target. These data highlighted a direct correlation between binding energy and antagonist activity. It is worth mentioning that the described binding energies, obtained with the MMGBSA method, do not include the entropic contribution, so they are relative binding energies; however, the discussed results are not affected because our objective was to verify if the presented TLR4 dimeric model was able to distinguish between antagonists and inactive molecules. Besides that, the importance of the residues in the binding pocket in terms of ligand binding contribution was assessed by a quantitative measure of the decomposition of free energies. Particularly, Arg780*, Leu778*, Leu779*, Gln743*, Gln782, and Tyr751 were found to be the strongest contributors in antagonist recognition. Cys747 and Cys747* from both monomers were in the close proximity (within 5 Å) to the

compounds within the binding site. In conclusion, our work disclosed the dynamical and structural perspectives to explain the molecular interactions between TLR4 receptor and its small molecule inhibitors, leading to further optimization of new derivatives.

3.4. References

1. Mollen, K. P.; Anand, R. J.; Tsung, A.; Prince, J. M.; Levy, R. M.; Billiar, T. R. Emerging Paradigm: Toll-like Receptor 4-Sentinel for the Detection of Tissue Damage. *Shock*. **2006**, *26*, 430–437.
2. Yu, M.; Wang, H.; Ding, A.; Golenbock, D. T.; Latz, E.; Czura, C. J.; Fenton, M. J.; Tracey, K. J.; Yang, H. HMGB1 Signals through Toll-like Receptor (TLR) 4 and TLR2. *Shock*. **2006**, *26*, 174–179.
3. Raghavan, B.; Martin, S. F.; Esser, P. R.; Goebeler, M.; Schmidt, M. Metal allergens nickel and cobalt facilitate TLR4 homodimerization independently of MD2. *EMBO Rep*. **2012**, *13*, 1109–1115.
4. Kawasaki, T.; Kawai, T. Toll-like Receptor Signaling Pathways. *Front. Immunol*. **2012**, *5*, 461–469.
5. Singh, A.; Singh, V.; Tiwari, R. L.; Chandra, T.; Kumar, A.; Dikshit, M.; Barthwal, M. K. The IRAK-ERK-p67phox-Nox-2 Axis Mediates TLR4, 2-induced ROS Production for IL-1β Transcription and Processing in Monocytes. *Cell. Mol. Immunol*. **2016**, *13*, 745–763.
6. West, A. P.; Brodsky, I. E.; Rahner, C.; Woo, D. K.; Erdjument-Bromage, H.; Tempst, P.; Walsh, M. C.; Choi, Y.; Shadel, G. S.; Ghosh, S. TLR Signalling Augments Macrophage Bactericidal Activity through Mitochondrial ROS. *Nature*. **2011**, *472*, 476–480.
7. Haase, R.; Kirschning, C. J.; Sing, A.; Schröttner, P.; Fukase, K.; Kusumoto, S.; Wagner, H.; Heesemann, J.; Ruckdeschel, K. A Dominant Role of Toll-like Receptor 4 in the Signaling of Apoptosis in Bacteria-faced Macrophages. *J. Immunol. Res*. **2003**, *171*, 4294–4303.
8. Matsunaga, N.; Tsuchimori, N.; Matsumoto, T.; Ii, M. TAK-242 (Resatorvid), a Small-molecule Inhibitor of Toll-like Receptor (TLR) 4 Signaling, Binds Selectively to TLR4 and Interferes with Interactions Between TLR4 and its Adaptor Molecules. *Mol. Pharmacol.* **2011**, 79, 34–41.
9. Lou, Y.; Yu, Q.; Xu, K.; Tu, Y.; Balelang, M. F.; Lu, G.; Zhu, C.; Dai, Q.; Geng, W.; Mo, Y.; Wang, J. Electroacupuncture Pre-conditioning Protects from Lung Injury Induced by Limb Ischemia/reperfusion through TLR4 and NF-κB in Rats. *Mol. Med. Rep.* **2020**, *22*, 3225–3232.
10. Imanaka-Yoshida, K. Inflammation in Myocardial Disease: From Myocarditis to Dilated Cardiomyopathy. *Pathol. Int*. **2020**, *70*, 1–11.
11. Gao, W.; Xiong, Y.; Li, Q.; Yang, H. Inhibition of Toll-like Receptor Signaling as a Promising Therapy for Inflammatory Diseases: a Journey from Molecular to Nano Therapeutics. *Front. Physiol.* **2017**, *8*, 508–528.

12. Wu, M. Y.; Yiang, G. T.; Liao, W. T.; Tsai, A. P. Y.; Cheng, Y. L.; Cheng, P. W.; Li, C. Y.; Li, C. J. Current Mechanistic Concepts in Ischemia and Reperfusion Injury. *Cell. Physiol. Biochem.* **2018**, *46*, 1650–1667.

13. Leon, C. G.; Tory, R.; Jia, J.; Sivak, O.; Wasan, K. M. Discovery and Development of Toll-like Receptor 4 (TLR4) Antagonists: A New Paradigm for Treating Sepsis and other Diseases. *Pharm. Res.* **2008**, 25, 1751–1761.

14. Achek, A.; Yesudhas, D.; Choi, S. Toll-like Receptors: Promising Therapeutic Targets for Inflammatory Diseases. *Arch. Pharm. Res.* **2016**, *39*, 1032–1049.

15. Kawamoto, T.; Ii, M.; Kitazaki, T.; Iizawa, Y.; Kimura, H. TAK-242 Selectively Suppresses Toll-like Receptor 4-Signaling Mediated by the Intracellular Domain. *Eur. J. Pharmacol.* **2008***, 584*, 40–48.

16. Takashima, K.; Matsunaga, N.; Yoshimatsu, M.; Hazeki, K.; Kaisho, T.; Uekata, M.; Hazeki, O.; Akira, S.; Iizawa, Y.; Ii, M. Analysis of Binding Site for the Novel Small-Molecule TLR4 Signal Transduction Inhibitor TAK-242 and its Therapeutic Effect on Mouse Sepsis Model. *Br. J. Pharmacol.* **2009***, 157*, 1250–1262.

17. Hua, F.; Tang, H.; Wang, J.; Prunty, M. C.; Hua, X.; Sayeed, I.; Stein, D. G. TAK-242, an Antagonist for Toll-like Receptor 4, Protects Against Acute Cerebral Ischemia/reperfusion Injury in Mice. *J. Cereb. Blood Flow Metab.* **2015**, *35*, 536–542.

18. Mahita, J., Harini, K., Rao Pichika, M., Sowdhamini, R. An In Silico Approach towards the Identification of Novel Inhibitors of the TLR-4 Signaling Pathway. *J. Biomol. Struct*. **2016**, *34*, 1345–1362.

19. Bovijn, C.; Ulrichts, P.; De Smet; A. S.; Catteeuw, D.; Beyaert, R.; Tavernier, J.; Peelman, F. Identification of Interaction Sites for Dimerization and Adapter Recruitment in Toll/interleukin-1 receptor (TIR) Domain of Toll-like Receptor 4. *Int. J. Biol. Chem.* **2012**, *287*, 4088–4098.

20. Khan, J. A.; Brint, E. K.; O'Neill, L. A.; Tong, L. Crystal Structure of the Toll/interleukin-1 Receptor Domain of Human IL-1RAPL. *Int. J. Biol. Chem.* **2004**, *279*, 31664–31670.

21. Ii, M.; Matsunaga, N.; Hazeki, K.; Nakamura, K.; Takashima, K.; Seya, T.; Hazeki, O.; Kitazaki, T.; Iizawa, Y. A Novel Cyclohexene Derivative, Ethyl (6R)-6-[N-(2-Chloro-4-fluorophenyl) sulfamoyl] Cyclohex-1-ene-1-carboxylate (TAK-242), Selectively Inhibits Toll-like Receptor 4-mediated Cytokine Production through Suppression of Intracellular Signaling. *Mol. Pharmacol.* **2006**, *69*, 1288–1295.

22. Babolmorad, G.; Latif, A.; Domingo, I. K.; Pollock, N. M.; Delyea, C.; Rieger, A. M.; Allison, W. T.; Bhavsar, A. P.Toll-like Receptor 4 is Activated by Platinum and Contributes to Cisplatin-induced Ototoxicity. *EMBO Rep.* **2021**, *22*, 51280–51294.

23. Mineev, K. S.; Goncharuk, S. A.; Goncharuk, M. V.; Volynsky, P. E.; Novikova, E. V.; Aresinev, A. S. Spatial Structure of TLR4 Transmembrane Domain in Bicelles Provides the Insight into the Receptor Activation Mechanism. *Sci. Rep.* **2017***, 7*, 1–12.

24. Park, B. S.; Song, D. H.; Kim, H. M.; Choi, B. S.; Lee, H.; Lee, J. O. The Structural Basis of Lipopolysaccharide Recognition by the TLR4–MD-2 complex. *Nature*. **2009**, *458*, 1191–1195.

25. Patra, M. C.; Kwon, H. K.; Batool, M.; Choi, S. Computational Insight into the Structural Organization of Full-length Toll-like Receptor 4 Dimer in a Model Phospholipid Bilayer. *Front. Immunol.* **2018**, *9*, 489–504.

26. Magrane, M. UniProt Knowledgebase: A Hub of Integrated Protein Data. *Database*, **2011**, *2011*, 1–13.

27. Arnold, K.; Bordoli, L.; Kopp, J.; Schwede, T. The SWISS-MODEL Workspace: A Web-based Environment for Protein Structure Homology Modelling. *J. Bioinform.* **2006**, *22*, 195–201.

28. Colovos, C.; Yeates, T. Verification of Protein Structures: Patterns of Nonbonded Atomic Interactions. *Protein Sci.* **1993**, *2*, 1511–1519.

29. Laskowski, R. A.; MacArthur, M. W.; Moss, D. S.; Thornton, J. M. PROCHECK: A Program to Check the Stereochemical Quality of Protein Structures. *J. Appl. Crystallogr.* **1993**, *26*, 283–291.

30. Brown, T. ChemDraw. *Sci. Teach.* **2014**, *81*, 67.

31. Chemical Computing Group Inc. Molecular operating environment (MOE). **2016.**

32. Labute, P. Assignment of Protonation States and Geometries to Macromolecular Structures using Unary Quadratic Optimization. *Chem. Cent. J.* **2008**, *2*, 13.

33. Nussinov, R.; Wolfson, H. J. Efficient Detection of Three-dimensional Structural Motifs in Biological Macromolecules by Computer Vision Techniques. *Proc. Natl. Acad. Sci.* **1991**, *88*, 10495–10499.

34. Labute, P. The Generalized Born/Volume Integral Implicit Solvent Model: Estimation of the Free Energy of Hydration using London Dispersion Instead of Atomic Surface Area. *J. Comput. Chem.* **2008**, *29*, 1693–1698.

35. Kalé, L.; Skeel, R.; Bhandarkar, M.; Brunner, R.; Gursoy, A.; Krawetz, N.; Phillips, J.; Shinozaki, A.; Varadarajan, K.; Schulten, K. NAMD2: Greater Scalability for Parallel Molecular Dynamics. *J. Comput. Phys.* **1999**, *151*, 283–312.

36. Tian, C.; Kasavajhala, K.; Belfon, K. A.; Raguette, L.; Huang, H.; Migues, A. N.; Bickel, J.; Wang, Y.; Pincay, J.; Wu, Q.; Simmerling, C. ff19SB: Amino-acid-specific Protein Backbone Parameters Trained Against Quantum Mechanics Energy Surfaces in Solution. J. *Chem. Theory Comput.* **2016**, *16*, 528–552.

37. Mark, P.; Nilsson, L. Structure and Dynamics of the TIP3P, SPC, and SPC/E Water Models at 298 K. *J. Phys. Chem. A.* **2001**, *105*, 9954–9960.

38. Ryckaert, J. P.; Ciccotti, G.; Berendsen, H. J. Numerical Integration of the Cartesian Equations of Motion of a System with Constraints: Molecular Dynamics Of N-Alkanes. *J. Comput. Phys.* **1977**, *23*, 327–341.
39. Loncharich, R. J.; Brooks, B. R.; Pastor, R.W. Langevin Dynamics of Peptides: The Frictional Dependence of Isomerization Rates of N-acetylalanyl-N′-methylamide. *Biopolymers*. **1992**, 32, 523–535.
40. De Souza, O .N.; Ornstein, R. L. Effect of Periodic Box Size on Aqueous Molecular Dynamics Simulation of a DNA Dodecamer with Particle-mesh Ewald Method. *Biophys. J.* **1997**, *72*, 2395–2397.
41. Wang, J.; Wolf, R. M.; Caldwell, J. W.; Kollman, P. A.; Case, D. A. Development and Testing of a General Amber Force Field. *J. Comput. Chem.* **2004**, *25*, 1157–1174.
42. Wang, J.; Wang, W.; Kollman, P. A.; Case, D. A. Antechamber: An Accessory Software Package for Molecular Mechanical Calculations. *J. Am. Chem. Soc.* **2001**, *222*, 403–444.
43. Roe, D. R.; Cheatham III, T. E. PTRAJ and CPPTRAJ: Software for Processing and Analysis of Molecular Dynamics Trajectory Data. *J. Chem. Theory Comput.* **2013**, *9*, 3084–3095.
44. Williams, T.; Kelley, C. Gnuplot 4.4: An Interactive Plotting Program. **2010**.
45. Humphrey, W.; Dalke, A.; Schulten, K. VMD: Visual Molecular Dynamics. *J. Mol. Graph.* **1996**, *14*, 33–38.
46. Onufriev, A.; Bashford, D.; Case, D. A. Exploring Protein Native States and Large-scale Conformational Changes with a Modified Generalized Born Model. *Proteins*. **2004**, *55*, 383–394.
47. Miller III, B. R.; McGee Jr, T. D.; Swails, J. M.; Homeyer, N.; Gohlke, H.; Roitberg, A. E. MMPBSA. py: An Efficient Program for End-state Free Energy Calculations. *J. Chem. Theory Comput.* **2012**, *8*, 3314–3321.
48. Kollman, P. A.; Massova, I.; Reyes, C.; Kuhn, B.; Huo, S.; Chong, L.; Lee, M..; Lee, T.; Duan, Y.; Wang, W.; Donini, O. Calculating Structures and Free Energies of Complex Molecules: Combining Molecular Mechanics and Continuum Models. *Acc. Chem. Res.* **2000**, *33*, 889–897.
49. Shao, J.; Tanner, S. W.; Thompson, N.; Cheatham, T. E. Clustering Molecular Dynamics Trajectories: Characterizing the Performance of Different Clustering Algorithms. *J. Chem. Theory Comput.* **2007**, *3*, 2312–2334.
50. Davies, D. L.; Bouldin, D. W. A Cluster Separation Measure. *IEEE Trans. Pattern Anal. Mach. Intell.* **1979**, *2*, 224–227.
51. Lushpa, V. A.; Goncharuk, M. V.; Lin, C.; Zalevsky, A. O.; Talyzina, I. A.; Luginina, A. P.; Vakhrameev, D. D.; Shevtsov, M. B.; Goncharuk, S. A.; Arseniev, A. S.; Borshchevskiy, V. I. Modulation of Toll-Like Receptor 1 Intracellular Domain Structure and Activity by Zn^{2+} Ions. *Commun. Biol.* **2021**, *4*, 1–12.

52. Yamada, M.; Ichikawa, T.’ Ii, M.’ Sunamoto, M.’ Itoh, K.’ Tamura, N.; Kitazaki, T. Discovery of Novel and Potent Small-molecule Inhibitors of NO and Cytokine Production as Antisepsis Agents: Synthesis and Biological Activity of Alkyl 6-(N-Substituted sulfamoyl) Cyclohex-1-ene-1-carboxylate. *J. Med. Chem.* **2005**, *48*, 7457–7467.

Chapter 4

Inhibition of Triple Negative Breast Cancer Metastasis and Invasiveness by Novel Drugs that Target Epithelial to Mesenchymal Transition*

4.1 Introduction

Invasive breast cancer (BrCa) is a devastating disease that will affect 1 in 9 women in their lifetime;[1] 1 in 32 women will die from this disease.[1] In 2018, BrCa was estimated to account for 1 in 4 cancer cases diagnosed in women and accounted for the second largest amount of new cancer cases.[2] BrCa is the leading cause of mortality in women with cancer and the 17th leading cause of death overall in the world.[3,4] BrCa is the most common type of cancer in 15–49 years old women and the third most common type of cancer in women 50–59 years old. Invasive BrCas often display a basal-like phenotype, defined by the expression of human epidermal growth factor receptor 2 (EGFR2 or HER2) and vimentin, and/or the triple-negative (TN) phenotype, which is negative for progesterone receptor, estrogen receptor, and HER2. Basal-like/triple-negative breast cancers (TNBC) comprise the most aggressive forms of BrCa with higher mortality due to a disproportionate number of metastatic diseases cases.[5,6] About 10–20% of all invasive breast cancer cases are TNBC.[7] TNBC, when compared to other BrCa subtypes, is more resistant to conventional therapy, which currently involves a combination of surgery, radiation therapy, and neoadjuvant chemotherapy. Resistance may be related to reversion of germline BRCA1 mutations in TNBC, which leads to reduction in sensitivity to DNA damaging agents, worsening patient prognosis.[8] Targeted therapies, an excellent approach to inhibiting tumor growth,[9] such as PARP inhibitors (Olaparib, Talazoparib) to induce synthetic lethality, have been approved

*The contents of this chapter have been copied and/or adapted from the following publication: "Garcia, E.; Luna, I.; Persad, K. L.; Agopsowicz, K.; Jay, D. A.; West, F. G.; Hitt, M. M.; Persad, S. Inhibition of Triple Negative Breast Cancer Metastasis and Invasiveness by Novel Drugs that Target Epithelial to Mesenchymal Transition. *Sci. Rep.* **2021**, *11*, 1–15."

recently by the US FDA for use in patients with deleterious (or suspect deleterious) germline BRCA mutation.[10,11] As an alternate approach, immunotherapy (Atezolizumab) in combination with chemotherapy (Paclitaxel) for unresectable locally advanced/metastatic PD-L1-positive TNBC is currently under investigation in several trials. However, the pathogenesis of TNBC is still understood poorly, and the mechanism(s) that drives these tumor cells to proliferate and metastasize remains unclear.[6] As a result, there is no standard targeted therapeutic regimen for the treatment of these types of cancer, which ultimately may contribute to the overall poor prognosis.[6] This paucity of options for TNBC treatment highlights the need for additional innovative treatment approaches.

Nitrofen (Figure 4.1) is an herbicide that interferes with both oxidative and photosynthetic phosphorylation in the mitochondria and chloroplasts of plants.[12] Nitrofen was shown to have no adverse effects in adult rats upon exposure but induced multiple organ defects in embryos exposed at mid-gestation,[12–16] including congenital diaphragmatic herniation (CDH). The developmental toxicity displayed by nitrofen has been attributed to its effect in altering the thyroid hormone status by binding receptors for T3.[12–17] Incidentally, many current chemo-therapeutics (alkylating agents, topoisomerase inhibitors, histone deacetylase inhibitors) are also teratogens.[18] In adult animals, nitrofen has been shown to be slightly toxic by oral, dermal, and inhalation routes with an oral LD_{50} of 2.4–3.6 g/kg in rodents.[12,16] The non-observable adverse effect level (NOAEL) of nitrofen for liver toxicity is 200 mg/kg/day.[16] Interestingly, nitrofen's toxicity is much lower than that of many agents currently used for the treatment of BrCa that are associated with serious adverse health effects at therapeutic doses.[19–21] This project has grown out of an earlier study that examined the mechanism by which nitrofen induces developmental anomalies in rodent embryos. We proposed that nitrofen's effects in developmental abnormalities may be mediated by perturbations in epithelial-mesenchymal transition (EMT), a key development component underlying organogenesis. By extrapolation, we hypothesized that if nitrofen reduces EMT, a process that has been implied to confer metastatic properties upon cancer cells by enhancing mobility, invasion, and resistance to apoptotic stimuli,

then it might also have an impact on cancer metastasis. In this study, we tested this hypothesis using a highly invasive/metastatic model of TNBC.

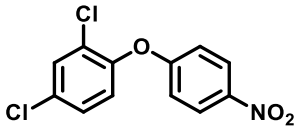

Figure 4.1. The structure of the reference hit, nitrofen.

Using an in vitro Matrigel invasion assay as readout, we observed that TNBC cell lines (MDA-MB-468, MDA- MB-436, MDA-MB-231, MDA-MB-231-Luc, SUM 149) showed a higher invasive potential than non-TNBC cell lines (MCF7, T47D, SKbr3) and that nitrofen treatment (1 & 10 μM) reduced the invasive potential of TNBC lines to a greater extent than non-TNBC lines. Further, we present compelling in vivo data which show that nitrofen efficiently blocks TNBC tumor metastasis, especially to the liver, following establishment of orthotopic xenografts of a luciferase-expressing derivative of the prototypical human TNBC cell line, MDA-MB-231 (MDA-MB-231-Luc) in nude mice. In vitro data suggest that this is not due to cytotoxicity but rather is due to impairment of the invasive capacity of the cells. Further, using an in vitro model of EMT, we show that nitrofen indeed interferes with the process of EMT and promotes mesenchymal to epithelial transformation. This may be a potential mechanism by which nitrofen affects the invasive potential TNBC cells.

However, several structural properties/components of nitrofen raise concerns regarding its putative efficacy as a therapeutic, including its high lipophilicity (cLogP of nearly 5)[22] and a potential toxophore in the form of a nitroarene group. Therefore, we developed analogues of nitrofen that lack the nitro group and/or have replaced the diaryl ether linker with a diarylamine that could allow modulation of polarity. We show that three of the nitrofen analogues significantly reduced the invasive potential of TNBC, with two of them reducing the invasive potential more efficiently compared to the parent compound, nitrofen. This inhibition of invasive potential may, at least partially, be attributed to the analogues' ability to promote mesenchymal to epithelial-like transformation of TNBC cells.

4.2 Materials and Methods

4.2.1 Cell Lines and Culture Conditions

Cell lines used were: MCF7, T47D, SKBr3, MDA-MB-468, MDA- MB-436, SUM 149 and DU145 MDA-MB-231 (ATCC); MDA-MB-231-luc-D3H2LN (Caliper Life Sciences). The MDA-MB-231-luc-D3H2LN cell line was derived from a tumor isolated from the lymph node of a mouse after a mammary fat pad injection with a luciferase-expressing MDA-MB-231 human breast cancer cell line.[23] STR profiling done on the MDA-MB-231-luc D3H2LN cell line matched MDA-MB-231 in the ATCC STR database. All cell lines were cultured in Dulbecco's modified Eagle's (DMEM) (Gibco), supplemented with 10% fetal bovine serum (FBS) (Gibco), 100 U/ml penicillin, 100 U/ml streptomycin (Gibco), and 2 mM L-glutamine, incubated at 37 °C, and 95% O_2 / 5% CO_2. Insulin 0.01 mg/ml (SIGMA) was added to the medium for MCF7. Nitrofen treatment in vitro was carried out at 1 μM and 10 μM concentrations for 24 h in a culture medium containing 1% FBS. This was the effective dose of nitrofen reported in two previous studies using cell culture assays without causing cell death.[24,25]

4.2.2 Primary Brain Cortical Cell Culture

Rat cortical tissue was prepared from postnatal day 2 Long–Evan rats of either sex. Brains were dissected and cortices were removed from meninges, isolated, and transferred to a Petri dish containing calcium- and magnesium-free (CMF) Hank's Balanced Salt Solution (HBSS) (Gibco). Cortical tissues were digested enzymatically by 1 mg/mL papain (Thermo Scientific) for 10 min at 37 °C. DNase I (Millipore Sigma) was added to the digestion mix in the last 5 min of incubation. Fetal bovine serum (FBS) Gibco) was added to stop the action of papain. Samples were centrifuged at 200 g for 1 min, and the supernatant was aspirated. Cortices were triturated by pipetting 10 times with a glass Pasteur pipette. The cell suspension was filtered through a 70 μm Nylon mesh cell strainer with a cell culture medium containing Neurobasal-A medium, supplemented with 2X B27, 4X glutaMAX I, and 2X Antibiotic–Antimycotic (Thermo Fisher Scientific Inc.). The cells were plated on poly-D-lysine coated wells at a density

of 3×10^4 cells/well in 24-well plates. The medium was changed 24 h after plating and every 3 days thereafter. Treatment with nitrofen or analogues was started on day 7 in culture.

4.2.3 TGF-β Treatment EMT Model

MCF7 BrCa cells were serum starved overnight and then treated with 2 ng/ml TGF-β in 0.2% BSA. The effect of TGF-β treatment was confirmed by monitoring of the constitutive phosphorylation of Smad 2/3 transcription factor.

4.2.4 Animals and Drug Delivery

All the studies reported in this manuscript were conducted with the approval of the University of Alberta Health Sciences Animal Care and Use Committee, in accordance with guidelines from the Canadian Council for Animal Care. We followed ARRIVE guidelines (as they apply to small animal study). We used a stratified randomization approach, and personnel who carried out bioluminescence imaging and monitored metastases were blinded to the treatment groups.

4.2.4.1 Tumor Establishment

To establish single or bilateral orthotopic tumors, 2×10^6 human MDA-MB-231-luc-D3H2LN cells (Caliper Life Science, Hopkinton, MA) were mixed 1:1 in Matrigel (Corning, Bedford, MA) to a total volume of 50 μL, which then was injected into the right (or both right and left) abdominal mammary fat pads of 6–8 weeks old female NIH-III mice (Charles River Laboratories). The MDA-MB-231-luc-D3H2LN cells line was validated by STR profiling. Tumor sizes were measured twice weekly with calipers, and volumes calculated as described previously.[26] Mice with tumor volumes exceeding 1500 mm^3 were euthanized.

4.2.4.2 Nitrofen Treatment

Nitrofen (Sigma Aldrich Canada) was dissolved in olive oil and administered to anesthetized tumor bearing mice by oral gavage on alternate days in doses of 1, 3, or 6 mg/kg body weight. Treatment was initiated when tumors became palpable (~2–3

weeks post-tumor cell injection). Control animals were administered with an olive oil vehicle by oral gavage.

4.2.4.3 In vivo Bioluminescence

Bioluminescence imaging was carried out weekly to monitor metastases. Briefly, anesthetized mice were injected subcutaneously with 150 mg/kg of D-luciferin (Caliper Biosciences). Then, the mice were imaged with a Xenogen IVIS Spectrum 200 imaging system (Perkin Elmer, Waltham, MA, USA). For ex vivo luciferase detection, mice were injected with luciferin as above, then euthanized. Primary tumors, lungs, and livers were excised and bathed in a solution of luciferin, then imaged.

4.2.5 General Experimental Procedures for NT Analogues Synthesis

Synthetic routes of nitrofen analogues A1–A8 are described in Figure 4.2. All starting materials and solvents were purchased from commercial suppliers and were used without further purification, unless otherwise noted. Reactions were carried out in flame-dried glassware under a nitrogen atmosphere using a standard Schlenk technique, unless otherwise stated. Transfer of anhydrous solvents and reagents was accomplished with oven-dried syringes. Thin layer chromatography was performed on glass plates precoated with 0.25 mm silica gel. Column chromatography was performed using 230−400 mesh silica gel. Samples were dissolved in $CDCl_3$ to obtain nuclear magnetic resonance (NMR) spectra. Proton nuclear magnetic resonance spectra (^{1}H NMR) were recorded at 500 MHz. Chemical shifts are given in ppm (parts per million) relative to residual $CHCl_3$ (7.26 ppm), and coupling constants (*J*) are reported in hertz (Hz). Standard notation was used to describe the multiplicity of signals observed in ^{1}H NMR spectra: broad (br), multiplet (m), singlet (s), doublet (d), triplet (t), etc. Carbon nuclear magnetic resonance spectra (^{13}C NMR) were recorded at 125 MHz and are reported (ppm) relative to the center line of the triplet from chloroform-d (77.0 ppm). Infrared (IR) spectra were measured with an FT-IR 3000 spectrophotometer. Mass spectra were determined on a high-resolution electrospray positive ion mode spectrometer.

4.2.5.1 Synthesis of Nitrofen Analogues A1–A8

A) Hydrogenation followed by amidation reaction

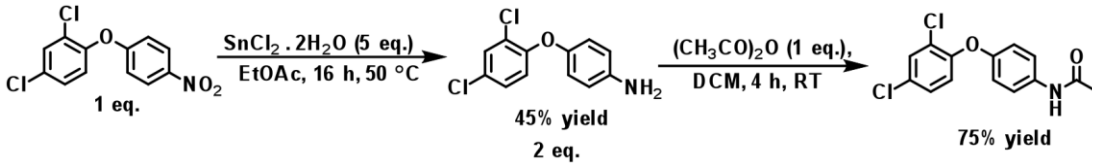

S_NAr reaction:

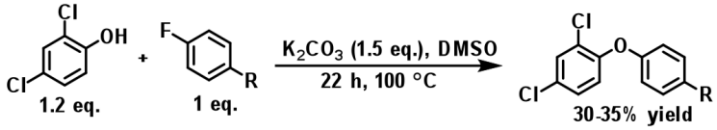

B) Buchwald–Hartwig coupling reaction:

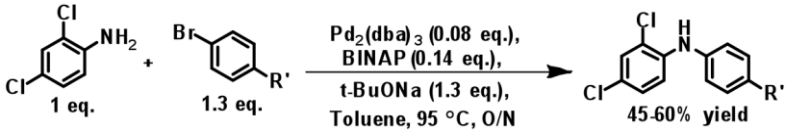

Scheme 4.1. Synthetic routes to analogues A1–A8: reduction/acylation of nitro group, formation of diaryl ether via nucleophilic aromatic substitution or palladium-catalyzed aromatic amination via Buchwald–Hartwig coupling reaction.

4.2.6 Synthesis and Characterization of Nitrofen Analogues (A1–A8)

4-(2,4-Dichlorophenoxy)aniline (A1)

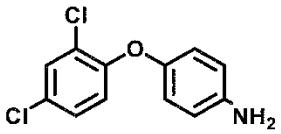

A1

Known compound **A1** was synthesized using the method available in the literature.[27] 2,4-Dichloro-1-(4-nitrophenoxy)benzene (1.0 mmol, 0.28 g, 1.0 equiv) was dissolved in 10 mL of EtOAc, and then $SnCl_2.2H_2O$ (5.0 mmol, 1.13 g, 5.0 equiv) was added into the solution. The reaction mixture was stirred at 50 °C for 16 h. Completion of the reaction was monitored by TLC with a 20% EtOAc/hexane eluent system. The reaction mixture was partitioned between EtOAc and sat. $NaHCO_3$. The organic layer was collected, and the aqueous layer was extracted with EtOAc (2 × 50 mL). The organic

layers were combined, washed with sat. $NaHCO_3$, brine, dried with Na_2SO_4, filtered, and concentrated. The crude material was purified by column chromatography (gradient elution with 5% to 10% EtOAc/hexanes) to obtain compound **A1** as a brown solid (1.3 g, 52% yield); IR (cast film) ν_{max} = 3444, 3377, 3213, 3091, 3043, 1623, 1582, 1573, 1507, 1472, 1389, 1321, 1255, 1244, 875, 824, 782 cm^{-1}; ^1H NMR (500 MHz, $CDCl_3$) δ 7.42 (d, *J* = 2.6 Hz, 1H), 7.10 (dd, *J* = 8.8, 2.5 Hz, 1H), 6.83 (app d, *J* = 8.8 Hz, 2H), 6.75 (d, *J* = 8.8 Hz, 1H), 6.67 (app d, *J* = 8.9 Hz, 2H), 3.61 (br s, 1H); ^{13}C NMR (125 MHz, $CDCl_3$) δ 153.2, 148.0, 143.2, 130.2, 127.7, 127.5, 124.9 (2C), 120.5, 118.8, 116.2 (2C); HRMS (ESI) *m/z* calcd for $C_{12}H_{10}Cl_2NO$ $[M + H]^+$ 254.0134; found 254.0139.

2,4-Dichloro-1-(4-acetamidophenoxy)benzene (A2)

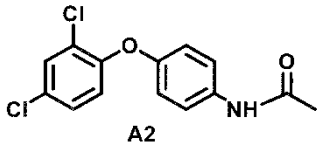

A2

Synthesis of compound **A2** was carried out through amidation reaction between analogue **A1** and acetic anhydride, according to the reported procedures.[28] 4-(2,4-Dichlorophenoxy)benzenamine (1.9 mmol, 0.48 g, 1.0 equiv) was dissolved in dry DCM (5 mL), acetic anhydride (2.3 mmol, 0.2 mL, 1.2 equiv) was added to the solution, and the reaction was stirred at room temperature for around 3 h and monitored by TLC. Upon completion, the reaction mixture was washed with a saturated solution of Na_2CO_3, the organic layers dried with Na_2SO_4, and the solvent removed under reduced pressure. The product was obtained (1.4 g, 75% yield) as a yellowish solid; IR (cast film) ν_{max} = 3258, 3199, 3136, 3061, 1664, 1618, 1560, 1538, 1505, 1471, 1277, 1254, 1196, 1098, 825, 699 cm^{-1}; ^1H NMR (500 MHz, $CDCl_3$) δ 7.48–7.54 (m, 3H), 7.17 (dd, *J* = 6.3, 2.4 Hz, 1H), 7.10 (br s, 1H), 6.9 (app d, *J* = 8.9 Hz, 2H), 6.87 (d, *J* = 8.7 Hz, 1H); ^{13}C NMR (125 MHz, $CDCl_3$) δ 168.1, 152.9, 151.7, 133.8, 130.5, 128.9, 127.9, 126.2, 121.7 (2C), 120.8, 118.8 (2C), 24.5; HRMS (ESI) *m/z* calcd for $C_{14}H_{12}C_{l2}NO_2$ $[M + H]^+$ 296.0240; found 296.0253.

4-(2,4-Dichlorophenoxy)benzaldehyde (A3)

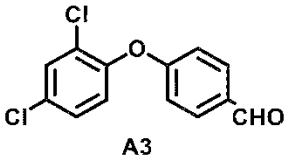

A3

Synthesis of compound **A3** was carried out by employing an S_NAr reaction, according to the reported procedure with minor modifications.[29] To a solution of 4-fluorobenzaldehyde (1.0 mmol, 0.1 mL, 1.0 equiv) and 2,4-dichlorophenol (1.2 mmol, 0.19 g, 1.2 equiv) in DMSO (1 mL), K_2CO_3 (0.15 mmol, 0.21 g) was added, and the mixture was heated to 100 °C for 2 h. TLC confirmed the completion of reaction. Then, the reaction mixture was poured into iced water (100 mL), which caused formation of precipitation, and the solid was collected by filtration. The filtered cake was washed with water and then dried over under reduced pressure. Further purification was not required. Compound **A3** was obtained as an off-white solid (0.8 g) with 30% yield; IR (cast film) ν_{max} = 3082, 2832, 2741, 1693, 1603, 1579, 1502, 1472, 1425, 1301, 1258, 1214, 1157, 1099, 1057, 853, 829, 787, 728 cm^{-1}; ^1H NMR (500 MHz, $CDCl_3$) δ 9.93 (s, 1H), 7.86 (app d, *J* = 8.8 Hz, 2H), 7.52 (d, *J* = 2.5 Hz, 1H), 7.30 (dd, *J* = 6.1, 2.6 Hz, 1H), 7.08 (d, *J* = 8.7 Hz, 1H), 7.00 (app d, *J* = 8.5 Hz, 2H); ^{13}C NMR (125 MHz, $CDCl_3$) δ 190.6, 162.1, 149.3, 132.0 (2C), 131.8, 131.2, 130.9, 128.5, 127.9, 123.5, 116.8 (2C); HRMS (EI) m/z calcd for $C_{13}H_8Cl_2O_2$ $[M]^+$ 265.9901; found 265.9903.

4-(2,4-Dichlorophenoxy)benzonitrile (A4)

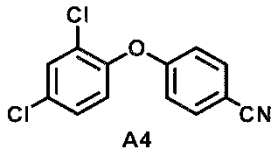

A4

The method used above for **A3** was employed to synthesize compound **A4** with the following stoichiometric amounts: 4-fluorobenzonitrile (1.0 mmol, 0.12 g, 1.0 equiv), 2,4-dichlorophenol (1.2 mmol, 0.19 g, 1.2 equiv), and K_2CO_3 (0.15 mmol, 0.21 g) to afford compound **A4** as a brownish solid in 35% yield; IR (cast film) ν_{max} = 3094, 3079,

2227, 1606, 1581, 1501, 1472, 1415, 1382, 1296, 1256, 1238, 1166, 1099, 1057, 1014, 833, 809, 753, 708, 677, 661 cm^{-1}; ^{1}H NMR (500 MHz, $CDCl_3$) δ 7.62 (app d, *J* = 8.8 Hz, 2H), 7.51 (d, *J* = 2.5 Hz, 1H), 7.30 (dd, *J* = 6.2, 2.5 Hz, 1H), 7.06 (d, *J* = 8.7 Hz, 1H), 6.94 (app d, *J* = 8.8 Hz, 2H); ^{13}C NMR (125 MHz, $CDCl_3$) δ 160.5, 148.9, 134.3 (2C), 131.5, 130.9, 128.6, 123.5, 118.5, 117.1 (2C), 106.6; HRMS (EI) *m/z* calcd for $C_{13}H_7Cl_2NO$ $[M]^+$ 262.9905; found 262.9907.

2,4-Dichloro-N-(4-nitrophenyl)-benzenamine (A5)

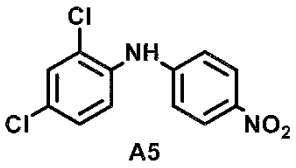

A5

Synthesis of compound **A5** was carried out by employing a Buchwald–Hartwig cross coupling reaction, according to the reported procedure with minor modifications.[30] 2,4-Dichlorobenzenamine (1.0 mmol, 0.16 g), 1-bromo-4-nitrobenzene (1.3 mmol, 0.26 g), $Pd_2(dba)_3$ [tris(dibenzylideneacetone)dipalladium(0)] (0.08 mmol, 0.07 g), BINAP (2,2′-bis(diphenylphosphino)-1,1′-binaphthyl) (0.14 mmol, 0.08 g), and sodium tert-butoxide (1.3 mmol, 0.12 g) were dissolved in 10 mL of toluene and stirred at 95 °C under overnight reflux. The course of the reaction was followed by TLC. On cooling to room temperature, the reaction mixture was partitioned between 1.0 M aqueous sodium bisulphate and diethylether. The diethylether phase was washed once with saturated sodium bicarbonate and brine, dried over $MgSO_4$, filtered, and concentrated. The crude product was purified by column chromatography (gradient elution with 5% to 10% EtOAc/hexanes) to obtain compound **A5** as a brown solid (0.15 g, 53% yield); IR (cast film) ν_{max} = 3355, 3086, 3064, 1604, 1583, 1535, 1484, 1471, 1424, 1380, 1340, 1326, 1114, 1101, 1052, 856, 840, 819, 796, 747, 703, 688, 675, 655 cm^{-1}; ^{1}H NMR (500 MHz, $CDCl_3$) δ 8.17 (app d, *J* = 9.2 Hz, 2H), 7.47 (d, *J* = 2.4 Hz, 1H), 7.38 (d, *J* = 8.7 Hz, 1H), 7.25 (dd, *J* = 5.6, 3.0 Hz, 2H), 7.02 (app d, *J* = 9.1 Hz, 2H); ^{13}C NMR (125 MHz, $CDCl_3$) δ 148.2, 141.2, 135.6, 130.1 (2C), 128.9, 127.9, 126.2, 126.1,

121.4, 115.4 (2C); HRMS (ESI) *m/z* calcd for $C_{12}H_7C_{l2}N_2O_2$ $[M - H]^-$ 280.9890; found 280.9889.

4-[(2,4-Dichlorophenyl)amino]-benzonitrile (A6)

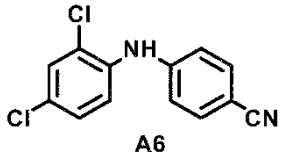

A6

The method used above for **A5** was employed to synthesize compound **A6** with the following stoichiometric amounts: 2,4-dichlorobenzenamine (1.0 mmol, 0.16 g), 1-bromo-4-benzonitrile (1.3 mmol, 0.28 g), $Pd_2(dba)_3$ [tris(dibenzylideneacetone)dipalladium(0)] (0.08 mmol, 0.07 g), BINAP (2,2′-bis(diphenylphosphino)-1,1′-binaphthyl) (0.14 mmol, 0.08 g), and sodium tert-butoxide (1.3 mmol, 0.12 g) to afford compound **A6** as a brownish solid (0.12 g) in 50% yield; IR (cast film) ν_{max} = 3330, 3070, 2220, 1609, 1589, 1516, 1466, 1417, 1327, 1226, 1176, 1101, 868, 825, 767, 746, 694, 665 cm^{-1}; ^1H NMR (500 MHz, $CDCl_3$) δ 7.55 (app d, *J* = 4.9 Hz, 2H), 7.45 (d, *J* = 2.4 Hz, 1H), 7.33 (d, *J* = 8.7 Hz, 1H), 7.22 (dd, *J* = 5.3, 2.4 Hz, 1H), 7.05 (app d, *J* = 8.8 Hz, 2H), 6.19 (br s, 1H); ^{13}C NMR (125 MHz, $CDCl_3$) δ 146.1, 136.1, 133.9 (2C), 129.9, 128.1, 127.8, 125.4, 120.1, 119.3, 116.7 (2C), 103.8; HRMS (ESI) *m/z* calcd for $C_{13}H_7Cl_2N_2$ $[M - H]^-$ 260.9992; found 260.9991.

(4-Chloro-phenyl)-(2,4-dichloro-phenyl)-amine (A7)

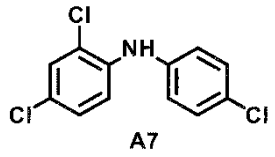

A7

The method used above for **A5** was employed to synthesize compound **A7** with the following stoichiometric amounts: 2,4-dichlorobenzenamine (1.0 mmol, 0.16 g), 1-bromo-4-chlorobenzene (1.3 mmol, 0.25 g), $Pd_2(dba)_3$ [tris(dibenzylideneacetone)dipalladium(0)] (0.08 mmol, 0.07 g), BINAP

(2,2′-bis(diphenylphosphino)-1,1′-binaphthyl) (0.14 mmol, 0.08 g), and sodium tert-butoxide (1.3 mmol, 0.12 g) to afford compound **A7** as a brownish solid (0.16 g) in 60% yield; IR (cast film) ν_{max} = 3406, 3062, 2924, 2850, 1590, 1505, 1459, 1408, 1383, 1316, 1264, 1220, 1176, 1093, 1048, 1011, 868, 813, 759, 710, 658 cm^{-1}; ^{1}H NMR (500 MHz, $CDCl_3$) δ 7.36 (app s, 1H), 7.28 (app d, *J* = 6.7 Hz, 2H), 7.10 (d, *J* = 1.9 Hz, 2H), 7.05 (app d, *J* = 6.7 Hz, 2H), 5.99 (br s, 1H); ^{13}C NMR (125 MHz, $CDCl_3$) δ 139.8, 138.8, 129.6, 129.4 (2C), 127.9, 127.6, 124.8, 122.1, 121.6 (2C), 116.3; HRMS (EI) *m/z* calcd for $C_{12}H_8Cl_3N$ $[M]^+$ 270.9722; found 270.9720.

2,4-Dichloro-N-phenylaniline (A8)

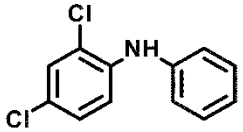

A8

The method used above for **A5** was employed to synthesize compound **A8** with the following stoichiometric amounts: 2,4-dichlorobenzenamine (1.0 mmol, 0.16 g), bromobenzene (1.3 mmol, 0.14 mL), $Pd_2(dba)_3$ [tris(dibenzylideneacetone)dipalladium(0)] (0.08 mmol, 0.07 g), BINAP (2,2′-bis(diphenylphosphino)-1,1′-binaphthyl) (0.14 mmol, 0.08 g), and sodium tert-butoxide (1.3 mmol, 0.12 g) to afford compound 9 as a brownish solid (0.9 g) in 40% yield; IR (cast film) ν_{max} = 3407, 3068, 3048, 3026, 2955, 2925, 2853, 1594, 1519, 1467, 1390, 1315, 1048, 830, 807, 739, 694 cm^{-1}; ^{1}H NMR (500 MHz, $CDCl_3$) δ 7.35 (d, *J* = 2.4 Hz, 1H), 7.33 (app t, *J* = 7.9 Hz, 2H), 7.17 (d, *J* = 8.8 Hz, 1H), 7.13 (app d, *J* = 1.0 Hz, 2H), 7.09–7.05 (m, 2H), 6.04 (br s, 1H); ^{13}C NMR (125 MHz, $CDCl_3$) δ 141.1, 139.3, 129.6 (2C), 129.3, 127.6, 124.2, 123.2 (2C), 121.8, 120.5 (2C), 116.5; HRMS (EI) *m/z* calcd for $C_{12}H_9Cl_2N$ $[M]^+$ 237.0112 ; found 237.0111.

4.2.7 Antibodies

Antibodies to E-cadherin (1:1000), N-cadherin (1:1000), phospho-Smad 2/3 (1:500), Smad (1:500), Phospho-Serine 473-AKT (1:1000), AKT (1:1000), and anti-vimentin

(1:500) were from Cell Signaling (Beverly, MA, USA). Antibodies to ZO-1 (1:500), Twist (1:500), Snail (1:250) were from Abcam (USA). Antibody to β-actin (Santa Cruz) (1:5000), Anti-mouse IgG (1:5000), Anti-rabbit IgG (1:2000) were from GE Healthcare UK Ltd.

4.2.8 Immunoblotting

Immunoblotting was done as described previously.[31] Cells were washed with PBS and lysed with 50 mM Tris buffer (pH 8.0) containing 150 mM NaCl, 1% NP-40, 0.5% sodium deoxycholate, 1 mM phenylmethylsulphonyl fluoride, 5 µg/ml leupeptin, and 25 µg/ml aprotinin. The protein concentration was quantified by bicinchoninic protein assay (Thermo Fisher Scientific Inc., Waltham, MA, U.S.A.). Proteins were separated by sodium dodecyl sulphate–polyacrylamide gel electrophoresis and transferred on to polyvinylidene difluoride (PVDF) membranes (Millipore, Billerica, MA, U.S.A.). PVDF membranes were blocked with 5% milk, probed with specific primary antibodies followed by peroxidase-conjugated secondary antibodies (GE Healthcare UK Ltd, Little Chalfont, U.K.), and visualized using Western Lightning® Plus-ECL (PerkinElmer, LAS Inc., Shelton, CT, U.S.A.) and X-ray developer (Fuji). In some instances, images were derived using Chemi DOC MP (Bio-Rad) and Image-Lab Touch Software (Bio-Rad). Densitometric analysis was performed by IMAGE J software (http://www.rsbweb.nih.gov/ij/). Histograms are representative of three or more independent experiments.

4.2.9 Transwell® Invasion Assay

The cell invasion assay was carried out using Transwell® unit (8 µM) coated with BD Matrigel Basement Matrix (Corning, Bedford, MA). Cells were added at 5×10^4 per invasion chamber and allowed to invade for 24 h at 37 °C and 95% O_2 / 5% CO_2 towards a lower compartment with media containing 10% FBS. On completion of the incubation period, invaded cells were fixed with ice-cold 100% methanol (−20 °C), stained with 0.5% crystal violet and a number of invaded cells analyzed using 10X High Content Microscope and MetaExpress software.

4.2.10 Alamar Blue Viability Assay

The relative cytotoxicity of the nitrofen analogues was established using a primary rat brain cell culture and an AlamarBlue assay. The AlamarBlue assay was carried out according to the manufacturer's instructions (ThermoFisher Scientific Inc.). Briefly, cells were incubated with 1 μM nitrofen or the analogues (A1, A5, A8) for 24 h in a culture medium containing 1% FBS. Untreated cells were used as controls. After 24 h incubation, an AlamarBlue solution (10% [v/v] solution of AlamarBlue dye) in a complete medium was added to each well. Wells containing only the AB solution/medium without cells were used as the blank. Following a 2 h incubation, AlamarBlue fluorescence was quantified at the excitation and emission wavelengths of 540 and 595 nm, respectively, using a LUMIstar Omega reader. The percent viability was normalized to untreated cells: (sample relative fluorescent unit (RFU − Blank) × 100/ (Untreated cells RFU – Blank).

4.2.11 High Content Microscopy

High content microscopy was done as described previously.[31] Images were taken at 10X (NA 0.3) magnification using an automated, high content screening system, ImageXpress Micro XLS, Molecular Devices (USA). Briefly, a defined (3X3) number of images was taken per well, and the resulted images were stored in a data storage server and analyzed using a predefined cell scoring algorithm in a MetaXpress software package that measures the blue staining in a bright field optical image on a per cell base, then averages the signal for the total population of cells.

4.2.12 Statistics

A One-Way ANOVA, Dunnett test, n =3 test (GraphPad PRISM Software; GraphPad Software, Inc., CA, USA) was used to compare differences between groups. Results are presented as Mean ± SE and values.

4.3 Results

4.3.1 Nitrofen Reduces In Vitro Invasive Activity of BrCa Cells

Using an in vitro Matrigel invasion assay, we observed that TNBC cell lines (MDA-MB-468, MDA-MB-436, MDA-MB-231, SUM 149) showed a higher invasive potential than non-TNBC cell lines (MCF7, T47D, SKbr3). Further, nitrofen treatment (1 & 10 μM) reduced the invasive potential of TNBC lines to a greater extent than non-TNBC lines (Figure 4.2).

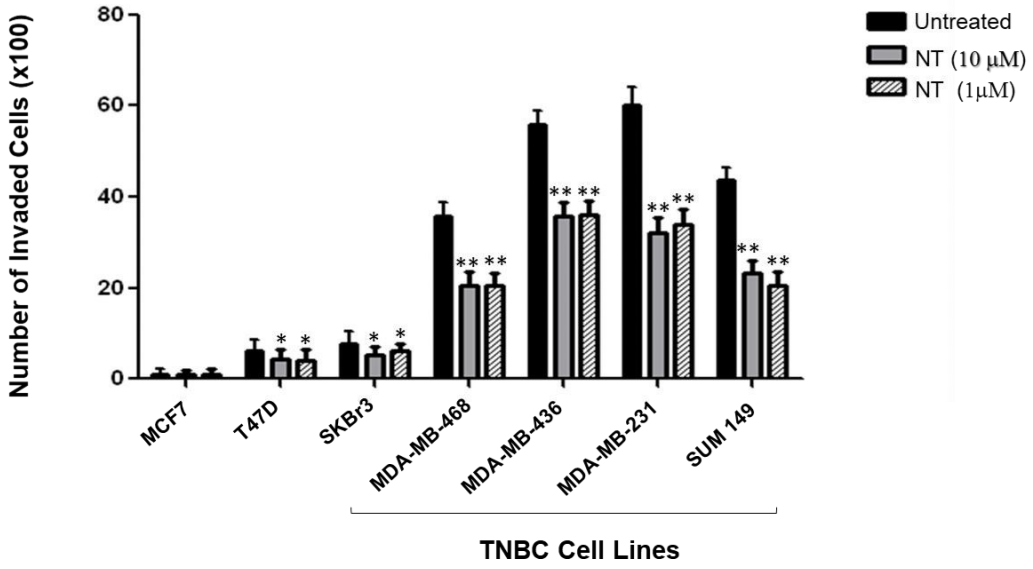

Figure 4.2. Matrigel invasion assay of breast cancer cell lines with and without nitrofen treatment (1 μM and 10 μM). TNBC cell lines (MDA-MB-468, MDA-MB-436, MDA-MB-231, MDA-MB-231-Luc, SUM 149) showed a higher invasive potential than non-TNBC cell lines (MCF7, T47D, SKbr3). Nitrofen treatment (1 & 10 μM) reduced the invasive potential of TNBC lines to a greater extent than non-TNBC lines. The data are representative of 4 separate experiments. * $p < 0.05$ vs. untreated; ** $p < 0.01$ vs. untreated. [NT= Nitrofen].

We further determined the effect of nitrofen on the invasive potential of the luciferase expressing MDA-MB-231 (MDA- MB-231-luc-D3H2LN) cell line (MDA-MD-231-Luc). Accordingly, we used MDA-MB-231-luc-D3H2LN (MDA-MB-231-Luc) cells to carry out in vitro cell invasion assays in the presence and absence of 1 and 10 μM nitrofen. We observed a significant reduction in invasive potential of MDA-MB-231-Luc cells in the presence of 1 and 10 μM nitrofen relative to the untreated control (Figure 4.3A). An AlamarBlue assay done under the same conditions shows that there is no change in relative viability of cells upon any treatments (Figure 4.3B).

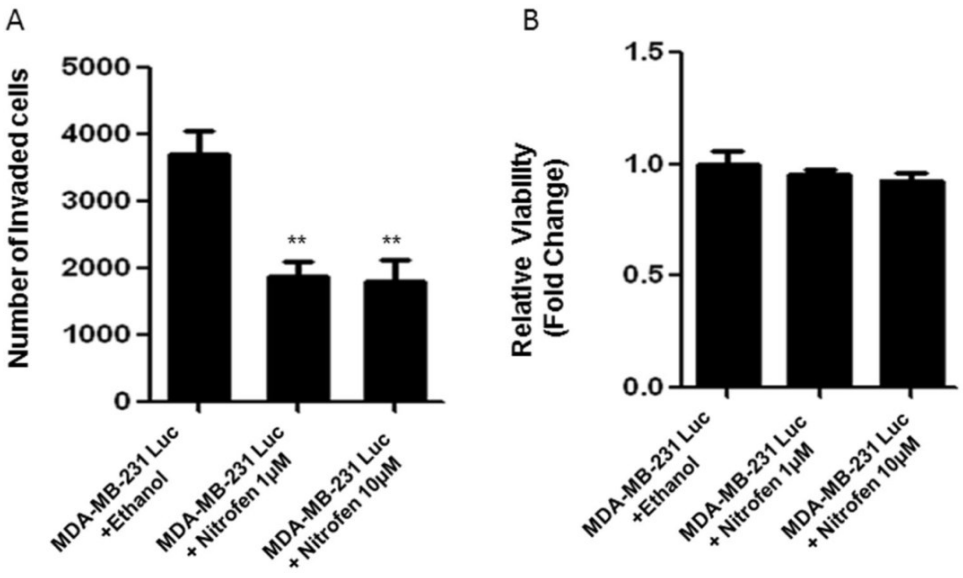

Figure 4.3. (**A**) Quantification of a Matrigel invasion assay demonstrating that nitrofen (1 μM) significantly reduces the invasive potential of MDA-MB-231-Luc cells. The Invasion assay was carried out using 40,000 cells/well, incubated for 24 h. Nitrofen was dissolved in ethanol to prepare the stock concentration of 100 mM and diluted in DMSO to a final concentration of 1 μM and 10 μM. (**B**) The AlamarBlue cell viability assay done under the same conditions shows that there is no change in the relative viability of cells upon treatments. The data are representative of 6 separate experiments, each done in triplicate. ** significantly altered from the untreated control $p < 0.01$.

4.3.2 Nitrofen Reduces In Vivo Metastasis of MDA-MB-231-Luc-D3H2LN BrCa Cells

We used an orthotopic tumor model with MDA-MB-231-luc-D3H2LN (MDA-MB-231-Luc) cells to allow in vivo tracking of tumor burden and metastasis in NIH-III nude mice. Mice were treated with low doses of nitrofen (1, 3, and 6 mg/kg/day, alternate days) or vehicle (olive oil) for 6 weeks. Mice were monitored for primary tumor growth and were examined weekly for metastasis by in vivo bioluminescence imaging. At 8 weeks post-tumor-implantation, tissues were examined by ex-vivo bioluminescence imaging. BrCa is known to metastasize preferentially to the lungs, liver, and bone. Figure 4.4 shows quantifiable bioluminescence 'heat maps' of MDA-MB-231-Luc tumors in abdominal mammary fat pads and at metastatic sites by in vivo imaging and demonstrated extensive metastases in untreated mice by 8 weeks post-tumor implantation (Figure 4.4).

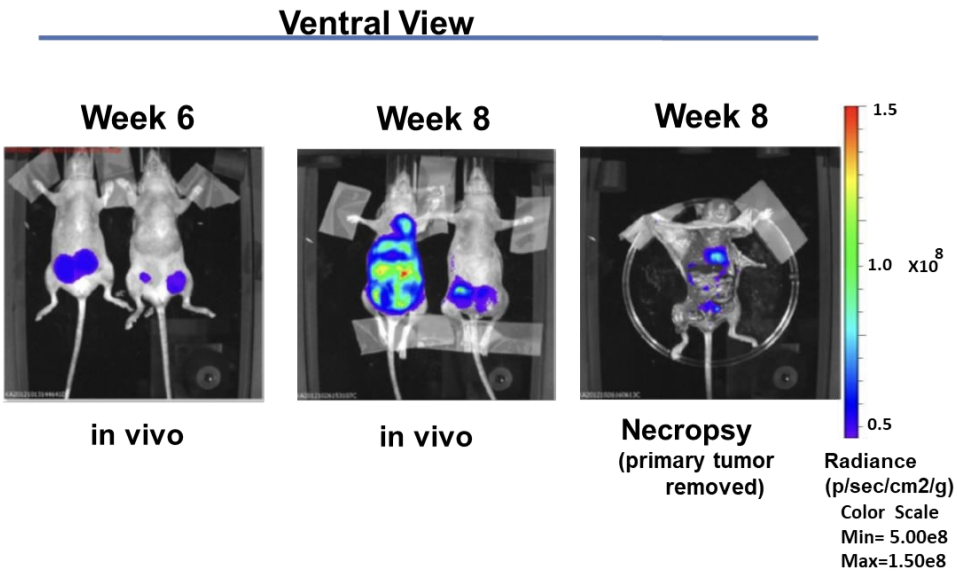

Figure 4.4. Growth of untreated 231-Luc tumors in the mammary fat pad. Representative bioluminescence image of human MDA-MB-231-Luc-D3H2LN (Caliper Life Sciences) breast tumors established in bilateral abdominal mammary fat pads of NIH-III nude mice. Images were acquired following s.c. injection with 15 mg/kg luciferin. By week 8, metastases were consistently and clearly visible in tumor-bearing mice by in vivo and/or ex vivo imaging.

Nitrofen had no significant effect on primary tumor growth (Figure 4.5A). The body weight of mice remained statistically comparable under the different treatment conditions through the duration of the treatments (Figure 4.5B), suggesting that there were no significant adverse effects of the treatments on the mice.

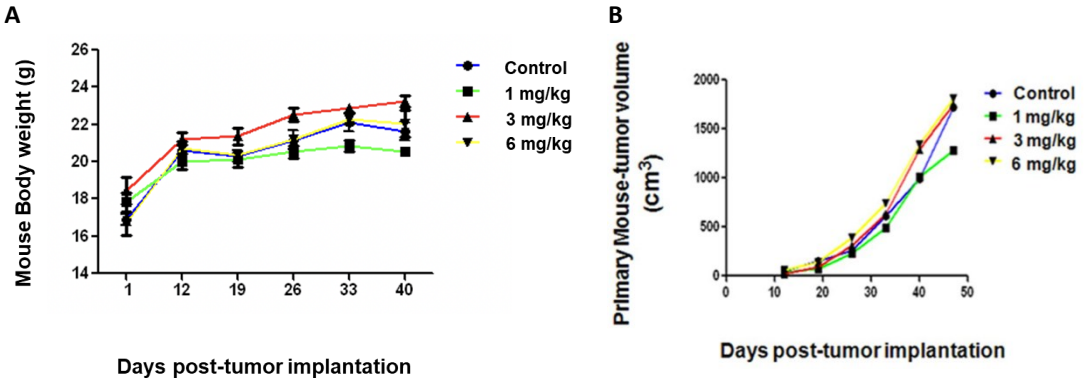

Figure 4.5. (A) Body weight of mice under various treatment conditions. The body weight of mice, which was monitored over the duration of the various treatment conditions, showed no significant difference between the various treatment conditions. $n = 5–10$ tumor bearing mice per group. **(B)** Growth of primary tumors following treatment with nitrofen. Mice with established bilateral orthotopic 231-Luc tumors were administered the following agents by oral gavage on alternate days for 6 weeks, starting on day 12: olive oil (control) or nitrofen at 1, 3, or 6 mg/kg body weight as indicated.

Ex vivo bioluminescence imaging at the end point showed extensive bioluminescence signal fluxes in both lungs and liver of untreated mice (Figure 4.6A). However, 6 weeks of oral gavage treatment with nitrofen with doses of 6 mg/kg (Figure 4.6B), 3 mg/kg (Figure 4.6C), or 1 mg/kg (Figure 4.6D) body weight on alternate days significantly reduced metastatic growth in the lungs and liver.

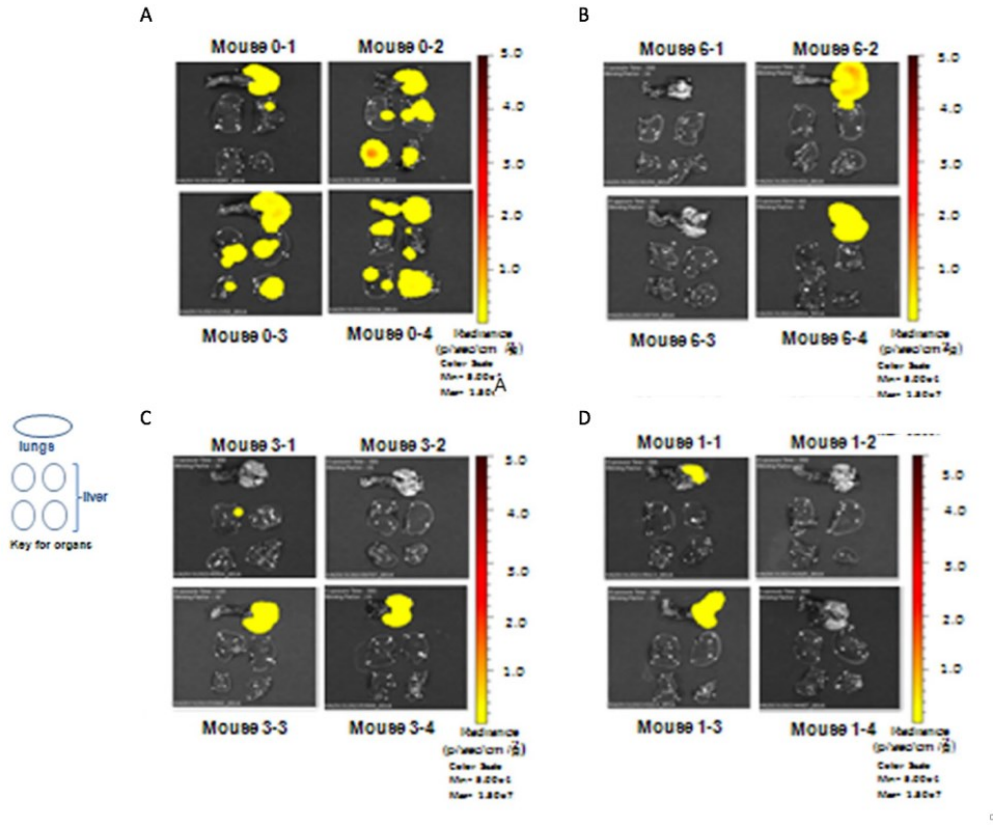

Figure 4.6. Bioluminescence 'heat map' of metastases in the lungs and liver of tumor-bearing animals from this experiment. (**A**) Untreated (control (fed with olive oil): Mouse 0–1 to 0–4); (**B**) Nitrofen at 6 mg/kg body Wt: Mouse 6–1 to 6–4; (**C**) Nitrofen at 3 mg/kg body Wt: Mouse 3–1 to 3–4; (**D**) Nitrofen at 1 mg/kg body Wt: Mouse 1–1 to 1–4.

Quantification of the number of metastases (metastatic score) using ex vivo IVIS bioluminescence flux analysis shows a significant decrease of metastases in both lungs and liver upon treatment of tumor bearing mice with all doses of nitrofen (1, 3, and 6 mg/kg body weight) (Figure 4.7).

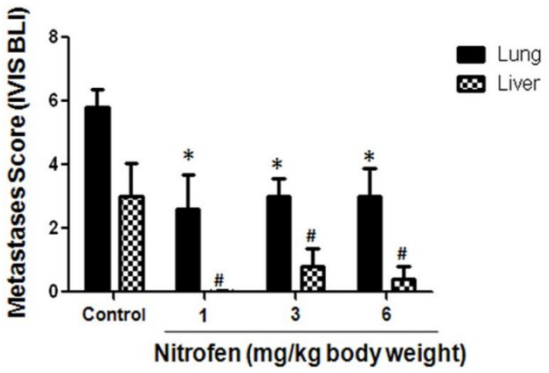

Figure 4.7. Metastasis score determined by quantification of IVIS bioluminescence (shown in Figure 4.7A–D) in the lungs and liver of untreated animals (control) or treated with various doses of nitrofen (1, 3, 6 mg/kg body Wt) every alternate day for 6 weeks. *n* = 5–10 tumor bearing mice per group. * significantly different compared to control lungs $P < 0.05$, # significantly different compared to control liver $P < 0.05$.

4.3.4 Nitrofen Inhibits Epithelial to Mesenchymal Transition

Previously, we have observed, in an unrelated study, that nitrofen induces perturbation in epithelial–mesenchymal transition (EMT) using a PTEN-knockdown model of prostate cancer cell lines (Figure 4.8).

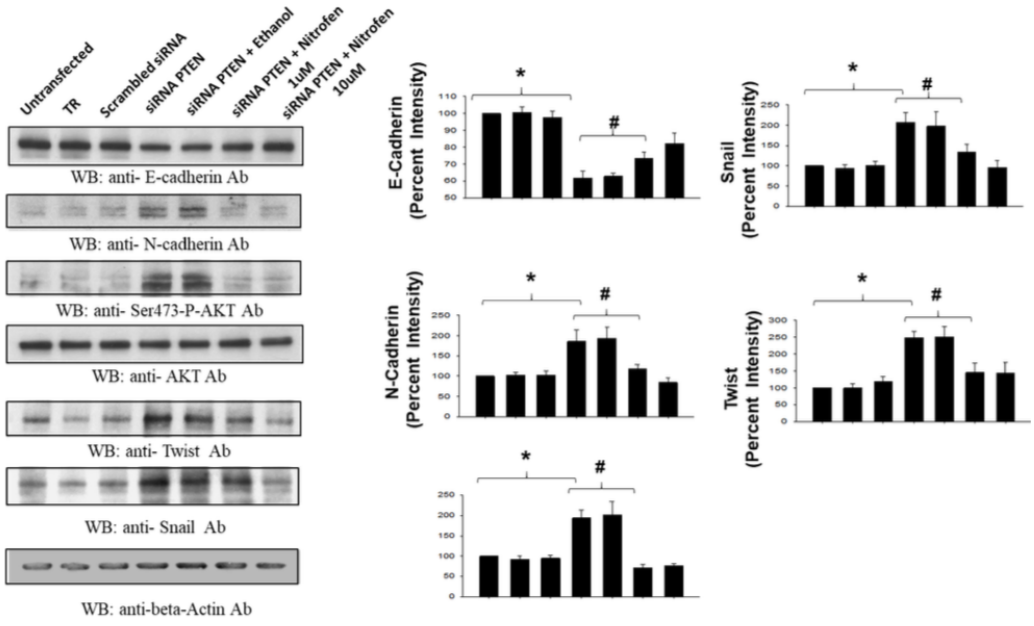

Figure 4.8. Nitrofen promotes MET changes in a PTEN-knockdown model of EMT of DU145 prostate cancer cells. Knockdown of PTEN resulted in a down-regulation of E-cadherin, an up-regulation of N-cadherin, and an increase in the protein levels of the transcription factors Snail and Twist. These alterations were significantly attenuated in the presence of 1 μM and 10 μM nitrofen for 24 h. The data are representative of 6 separate experiments, each done in triplicate. * significantly altered from untransfected control cells $p < 0.01$; # significantly altered from the siRNA-PTEN transfected cells $p < 0.01$. [TR = Transfection reagent].

Knockdown of PTEN resulted in EMT alterations that were attenuated significantly in the presence of 1 μM and 10 μM nitrofen (Figure 4.8).

In the present study, we induced EMT in the MCF7 breast cancer cell line by treatment of these cells with 2 ng/ml TGF-β. Immunofluorescence analysis of the cells shows that while treatment with TGF-β resulted in a down-regulation of epithelial marker E-cadherin and an up-regulation of the mesenchymal marker N-cadherin levels (Figure 4.9A, B), these alterations were prevented significantly in the presence of 1 μM nitrofen (Figure 4.9A, B).

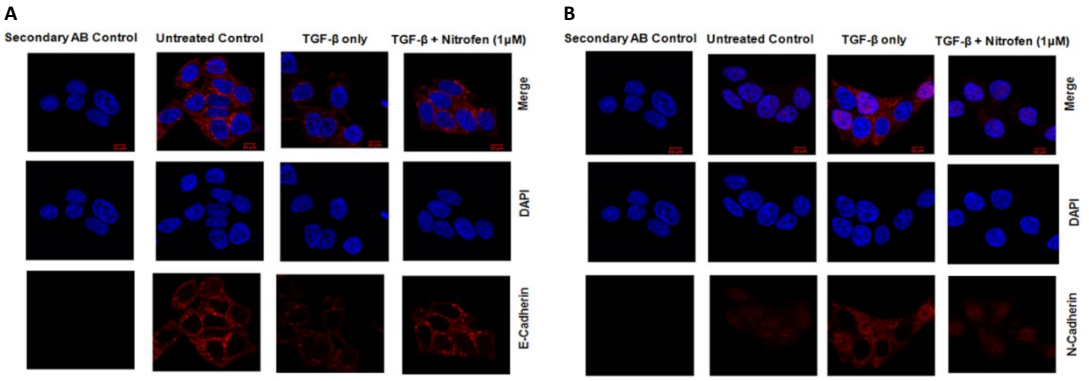

Figure 4.9A, B. TGF-β-induced EMT changes in MCF-7 breast cancer cells are prevented in the presence of nitrofen (1 μM) for 24 h: TGF-β treatment caused a significant decrease in E-cadherin levels (left) and an increase in N-cadherin levels (right) in MCF-7 breast cancer cells, which was prevented in the presence of nitrofen (1 μM).

This is confirmed by an immunoblot analysis, which shows a down-regulation of the epithelial marker E-cadherin and an up-regulation of the mesenchymal markers N-cadherin and Snail upon treatment with TGF-β (Figure 4.9C). These alterations were reversed/prevented significantly in the presence of 1 μM nitrofen (Figure 4.9C). Treatment with TGF-β increased phosphorylation of Smad 2/3, which was significantly lower in the presence of 1 μM nitrofen (Figure 4.9C). These results suggest that nitrofen effectively reduced EMT alterations induced by treatment with TGF-β.

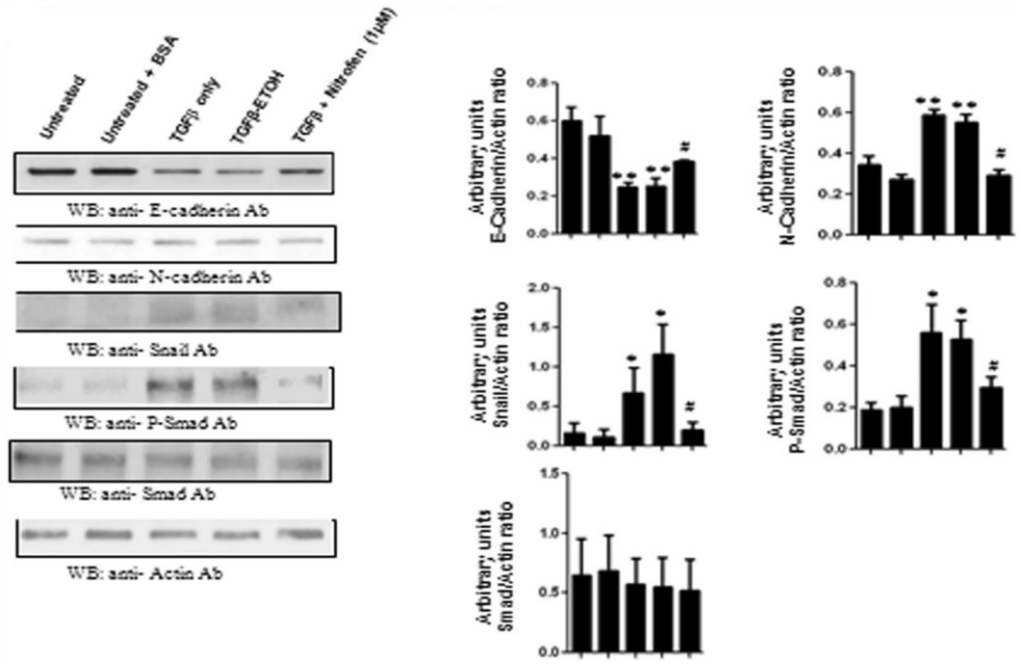

Figure 4.9C. TGF-β-induced EMT changes in MCF-7 breast cancer cells are prevented in the presence of nitrofen (1 μM) for 24 h: Western blot analysis. The data are representative of 6 separate experiments, each done in triplicate. * $p < 0.01$ significantly different from the untreated control; # $p < 0.01$ significantly different from TGF-β treated.

4.3.5 Synthesis of Nitrofen Analogues

Although nitrofen showed anti-invasion activity both in vitro and in vivo, there is no compelling reason to believe that its structure is optimized for the as-yet-unknown cellular target. We chose to make several modifications to probe the importance of various structural elements of nitrofen, especially those that raise concerns, such as the nitroarene (a potential toxophore) and the relatively nonpolar diaryl ether. (Note that nitrofen has a cLogP value of nearly 5.) Thus, we prepared eight analogues (A1–A8; Figure 4.10A) in which the nitro group was replaced with a reduced aniline or acetanilide, other electron-withdrawing groups (chloride, aldehyde, or nitrile), or removed entirely. Furthermore, for several derivatives, the diaryl ether was replaced with a less lipophilic diarylamine. These simple changes were designed to obtain a preliminary assessment of the extent to which the scaffold could be perturbed, which would be useful in the eventual design of probe molecules to identify the protein target of nitrofen, but we also imagined that some of these compounds might display superior properties to the parent.

4.3.6 Nitrofen Analogues Reduce In Vitro Invasive Activity of BrCa Cells

We examined the efficacy of 1 μM concentrations of all the analogues (Figure 10A) on the in vitro invasive potential of MDA-MB-231-Luc cells (Figure 4.10B). Our results show that 1 μM concentrations of 3 of the 8 analogues (A1, A5, A8) significantly reduced the invasive potential of MDA-MB-231-Luc cells relative to the untreated control, and 2 of them (A1 & A8) were superior to the parent compound nitrofen in reducing the invasive potential of these cells (Figure 4.10B). An AlamarBlue assay under the same conditions showed that there was no alteration in the relative viability of treated cells compared to untreated cells (data not shown). A similar efficacy of nitrofen analogues (A1, A5, A8) in inhibiting the invasive potential also was observed in another Basal B TNBC cell line MDA-MB-436 (data not shown).

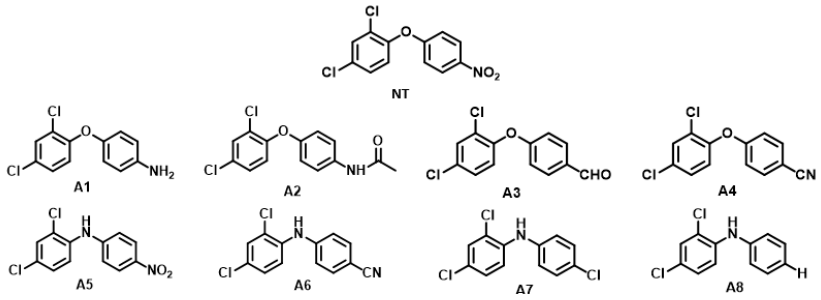

Figure 4.10A. Nitrofen (NT) and its analogues (A1–A8) generated from the parental nitrofen that lack the nitro group and/or have replaced the diaryl ether group with a diarylamine.

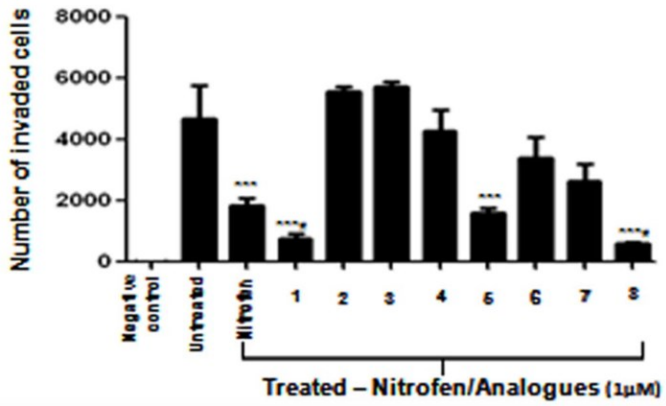

Figure 4.10B. Quantification of a Matrigel invasion assay of MDA-MB-231-Luc cells treated with nitrofen and its analogues (A1–A8), with the same conditions as in Figure 4.10.

We also examined whether nitrofen analogues (A1, A5, A8) inhibited the invasive potential of the Basal A TNBC cell line MDA- MB-468. Our results show that 1 µM concentrations of 3 of the 8 analogues (A1, A5, A8) significantly reduced the invasive potential of MDA-MB-468 cells with no significant alterations in relative viability of cells (Figure 4.11A–C).

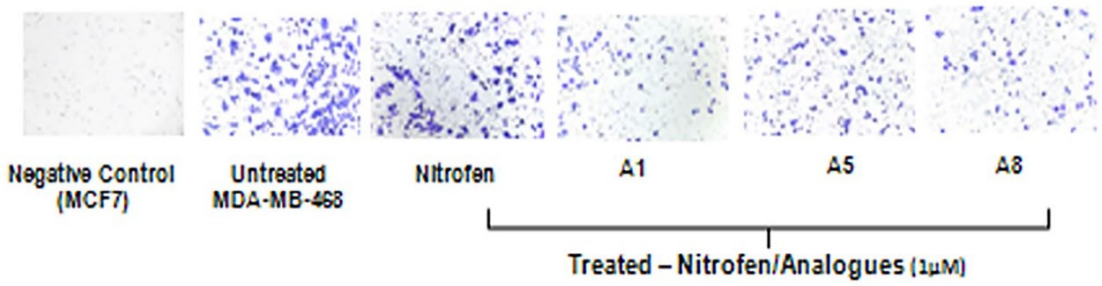

Figure 4.11A. Photomicrograph of invading MDA-MB-468 TNBC cells in the presence or absence of treatment with nitrofen and analogues A1, A5, and A8.

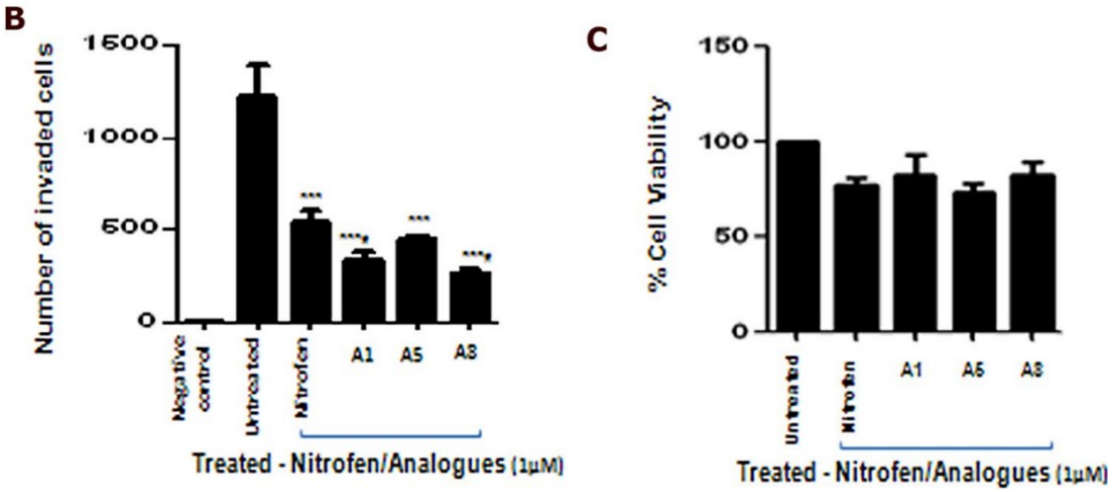

Figure 4.11B, C. Quantification of a Matrigel invasion assay of MDA-MB-468 cells treated with nitrofen and nitrofen analogues A1, A5, and A8 (left). AlamarBlue cell viability assay. Non-invasive MCF-7 cells were used as a negative control. The data are representative of 6 separate experiments, each done in triplicate. * significantly altered from the untreated control $p < 0.05$; # significantly altered from the nitrofen-treated cells $p < 0.05$ (right).

We further assessed the potential cytotoxic effects of nitrofen and the three effective analogues (A1, A5, A8) using a primary rat brain culture of mixed brain cells (neurons, astrocytes, microglia) and the Live/Dead assay. Our results show that

treatment with 1 μM nitrofen or analogues (A1, A5, A8) was not cytotoxic to these primary rat brain cortical cell cultures (Figure 4.12).

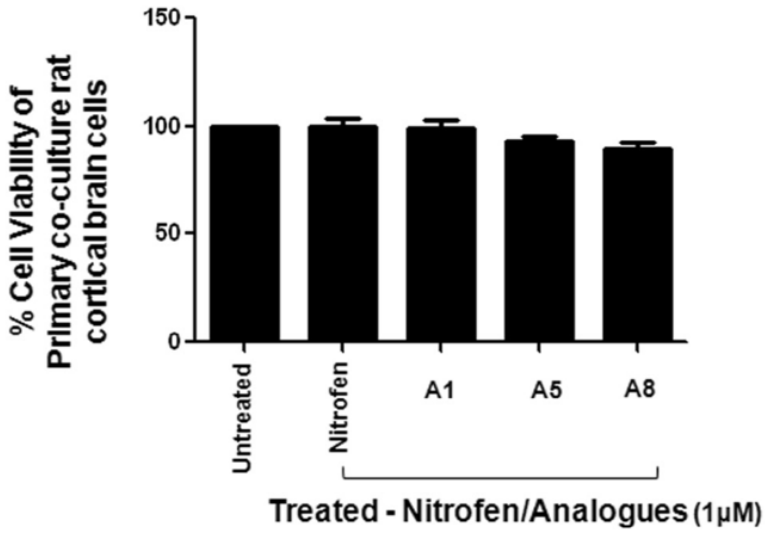

Figure 4.12. AlamarBlue cell viability assay of primary culture of rat cortical brain cells treated with nitrofen and nitrofen analogues (A1, A5, and A8). The data show that there is no change in relative viability of cells with any treatments. The data are representative of 6 separate experiments, each done in triplicate.

4.3.7 Nitrofen and Its Analogues Induce Mesenchymal to Epithelial Type Transition (MET) in Mesenchymal TNBC Cell Lines

Mesenchymal-like TNBC is a subgroup of TNBC that harbors mesenchymal-like features, such as an enriched expression of genes involved in EMT. It is recognized that elevated vimentin and decreased E-cadherin protein levels are characteristic of mesenchymal-like TNBC subgroups. MDA-MB 231 cells do not express E-cadherin but do express copious levels of vimentin protein. MDA-MB-231 cells do not express N-cadherin. Treatment with nitrofen (1 μM) or nitrofen analogues A1, A5, and A8 (1 μM) resulted in the appearance of E-cadherin (Figure 4.13A) in these cells and a significant down-regulation of vimentin protein (Figure 4.13B) reminiscent of a mesenchymal to epithelial like transition. MET alterations were confirmed further by an immunoblot analysis for the epithelial marker E-cadherin, which was upregulated significantly, the mesenchymal marker vimentin, and Snail (Figure 4.13C), which were down-regulated significantly, upon treatment with nitrofen analogues (A1, A5, A8).

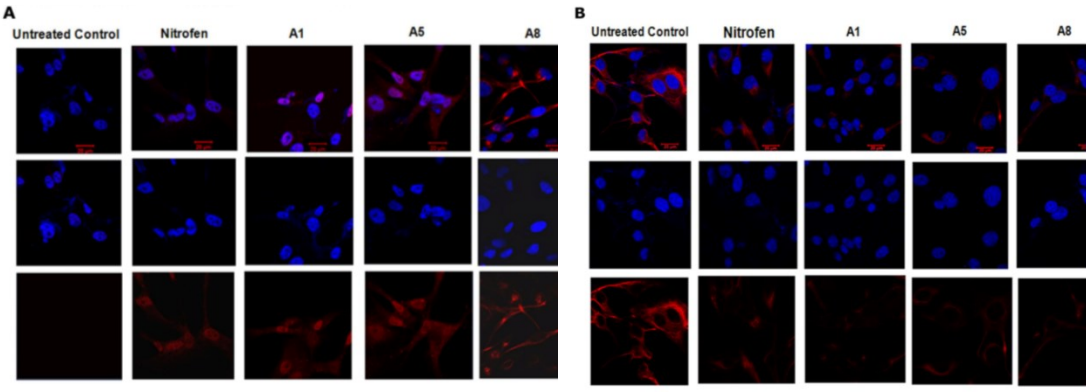

Figure 4.13A, B. Treatment with nitrofen and analogues A1, A5, and A8 at 1 μM concentration for 24 h results in the appearance of the epithelial marker E-cadherin (left) and a decrease in cellular expression of vimentin protein (right) in the MDA-MB-231-Luc TNBC cell line. The data are representative of 6 separate experiments, each done in triplicate.

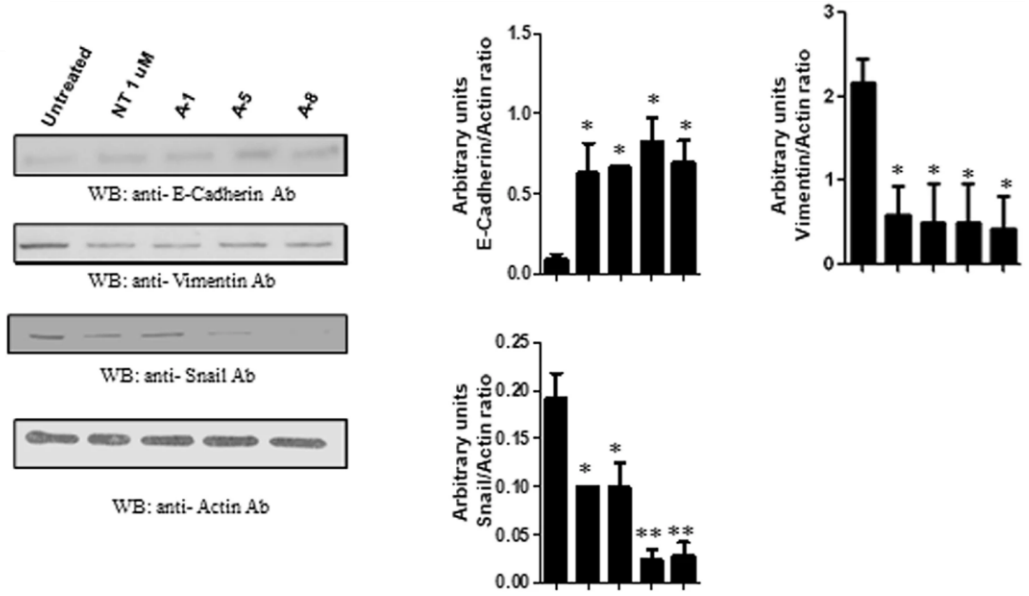

Figure 4.13C. Western blot analysis. The data are representative of 6 separate experiments, each done in triplicate. *significantly altered from the untreated control $p < 0.05$; ** significantly altered from the untreated control $p < 0.01$.

Similar results were seen upon treatment of another mesenchymal cell line MDA-MB-436 (Figure 4.14). It should be pointed out that we immunoblotted for the epithelial marker ZO-1 in the MDA-MB-436 cells, as we were unable to detect any expression of E-cadherin protein in these cells in the presence and absence of treatments. This is likely because the CDH1 (E-cadherin gene) is known to be highly methylated in this cell line and does not express any mRNA for E-cadherin.

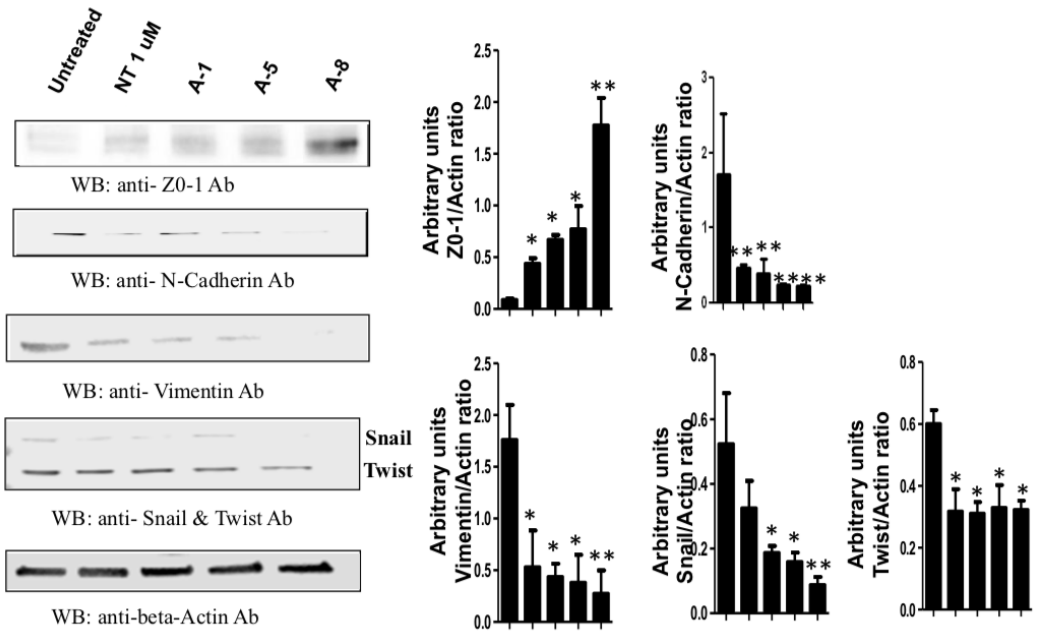

Figure 4.14. Nitrofen analogues promote mesenchymal to epithelial transformation in the MDA-MB-436 TNBC cell line. Western blot analysis shows that treatment with nitrofen and analogues A1, A5, and A8 at 1μM concentration for 24 h results in the appearance of the epithelial marker ZO-1 in MDA-MB-436 cell line, which is mesenchymal-like in phenotype. Treatment with nitrofen and analogues A1, A5, and A8 results in a significant decrease in cellular expression of mesenchymal markers N-cadherin, vimentin, Twist, and Snail in the MDA-MB- 436 cell line. The data are representative of 6 separate experiments, each done in triplicate. * significantly altered from untreated control $p < 0.05$; ** significantly altered from untreated control $p < 0.01$.

4.4 Discussion

Invasive breast cancer is a devastating disease, the most aggressive form of which is the basal-like/triple-negative phenotype (TNBC). TNBC does not express estrogen receptors or progesterone receptors and lacks HER2 amplification. Patients diagnosed with TNBC have a higher risk of disease relapse within 5 years than patients treated for other breast cancer subtypes. This highlights the need for innovative treatment approaches. This study tested a novel pharmacological approach to inhibiting invasion and metastasis of TNBC in vitro and in an in vivo mouse model. This avenue of research is derived from an unrelated earlier study in our lab examining the mechanism of action by which the compound nitrofen induces known developmental anomalies in rodent embryos. We speculated that nitrofen's effects in developmental abnormalities may, at least partially, be related to a perturbation in EMT, a key development component underlying organogenesis. Indeed, using a PTEN-knockdown in DU145

prostate cancer cells as a model for EMT we have shown that nitrofen in fact does interfere with the process of EMT (Figure 4.8): knockdown of PTEN resulted in a down-regulation of E-cadherin and an up-regulation of N-cadherin in DU145 prostate cancer cells (Figure 4.8). These alterations were attenuated significantly in the presence of 1 μM and 10 μM nitrofen. Knockdown of PTEN in DU145 cells also resulted in an increase in the levels of the transcription factors Snail and Twist, which were prevented significantly in the presence of 1 μM and 10 μM nitrofen (Figure 4.8). In the present study, we tested this hypothesis using TGFβ-induced EMT in the MCF7 breast cancer cell line. Treatment of MCF7 cells with TGFβ resulted in a down-regulation of E-cadherin and an up-regulation of N-cadherin. These alterations were significantly attenuated in the presence of 1 μM nitrofen. By extrapolation, we hypothesized that if nitrofen perturbs EMT, then it may have an impact on cancer metastasis and, therefore, could be a putative starting point in developing an effective new drug for treating metastatic BrCa where EMT is a critical component of the pathogenesis.

We present provocative in vivo data which show that nitrofen (2,4-dichloro-4'-nitrodiphenyl ether) efficiently blocks metastatic tumor growth, following the establishment of orthotopic xenografts in nude mice of a luciferase-expressing derivative of the prototypical human TNBC cell line MDA-MB-231. MDA-MB-231 cells undergo spontaneous metastasis via unconfirmed mechanisms, although microRNA, especially miR-21, is thought to play a role.[32, 33] Our results show that while nitrofen had little effect on the primary tumor weight or body weight, the level of metastases was appreciably lower in the lungs and liver of mice treated with 6, 3, or 1 mg/kg/day nitrofen. It is notable that the effect of nitrofen treatment is more robust in the livers of the treated animals than in the lungs. This may be due to the oral mode of administration of nitrofen and the effectively greater concentrations of the drug in the liver. Evaluation of the effects of nitrofen on the invasive potential of a panel of BrCa cell lines as well as the MDA-MB-231-Luc cell line using an in vitro Matrigel invasion assay showed that nitrofen significantly attenuates the invasive potential of BrCa cell lines, with a significantly greater inhibitory effect on the invasive potential of TNBC cell lines compared to the non-TNBC lines. These results corroborated our observations in the in vivo model, suggesting that nitrofen's effect in altering the

invasive potential is, at least partially, responsible for the observed attenuation of MDA-MB-231-Luc metastasis in the in vivo mouse model.

Cumulatively, these data suggest that nitrofen is effective in decreasing the invasive potential of breast cancer cells in vitro, effectively blocking metastasis in vivo, which may have significant implications in blocking/limiting BrCa metastasis in patients.

We also developed analogues of nitrofen designed to have reduced lipophilicity and lacking the aromatic nitro group that may undergo conversion to toxic metabolites. The aim was to generate feasible structurally modified nitrofen analogues that retain anti-invasive activity with potentially superior pharmacokinetic properties and reduced long-term toxicity. Here, we report the synthesis of 8 analogues of nitrofen, all of which lack the nitro group and/or have replaced the diaryl ether group with a diarylamine; 3 of the 8 compounds significantly reduced the invasive potential of two TNBC cell lines, MDA-MB-231-Luc and MDA-MB-468, in vitro relative to the untreated control, and 2 of them (A1 & A8) were superior to the parent compound nitrofen. Further, nitrofen and the three analogues were completely nontoxic to both cell lines at the concentration that caused a greater than two-fold decrease in the invasive potential compared to the untreated controls. Importantly, treatment of a very vulnerable primary culture of normal cortical brain cells with nitrofen or its analogues (A1, A5, A8) did not result in any cytotoxicity. This is very significant, as these observations stand in contrast to the cytotoxic effects on normal cell lines that frequently are seen with many chemotherapeutic agents.

TNBC is a heterogeneous disease based on gene expression signatures, biological properties, and clinical outcome. TNBC can be separated into 6 TNBC subtypes displaying unique GE and ontologies, including 2 basal-like (BL1 and BL2), an immunomodulatory (IM), a mesenchymal (M), a mesenchymal stem–like (MSL), and a luminal androgen receptor (LAR) subtype.[34] TNBC-BL exhibits the highest responsiveness to chemotherapy,[35] including platinum-based chemotherapy that is directed at targeting the DNA-repair deficiency.[36–39] Immune based therapies, including immune-checkpoint blockade[40,41] and tumor vaccines,[42,43] are being developed actively to treat the "immunomodulatory" subtype of TNBC.

Luminal/apocrine TNBC with androgen receptor overexpression and HER-2-enriched TNBC overlap significantly with the other three subgroups, and clinical trials are currently underway to test combinatorial therapies using AR inhibitors for the luminal/apocrine TNBC group and HER2 targeted therapies for the HER2-enriched TNBC.[44–46] For mesenchymal-like TNBC (ML-TNBC), a cancer stem cell profile and expression of mesenchymal markers are correlated highly to chemotherapy resistance.[47] These tumors are very difficult to treat, although many promising treatments targeted at components of pathways that promote EMT (MAPK or WNT pathways) are under investigation.[48–53] Our data show that nitrofen and its analogues very effectively reverse the mesenchymal-like phenotype of the TNBC cell lines to a more epithelial phenotype. We postulate that this is, at least partially, is responsible for the effectiveness of these drugs in inhibiting in vivo metastasis of TNBC tumors and in vitro invasive potential of TNBC cell lines. However, the exact EMT-promoting pathway that is targeted by this group of drugs is not known at present and is currently under investigation.

Our cumulative data show that nitrofen and, more importantly, its analogues that lack the potentially toxic aromatic nitro group are significantly effective in limiting the invasive potential of TNBC cell lines with minimal cytotoxic effect to normal cells. Although we have demonstrated that this group of compounds is very effective in reversing a mesenchymal phenotype to a more epithelial-like phenotype, determination of their molecular target(s) is paramount to deciphering the putative clinical relevance of this treatment. Importantly, nitrofen analogues potentially could be of benefit in combinatorial treatment with other chemotherapeutics for patients with a mesenchymal-TNBC tumor subtype who are well known to exhibit a high resistance to chemotherapy. However, in addition to the potential and very beneficial effect on the mesenchymal (Basal B) subgroup of TNBC, nitrofen analogues likely have cellular effects in addition to inducing MET. This is evident by the ability of these compounds in inhibiting the invasive potential of the epithelial (Basal A) TNBC cell line MDA-MB-468. This suggests that nitrofen analogues have a broader spectrum of efficacy in the treatment of TNBC, as they are effective in treating both epithelial and mesenchymal subgroups of TNBC, albeit via different mechanisms.

4.5 Conclusion

In conclusion, this study demonstrates the efficacy of nitrofen in preclinical models but, more importantly, it highlights the efficacy of its analogues in blocking the invasive properties of TNBC and sheds light on a putative mechanism for this effect. Further work must be carried out to determine the exact pathways by which these drugs suppress TNBC invasiveness/metastasis. This will assist in future development of the selected nitrofen analogues into a clinically usable form and the development of novel treatment strategies for metastatic BrCa, with high potential for clinical translation.

4.6 References

1. Report on Breast Cancer Statistics in Canada. *Canadian Breast Cancer Society* **2009.**
2. Bray, F.; Ferlay, J.; Soerjomataram, I.; Siegel, R.L.; Torre, L.A.; Jemal, A. Global Cancer Statistics 2018: GLOBOCAN Estimates of Incidence and Mortality Worldwide For 36 Cancers in 185 Countries. *CA Cancer J. Clin.* **2020**, *70*, 313–313.
3. Mattiuzzi, C.; Lippi, G. Current Cancer Epidemiology. *J. Epidemiol. Glob. Health* **2019**, *9*, 217–222.
4. World Health Organization, Projections of Mortality and Causes of Death, 2016 to 2060. *Obtenido de*. **2018**.
5. Sarrió, D.; Rodriguez-Pinilla, S.M.; Hardisson, D.; Cano, A.; Moreno-Bueno, G.; Palacios, J. Epithelial-mesenchymal Transition in Breast Cancer Relates to the Basal-like Phenotype. *Cancer Res.* **2008**, *68*, 989–997.
6. Rakha, E.A.; Ellis, I.O. Triple-negative/Basal-like Breast Cancer. *Pathology* **2009,** 41, 40–47.
7. Kumar, P.; Aggarwal, R. An Overview of Triple-Negative Breast Cancer. *Arch. Gynecol. Obste.* **2016**. *283*, 247–269.
8. Afghahi, A.; Timms, K. M.; Vinayak, S.; Jensen, K. C.; Kurian, A. W.; Carlson, R. W.; Chang, P. J.; Schackmann, E.; Hartman, A. R.; Ford, J. M.; Telli, M. L. Tumor BRCA1 Reversion Mutation Arising During Neo Adjuvant Platinum-Based Chemotherapy in Triple-Negative Breast Cancer Is Associated with Therapy Resistance. *Clin. Cancer Res.* **2017**, *23*, 3365–3370.
9. Lev, S. Targeted Therapy and Drug Resistance in Triple-Negative Breast Cancer: The EGFR Axis. *Biochem. Soc. Trans.* **2020**, *48*, 657–665.
10. Robson, M.; Im, S.A.; Senkus, E.; Xu, B.; Domchek, S. M.; Masuda, N.; Delaloge, S.; Li, W.; Tung, N.; Armstrong, A.; Wu, W. 2017. Olaparib for Metastatic Breast Cancer in Patients with A Germline BRCA Mutation. *N. Engl. J. Med.* **2017**, *377*, 523–533.
11. Litton, J. K.; Rugo, H. S.; Ettl, J.; Hurvitz, S. A.; Gonçalves, A.; Lee, K. H.; Fehrenbacher, L.; Yerushalmi, R.; Mina, L. A.; Martin, M.; Roché, H. Talazoparib in Patients with Advanced Breast Cancer and A Germline BRCA Mutation. *N.Engl.J.Med.* **2018**, *379*, 753–763.
12. Manson, J. M. Mechanism of Nitrofen Teratogenesis. *Environ. Health Perspect* . **1986**, *70,* 137–147.
13. Greer, J. J.; Babiuk, R. P.; Thebaud, B. Etiology of Congenital Diaphragmatic Hernia: The Retinoid Hypothesis. *Pediatr. Res.* **2003**, *53*, 726–730.
14. Greer, J. J.; Allan, D. W.; Babiuk, R. P.; Lemke, R. P. Recent Advances in Understanding the Pathogenesis of Nitrofen-induced Congenital Diaphragmatic Hernia. *Pediatr. Pulmonol.* **2000**, *29*, 394–399.
15. Acosta, J. M.; Chai, Y.; Meara, J. G.; Bringas, Jr, P.; Anderson, K. D.; Warburton, D. Prenatal Exposure to Nitrofen Induces Fryns Phenotype in Mice. *Ann.Plast.Surg.* **2001***, 46*, 635–640.

16. Hurt, S. S. B.; Smith, J. M.; Hayes, A. W. Nitrofen: A Review and Perspective. *Toxicology* **1983**, *29*, 1–37.
17. Gray, L. E.; Kavlock, R. J. The Effects of The Herbicide 2,4-Dichlorophenyl-P-Nitrophenyl Ether (NIT) on Serum Thyroid Hormones in Adult Female Mice. *Toxicol. Lett.* **1983**, *15*, 231–235.
18. Blagosklonny, M. V. Teratogens as anticancer drugs. *Cell Cycle* **2009**, *4*, 1518–1521.
19. Wonders, K. Y.; Reigle, B. S. Trastuzumab and Doxorubicin-Related Cardiotoxicity and the Cardioprotective Role of Exercise. *Integr. Cancer Ther.* **2009**, *8*, 17–21.
20. Telli, M. L.; Witteles, R. M. Trastuzumab-related Cardiac Dysfunction. *J. Natl. Compr. Cancer Netw.* **2011**, *9*, 243–249.
21. Chien, A. J.; Rugo, H. S. The Cardiac Safety of Trastuzumab in the Treatment of Breast Cancer. *Expert Opin. Drug Saf.* **2010**, *9*, 35–346.
22. (a)www.chemspider.com/ChemicalStructure.15010.html;accessed30March,2016,16:27.(b)www.vitasmlab.com/catalog-search? searchValue=STK365913; accessed 30 March, 2016, 16:29.
23. Jenkins, D. E.; Oei, Y.; Hornig, Y. S.; Yu, S. F.; Dusich, J., Purchio, T.; Contag, P. R. Bioluminescent Imaging (BLI) to Improve and Refine Traditional Murine Models of Tumor Growth and Metastasis. *Clin. Exp. Metastasis* **2003**, *20*, 733–744.
24. Mey, J.; Babiuk, R. P.; Clugston, R.; Greer, J. J. Retinal Dehydrogenase-2 is Inhibited by Compounds that Induce Congenital Diaphragmatic Hernias in Rodents. *Am. J. Pathol.* **2003**, *162*, 673–679.
25. Noble, B. R., Babiuk, R. P.; Clugston, R. D.; Underhill, T. M.; Sun, H.; Kawaguchi, R.; Walfish, P. G.; Blomhoff, R., Gundersen, T. E.; Greer, J. J.; Mechanisms of Action of the Congenital Diaphragmatic Hernia-inducing Teratogen Nitrofen. *Am. J. Physiol. Lung Cell Mol. Physiol.* **2007**, *293*, 1079–1087.
26. Chaurasiya, S.; Hew, P.; Crosley, P.; Sharon, D.; Potts, K.; Agopsowicz, K.; Long, M.; Shi, C.; Hitt, M. M. Breast Cancer Gene Therapy Using an Adenovirus Encoding Human IL-2 Under Control of Mammaglobin Promoter/Enhancer Sequences. *Cancer Gene Ther.* **2016**, *23*, 178–187.
27. Lanning, M. E.; Yu, W.; Yap, J. L.; Chauhan, J.; Chen, L.; Whiting, E.; Pidugu, L. S.; Atkinson, T.; Bailey, H., Li, W.; Roth, B.M.; Hynicka, L.; Chesko, K.; Toth, E. A.; Shapiro, P.; MacKerell Jr., A. D.; Wilder, P. T.; Fletcher, S. Structure-Based Design of N-Substituted 1-Hydroxy-4-sulfamoyl-2-naphthoates as Selective Inhibitors of the Mcl-1 Oncoprotein. Eur. J. Med. Chem. **2016**, *113*, 273–292.
28. Kathiravan, S.; Nicholls, I. A. Monoprotected l-Amino Acid (l-MPAA), Accelerated Bromination, Chlorination, and Iodination of C (sp2)−H Bonds by Iridium (III) Catalysis. Chem. Eur. J **2017**, *23*, 7031–7036.
29. Zhu, X. L.; Zhang, R.; Wu, Q. Y.; Song, Y. J.; Wang, Y. X.; Yang, J. F.; Yang, G. F. Natural Product Neopeltolide as a Cytochrome bc_1 Complex Inhibitor: Mechanism of Action and Structural Modification. J. Agric. Food Chem. **2019**, *67*, 2774–2781.

30. Wolfe, J. P.; Wagaw, S.; Buchwald, S. L. An Improved Catalyst System for Aromatic Carbon−Nitrogen Bond Formation: The Possible Involvement of Bis (Phosphine) Palladium Complexes as Key Intermediates. J. Am. Chem. Soc. **1996**, *118*, 7215–7216.
31. Ali, N.; Venkateswaran, G.; Garcia, E.; Landry, T.; McColl, H.; Sergi, C.; Persad, A.; Abuetabh, Y.; Eisenstat, D. D.; Persad, S. Osteosarcoma Progression is Associated with Increased Nuclear Levels and Transcriptional Activity of Activated B-Catenin. *Genes Cancer* **2019**, *10*, 63–79.
32. Han, M.; Liu, M.; Wang, Y.; Chen, X.; Xu, J.; Sun, Y.; Zhao, L.; Qu, H.; Fan, Y.; Wu, C. Antagonism of Mir-21 Reverses Epithelial-Mesenchymal Transition and Cancer Stem Cell Phenotype Through AKT/ERK1/2 Inactivation by Targeting PTEN. *PLoS ONE* **2012**, *7*, 1–10.
33. Du, J.; Yang, S.; An, D.; Hu, F.; Yuan, W.; Zhai, C.; Zhu, T. BMP-6 Inhibits Microrna-21 Expression in Breast Cancer Through Repressing Δef1 and AP-1. *Cell Res.* **2009**, *19*, 487–496.
34. Lehmann, B.D.; Bauer, J.A.; Chen, X.; Sanders, M.E.; Chakravarthy, A.B.; Shyr, Y.; Pietenpol, J.A. Identification of Human Triple-negative Breast Cancer Subtypes and Preclinical Models for Selection of Targeted Therapies. *J. Clin. Invest.* **2011**, *121*, 2750–2767.
35. Rouzier, R.; Perou, C. M.; Symmans, W. F.; Ibrahim, N.; Cristofanilli, M.; Anderson, K.; Hess, K. R.; Stec, J.; Ayers, M.; Wagner, P.; Morandi, P. Breast Cancer Molecular Subtypes Respond Differently to Preoperative Chemotherapy. *Clin. Cancer Res.* **2005,** *15*, 5678–5685.
36. Silver, D. P.; Richardson, A. L.; Eklund, A. C.; Wang, Z. C.; Szallasi, Z.; Li, Q.; Juul, N.; Leong, C. O.; Calogrias, D.; Buraimoh, A.; Fatima, A. Efficacy of Neoadjuvant Cisplatin in Triple-Negative Breast Cancer. *J. Clin. Oncol.* **2010**, *1*, 1145–1153.
37. Sikov, W. M.; Berry, D. A.; Perou, C. M.; Singh, B.; Cirrincione, C.; Tolaney, S.; Kuzma, C. S. Impact of The Addition of Carboplatin and/or Bevacizumab to Neoadjuvant Once-per-week Paclitaxel Followed by Dose-dense Doxorubicin and Cyclophosphamide on Pathologic Complete Response Rates in Stage II to III Triple-Negative Breast Cancer: CALGB 40603 (Alliance). *J. Clin. Oncol.* **2015**, *3*, 13–21.
38. Von Minckwitz, G.; Schneeweiss, A.; Loibl, S.; Salat, C.; Denkert, C.; Rezai, M.; Blohmer, J. U.; Jackisch, C.; Paepke, S.; Gerber, B.; Zahm, D. M. Neoadjuvant Carboplatin in Patients with Triple-negative and HER2-positive Early Breast Cancer (GeparSixto; GBG 66): A Randomised Phase 2 trial. *Lancet Oncol.* **2014**, *15*, 747–756.
39. Von Minckwitz, G.; Hahnen, E.; Fasching, P. A.; Hauke, J.; Schneeweiss, A.; Salat, C.; Rezai, M.; Blohmer, J. U.; Zahm, D. M.; Jackisch, C.; Gerber, B. Pathological Complete Response (Pcr) Rates After Carboplatin-containing Neoadjuvant Chemotherapy in Patients with Germline BRCA (Gbrca) Mutation and Triple-negative Breast Cancer (TNBC): Results from Geparsixto. *J. Clin. Oncol.* **2014**, *32*, 1005–1035.
40. Mittendorf, E. A.; Philips, A. V.; Meric-Bernstam, F.; Qiao, N.; Wu, Y.; Harrington, S.; Su, X.; Wang, Y.; Gonzalez-Angulo, A. M.; Akcakanat, A.; Chawla, A. PD-L1 Expression in Triple-negative Breast Cancer. *Cancer Immunol. Res.* **2014**, *2*, 361–370.

41. Topalian, S. L.; Hodi, F. S.; Brahmer, J. R.; Gettinger, S. N.; Smith, D. C.; McDermott, D. F.; Powderly, J. D.; Carvajal, R. D.; Sosman, J. A.; Atkins, M. B.; Leming, P. D. *N. Engl. J. Med.* **2012,** *366*, 2443–2454.
42. Ademuyiwa, F. O.; Bshara, W.; Attwood, K.; Morrison, C.; Edge, S. B.; Ambrosone, C. B.; O'Connor, T. L.; Levine, E. G.; Miliotto, A.; Ritter, E.; Ritter, G. NY-ESO-1 Cancer Testis Antigen Demonstrates High Immunogenicity in Triple Negative Breast Cancer. *PLoS One* **2012***, 7*, 1–9.
43. Tessari, A.; Paolini, B.; Mariani, L.; Pilla, L.; Carcangiu, M. L.; Moliterni, A.; De Braud, F. G.; Cresta, S. Expression of PD-L1 and NY-ESO-1 in Early and Advanced Triple-negative Breast Cancer. *J. Clin. Oncol.* **2014**, *32*, 1101–1110.
44. Park, S.; Koo, J.; Park, H. S.; Kim, J. H.; Choi, S. Y.; Lee, J. H.; Park, B. W.; Lee, K. S. Expression of Androgen Receptors in Primary Breast Cancer. *Ann. Oncol.* **2010**, *21*, 488–492.
45. Mittendorf, E. A.; Schneble, E. J.; Perez, S. A.; Symanowski, J. T.; Patil, R.; Vreeland, T. J.; Berry, J. S.; Trappey, A. F.; Clifton, G. T.; von Hofe, E.; Ardavanis, A. Primary Analysis of the Prospective, Randomized, Single-blinded Phase II Trial of AE37 Vaccine Versus GM-CSF Alone Administered in the Adjuvant Setting to High-risk Breast Cancer Patients. *J. Clin. Oncol.* **2014***, 32*, 638–648.
46. Schneble, E. J.; Perez, S. A.; Berry, J. S.; Trappey, A. F.; Vreeland, T.; Hale, D. F.; Sears, A. K.; Clifton, G. T.; von Hofe, E.; Ardavanis, A.; Shumway, N. M. Comparison of Recurrent and Nonrecurrent Breast Cancer Patients Undergoing AE37 Peptide Vaccine Therapy. *J. Clin. Oncol.* **2014***,* 32, 613–618.
47. Creighton, C. J.; Li, X.; Landis, M.; Dixon, J. M.; Neumeister, V. M.; Sjolund, A.; Rimm, D. L.; Wong, H.; Rodriguez, A.; Herschkowitz, J. I.; Fan, C. Residual Breast Cancers after Conventional Therapy Display Mesenchymal as well as Tumor-initiating Features. *Proc. Natl. Acad. Sci.* **2009**, *106*, 13820–51382.
48. Gupta, P. B.; Onder, T. T.; Jiang, G.; Tao, K.; Kuperwasser, C.; Weinberg, R. A.; Lander, E. S. Identification of Selective Inhibitors of Cancer Stem Cells by High-throughput Screening. *Cell* **2009***, 138*, 645–659.
49. Wang, K.; Zhang, Q.; Li, D.; Ching, K.; Zhang, C.; Zheng, X.; Ozeck, M.; Shi, S.; Li, X.; Wang, H.; Rejto, P. PEST Domain Mutations in Notch Receptors Comprise an Oncogenic Driver Segment in Triple-negative Breast Cancer Sensitive to a γ-Secretase Inhibitor. *Clin. Cancer Res.* **2015**, *21*, 1487–1496.
50. Thiery, J. P. Epithelial-Mesenchymal Transitions in Tumour Progression. *Nat. Rev. Cancer.* **2002**, *2*, 442–454.
51. Daniel, B. R.; Campone, M.; Dieras, V.; Ervin, T.; Yu, W.; Paton, V. E.; Xia, Q.; Peterson, A. OT3-01-11: A Randomized, Phase II Multicenter, Double-Blind, Placebo-Controlled Trial Evaluating MetMAb and/or Bevacizumab in Combination with Weekly Paclitaxel in Patients with Metastatic Triple-Negative Breast Cancer. *Cancer Res.* **2011**, 71.

52. Shipitsin, M.; Campbell, L. L.; Argani, P.; Weremowicz, S.; Bloushtain-Qimron, N.; Yao, J.; Nikolskaya, T.; Serebryiskaya, T.; Beroukhim, R.; Hu, M., Halushka, M. K. Molecular Definition of Breast Tumor Heterogeneity. *Cancer Cell* **2007***, 11*, 259–273.
53. Oettle, H.; Hilbig, A.; Seufferlein, T.; Luger, T.; Schmid, R. M.; Von Wichert, G.; Schmaus, S.; Heinrichs, H.; Schlingensiepen, K. Trabedersen (AP 12009) in the Treatment of Patients with Advanced Tumors: Completion of Dose-Escalation and First Efficacy Data. *J. Clin. Oncol.* **2010**, *28*, 2611.

Chapter 5

General Conclusions and Future Directions

5.1 General Conclusions

Cisplatin is an effective chemotherapeutic agent used in cancer patients to treat solid tumors ranging from ovarian, lung, head, and neck to testicular cancer. It contributes to the approximately 80% five-year survival rate for childhood cancer patients. Despite its effectiveness, cisplatin causes several toxicities, particularly ototoxicity which manifests as irreversible and bilateral sensorineural hearing loss. Hearing loss stems from apoptotic damage in the cochlea, where cisplatin has been shown to accumulate, particularly in the outer hair cells (OHC) of the Organ of Corti. Children showed greater risk for developing ototoxicity following cisplatin treatment than adults. Cisplatin-induced ototoxicity (CIO) can have life-long debilitating consequences in children by impairing speech and language development, social-emotional development and increasing the risk of learning difficulties. When childhood patients exhibit CIO, cisplatin doses are reduced, which compromises the anti-cancer efficacy. To date, limited success in otoprotection without compromised anticancer effect has been observed in clinical trials. Development of effective therapies for preventing hearing loss is therefore of primary importance. Studies from the lab of Dr. Amit Bhavsar (MMI) identified a significant and biologically plausible association between CIO susceptibility and expression of Toll-like receptor 4 (TLR4), an innate immune receptor protein. TLR4 is a transmembrane receptor protein present in OHC of Organ of Corti. It is a canonical receptor of lipopolysaccharide (LPS), a component of the outer membrane of gram-negative bacteria. It is found that cisplatin treatment induces TLR4 expression and TLR4 deletion causes decrease in CIO. From these data we identified TLR4 protein as a target to mitigate CIO.

Upon cisplatin treatment, Organ of Corti cell lines display key in vitro cisplatin ototoxic phenotypes such as increased pro-inflammatory IL-6 signalling, which can upregulate reactive oxygen species (ROS) generation that in turn, can lead to morphological and functional alterations, causing apoptotic cell death. A group at Takeda Pharmaceutical Company reported that the novel inhibitor TAK-242 inhibits

TLR4 signaling upon binding to the protein's intracellular domain. TAK-242 inhibits proinflammatory cytokine interleukin-6 secretion mediated by both LPS and cisplatin treatment.

Starting with the reference hit TAK-242, we used robust synthetic methods to probe the significance of various structural motifs through selective chemical modification of the TAK-242 scaffold in order to optimize binding to TLR4 as an otoprotection strategy. Robust in vitro cisplatin "ototoxicity" platforms were developed to assess the efficacy of synthesized TLR4 inhibitors in reducing cisplatin "ototoxicity" phenotypes. Promising small molecule candidates were tested in a zebrafish CIO model in vivo. Two of the new TAK-242 based derivatives were shown to have a potent inhibitory effect on CIO in both in vitro and in vivo experiments.

We carried out in silico docking studies with the synthesized inhibitors and TLR4 protein to interpret molecular interaction and refine the preferred structural features for effective inhibition. A detailed analysis of the predicted binding mode derived from molecular dynamics simulations was performed in order to further design in silico guided TLR4 inhibitors.

5.2 Future Directions

In a major part of this thesis, we focused on developing new TLR4 antagonists to inhibit cisplatin induced childhood ototoxicity and understanding the molecular interactions between the ligand and the target protein receptor through in silico studies. We believe this project will improve children's health in the immediate response to cisplatin therapy and reduce the severity of longer-term adverse health and psychosocial outcomes.

Future work is needed to explore a wider range of functional groups to be installed on the carboxylate group (**Figure 5.1**) via selective modifications such as amidation, reduction, etherification, esterification, etc. By doing these modifications, we will get a better understanding and deep insight about the structure activity relationship in order to identify an optimized lead compound. Furthermore, through previous mutational studies it has been hypothesized that TAK-242 binds covalently with the Cys747 of TLR4 receptor through Michael addition.[1] Therefore, modifying

the cyclohexane moiety of TAK-242 would affect the ability of the molecule to function as an electrophile.

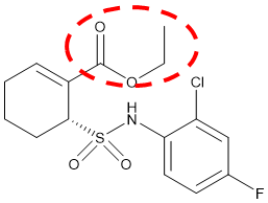

Figure 5.1. Structural modifications on TAK-242 for lead optimization.

Compounds **A3** and **A4** have shown potent inhibitory properties in both in vitro and in vivo studies. Furthermore, they also showed optimal binding affinities towards TLR4 receptor. Therefore, these two compounds can be modified further in order to maximize their potency. Some structures of possible lead compounds derived from **A3** and **A4** are shown in **Figure 5.2** which can be synthesized in future.

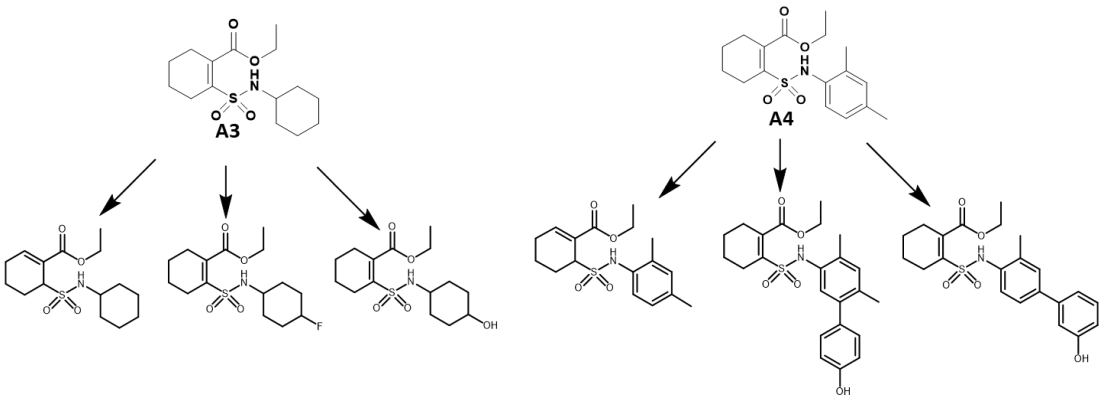

Figure 5.2. Structures of proposed lead compounds derived from the compounds **A3** and **A4**.

TAK-242 is known to interact with the cytosolic domain of the TLR4 to block the activation of the TLR4 adaptor proteins.[1] In our in silico studies we used the intracellular (TIR) domain of TLR4 dimer to investigate the structure activity relationship between the ligands and the binding domain of the receptor. From our in silico experiments we found that the C5 atom of TAK-242 would be involved in covalent bond-formation with Cys 747 was on average ~4 Å away from the S atom of Cys747 throughout last 20 ns (or 10000 frames) MD simulation time (**Figure 5.3**). Therefore, the future work should focus on implementing hybrid QM/MM (quantum

mechanics/molecular mechanics) approach using the full-length dimeric model of membrane-bound TLR4, which will allow study of the possibility for a covalent linkage between TAK-242 and TLR4 receptor in a more realistic in silico environment.

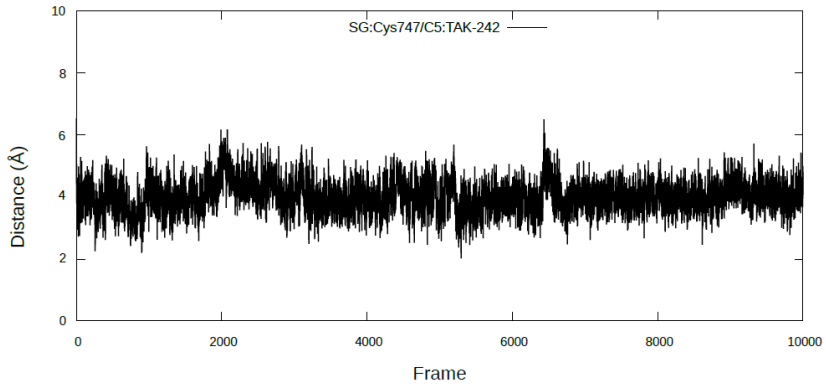

Figure 5.3. Distance between the C5 atom of TAK-242 and the S atom of C747 of TLR4-TIR domain.

To implicate the binding pocket experimentally, photoaffinity labeling (PAL) could be implemented which employs a photoreactive group and enrichment handle on the small molecule of interest. When irradiated with light, the photoaffinity probe covalently modifies nearby proteins, which can then be identified via protein enrichment and MS analysis (**Figure 5.4 a** and **b**).

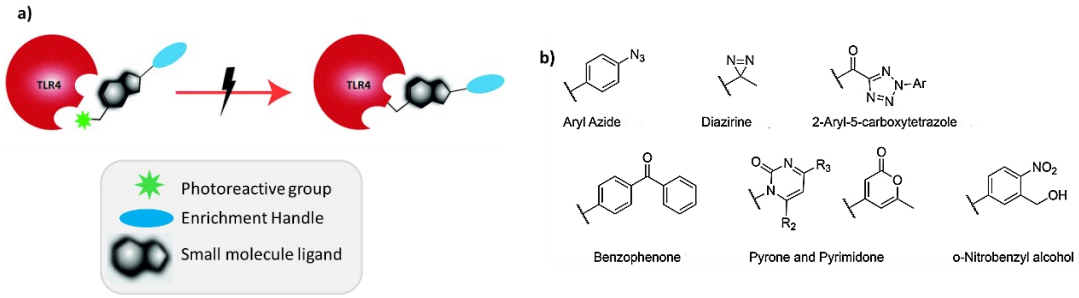

Figure 5.4. a) Workflow for photoaffinity labeling (PAL) between small molecule ligand (shown in black) and TLR4 receptor (shown in red). **b)** Structures of commonly used photoreactive groups. (Figure adapted with permission from Burton et al.[2])

Future work is still needed to validate the in vitro results of the active inhibitors by performing in vivo studies using humanized TLR4 transgenic zebra fish. Two transgenic lines, myo6b:CaMPARI and myo6b:Hsa.Tlr4 zebrafish were successfully

bred and grafted in the Allison Lab, UofA. The calcium-modulated photoactivatable radiometric integrator (CaMPARI) transgenic fish provides a way to monitor changes in intracellular calcium levels of the zebrafish hair cells.[3] CaMPARI is a green fluorescent protein that, when illuminated with UV light, converts to a bright red fluorescent species in high calcium conditions.[4] When applied alongside the TLR4 antagonists, CaMPARI transgenic fish will provide an objective measurement system for hair cell death. Human TLR4 transgenic fish will provide a more accurate model for cisplatin toxicity on human hair cells.

The involvement of the TLR4 signaling pathway in tumor drug resistance and metastasis has been studied by several groups. For example, the activation of the TLR4 signaling in human lung cancer cells causes the immune escape of tumor cells and apoptosis resistance by the production of immunosuppressive cytokines (TGF-β, VEGF, pro-angiogenic chemokine IL8).[5] Furthermore, LPS or paclitaxel mediated TLR4 signaling increased the resistance to drug-induced apoptosis in the SCOV3 ovarian cancer cell line.[6] The TLR4 expression in the breast (MCF7) and ovarian (2008C13) cancer cells increased after treatment with chemotherapeutic drugs (paclitaxel, cisplatin, doxorubicin, and arsenic trioxide). Interestingly, TAK-242 has been reported to enhance the chemosensitivity of these cell lines.[7] To evaluate the influence of our synthesized active TLR4 antagonists on the anti-cancer effect of cisplatin, ovarian lung, and breast cancer cell lines expressing TLR4 receptor will be co-treated with cisplatin and synthetic drug. DMF and TAK-242 will be used as controls. Annexin V/PI apoptosis test and MTT assay will be performed to study the apoptosis and cell viability. Cisplatin IC_{50} values will be determined as well in the presence of vehicle, or otoprotectant. The anti-tumor activity of cisplatin is based on its formation of intra-strand and inter-strand DNA crosslinks that activate multiple signal transduction pathways leading to cell-cycle arrest and programmed cell death.[8] Since TLR4 antagonists are not interfering with cisplatin-mediated DNA crosslink, we predict that TLR4 antagonists should not impact the anti-cancer properties of cisplatin.

In addition, finding an active targeting modality to selectively target TLR4 inhibitors to the ear hair cells is crucially required. The importance of this approach is to reduce the off-target toxicity of inhibitors, thus reducing a wide array of adverse

effects associated with such off-targeting. To address this issue, we need to implement targeted drug delivery approach.

The long-term plan of this research project is to gain a mechanistic understanding of the signaling pathways activated by cisplatin that contribute to hearing loss, and to exploit this knowledge to prevent hearing loss. To do this experiment in Dr. Bhavsar lab, HEI-OC1 cells will be pretreated with the compounds or TAK-242 before cisplatin or LPS stimulation at the early and late time points. Cells pretreated with DMF will be used as a control. Cell lysates will be used to monitor the phosphorylation of downstream pathways using rapid-robotic phosphoproteomics (R2-P2) method[9] in collaboration with Dr. Olivier Julien's group or western blot analysis.

Our collaborator, Dr. Amit Bhavsar at the Department of MMI, University of Alberta, will use a functional genomic strategy to identify CIO genes, which is important because TLR4 may only partially contribute to CIO, and because other CIO genes could be better targets for otoprotectant development.

5.3 References

1. Takashima, K.; Matsunaga, N.; Yoshimatsu, M.; Hazeki, K.; Kaisho, T.; Uekata, M.; Hazeki, O.; Akira, S.; Iizawa, Y.; Ii, M. Analysis of Binding Site for the Novel Small-Molecule TLR4 Signal Transduction Inhibitor TAK-242 and Its Therapeutic Effect on Mouse Sepsis Model. *Br. J. Pharmacol.* **2009**, *157*, 1250–1262.
2. Burton, N.R.; Kim, P.; Backus, K. M. Photoaffinity Labelling Strategies for Mapping the Small Molecule–Protein Interactome. *Org. Biomol. Chem.* **2021**, *19*, 7792–7809.
3. Kettunen, P. Calcium Imaging in the Zebrafish. *Calcium Signal.* **2012**, *740*, 1039–1071.
4. Ebner, C.; Ledderose, J.; Zolnik, T. A.; Dominiak, S. E.; Turko, P.; Papoutsi, A.; Poirazi, P.; Eickholt, B. J.; Vida, I.; Larkum, M. E.; Sachdev, R. N. Optically Induced Calcium-dependent Gene Activation and Labeling of Active Neurons Using CaMPARI and Cal-light. *Front. Synaptic Neurosci*. **2019**, *11*, 1–16.
5. He, W.; Liu, Q.; Wang, L.; Chen, W.; Li, N.; Cao, X. TLR4 Signaling Promotes Immune Escape of Human Lung Cancer Cells by Inducing Immunosuppressive Cytokines and Apoptosis Resistance. *Mol. Immunol.* **2007**, *44*, 2850–2859.
6. Szajnik, M.; Szczepanski, M. J.; Czystowska, M.; Elishaev, E.; Mandapathil, M.; Nowak-Markwitz, E.; Spaczynski, M.; Whiteside, T. L. TLR4 Signaling Induced by Lipopolysaccharide or Paclitaxel Regulates Tumor Survival and Chemoresistance in Ovarian Cancer. *Oncogene*. **2009**, *28*, 4353–4363.
7. Kashani, B.; Zandi, Z.; Karimzadeh, M. R.; Bashash, D.; Nasrollahzadeh, A.; Ghaffari, S. H., 2019. Blockade of TLR4 using TAK-242 (Resatorvid) Enhances Anti-cancer Effects of Chemotherapeutic Agents: A Novel Synergistic Approach for Breast and Ovarian Cancers. *Immunol. Res.* **2019**, *67*, 505–516.
8. Siddik, Z. H. Cisplatin: Mode of Cytotoxic Action and Molecular Basis of Resistance. *Oncogene*. **2003**, *47*, 7265–7279.
9. Leutert, M.; Rodríguez-Mias; R. A.; Fukuda, N. K.; Villén, J. R2-P2 Rapid-robotic Phosphoproteomics Enables Multidimensional Cell Signaling Studies. *Mol. Syst. Biol.* **2019**, *15*, 9021–9041.

Compiled References

Chapter 1

1. Dasari, S.; Paul, B. T. Cisplatin in Cancer Therapy: Molecular Mechanisms of Action. *Eur. J. Pharmacol.* **2014**, *740*, 364–378.
2. Siddik, Z. H. Cisplatin: Mode of Cytotoxic Action and Molecular Basis of Resistance. *Oncogene*. **2003**, *47*, 7265–7279.
3. Rocha, C. R. R.; Silva, M. M.; Quinet, A.; Cabral–Neto, J. B.; Menck, C. F. M. DNA Repair Pathways and Cisplatin Resistance: An Intimate Relationship. *Clinics.* **2018**, *73*, 1–10.
4. Khan, M. Z.; Rayaan, F. Contrast–Induced Nephropathy. *J. Med. Sci.* **2018**, *26*, 79–84.
5. Breglio, A. M.; Aaron, E. R.; Eric, D. S.; Katharine, A. F.; Katie K. S.; Katherine, M. M.; Matthew, D. H.; Lauren, A.; Lisa, L. C. Cisplatin is Retained in the Cochlea Indefinitely Following Chemotherapy. *Nat. Commun.* **2017**, *8*, 1–9.
6. Blair, J. C. The Effects of Mild Sensorineural Hearing Loss on Academic Performance of Young School–Age Children. *Volta Rev.* **1985**, *87*, 87–93.
7. Gurney, J. G.; Kevin, R. K., Nina, K. H.; Stacy, N.; Paul, C. N.; Brad, Z.; Jean, M. T.; Kirsten, K. N. Social Outcomes in the Childhood Cancer Survivor Study Cohort. *J. Clin. Oncol*. **2009**, *27*, 2390–2405.
8. Gurney, J. G.; Jean, M. T.; Kirsten, K. N.; Wendy, L.; Katherine. K. M.; Mary, L. S. Hearing Loss, Quality of Life, and Academic Problems in Long–Term Neuroblastoma Survivors: A Report from the Children's Oncology Group. *Pediatrics.* **2007**, *120*, 1229–1236.
9. Chu, Y.; Martha, S.; Jorge, O. E.; Amanda, R. P. D.; Thomas, D.; Qi, W.; Martina, R.; Peter, S. S.; Robert, M. S. Systemic Delivery and Biodistribution of Cisplatin In Vivo. *Mol. Pharm.* **2016**, *13*, 2677–2682.
10. Mukherjea, D.; Sarvesh, J.; Craig, W.; Jennifer, R. B.; Jeremy, G. T.; Leonard, P. R.; Vickram, R. Short Interfering RNA Against Transient Receptor Potential Vanilloid 1 Attenuates Cisplatin–Induced Hearing Loss in the Rat. *J. Neurosci.* **2008**, *28*, 13056–13065.
11. Chang, K. W.; Chinosornvatana, N. 2010. Practical Grading System for Evaluating Cisplatin Ototoxicity in Children. *J. Clin. Oncol*. **2010**, *28*,1788–1795.
12. Langer, T.; Zehnhoff–Dinnesen, A.; Radtke, S.; Meitert, J.; Zolk, O. Understanding Platinum–Induced Ototoxicity. *Trends Pharmacol. Sci.* **2013**, *34,* 458–469.
13. Schell, M. J.; McHaney, V. A.; Green, A. A.; Kun, L. E.; Hayes, F. A.; Horowitz, M.; Meyer, W. H. Hearing Loss in Children and Young Adults Receiving Cisplatin with or without Prior Cranial Irradiation. *J. Clin. Oncol*, **1989**, *7*, 754–760.
14. Ross, C. J.; Katzov–Eckert, H.; Dubé, M. P.; Brooks, B.; Rassekh, S. R.; Barhdadi, A.; Feroz–Zada, Y.; Visscher, H.; Brown, A. M.; Rieder, M. J.; Rogers, P. C. 2009. Genetic Variants in

TPMT and COMT are Associated with Hearing Loss in Children Receiving Cisplatin Chemotherapy. *Nat. Genet.* **2009**, *41*,1345–1349.

15. Travis, L. B.; Fossa, S. D.; Sesso, H. D.; Frisina, R. D.; Herrmann, D. N.; Beard, C. J.; Feldman, D. R.; Pagliaro, L. C.; Miller, R. C.; Vaughn, D. J.; Einhorn, L. H. Chemotherapy–Induced Peripheral Neurotoxicity and Ototoxicity: New Paradigms for Translational Genomics. *J. Natl. Cancer Inst*. **2014**, *106,* 1–13.
16. Hudson, M. M.; Ness, K. K.; Gurney, J. G.; Mulrooney, D. A.; Chemaitilly, W.; Krull, K. R.; Green, D. M.; Armstrong, G. T.; Nottage, K. A.; Jones, K. E.; Sklar, C. A. Clinical Ascertainment of Health Outcomes Among Adults Treated for Childhood Cancer. *Jama*. **2013**, *309*, 2371–2381.
17. Dionne, F.; Mitton, C.; Rassekh, R.; Brooks, B.; Ross, C.; Hayden, M., Carleton, B. Economic Impact of a Genetic Test for Cisplatin–Induced Ototoxicity. *Pharmacogenomics J*. **2012**, *12*, 205–213.
18. Lim, D. J. Functional Structure of The Organ of Corti: A Review. *Hear. Res*. **1986**, *22*, 117–146.
19. Schellack, N.; Naude, A. An Overview of Pharmacotherapy–Induced Ototoxicity. *S. Afr. Fam. Pract.* **2013**, *55*, 357–366.
20. Kopke, R.; Allen, K. A., Henderson, D.; Hoffer, M.; Frenz, D.; Van De Water, T. A Radical Demise: Toxins and Trauma Share Common Pathways in Hair Cell Death. *Ann. N. Y. Acad. Sci*. **1999**, *884*, 171–191.
21. Ford, M. S.; Maggirwar, S. B.; Rybak, L. P.; Whitworth, C.; Ramkumar, V. Expression and Function of Adenosine Receptors in the Chinchilla Cochlea. *Hear. Res*. **1997**, *105*, 130–140.
22. Oh, S. H.; Yu, W. S.; Song, B. H.; Lim, D.; Koo, J. W.; Chang, S. O.; Kim, C. S. Expression of Heat Shock Protein 72 in Rat Cochlea with Cisplatin–Induced Acute Ototoxicity. *Acta Oto-laryngologica*. **2000**, *120*, 146–150.
23. Mukherjea, D.; Whitworth, C. A.; Nandish, S.; Dunaway, G. A.; Rybak, L. P.; Ramkumar, V. Expression of the Kidney Injury Molecule 1 in the Rat Cochlea and Induction by Cisplatin. *Neurosci. J.* **2006**, *139*, 733–740.
24. So, H. S.; Kim, H. J.; Lee, J. H.; Park, S. Y.; Park, C.; Kim, Y. H.; Kim, J. K.; Lee, K. M.; Kim, K. S.; Chung, S. Y.; Jang, W. C. Flunarizine Induces Nrf2–Mediated Transcriptional Activation of Heme Oxygenase–1 in Protection of Auditory Cells from Cisplatin. *Cell Death Differ*. **2006**, *13*, 1763–1775.
25. Clerici, W. J.; Yang, L. Direct Effects of Intraperilymphatic Reactive Oxygen Species Generation on Cochlear Function. *Hear. Res*. **1996**, *101*, 14–22.
26. Kopke, R. D.; Liu, W.; Gabaizadeh, R.; Jacono, A.; Feghali, J. Use of Organotypic Cultures of Corti's Organ to Study the Protective Effects of Antioxidant Molecules on Cisplatin–Induced Damage of Auditory Hair Cells. *An. J. Otol*. **1997**, *18*, 559–571.

27. Church, M. W.; Kaltenbach, J. A.; Blakley, B. W.; Burgio, D. L. The Comparative Effects of Sodium Thiosulfate, Diethyldithiocarbamate, Fosfomycin and WR–2721 on Ameliorating Cisplatin–Induced Ototoxicity. *Hear. Res*. **1995**, *86*, 195–203.
28. Rybak, L. P.; Ravi, R.; Somani, S. M. Mechanism of Protection by Diethyldithiocarbamate Against Cisplatin Ototoxicity: Antioxidant System. *Fundam. Appl. Toxicol.* **1995**, *26*, 293–300.
29. Kim, H. J.; Lee, J. H.; Kim, S. J.; Oh, G. S.; Moon, H. D.; Kwon, K. B.; Park, C.; Park, B. H.; Lee, H. K.; Chung, S. Y.; Park, R. Roles of NADPH Oxidases in Cisplatin–Induced Reactive Oxygen Species Generation and Ototoxicity. *J. Neurosci*. **2010**, *30*, 3933–3946.
30. Ravi, R.; Somani, S. M.; Rybak, L. P. Mechanism of Cisplatin Ototoxicity: Antioxidant System. *Pharmacol. Toxicol*. **1995**, *76*, 386–394.
31. So, H.; Kim, H.; Lee, J. H.; Park, C.; Kim, Y.; Kim, E.; Kim, J. K.; Yun, K. J.; Lee, K. M.; Lee, H. Y.; Moon, S. K. Cisplatin Cytotoxicity of Auditory Cells Requires Secretions of Proinflammatory Cytokines Via Activation of ERK and NF–κ B. *J. Assoc. Res. Otolaryngol*. **2007**, *8*, 338–355.
32. Ruijven, M. W.; Groot, J. C.; Smoorenburg, G. F. Time Sequence of Degeneration Pattern in the Guinea Pig Cochlea During Cisplatin Administration.: A Quantitative Histological Study. *Hear. Res*. **2004**, *197*, 44–54.
33. Thomas, A. J.; Hailey, D.W.; Stawicki, T. M.; Wu, P.; Coffin, A. B.; Rubel, E. W.; Raible, D.W.; Simon, J. A., Ou, H. C. Functional Mechanotransduction Is Required for Cisplatin–Induced Hair Cell Death in the Zebrafish Lateral Line. *J. Neurosci*. **2013**, *33*, 4405–4414.
34. Rybak, L. P.; Whitworth, C. A.; Mukherjea, D.; Ramkumar, V. Mechanisms of Cisplatin–Induced Ototoxicity and Prevention. *Hear. Res*. **2007**, *226*, 157–167.
35. Dickey, D. T.; Muldoon, L. L.; Doolittle, N. D.; Peterson, D. R.; Kraemer, D. F.; Neuwelt, E. A. Effect of N–acetylcysteine Route of Administration on Chemoprotection Against Cisplatin–Induced Toxicity in Rat Models. *Cancer Chemother. Pharmacol.* **2008**, *62*, 235–241.
36. Choe, W. T.; Chinosornvatana, N.; Chang, K. W. Prevention of Cisplatin Ototoxicity Using Transtympanic N–Acetylcysteine and Lactate. *Otol. Neurotol.* **2004**, *25*, 910–915.
37. Otto, W. C.; Brown, R. D.; Gage–White, L.; Kupetz, S.; Anniko, M.; Penny, J. E.; Henley, C. M. Effects of Cisplatin and Thiosulfate Upon Auditory Brainstem Responses of Guinea Pigs. *Hear. Res*, **1988**, *35*, 79–85.
38. Wimmer, C.; Mees, K.; Stumpf, P.; Welsch, U.; Reichel, O.; Suckfüll, M. Round Window Application of D–methionine, Sodium Thiosulfate, Brain–Derived Neurotrophic Factor, and Fibroblast Growth Factor–2 in Cisplatin–Induced Ototoxicity. *Otol. Neurotol.* **2004**, *25*, 33–40.
39. Church, M. W.; Blakley, B. W.; Burgio, D. L.; Gupta, A. K. WR–2721 (Amifostine) Ameliorates Cisplatin–Induced Hearing Loss but Causes Neurotoxicity in Hamsters: Dose–Dependent Effects. *J. Assoc. Res. Otolaryngol*. **2004**, *5*, 227–237.

40. Ekborn, A.; Laurell, G.; Johnström, P.; Wallin, I.; Eksborg, S.; Ehrsson, H. D–Methionine and Cisplatin Ototoxicity in the Guinea Pig: D–Methionine Influences Cisplatin Pharmacokinetics. *Hear. Res*. **2002**, *165,* 53–61.
41. Marina, N.; Chang, K. W.; Malogolowkin, M.; London, W. B.; Frazier, A. L.; Womer, R. B.; Rescorla, F.; Billmire, D. F.; Davis, M. M.; Perlman, E. J.; Giller, R. Amifostine Does Not Protect Against the Ototoxicity of High-Dose Cisplatin Combined with Etoposide and Bleomycin in Pediatric Germ-Cell Tumors: A Children's Oncology Group Study. *Cancer*. **2005**, *104*, 841–847
42. Sastry, J.; Kellie, S. J. Severe Neurotoxicity, Ototoxicity and Nephrotoxicity Following High–Dose Cisplatin and Amifostine. *Pediatr. Hematol. Oncol.* **2005***, 22*, 441–445.
43. More, S. S.; Akil, O.; Ianculescu, A. G.; Geier, E. G.; Lustig, L. R.; Giacomini, K. M. Role of the Copper Transporter, CTR1, in Platinum–Induced Ototoxicity. *J. Neurosci*. **2010**, *30*, 9500–9509.
44. Lanvers–Kaminsky, C.; Sprowl, J. A.; Malath, I.; Deuster, D.; Eveslage, M.; Schlatter, E.; Mathijssen, R. H.; Boos, J.; Jürgens, H.; am Zehnhoff–Dinnesen, A. G.; Sparreboom, A. Human OCT2 Variant c.808G> T Confers Protection Effect Against Cisplatin–Induced Ototoxicity. *Pharmacogenomics J*. **2015**, *16*, 323–332.
45. Freyer, D. R.; Chen, L.; Krailo, M. D.; Knight, K.; Villaluna, D.; Bliss, B.; Pollock, B. H.; Ramdas, J.; Lange, B.; Van Hoff, D.; VanSoelen, M. L. Effects of Sodium Thiosulfate Versus Observation on Development of Cisplatin–Induced Hearing Loss in Children with Cancer (ACCL0431): A Multicentre, Randomised, Controlled, Open–Label, Phase 3 Trial. *Lancet Oncol.* **2017**, *18*, 63–74.
46. Mukherjea, D.; Rybak, L. P. Pharmacogenomics of Cisplatin–Induced Ototoxicity. *Pharmacogenomics J*. **2011**, *12*, 1039–1050.
47. Lee, J. W.; Pussegoda, K.; Rassekh, S. R.; Monzon, J. G.; Liu, G.; Hwang, S.; Bhavsar, A. P.; Pritchard, S.; Ross, C. J.; Amstutz, U.; Carleton, B. C. Clinical Practice Recommendations for the Management and Prevention of Cisplatin–Induced Hearing Loss Using Pharmacogenetic Markers. *Ther. Drug Monit.* **2016**, *38*, 423–431.
48. Pussegoda, K.; Ross, C. J.; Visscher, H.; Yazdanpanah, M.; Brooks, B.; Rassekh, S. R.; Zada, Y. F.; Dubé, M. P.; Carleton, B. C.; Hayden, M. R. Replication of TPMT and ABCC3 Genetic Variants Highly Associated with Cisplatin-Induced Hearing Loss in Children. *Clin. Pharm. Therap.* **2013**, *94*, 243–251.
49. Maranville, J. C.; Cox, N. J. Pharmacogenomic Variants have Larger Effect Sizes Than Genetic Variants Associated with Other Dichotomous Complex Traits. *Pharmacogenomics J*. **2016**, *16*, 388–392.

50. Bhavsar, A. P.; Gunaretnam, E. P.; Li, Y.; Hasbullah, J. S.; Carleton, B. C.; Ross, C. J. Pharmacogenetic Variants in TPMT Alter Cellular Responses to Cisplatin in Inner Ear Cell Lines. *PloS one*. **2017**, *12*, 711–727.
51. Oh, G. S.; Kim, H. J.; Choi, J. H.; Shen, A.; Kim, C. H.; Kim, S. J.; Shin, S. R.; Hong, S. H.; Kim, Y.; Park, C.; Lee, S. J. Activation of Lipopolysaccharide–TLR4 Signaling Accelerates the Ototoxic Potential of Cisplatin in Mice. *J. Immunol.* **2011**, *186*, 1140–1150.
52. Kalinec, G. M.; Webster, P.; Lim, D. J.; Kalinec, F. A Cochlear Cell Line as an In Vitro System for Drug Ototoxicity Screening. *Audiol. Neurootol.* **2003**, *8*, 177–189.
53. Ragnarsdottir, B.; Jönsson, K.; Urbano, A.; Grönberg–Hernandez, J.; Lutay, N.; Tammi, M.; Gustafsson, M.; Lundstedt, A. C.; Leijonhufvud, I.; Karpman, D.; Wullt, B. Toll–Like Receptor 4 Promoter Polymorphisms: Common TLR4 Variants May Protect Against Severe Urinary Tract Infection. *PloS one*. **2010**, *5*, 10734–10751.
54. Faure, E.; Thomas, L.; Xu, H.; Medvedev, A. E.; Equils, O.; Arditi, M. Bacterial Lipopolysaccharide and IFN–α Induce Toll–Like Receptor 2 and Toll–Like Receptor 4 Expression in Human Endothelial Cells: Role Of NF–κB Activation. *J. Immunol.* **2001**, *166*, 2018–2024.
55. Muzio, M.; Bosisio, D.; Polentarutti, N.; D'amico, G.; Stoppacciaro, A.; Mancinelli, R.; van't Veer, C.; Penton–Rol, G.; Ruco, L. P.; Allavena, P.; Mantovani, A. Differential Expression and Regulation of Toll–Like Receptors (TLR) in Human Leukocytes: Selective Expression of TLR3 in Dendritic Cells. *J. Immunol.* **2000**, *164*, 5998–6004.
56. Babolmorad, G.; Latif, A.; Domingo, I. K.; Pollock, N. M.; Delyea, C.; Rieger, A. M.; Allison, W. T.; Bhavsar, A. P. Toll-Like Receptor 4 is Activated by Platinum and Contributes to Cisplatin-Induced Ototoxicity. *EMBO Rep*. **2021**, *22*, 51280–51298.
57. Kawasaki, T.; Kawai, T. Toll–Like Receptor Signaling Pathways. *Front. Immunol.* **2014**, *5*, 461–478.
58. Salaun, B.; Romero, P.; Lebecque, S. Toll-Like Receptors' Two-Edged Sword: When Immunity Meets Apoptosis. *Eur. J. Immunol*. **2007***, 37*, 3311–3318.
59. Wardill, H. R.; Van Sebille, Y. Z.; Mander, K. A.; Gibson, R. J.; Logan, R. M.; Bowen, J. M.; Sonis, S. T. Toll–Like Receptor 4 Signaling: A Common Biological Mechanism of Regimen–Related Toxicities: An Emerging Hypothesis for Neuropathy and Gastrointestinal Toxicity. *Cancer Treat. Rev.* **2005**, *41*, 122–128.
60. Park, B. S.; Lee, J. O. Recognition of Lipopolysaccharide Pattern by TLR4 Complexes. *Exp. Mol. Med.* **2013**, *45*, 66–76.
61. Singh, A.; Singh, V.; Tiwari, R. L.; Chandra, T.; Kumar, A.; Dikshit, M.; Barthwal, M. K. The IRAK–ERK–P67phox–Nox–2 Axis Mediates TLR4, 2–Induced ROS Production For IL–1 B Transcription and Processing in Monocytes. *Cell. Mol. Immunol.* **2016**, *13*, 745–763.

62. West, A. P.; Brodsky, I. E.; Rahner, C.; Woo, D. K.; Erdjument–Bromage, H.; Tempst, P.; Walsh, M. C.; Choi, Y.; Shadel, G. S.; Ghosh, S. TLR Signalling Augments Macrophage Bactericidal Activity Through Mitochondrial ROS. *Nature*, **2011**, *472*, 476–480.
63. Haase, R.; Kirschning, C. J.; Sing, A.; Schröttner, P.; Fukase, K.; Kusumoto, S.; Wagner, H.; Heesemann, J.; Ruckdeschel, K. A Dominant Role of Toll–Like Receptor 4 in the Signaling of Apoptosis in Bacteria–Faced Macrophages. *J. Immunol.* **2003**, *171*, 4294–4303.
64. Jalleh, R.; Koh, K.; Choi, B.; Liu, E.; Maddison, J.; Hutchinson, M. R. Role of Microglia and Toll–Like Receptor 4 in the Pathophysiology of Delirium. *Med. Hypotheses.* **2012**, *79*, 735–739.
65. Kalinec, G.; Thein, P.; Park, C.; Kalinec, F. HEI–OC1 Cells as a Model for Investigating Drug Cytotoxicity. *Hear. Res*. **2016**, *335*, 105–117.
66. Kaur, T.; Mukherjea, D.; Sheehan, K.; Jajoo, S.; Rybak, L. P.; Ramkumar, V. Short Interfering RNA Against STAT1 Attenuates Cisplatin–Induced Ototoxicity in The Rat by Suppressing Inflammation. *Cell Death Dis.* **2011**, *2*, 180–190.
67. Rivolta, M. N.; Holley, M. C. Cell Lines in Inner Ear Research. *J. Neurobiol.* **2002**, *53*, 306–318.
68. Ohnishi, H.; Skerleva, D.; Kitajiri, S. I.; Sakamoto, T.; Yamamoto, N.; Ito, J.; Nakagawa, T. Limited Hair Cell Induction from Human Induced Pluripotent Stem Cells Using a Simple Stepwise Method. *Neurosci. J. Letters*. **2015**, *599*, 49–54.
69. Oshima, K.; Shin, K.; Diensthuber, M.; Peng, A. W.; Ricci, A. J., Heller, S. Mechanosensitive Hair Cell–Like Cells from Embryonic and Induced Pluripotent Stem Cells. *Cell*. **2010**, *141*, 704–716.
70. Devarajan, P.; Savoca, M.; Castaneda, M. P.; Park, M. S.; Esteban-Cruciani, N.; Kalinec, G.; Kalinec, F. Cisplatin-Induced Apoptosis in Auditory Cells: Role of Death Receptor and Mitochondrial Pathways. *Hear. Res*. **2002**, *174*, 45–54.
71. Kalinec, F.; Kalinec, G.; Boukhvalova, M., Kachar, B. Establishment and Characterization of Conditionally Immortalized Organ of Corti Cell Lines. *Cell Biol. Int.* **1999***, 23*, 175–184.
72. So, H.; Kim, H.; Kim, Y.; Kim, E.; Pae, H. O.; Chung, H. T.; Kim, H. J.; Kwon, K. B.; Lee, K. M.; Lee, H. Y.; Moon, S. K. Evidence that Cisplatin–Induced Auditory Damage is Attenuated by Downregulation of Pro–Inflammatory Cytokines via Nrf2/HO–1. *J. Assoc. Res. Otolaryngol*, **2008**, *9*, 290–306.
73. Yin, H.; Sun, G.; Yang, Q.; Chen, C.; Qi, Q.; Wang, H.; Li, J. NLRX1 Accelerates Cisplatin–Induced Ototoxity in HEI–OC1 Cells via Promoting Generation of ROS and Activation of JNK Signaling Pathway. *Sci. Rep*. **2017**, *7*, 1–14.
74. Ton, C.; Parng, C. The Use of Zebrafish for Assessing Ototoxic and Otoprotective Agents. *Hear. Res*. **2005**, *208*, 79–88.

75. Kari, G.; Rodeck, U.; Dicker, A. P. Zebrafish: An Emerging Model System for Human Disease and Drug Discovery. *Clin. Pharm. Therap.* **2007**, *82*, 70–80.
76. Ou, H. C.; Raible, D. W.; Rubel, E. W. Cisplatin–Induced Hair Cell Loss in Zebrafish (Danio Rerio) Lateral Line. *Hear. Res*. **2007**, *233*, 46–53.
77. Uribe, P. M.; Mueller, M. A.; Gleichman, J. S.; Kramer, M. D.; Wang, Q.; Sibrian–Vazquez, M.; Strongin, R. M.; Steyger, P. S.; Cotanche, D. A.; Matsui, J. I. Dimethyl Sulfoxide (DMSO) Exacerbates Cisplatin–Induced Sensory Hair Cell Death in Zebrafish (Danio Rerio). *PLoS One*. **2013**, *8*, 55359–55370.
78. Coffin, A. B.; Ramcharitar, J. Chemical Ototoxicity of the Fish Inner Ear and Lateral Line. *Fish Hearing and Bioacoustics*. **2016**, 419–437.
79. Sepulcre, M. P.; Alcaraz–Pérez, F.; López–Muñoz, A.; Roca, F. J.; Meseguer, J.; Cayuela, M. L.; Mulero, V. Evolution of Lipopolysaccharide (LPS) Recognition and Signaling: Fish TLR4 Does Not Recognize LPS and Negatively Regulates NF–κB Activation. *J. Immunol.* **2009**, *182*, 1836–1845.
80. He, Q.; Zhang, C.; Wang, L.; Zhang, P.; Ma, D.; Lv, J.; Liu, F. Inflammatory Signaling Regulates Hematopoietic Stem and Progenitor Cell Emergence in Vertebrates. *Am. J. Hematol*. **2015**, *125*, 1098–1106.
81. Chang, M. Y.; Cheng, Y. C.; Hsu, S. H.; Ma, T. L.; Chou, L. F.; Hsu, H. H.; Tian, Y. C.; Chen, Y. C.; Sun, Y. J.; Hung, C. C.; Pan, R. L. Leptospiral Outer Membrane Protein Lipl32 Induces Inflammation and Kidney Injury in Zebrafish Larvae. *Sci. Rep.* **2016**. *6*, 1–12.
82. Yamada, M.; Ichikawa, T.; Ii, M.; Sunamoto, M.; Itoh, K.; Tamura, N.; Kitazaki, T. Discovery of Novel and Potent Small–Molecule Inhibitors of NO And Cytokine Production as Antisepsis Agents: Synthesis and Biological Activity of Alkyl 6– (N–Substituted Sulfamoyl) Cyclohex–1–Ene–1–Carboxylate. *J. Med. Chem.* **2005**, *48*, 7457–7467.
83. Jackson, P. A.; Widen, J. C.; Harki, D. A.; Brummond, K. M. 2017. Covalent Modifiers: A Chemical Perspective on the Reactivity of α, β–unsaturated Carbonyls with Thiols via Hetero–Michael Addition Reactions. *J. Med. Chem.* **2017**, *60*, 839–885.
84. Patra, M. C.; Choi, S. Recent Progress in The Development of Toll–Like Receptor (TLR) Antagonists. *Expert. Opin. Ther. Pat*. **2016**, *26*, 719–730.
85. Bhattacharyya, S.; Wang, W.; Tamaki, Z.; Shi, B.; Yeldandi, A.; Tsukimi, Y.; Yamasaki, M.; Varga, J. Pharmacological Inhibition of Toll–Like Receptor–4 Signaling by TAK242 Prevents and Induces Regression of Experimental Organ Fibrosis. *Front. Immunol.* **2018**, *9*, 2434–2448.
86. Medzhitov, R.; Preston–Hurlburt, P.; Janeway, C. A. A Human Homologue of The Drosophila Toll Protein Signals Activation of Adaptive Immunity. *Nature*. **2018**, *388*, 394–397.
87. Krishnan, J.; Anwar, M. A.; Choi, S. TLR4 (Toll–Like Receptor 4). *Journal: Encyclopedia of Signaling Molecules*. **2018**, 5472–5483.

88. Mineev, K. S.; Goncharuk, S. A.; Goncharuk, M. V.; Volynsky, P. E.; Novikova, E. V.; Aresinev, A. S., 2017. Spatial Structure of TLR4 Transmembrane Domain in Bicelles Provides the Insight into the Receptor Activation Mechanism. *Sci. Rep.* **2017**, *7*, 1–12.
89. Park, B. S.; Song, D. H.; Kim, H. M.; Choi, B. S.; Lee, H.; Lee, J. O. The Structural Basis of Lipopolysaccharide Recognition by the TLR4–MD–2 Complex. *Nature*. **2009**, *458*, 1191–1195.
90. Patra, M. C.; Kwon, H. K.; Batool, M.; Choi, S. Computational Insight into the Structural Organization of Full–Length Toll–Like Receptor 4 Dimer in a Model Phospholipid Bilayer. *Front. Immunol.* **2018***, 9*, 489–502.
91. Takashima, K.; Matsunaga, N.; Yoshimatsu, M.; Hazeki, K.; Kaisho, T.; Uekata, M.; Hazeki, O.; Akira, S.; Iizawa, Y.; Ii, M. Analysis of Binding Site for the Novel Small-Molecule TLR4 Signal Transduction Inhibitor TAK-242 and Its Therapeutic Effect on Mouse Sepsis Model. *Br. J. Pharmacol*. **2009**, *157*, 1250–1262.
92. Dragovich, P. S.; Webber, S. E.; Babine, R. E.; Fuhrman, S. A.; Patick, A. K.; Matthews, D. A.; Reich, S. H.; Marakovits, J. T.; Prins, T. J.; Zhou, R.; Tikhe, J. Structure–Based Design, Synthesis, and Biological Evaluation of Irreversible Human Rhinovirus 3C Protease Inhibitors. 2. Peptide Structure− Activity Studies. *J. Med. Chem.* **1998**, *41*, 2819–2834.
93. Zhu, S.; Hudson, T. H.; Kyle, D. E.; Lin, A. J. Synthesis and In Vitro Studies of Novel Pyrimidinyl Peptidomimetics as Potential Antimalarial Therapeutic Agents. *J. Med. Chem.* **2002**, *45*, 3491–3496.
94. Matthews, D. A.; Dragovich, P. S.; Webber, S. E.; Fuhrman, S. A.; Patick, A. K.; Zalman, L. S.; Hendrickson, T. F.; Love, R. A.; Prins, T. J.; Marakovits, J. T.; Zhou, R. Structure–Assisted Design of Mechanism–Based Irreversible Inhibitors of Human Rhinovirus 3C Protease with Potent Antiviral Activity Against Multiple Rhinovirus Serotypes. *Proc. Natl. Acad. Sci*. **1999**, *96*, 11000–11007.
95. Kong, W., Merino, E. and Nevado, C., 2014. Arylphosphonylation and arylazidation of activated alkenes. *Angewandte Chemie International Edition*, *53*(20), pp.5078–5082.
96. Liu, R.; Yue, Z.; Tsai, C. C.; Shen, J. Assessing Lysine and Cysteine Reactivities for Designing Targeted Covalent Kinase Inhibitors. *J. Am. Chem. Soc.* **2019**, *141*, 6553–6560.
97. Pettinger, J.; Carter, M.; Jones, K.; Cheeseman, M. D. Kinetic Optimization of Lysine–Targeting Covalent Inhibitors of HSP72. *J. Med. Chem.* **2019**, *62*, 11383–11398.
98. Zhang, T.; Hatcher, J. M.; Teng, M.; Gray, N. S.; Kostic, M. Recent Advances in Selective and Irreversible Covalent Ligand Development and Validation. *Cell Chem. Biol*. **2019**, *26*, 1486–1500.
99. Cheng, S. S.; Yang, G. J.; Wang, W.; Leung, C. H.; Ma, D. L. The Design and Development of Covalent Protein–Protein Interaction Inhibitors for Cancer Treatment. *J. Hematol. Oncol.* **2020**, *13*, 1–14.

100. Butler, K.V.; Ma, A.; Yu, W.; Li, F.; Tempel, W.; Babault, N.; Pittella–Silva, F.; Shao, J.; Wang, J.; Luo, M.; Vedadi, M. Structure–Based Design of a Covalent Inhibitor of the SET Domain–Containing Protein 8 (SETD8) Lysine Methyltransferase. *J. Med. Chem.* **2016**, *59*, 9881–9889.

Chapter 2

1. Takashima, K.; Matsunaga, N.; Yoshimatsu, M.; Hazeki, K.; Kaisho, T.; Uekata, M.; Hazeki, O.; Akira, S.; Iizawa, Y.; Ii, M. Analysis of Binding Site for the Novel Small-Molecule TLR4 Signal Transduction Inhibitor TAK-242 and Its Therapeutic Effect on Mouse Sepsis Model. *Br. J. Pharmacol.* **2009**, *157*, 1250–1262.
2. Yamada, M.; Ichikawa, T.; Ii, M.; Itoh, K.; Tamura, N.; Kitazaki, T. Novel Cyclohexene Derivatives as Anti-Sepsis Agents: Synthetic Studies and Inhibition of NO and Cytokine Production. *Bioorg. Med. Chem.* **2008**, *16*, 3941–3958.
3. Blair, J. C. The Effects of Mild Sensorineural Hearing Loss on Academic Performance of Young School-Age Children. *Volta Rev.* **1985**, *87*, 87–93.
4. Gurney, J. G.; Tersak, J. M.; Ness, K. K.; Landier, W.; Matthay, K. K.; Schmidt, M. L. Hearing Loss, Quality of Life, and Academic Problems in Long-Term Neuroblastoma Survivors: A Report from The Children's Oncology Group. *Pediatrics*. **2007**, *120*, 1229–1236.
5. Lee, E. H.; Choi, S. E. The Effects of Music Therapy by Self-Selected Music Listening on Terminal Cancer Patients' Affect and Stress by Pain Level. *Korean J. Hospice Palliat. Care.* **2012**, *15*, 77–87.
6. Brock, P. R.; Bellman, S. C.; Yeomans, E. C.; Pinkerton, C. R.; Pritchard, J. Cisplatin Ototoxicity in Children: A Practical Grading System. *Med. Pediatr. Oncol.* **1991**, *19*, 295–300.
7. Li, Y.; Womer, R. B.; Silber, J. H. Predicting Cisplatin Ototoxicity in Children: The Influence of Age and The Cumulative Dose. *Eur. J. Cancer.* **2004**, *40*, 2445–2451.
8. Blakley, B. W.; Myers, S. F. Patterns of Hearing Loss Resulting from Cis-Platinum Therapy. *Otolaryngol. Head Neck Surg.* **1993**, *109*, 385–391.
9. Skinner, R.; Pearson, A. D. J.; Amineddine, H. A.; Mathias, D. B.; Craft, A. W. Ototoxicity of Cisplatinum in Children and Adolescents. *Br. J. Cancer.* **1990**, *61*, 927–931.
10. Siddk, Z. H. Cisplatin: Mode of Cytotoxic Action and Molecular Basis of Resistence. *Oncogene*. **2003**, *22*, 7265–7279.
11. Yu, M.; Wang, H.; Ding, A.; Golenbock, D. T.; Latz, E.; Czura, C. J.; Fenton, M. J.; Tracey, K. J.; Yang, H. HMGB1 Signals Through Toll-Like Receptor (TLR) 4 and TLR2. *Shock*. **2006**, *26*, 174-179.

12. Ho, J. K. K. Formulation of a Systemic PEST Analysis for Strategic Analysis. *Eur. J. Acad. Res.* **2014**, *2*, 6478–6492.
13. Bovijn, C.; Ulrichts, P.; De Smet, A. S.; Catteeuw, D.; Beyaert, R.; Tavernier, J.; Peelman, F. Identification of Interaction Sites for Dimerization and Adapter Recruitment in Toll/Interleukin-1 Receptor (TIR) Domain of Toll-Like Receptor 4. *J. Biol. Chem.* **2012**, *287*, 4088–4098.
14. Park, B. S.; Lee, J. O. Recognition of Lipopolysaccharide Pattern by TLR4 Complexes. *Exp. Mol. Med.* **2013**, *45*, 66–76.
15. Pussegoda, K.; Ross, C. J.; Visscher, H.; Yazdanpanah, M.; Brooks, B.; Rassekh, S. R.; Zada, Y. F.; Dubé, M. P.; Carleton, B. C.; Hayden, M. R. Replication of and ABCC3 Genetic Variants Highly Associated with Cisplatin-Induced Hearing Loss in Children. *Clin. Pharmacol. Ther.* **2013**, *94*, 243–251.
16. Maranville, J. C.; Cox, N. J. Pharmacogenomic Variants have Larger Effect Sizes than Genetic Variants Associated with Other Dichotomous Complex Traits. *Pharmacogenomics J.* **2016**, *16*, 388–392.
17. Babolmorad, G.; Latif, A.; Domingo, I. K.; Pollock, N. M.; Delyea, C.; Rieger, A. M.; Allison, W. T.; Bhavsar, A. P. Toll-Like Receptor 4 is Activated by Platinum and Contributes to Cisplatin-Induced Ototoxicity. *EMBO reports*. **2011**, *22*, 51280–51293.
18. Lee, S.; Phuan, P. W.; Felix, C. M.; Tan, J. A.; Levin, M. H.; Verkman, A. S. Nanomolar-Potency Aminophenyl-1, 3, 5-Triazine Activators of the Cystic Fibrosis Transmembrane Conductance Regulator (CFTR) Chloride Channel for Prosecretory Therapy of Dry Eye Diseases. *J. Med. Chem.* **2017**, *60*, 1210–1218.
19. Kuang, Y.; Shi, J.; Li, J.; Yuan, D.; Alberti, K. A.; Xu, Q.; Xu, B. Pericellular Hydrogel/Nanonets Inhibit Cancer Cells. *Angew. Chem.* **2014**, *126*, 8242–8245.
20. Patra, M. C.; Kwon, H. K.; Batool, M.; Choi, S. Computational Insight into the Structural Organization of Full-Length Toll-Like Receptor 4 Dimer in a Model Phospholipid Bilayer. *Front. Immunol.***2018**, *9*, 489-511.
21. Yamada, M.; Ichikawa, T.; Ii, M.; Sunamoto, M.; Itoh, K.; Tamura, N.; Kitazaki, T. Discovery of Novel and Potent Small-Molecule Inhibitors of NO And Cytokine Production as Antisepsis Agents: Synthesis and Biological Activity of Alkyl 6-(N-Substituted Sulfamoyl) Cyclohex-1-Ene-1-Carboxylate. *J. Med. Chem.* **2005**, *48*, 7457–7467.
22. Molteni, M.; Gemma, S.; Rossetti, C. The Role of Toll-like Receptor 4 in Infectious and Noninfectious Inflammation. *Mediators Inflamm*. **2016**, *16*, 1–9.
23. El-Zayat, S. R.; Sibaii, H.; Mannaa, F. A. Toll-like Receptors Activation, Signaling, and Targeting: An Overview. *Doc. Bull. Natl. Res. Cent.* **2019**, *43*, 1–12.

24. Chiu, L. L.; Cunningham, L. L.; Raible, D. W.; Rubel, E. W.; Ou, H. C. Using The Zebrafish Lateral Line to Screen for Ototoxicity. *J. Assoc. Res. Otolaryngol.* **2008**, *9*, 178–190.

25. Domarecka, E.; Skarzynska, M.; Szczepek, A. J.; Hatzopoulos, S. Use of Zebrafish Larvae Lateral Line to Study Protection Against Cisplatin-induced Ototoxicity: A Scoping Review. *Int. J. Immunopathol. Pharmacol.* **2020**, *34*, 1–19.

26. Pickett, S. B.; Raible, D. W. Water waves to sound waves: Using Zebrafish to Explore Hair Cell Biology. *J. Assoc. Res. Otolaryngol.* **2019**, *20*, 1–19.

27. Suli, A.; Watson, G. M.; Rubel, E. W.; Raible, D. W. Rheotaxis in Larval Zebrafish Is Mediated by Lateral Line Mechanosensory Hair Cells. *PloS one*. **2012**, *7*, 29727–29749.

28. Loes, A. N.; Hinman, M. N.; Farnsworth, D. R.; Miller, A. C.; Guillemin, K.; Harms, M. J. Identification and Characterization of Zebrafish Tlr4 Coreceptor Md-2. *J. Immunol. Res.***2021**, *206*, 1046–1057.

29. Zhu, S.; Hudson, T. H.; Kyle, D. E.; Lin, A. J. Synthesis and In Vitro Studies of Novel Pyrimidinyl Peptidomimetics as Potential Antimalarial Therapeutic Agents. *J. Med. Chem.* **2002**, *45*, 3491–3496.

30. Coffin, A. B.; Ramcharitar, J. Chemical Ototoxicity of The Fish Inner Ear and Lateral Line. *Fish Hear. Bioacoustics*. **2016**; 419–437.

31. Mattila, L.; Kilpeläinen, M.; Terho, E. O.; Koskenvuo, M.; Helenius, H.; Kalimo, K. Prevalence of Nickel Allergy Among Finnish University Students In 1995. *Contact Derm.* **2001**, *44*, 218–223.

32. Lidén, C.; Skare, L.; Vahter, M. Release of Nickel from Coins and Deposition onto Skin from Coin Handling–Comparing Euro Coins and SEK. *Contact Derm.* **2008**, *59*, 31–37.

33. Nestle, F. O.; Speidel, H.; Speidel, M. O. High Nickel Release From 1-And 2-Euro Coins. *Nature*. **2002**, *419*, 132–132.

34. Spiewak, R.; Pietowska, J.; Curzytek, K. Nickel: A Unique Allergen–From Molecular Structure to European Legislation. *Expert Rev. Clin. Immunol.* **2007**, *3*, 851–859.

35. Grabbe, S.; Schwarz, T. Immunoregulatory Mechanisms Involved in Elicitation of Allergic Contact Hypersensitivity. *Immunol. Today.* **1998**, *19*, 37–44.

36. Martin, S. F.; Jakob, T. From Innate to Adaptive Immune Responses in Contact Hypersensitivity. *Curr. Opin. Allergy Clin. Immunol.* **2008**, *8*, 289–293.

37. Schmidt, M.; Raghavan, B.; Müller, V.; Vogl, T.; Fejer, G.; Tchaptchet, S.; Keck, S.; Kalis, C.; Nielsen, P. J.; Galanos, C.; Roth, J. Crucial Role for Human Toll-Like Receptor 4 in the Development of Contact Allergy to Nickel. *Nat. Immunol.***2010**, *11*, 814–819.

38. Rachmawati, D.; Bontkes, H. J.; Verstege, M. I.; Muris, J.; von Blomberg, B. M. E.; Scheper, R. J.; van Hoogstraten, I. M. Transition Metal Sensing by Toll-Like Receptor-4: Next to Nickel,

Cobalt and Palladium are Potent Human Dendritic Cell Stimulators. *Contact Derm.* **2013**, *68*, 331–338.

39. So, H.; Kim, H.; Lee, J. H.; Park, C.; Kim, Y.; Kim, E.; Kim, J. K.; Yun, K. J.; Lee, K. M.; Lee, H. Y.; Moon, S. K. Cisplatin Cytotoxicity of Auditory Cells Requires Secretions of Proinflammatory Cytokines Via Activation of ERK and NF-K B. *J. Assoc. Res. Otolaryngol.* **2007**, *8*, 338–355.
40. Schmidt, M.; Raghavan, B.; Müller, V.; Vogl, T.; Fejer, G.; Tchaptchet, S.; Keck, S.; Kalis, C.; Nielsen, P. J.; Galanos, C.; Roth, J. Crucial Role for Human Toll-Like Receptor 4 in the Development of Contact Allergy to Nickel. *Nat. Immunol.***2010**, *11*, 814–819.
41. Kiss, E.; Abdelwahab, E. H. M. M.; Steib, A.; Papp, E.; Torok, Z.; Jakab, L.; Smuk, G.; Sarosi, V.; Pongracz, J. E. Cisplatin Treatment Induced Interleukin 6 and 8 Production Alters Lung Adenocarcinoma Cell Migration in an Oncogenic Mutation Dependent Manner. *Respir. Res.***2020**, *21*, 1–13.
42. Westerfield, M. A Guide for the Laboratory Use of Zebrafish Danio (Brachydanio) Rerio. *University of Oregon*. **2007**.
43. Chowdhury, S.; Owens, K. N.; Herr, R. J.; Jiang, Q.; Chen, X.; Johnson, G.; Groppi, V. E.; Raible, D. W.; Rubel, E. W.; Simon, J. A. Phenotypic Optimization of Urea–Thiophene Carboxamides to Yield Potent, Well Tolerated, and Orally Active Protective Agents Against Aminoglycoside-Induced Hearing Loss. *J. Med. Chem.* **2018**, *61*, 84–97.

Chapter 3

1. Mollen, K. P.; Anand, R. J.; Tsung, A.; Prince, J. M.; Levy, R. M.; Billiar, T. R. Emerging Paradigm: Toll-like Receptor 4-Sentinel for the Detection of Tissue Damage. *Shock*. **2006**, *26*, 430–437.
2. Yu, M.; Wang, H.; Ding, A.; Golenbock, D. T.; Latz, E.; Czura, C. J.; Fenton, M. J.; Tracey, K. J.; Yang, H. HMGB1 Signals through Toll-like Receptor (TLR) 4 and TLR2. *Shock*. **2006**, *26*, 174–179.
3. Raghavan, B.; Martin, S. F.; Esser, P. R.; Goebeler, M.; Schmidt, M. Metal allergens nickel and cobalt facilitate TLR4 homodimerization independently of MD2. *EMBO Rep*. **2012**, *13*, 1109–1115.
4. Kawasaki, T.; Kawai, T. Toll-like Receptor Signaling Pathways. *Front. Immunol*. **2012**, *5*, 461–469.
5. Singh, A.; Singh, V.; Tiwari, R. L.; Chandra, T.; Kumar, A.; Dikshit, M.; Barthwal, M. K. The IRAK-ERK-p67phox-Nox-2 Axis Mediates TLR4, 2-induced ROS Production for IL-1β Transcription and Processing in Monocytes. *Cell. Mol. Immunol*. **2016**, *13*, 745–763.

6. West, A. P.; Brodsky, I. E.; Rahner, C.; Woo, D. K.; Erdjument-Bromage, H.; Tempst, P.; Walsh, M. C.; Choi, Y.; Shadel, G. S.; Ghosh, S. TLR Signalling Augments Macrophage Bactericidal Activity through Mitochondrial ROS. *Nature*. **2011**, *472*, 476–480.

7. Haase, R.; Kirschning, C. J.; Sing, A.; Schröttner, P.; Fukase, K.; Kusumoto, S.; Wagner, H.; Heesemann, J.; Ruckdeschel, K. A Dominant Role of Toll-like Receptor 4 in the Signaling of Apoptosis in Bacteria-faced Macrophages. *J. Immunol. Res*. **2003**, *171*, 4294–4303.

8. Matsunaga, N.; Tsuchimori, N.; Matsumoto, T.; Ii, M. TAK-242 (Resatorvid), a Small-molecule Inhibitor of Toll-like Receptor (TLR) 4 Signaling, Binds Selectively to TLR4 and Interferes with Interactions Between TLR4 and its Adaptor Molecules. *Mol. Pharmacol.* **2011**, 79, 34–41.

9. Lou, Y.; Yu, Q.; Xu, K.; Tu, Y.; Balelang, M. F.; Lu, G.; Zhu, C.; Dai, Q.; Geng, W.; Mo, Y.; Wang, J. Electroacupuncture Pre-conditioning Protects from Lung Injury Induced by Limb Ischemia/reperfusion through TLR4 and NF-κB in Rats. *Mol. Med. Rep.* **2020**, *22*, 3225–3232.

10. Imanaka-Yoshida, K. Inflammation in Myocardial Disease: From Myocarditis to Dilated Cardiomyopathy. *Pathol. Int*. **2020**, *70*, 1–11.

11. Gao, W.; Xiong, Y.; Li, Q.; Yang, H. Inhibition of Toll-like Receptor Signaling as a Promising Therapy for Inflammatory Diseases: a Journey from Molecular to Nano Therapeutics. *Front. Physiol.* **2017**, *8*, 508–528.

12. Wu, M. Y.; Yiang, G. T.; Liao, W. T.; Tsai, A. P. Y.; Cheng, Y. L.; Cheng, P. W.; Li, C. Y.; Li, C. J. Current Mechanistic Concepts in Ischemia and Reperfusion Injury. *Cell. Physiol. Biochem.* **2018**, *46*, 1650–1667.

13. Leon, C. G.; Tory, R.; Jia, J.; Sivak, O.; Wasan, K. M. Discovery and Development of Toll-like Receptor 4 (TLR4) Antagonists: A New Paradigm for Treating Sepsis and other Diseases. *Pharm. Res.* **2008**, 25, 1751–1761.

14. Achek, A.; Yesudhas, D.; Choi, S. Toll-like Receptors: Promising Therapeutic Targets for Inflammatory Diseases. *Arch. Pharm. Res.* **2016**, *39*, 1032–1049.

15. Kawamoto, T.; Ii, M.; Kitazaki, T.; Iizawa, Y.; Kimura, H. TAK-242 Selectively Suppresses Toll-like Receptor 4-Signaling Mediated by the Intracellular Domain. *Eur. J. Pharmacol.* **2008**, *584*, 40–48.

16. Takashima, K.; Matsunaga, N.; Yoshimatsu, M.; Hazeki, K.; Kaisho, T.; Uekata, M.; Hazeki, O.; Akira, S.; Iizawa, Y.; Ii, M. Analysis of Binding Site for the Novel Small-Molecule TLR4 Signal Transduction Inhibitor TAK-242 and its Therapeutic Effect on Mouse Sepsis Model. *Br. J. Pharmacol.* **2009**, *157*, 1250–1262.

17. Hua, F.; Tang, H.; Wang, J.; Prunty, M. C.; Hua, X.; Sayeed, I.; Stein, D. G. TAK-242, an Antagonist for Toll-like Receptor 4, Protects Against Acute Cerebral Ischemia/reperfusion Injury in Mice. *J. Cereb. Blood Flow Metab.* **2015**, *35*, 536–542.

18. Mahita, J., Harini, K., Rao Pichika, M., Sowdhamini, R. An In Silico Approach towards the Identification of Novel Inhibitors of the TLR-4 Signaling Pathway. *J. Biomol. Struct*. **2016**, *34*, 1345–1362.

19. Bovijn, C.; Ulrichts, P.; De Smet; A. S.; Catteeuw, D.; Beyaert, R.; Tavernier, J.; Peelman, F. Identification of Interaction Sites for Dimerization and Adapter Recruitment in Toll/interleukin-1 receptor (TIR) Domain of Toll-like Receptor 4. *Int. J. Biol. Chem.* **2012**, *287*, 4088–4098.

20. Khan, J. A.; Brint, E. K.; O'Neill, L. A.; Tong, L. Crystal Structure of the Toll/interleukin-1 Receptor Domain of Human IL-1RAPL. *Int. J. Biol. Chem.* **2004**, *279*, 31664–31670.

21. Ii, M.; Matsunaga, N.; Hazeki, K.; Nakamura, K.; Takashima, K.; Seya, T.; Hazeki, O.; Kitazaki, T.; Iizawa, Y. A Novel Cyclohexene Derivative, Ethyl (6R)-6-[N-(2-Chloro-4-fluorophenyl) sulfamoyl] Cyclohex-1-ene-1-carboxylate (TAK-242), Selectively Inhibits Toll-like Receptor 4-mediated Cytokine Production through Suppression of Intracellular Signaling. *Mol. Pharmacol.* **2006**, *69*, 1288–1295.

22. Babolmorad, G.; Latif, A.; Domingo, I. K.; Pollock, N. M.; Delyea, C.; Rieger, A. M.; Allison, W. T.; Bhavsar, A. P.Toll-like Receptor 4 is Activated by Platinum and Contributes to Cisplatin-induced Ototoxicity. *EMBO Rep.* **2021**, *22*, 51280–51294.

23. Mineev, K. S.; Goncharuk, S. A.; Goncharuk, M. V.; Volynsky, P. E.; Novikova, E. V.; Aresinev, A. S. Spatial Structure of TLR4 Transmembrane Domain in Bicelles Provides the Insight into the Receptor Activation Mechanism. *Sci. Rep.* **2017***, 7*, 1–12.

24. Park, B. S.; Song, D. H.; Kim, H. M.; Choi, B. S.; Lee, H.; Lee, J. O. The Structural Basis of Lipopolysaccharide Recognition by the TLR4–MD-2 complex. *Nature*. **2009**, *458*, 1191–1195.

25. Patra, M. C.; Kwon, H. K.; Batool, M.; Choi, S. Computational Insight into the Structural Organization of Full-length Toll-like Receptor 4 Dimer in a Model Phospholipid Bilayer. *Front. Immunol.* **2018**, *9*, 489–504.

26. Magrane, M. UniProt Knowledgebase: A Hub of Integrated Protein Data. *Database*, **2011**, *2011*, 1–13.

27. Arnold, K.; Bordoli, L.; Kopp, J.; Schwede, T. The SWISS-MODEL Workspace: A Web-based Environment for Protein Structure Homology Modelling. *J. Bioinform.* **2006**, *22*, 195–201.

28. Colovos, C.; Yeates, T. Verification of Protein Structures: Patterns of Nonbonded Atomic Interactions. *Protein Sci.* **1993**, *2*, 1511–1519.

29. Laskowski, R. A.; MacArthur, M. W.; Moss, D. S.; Thornton, J. M. PROCHECK: A Program to Check the Stereochemical Quality of Protein Structures. *J. Appl. Crystallogr.* **1993**, *26*, 283–291.
30. Brown, T. ChemDraw. *Sci. Teach.* **2014**, *81*, 67.
31. Chemical Computing Group Inc. Molecular operating environment (MOE). **2016.**
32. Labute, P. Assignment of Protonation States and Geometries to Macromolecular Structures using Unary Quadratic Optimization. *Chem. Cent. J.* **2008**, *2*, 13.
33. Nussinov, R.; Wolfson, H. J. Efficient Detection of Three-dimensional Structural Motifs in Biological Macromolecules by Computer Vision Techniques. *Proc. Natl. Acad. Sci.* **1991**, *88*, 10495–10499.
34. Labute, P. The Generalized Born/Volume Integral Implicit Solvent Model: Estimation of the Free Energy of Hydration using London Dispersion Instead of Atomic Surface Area. *J. Comput. Chem.* **2008**, *29*, 1693–1698.
35. Kalé, L.; Skeel, R.; Bhandarkar, M.; Brunner, R.; Gursoy, A.; Krawetz, N.; Phillips, J.; Shinozaki, A.; Varadarajan, K.; Schulten, K. NAMD2: Greater Scalability for Parallel Molecular Dynamics. *J. Comput. Phys.* **1999**, *151*, 283–312.
36. Tian, C.; Kasavajhala, K.; Belfon, K. A.; Raguette, L.; Huang, H.; Migues, A. N.; Bickel, J.; Wang, Y.; Pincay, J.; Wu, Q.; Simmerling, C. ff19SB: Amino-acid-specific Protein Backbone Parameters Trained Against Quantum Mechanics Energy Surfaces in Solution. J. *Chem. Theory Comput.* **2016**, *16*, 528–552.
37. Mark, P.; Nilsson, L. Structure and Dynamics of the TIP3P, SPC, and SPC/E Water Models at 298 K. *J. Phys. Chem. A.* **2001**, *105*, 9954–9960.
38. Ryckaert, J. P.; Ciccotti, G.; Berendsen, H. J. Numerical Integration of the Cartesian Equations of Motion of a System with Constraints: Molecular Dynamics Of N-Alkanes. *J. Comput. Phys.* **1977**, *23*, 327–341.
39. Loncharich, R. J.; Brooks, B. R.; Pastor, R.W. Langevin Dynamics of Peptides: The Frictional Dependence of Isomerization Rates of N-acetylalanyl-N′-methylamide. *Biopolymers*. **1992**, 32, 523–535.
40. De Souza, O .N.; Ornstein, R. L. Effect of Periodic Box Size on Aqueous Molecular Dynamics Simulation of a DNA Dodecamer with Particle-mesh Ewald Method. *Biophys. J.* **1997**, *72*, 2395–2397.
41. Wang, J.; Wolf, R. M.; Caldwell, J. W.; Kollman, P. A.; Case, D. A. Development and Testing of a General Amber Force Field. *J. Comput. Chem.* **2004**, *25*, 1157–1174.
42. Wang, J.; Wang, W.; Kollman, P. A.; Case, D. A. Antechamber: An Accessory Software Package for Molecular Mechanical Calculations. *J. Am. Chem. Soc.* **2001**, *222*, 403–444.
43. Roe, D. R.; Cheatham III, T. E. PTRAJ and CPPTRAJ: Software for Processing and Analysis of Molecular Dynamics Trajectory Data. *J. Chem. Theory Comput.* **2013**, *9*, 3084–3095.

44. Williams, T.; Kelley, C. Gnuplot 4.4: An Interactive Plotting Program. **2010**.
45. Humphrey, W.; Dalke, A.; Schulten, K. VMD: Visual Molecular Dynamics. *J. Mol. Graph.* **1996**, *14*, 33–38.
46. Onufriev, A.; Bashford, D.; Case, D. A. Exploring Protein Native States and Large-scale Conformational Changes with a Modified Generalized Born Model. *Proteins*. **2004**, *55*, 383–394.
47. Miller III, B. R.; McGee Jr, T. D.; Swails, J. M.; Homeyer, N.; Gohlke, H.; Roitberg, A. E. MMPBSA. py: An Efficient Program for End-state Free Energy Calculations. *J. Chem. Theory Comput.* **2012**, *8*, 3314–3321.
48. Kollman, P. A.; Massova, I.; Reyes, C.; Kuhn, B.; Huo, S.; Chong, L.; Lee, M..; Lee, T.; Duan, Y.; Wang, W.; Donini, O. Calculating Structures and Free Energies of Complex Molecules: Combining Molecular Mechanics and Continuum Models. *Acc. Chem. Res.* **2000**, *33*, 889–897.
49. Shao, J.; Tanner, S. W.; Thompson, N.; Cheatham, T. E. Clustering Molecular Dynamics Trajectories: Characterizing the Performance of Different Clustering Algorithms. *J. Chem. Theory Comput.* **2007**, *3*, 2312–2334.
50. Davies, D. L.; Bouldin, D. W. A Cluster Separation Measure. *IEEE Trans. Pattern Anal. Mach. Intell.* **1979**, *2*, 224–227.
51. Lushpa, V. A.; Goncharuk, M. V.; Lin, C.; Zalevsky, A. O.; Talyzina, I. A.; Luginina, A. P.; Vakhrameev, D. D.; Shevtsov, M. B.; Goncharuk, S. A.; Arseniev, A. S.; Borshchevskiy, V. I. Modulation of Toll-Like Receptor 1 Intracellular Domain Structure and Activity by Zn^{2+} Ions. *Commun. Biol.* **2021**, *4*, 1–12.
52. Yamada, M.; Ichikawa, T.' Ii, M.' Sunamoto, M.' Itoh, K.' Tamura, N.; Kitazaki, T. Discovery of Novel and Potent Small-molecule Inhibitors of NO and Cytokine Production as Antisepsis Agents: Synthesis and Biological Activity of Alkyl 6-(N-Substituted sulfamoyl) Cyclohex-1-ene-1-carboxylate. *J. Med. Chem.* **2005**, *48*, 7457–7467.

Chapter 4

1. Report on Breast Cancer Statistics in Canada. *Canadian Breast Cancer Society* **2009.**
2. Bray, F.; Ferlay, J.; Soerjomataram, I.; Siegel, R.L.; Torre, L.A.; Jemal, A. Global Cancer Statistics 2018: GLOBOCAN Estimates of Incidence and Mortality Worldwide For 36 Cancers in 185 Countries. *CA Cancer J. Clin.* **2020**, *70*, 313–313.
3. Mattiuzzi, C.; Lippi, G. Current Cancer Epidemiology. *J. Epidemiol. Glob. Health* **2019**, *9*, 217–222.
4. World Health Organization, Projections of Mortality and Causes of Death, 2016 to 2060. *Obtenido de*. **2018**.

5. Sarrió, D.; Rodriguez-Pinilla, S.M.; Hardisson, D.; Cano, A.; Moreno-Bueno, G.; Palacios, J. Epithelial-mesenchymal Transition in Breast Cancer Relates to the Basal-like Phenotype. *Cancer Res.* **2008**, *68*, 989–997.
6. Rakha, E.A.; Ellis, I.O. Triple-negative/Basal-like Breast Cancer. *Pathology* **2009,** 41, 40–47.
7. Kumar, P.; Aggarwal, R. An Overview of Triple-Negative Breast Cancer. *Arch. Gynecol. Obste.* **2016**. *283*, 247–269.
8. Afghahi, A.; Timms, K. M.; Vinayak, S.; Jensen, K. C.; Kurian, A. W.; Carlson, R. W.; Chang, P. J.; Schackmann, E.; Hartman, A. R.; Ford, J. M.; Telli, M. L. Tumor BRCA1 Reversion Mutation Arising During Neo Adjuvant Platinum-Based Chemotherapy in Triple-Negative Breast Cancer Is Associated with Therapy Resistance. *Clin. Cancer Res.* **2017**, *23*, 3365–3370.
9. Lev, S. Targeted Therapy and Drug Resistance in Triple-Negative Breast Cancer: The EGFR Axis. *Biochem. Soc. Trans.* **2020**, *48*, 657–665.
10. Robson, M.; Im, S.A.; Senkus, E.; Xu, B.; Domchek, S. M.; Masuda, N.; Delaloge, S.; Li, W.; Tung, N.; Armstrong, A.; Wu, W. 2017. Olaparib for Metastatic Breast Cancer in Patients with A Germline BRCA Mutation. *N. Engl. J. Med.* **2017**, *377*, 523–533.
11. Litton, J. K.; Rugo, H. S.; Ettl, J.; Hurvitz, S. A.; Gonçalves, A.; Lee, K. H.; Fehrenbacher, L.; Yerushalmi, R.; Mina, L. A.; Martin, M.; Roché, H. Talazoparib in Patients with Advanced Breast Cancer and A Germline BRCA Mutation. *N.Engl.J.Med.* **2018**, *379*, 753–763.
12. Manson, J. M. Mechanism of Nitrofen Teratogenesis. *Environ. Health Perspect* . **1986**, *70,* 137–147.
13. Greer, J. J.; Babiuk, R. P.; Thebaud, B. Etiology of Congenital Diaphragmatic Hernia: The Retinoid Hypothesis. *Pediatr. Res.* **2003**, *53*, 726–730.
14. Greer, J. J.; Allan, D. W.; Babiuk, R. P.; Lemke, R. P. Recent Advances in Understanding the Pathogenesis of Nitrofen-induced Congenital Diaphragmatic Hernia. *Pediatr. Pulmonol.* **2000**, *29*, 394–399.
15. Acosta, J. M.; Chai, Y.; Meara, J. G.; Bringas, Jr, P.; Anderson, K. D.; Warburton, D. Prenatal Exposure to Nitrofen Induces Fryns Phenotype in Mice. *Ann.Plast.Surg.* **2001***, 46*, 635–640.
16. Hurt, S. S. B.; Smith, J. M.; Hayes, A. W. Nitrofen: A Review and Perspective. *Toxicology* **1983***, 29*, 1–37.
17. Gray, L. E.; Kavlock, R. J. The Effects of The Herbicide 2,4-Dichlorophenyl-P-Nitrophenyl Ether (NIT) on Serum Thyroid Hormones in Adult Female Mice. *Toxicol. Lett.* **1983**, *15*, 231–235.
18. Blagosklonny, M. V. Teratogens as anticancer drugs. *Cell Cycle* **2009***, 4*, 1518–1521.
19. Wonders, K. Y.; Reigle, B. S. Trastuzumab and Doxorubicin-Related Cardiotoxicity and the Cardioprotective Role of Exercise. *Integr. Cancer Ther.* **2009**, *8*, 17–21.
20. Telli, M. L.; Witteles, R. M. Trastuzumab-related Cardiac Dysfunction. *J. Natl. Compr. Cancer Netw.* **2011***, 9*, 243–249.

21. Chien, A. J.; Rugo, H. S. The Cardiac Safety of Trastuzumab in the Treatment of Breast Cancer. *Expert Opin. Drug Saf.* **2010***, 9*, 35–346.
22. (a)www.chemspider.com/ChemicalStructure.15010.html;accessed30March,2016,16:27.(b)www.vitasmlab.com/catalog-search? searchValue=STK365913; accessed 30 March, 2016, 16:29.
23. Jenkins, D. E.; Oei, Y.; Hornig, Y. S.; Yu, S. F.; Dusich, J., Purchio, T.; Contag, P. R. Bioluminescent Imaging (BLI) to Improve and Refine Traditional Murine Models of Tumor Growth and Metastasis. *Clin. Exp. Metastasis* **2003**, *20*, 733–744.
24. Mey, J.; Babiuk, R. P.; Clugston, R.; Greer, J. J. Retinal Dehydrogenase-2 is Inhibited by Compounds that Induce Congenital Diaphragmatic Hernias in Rodents. *Am. J. Pathol.* **2003**, *162*, 673–679.
25. Noble, B. R., Babiuk, R. P.; Clugston, R. D.; Underhill, T. M.; Sun, H.; Kawaguchi, R.; Walfish, P. G.; Blomhoff, R., Gundersen, T. E.; Greer, J. J.; Mechanisms of Action of the Congenital Diaphragmatic Hernia-inducing Teratogen Nitrofen. *Am. J. Physiol. Lung Cell Mol. Physiol.* **2007**, *293*, 1079–1087.
26. Chaurasiya, S.; Hew, P.; Crosley, P.; Sharon, D.; Potts, K.; Agopsowicz, K.; Long, M.; Shi, C.; Hitt, M. M. Breast Cancer Gene Therapy Using an Adenovirus Encoding Human IL-2 Under Control of Mammaglobin Promoter/Enhancer Sequences. *Cancer Gene Ther.* **2016**, *23*, 178–187.
27. Lanning, M. E.; Yu, W.; Yap, J. L.; Chauhan, J.; Chen, L.; Whiting, E.; Pidugu, L. S.; Atkinson, T.; Bailey, H., Li, W.; Roth, B.M.; Hynicka, L.; Chesko, K.; Toth, E. A.; Shapiro, P.; MacKerell Jr., A. D.; Wilder, P. T.; Fletcher, S. Structure-Based Design of N-Substituted 1-Hydroxy-4-sulfamoyl-2-naphthoates as Selective Inhibitors of the Mcl-1 Oncoprotein. Eur. J. Med. Chem. **2016**, *113*, 273–292.
28. Kathiravan, S.; Nicholls, I. A. Monoprotected l-Amino Acid (l-MPAA), Accelerated Bromination, Chlorination, and Iodination of C (sp2)−H Bonds by Iridium (III) Catalysis. Chem. Eur. J **2017**, *23*, 7031–7036.
29. Zhu, X. L.; Zhang, R.; Wu, Q. Y.; Song, Y. J.; Wang, Y. X.; Yang, J. F.; Yang, G. F. Natural Product Neopeltolide as a Cytochrome bc_1 Complex Inhibitor: Mechanism of Action and Structural Modification. J. Agric. Food Chem. **2019**, *67*, 2774–2781.
30. Wolfe, J. P.; Wagaw, S.; Buchwald, S. L. An Improved Catalyst System for Aromatic Carbon−Nitrogen Bond Formation: The Possible Involvement of Bis (Phosphine) Palladium Complexes as Key Intermediates. J. Am. Chem. Soc. **1996**, *118*, 7215–7216.
31. Ali, N.; Venkateswaran, G.; Garcia, E.; Landry, T.; McColl, H.; Sergi, C.; Persad, A.; Abuetabh, Y.; Eisenstat, D. D.; Persad, S. Osteosarcoma Progression is Associated with Increased Nuclear Levels and Transcriptional Activity of Activated B-Catenin. *Genes Cancer* **2019**, *10*, 63–79.
32. Han, M.; Liu, M.; Wang, Y.; Chen, X.; Xu, J.; Sun, Y.; Zhao, L.; Qu, H.; Fan, Y.; Wu, C. Antagonism of Mir-21 Reverses Epithelial-Mesenchymal Transition and Cancer Stem Cell Phenotype Through AKT/ERK1/2 Inactivation by Targeting PTEN. *PLoS ONE* **2012**, *7*, 1–10.

33. Du, J.; Yang, S.; An, D.; Hu, F.; Yuan, W.; Zhai, C.; Zhu, T. BMP-6 Inhibits Microrna-21 Expression in Breast Cancer Through Repressing Δef1 and AP-1. *Cell Res.* **2009**, *19*, 487–496.
34. Lehmann, B.D.; Bauer, J.A.; Chen, X.; Sanders, M.E.; Chakravarthy, A.B.; Shyr, Y.; Pietenpol, J.A. Identification of Human Triple-negative Breast Cancer Subtypes and Preclinical Models for Selection of Targeted Therapies. *J. Clin. Invest.* **2011**, *121*, 2750–2767.
35. Rouzier, R.; Perou, C. M.; Symmans, W. F.; Ibrahim, N.; Cristofanilli, M.; Anderson, K.; Hess, K. R.; Stec, J.; Ayers, M.; Wagner, P.; Morandi, P. Breast Cancer Molecular Subtypes Respond Differently to Preoperative Chemotherapy. *Clin. Cancer Res.* **2005,** *15*, 5678–5685.
36. Silver, D. P.; Richardson, A. L.; Eklund, A. C.; Wang, Z. C.; Szallasi, Z.; Li, Q.; Juul, N.; Leong, C. O.; Calogrias, D.; Buraimoh, A.; Fatima, A. Efficacy of Neoadjuvant Cisplatin in Triple-Negative Breast Cancer. *J. Clin. Oncol.* **2010**, *1*, 1145–1153.
37. Sikov, W. M.; Berry, D. A.; Perou, C. M.; Singh, B.; Cirrincione, C.; Tolaney, S.; Kuzma, C. S. Impact of The Addition of Carboplatin and/or Bevacizumab to Neoadjuvant Once-per-week Paclitaxel Followed by Dose-dense Doxorubicin and Cyclophosphamide on Pathologic Complete Response Rates in Stage II to III Triple-Negative Breast Cancer: CALGB 40603 (Alliance). *J. Clin. Oncol.* **2015**, *3*, 13–21.
38. Von Minckwitz, G.; Schneeweiss, A.; Loibl, S.; Salat, C.; Denkert, C.; Rezai, M.; Blohmer, J. U.; Jackisch, C.; Paepke, S.; Gerber, B.; Zahm, D. M. Neoadjuvant Carboplatin in Patients with Triple-negative and HER2-positive Early Breast Cancer (GeparSixto; GBG 66): A Randomised Phase 2 trial. *Lancet Oncol.* **2014**, *15*, 747–756.
39. Von Minckwitz, G.; Hahnen, E.; Fasching, P. A.; Hauke, J.; Schneeweiss, A.; Salat, C.; Rezai, M.; Blohmer, J. U.; Zahm, D. M.; Jackisch, C.; Gerber, B. Pathological Complete Response (Pcr) Rates After Carboplatin-containing Neoadjuvant Chemotherapy in Patients with Germline BRCA (Gbrca) Mutation and Triple-negative Breast Cancer (TNBC): Results from Geparsixto. *J. Clin. Oncol.* **2014**, *32*, 1005–1035.
40. Mittendorf, E. A.; Philips, A. V.; Meric-Bernstam, F.; Qiao, N.; Wu, Y.; Harrington, S.; Su, X.; Wang, Y.; Gonzalez-Angulo, A. M.; Akcakanat, A.; Chawla, A. PD-L1 Expression in Triple-negative Breast Cancer. *Cancer Immunol. Res.* **2014**, *2*, 361–370.
41. Topalian, S. L.; Hodi, F. S.; Brahmer, J. R.; Gettinger, S. N.; Smith, D. C.; McDermott, D. F.; Powderly, J. D.; Carvajal, R. D.; Sosman, J. A.; Atkins, M. B.; Leming, P. D. *N. Engl. J. Med.* **2012,** *366*, 2443–2454.
42. Ademuyiwa, F. O.; Bshara, W.; Attwood, K.; Morrison, C.; Edge, S. B.; Ambrosone, C. B.; O'Connor, T. L.; Levine, E. G.; Miliotto, A.; Ritter, E.; Ritter, G. NY-ESO-1 Cancer Testis Antigen Demonstrates High Immunogenicity in Triple Negative Breast Cancer. *PLoS One* **2012***, 7*, 1–9.
43. Tessari, A.; Paolini, B.; Mariani, L.; Pilla, L.; Carcangiu, M. L.; Moliterni, A.; De Braud, F. G.; Cresta, S. Expression of PD-L1 and NY-ESO-1 in Early and Advanced Triple-negative Breast Cancer. *J. Clin. Oncol.* **2014**, *32*, 1101–1110.

44. Park, S.; Koo, J.; Park, H. S.; Kim, J. H.; Choi, S. Y.; Lee, J. H.; Park, B. W.; Lee, K. S. Expression of Androgen Receptors in Primary Breast Cancer. *Ann. Oncol.* **2010**, *21*, 488–492.
45. Mittendorf, E. A.; Schneble, E. J.; Perez, S. A.; Symanowski, J. T.; Patil, R.; Vreeland, T. J.; Berry, J. S.; Trappey, A. F.; Clifton, G. T.; von Hofe, E.; Ardavanis, A. Primary Analysis of the Prospective, Randomized, Single-blinded Phase II Trial of AE37 Vaccine Versus GM-CSF Alone Administered in the Adjuvant Setting to High-risk Breast Cancer Patients. *J. Clin. Oncol.* **2014***, 32*, 638–648.
46. Schneble, E. J.; Perez, S. A.; Berry, J. S.; Trappey, A. F.; Vreeland, T.; Hale, D. F.; Sears, A. K.; Clifton, G. T.; von Hofe, E.; Ardavanis, A.; Shumway, N. M. Comparison of Recurrent and Nonrecurrent Breast Cancer Patients Undergoing AE37 Peptide Vaccine Therapy. *J. Clin. Oncol.* **2014***,* 32, 613–618.
47. Creighton, C. J.; Li, X.; Landis, M.; Dixon, J. M.; Neumeister, V. M.; Sjolund, A.; Rimm, D. L.; Wong, H.; Rodriguez, A.; Herschkowitz, J. I.; Fan, C. Residual Breast Cancers after Conventional Therapy Display Mesenchymal as well as Tumor-initiating Features. *Proc. Natl. Acad. Sci.* **2009**, *106*, 13820–51382.
48. Gupta, P. B.; Onder, T. T.; Jiang, G.; Tao, K.; Kuperwasser, C.; Weinberg, R. A.; Lander, E. S. Identification of Selective Inhibitors of Cancer Stem Cells by High-throughput Screening. *Cell* **2009***, 138*, 645–659.
49. Wang, K.; Zhang, Q.; Li, D.; Ching, K.; Zhang, C.; Zheng, X.; Ozeck, M.; Shi, S.; Li, X.; Wang, H.; Rejto, P. PEST Domain Mutations in Notch Receptors Comprise an Oncogenic Driver Segment in Triple-negative Breast Cancer Sensitive to a γ-Secretase Inhibitor. *Clin. Cancer Res.* **2015**, *21*, 1487–1496.
50. Thiery, J. P. Epithelial-Mesenchymal Transitions in Tumour Progression. *Nat. Rev. Cancer.* **2002**, *2*, 442–454.
51. Daniel, B. R.; Campone, M.; Dieras, V.; Ervin, T.; Yu, W.; Paton, V. E.; Xia, Q.; Peterson, A. OT3-01-11: A Randomized, Phase II Multicenter, Double-Blind, Placebo-Controlled Trial Evaluating MetMAb and/or Bevacizumab in Combination with Weekly Paclitaxel in Patients with Metastatic Triple-Negative Breast Cancer. *Cancer Res.* **2011**, 71.
52. Shipitsin, M.; Campbell, L. L.; Argani, P.; Weremowicz, S.; Bloushtain-Qimron, N.; Yao, J.; Nikolskaya, T.; Serebryiskaya, T.; Beroukhim, R.; Hu, M., Halushka, M. K. Molecular Definition of Breast Tumor Heterogeneity. *Cancer Cell* **2007***, 11*, 259–273.
53. Oettle, H.; Hilbig, A.; Seufferlein, T.; Luger, T.; Schmid, R. M.; Von Wichert, G.; Schmaus, S.; Heinrichs, H.; Schlingensiepen, K. Trabedersen (AP 12009) in the Treatment of Patients with Advanced Tumors: Completion of Dose-Escalation and First Efficacy Data. *J. Clin. Oncol.* **2010**, *28*, 2611.

Chapter 5

1. Takashima, K.; Matsunaga, N.; Yoshimatsu, M.; Hazeki, K.; Kaisho, T.; Uekata, M.; Hazeki, O.; Akira, S.; Iizawa, Y.; Ii, M. Analysis of Binding Site for the Novel Small-Molecule TLR4 Signal Transduction Inhibitor TAK-242 and Its Therapeutic Effect on Mouse Sepsis Model. *Br. J. Pharmacol.* **2009**, *157*, 1250–1262.
2. Burton, N.R.; Kim, P.; Backus, K. M. Photoaffinity Labelling Strategies for Mapping the Small Molecule–Protein Interactome. *Org. Biomol. Chem.* **2021**, *19*, 7792–7809.
3. Kettunen, P. Calcium Imaging in the Zebrafish. *Calcium Signal.* **2012**, *740*, 1039–1071.
4. Ebner, C.; Ledderose, J.; Zolnik, T. A.; Dominiak, S. E.; Turko, P.; Papoutsi, A.; Poirazi, P.; Eickholt, B. J.; Vida, I.; Larkum, M. E.; Sachdev, R. N. Optically Induced Calcium-dependent Gene Activation and Labeling of Active Neurons Using CaMPARI and Cal-light. *Front. Synaptic Neurosci*. **2019**, *11*, 1–16.
5. He, W.; Liu, Q.; Wang, L.; Chen, W.; Li, N.; Cao, X. TLR4 Signaling Promotes Immune Escape of Human Lung Cancer Cells by Inducing Immunosuppressive Cytokines and Apoptosis Resistance. *Mol. Immunol.* **2007**, *44*, 2850–2859.
6. Szajnik, M.; Szczepanski, M. J.; Czystowska, M.; Elishaev, E.; Mandapathil, M.; Nowak-Markwitz, E.; Spaczynski, M.; Whiteside, T. L. TLR4 Signaling Induced by Lipopolysaccharide or Paclitaxel Regulates Tumor Survival and Chemoresistance in Ovarian Cancer. *Oncogene*. **2009**, *28*, 4353–4363.
7. Kashani, B.; Zandi, Z.; Karimzadeh, M. R.; Bashash, D.; Nasrollahzadeh, A.; Ghaffari, S. H., 2019. Blockade of TLR4 using TAK-242 (Resatorvid) Enhances Anti-cancer Effects of Chemotherapeutic Agents: A Novel Synergistic Approach for Breast and Ovarian Cancers. *Immunol. Res.* **2019**, *67*, 505–516.
8. Siddik, Z. H. Cisplatin: Mode of Cytotoxic Action and Molecular Basis of Resistance. *Oncogene*. **2003**, *47*, 7265–7279.
9. Leutert, M.; Rodríguez-Mias; R. A.; Fukuda, N. K.; Villén, J. R2-P2 Rapid-robotic Phosphoproteomics Enables Multidimensional Cell Signaling Studies. *Mol. Syst. Biol.* **2019**, *15*, 9021–9041.

Appendix I: NMR Spectra
(Chapter 2)

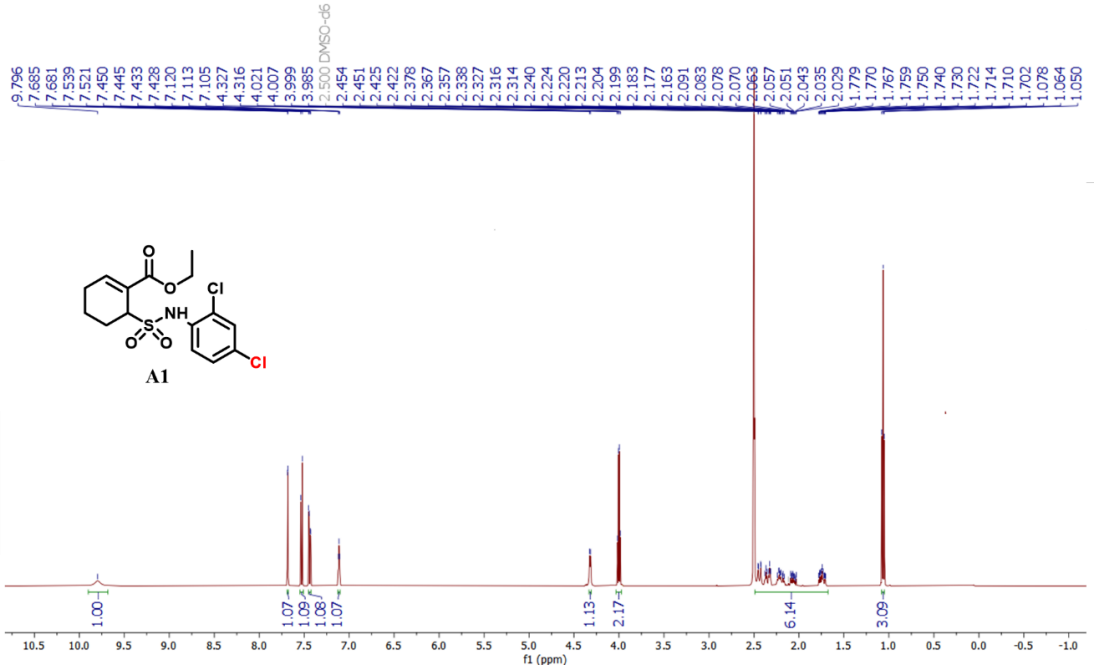
9.796
7.685
7.681
7.539
7.521
7.450
7.445
7.433
7.428
7.120
7.113
7.105
4.327
4.316
4.021
4.007
3.999
3.985
2.500 DMSO-d6
2.454
2.451
2.425
2.422
2.378
2.367
2.357
2.338
2.327
2.316
2.314
2.240
2.224
2.220
2.213
2.204
2.199
2.183
2.177
2.163
2.091
2.083
2.078
2.070
2.063
2.057
2.051
2.043
2.035
2.029
1.779
1.770
1.767
1.759
1.750
1.740
1.730
1.722
1.714
1.710
1.702
1.078
1.064
1.050
O
O
Cl
NH
S
O
O
Cl
A1
1.00
1.07
1.09
1.08
1.07
1.13
2.17
6.14
3.09
10.5
10.0
9.5
9.0
8.5
8.0
7.5
7.0
6.5
6.0
5.5
5.0
4.5
4.0
3.5
3.0
2.5
2.0
1.5
1.0
0.5
0.0
-0.5
-1.0
f1 (ppm)

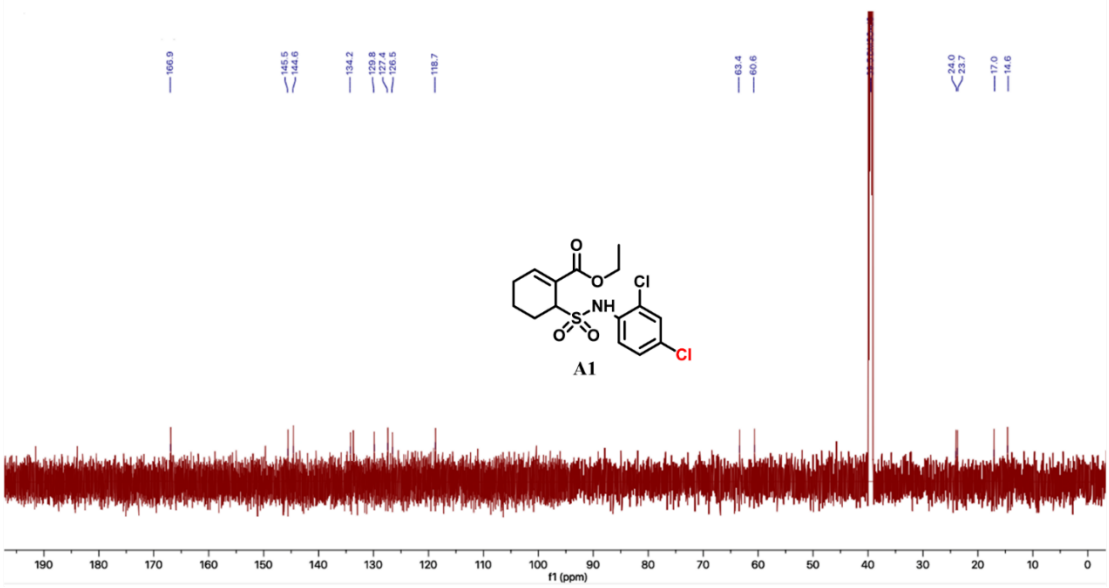
166.9
145.5
144.6
134.2
129.8
127.4
126.5
118.7
63.4
60.6
24.0
23.7
17.0
14.6
O
O
Cl
NH
S
O
O
Cl
A1
190
180
170
160
150
140
130
120
110
100
90
80
70
60
50
40
30
20
10
0
f1 (ppm)

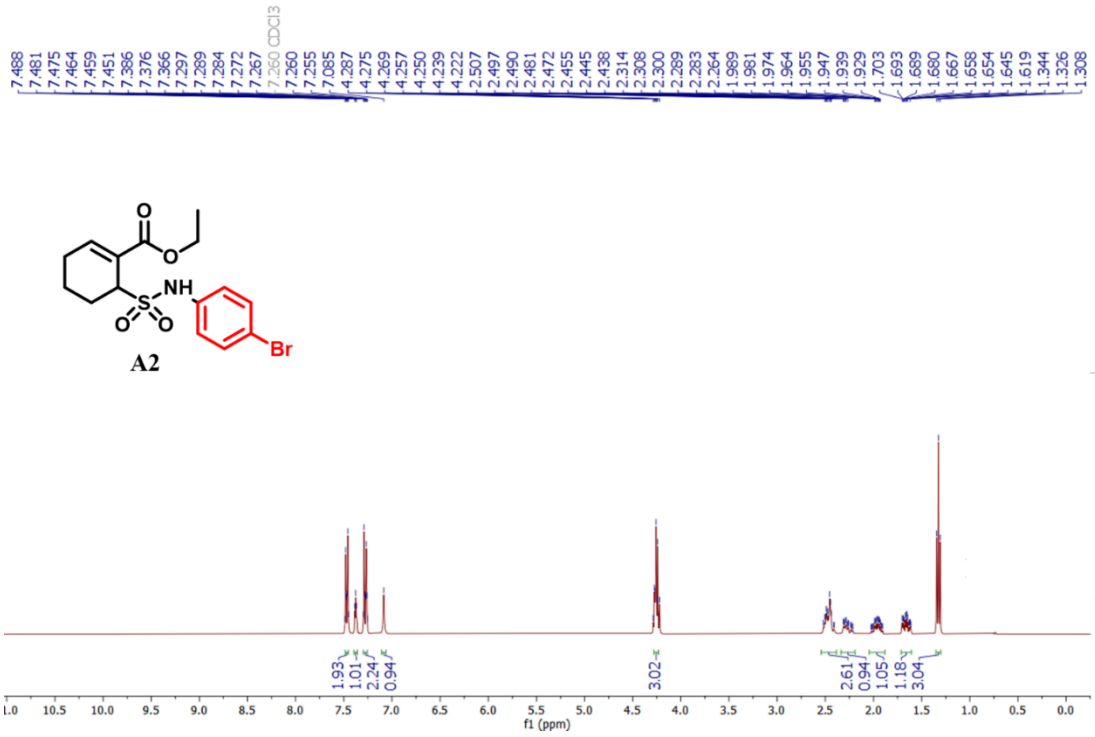
7.488
7.481
7.475
7.464
7.459
7.451
7.386
7.376
7.366
7.297
7.289
7.284
7.272
7.267
7.260 CDCl3
7.255
7.085
4.287
4.275
4.269
4.257
4.250
4.239
4.222
2.507
2.497
2.490
2.481
2.472
2.455
2.445
2.438
2.314
2.308
2.300
2.289
2.283
2.264
1.989
1.981
1.974
1.964
1.955
1.947
1.939
1.929
1.703
1.693
1.689
1.680
1.667
1.658
1.654
1.645
1.619
1.344
1.326
1.308
O
O
NH
S
O
O
Br
A2
1.93
1.01
2.24
0.94
3.02
2.61
0.94
1.05
1.18
3.04
f1 (ppm)

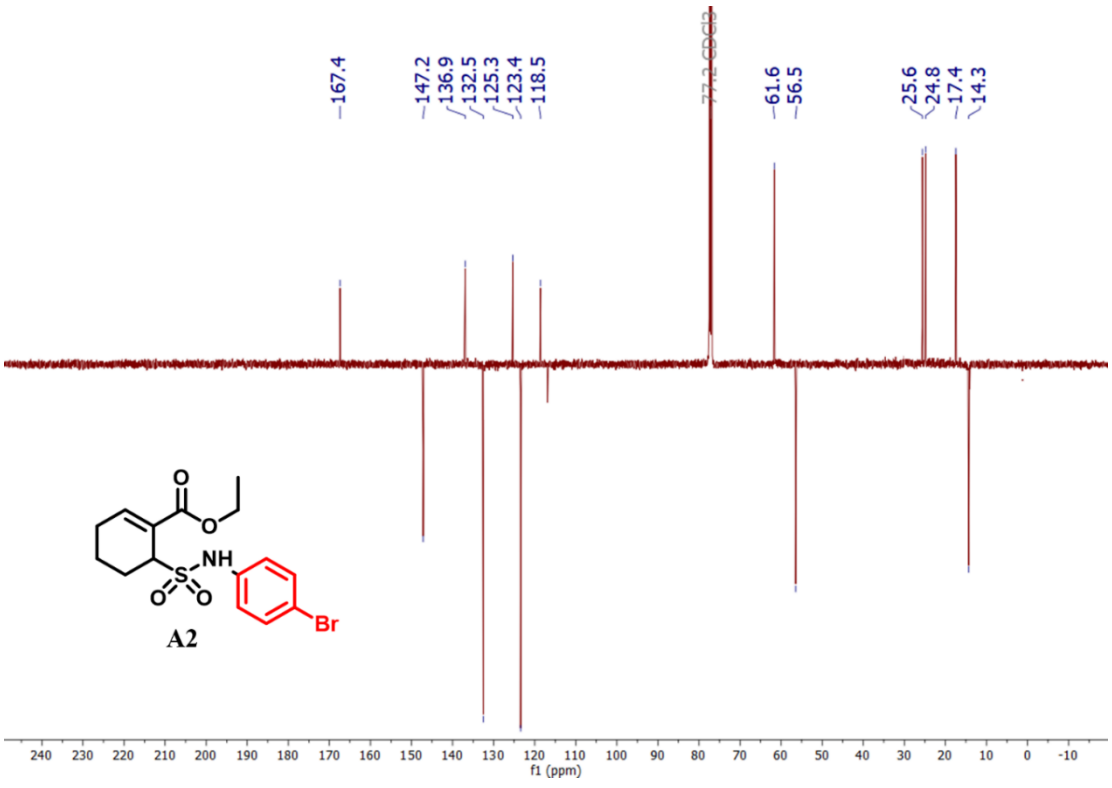
167.4
147.2
136.9
132.5
125.3
123.4
118.5
77.2 CDCl3
61.6
56.5
25.6
24.8
17.4
14.3
O
O
NH
S
O
O
Br
A2
f1 (ppm)

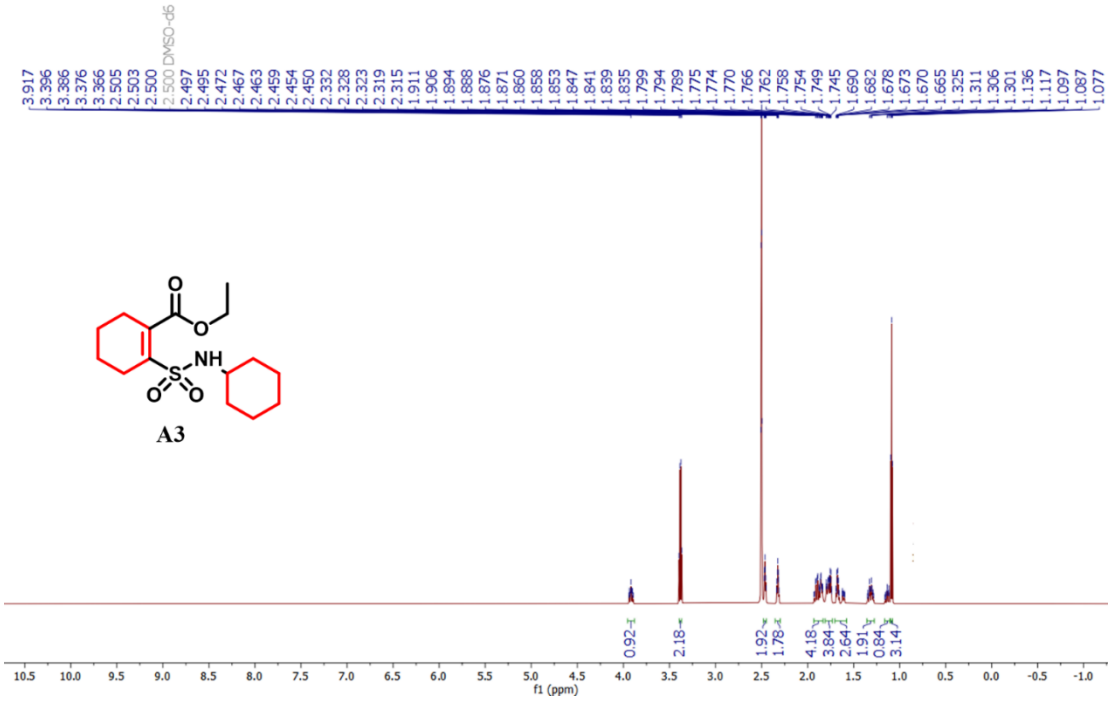
3.917
3.396
3.386
3.376
3.366
2.505
2.503
2.500
2.500 DMSO-d6
2.497
2.495
2.472
2.467
2.463
2.459
2.454
2.450
2.332
2.328
2.323
2.319
2.315
1.911
1.906
1.894
1.888
1.876
1.871
1.860
1.858
1.853
1.847
1.841
1.839
1.835
1.799
1.794
1.789
1.775
1.774
1.770
1.766
1.762
1.758
1.754
1.749
1.745
1.690
1.682
1.678
1.673
1.670
1.665
1.325
1.311
1.306
1.301
1.136
1.117
1.097
1.087
1.077
0.92
2.18
1.92
1.78
4.18
3.84
2.64
1.91
0.84
3.14
f1 (ppm)
A3

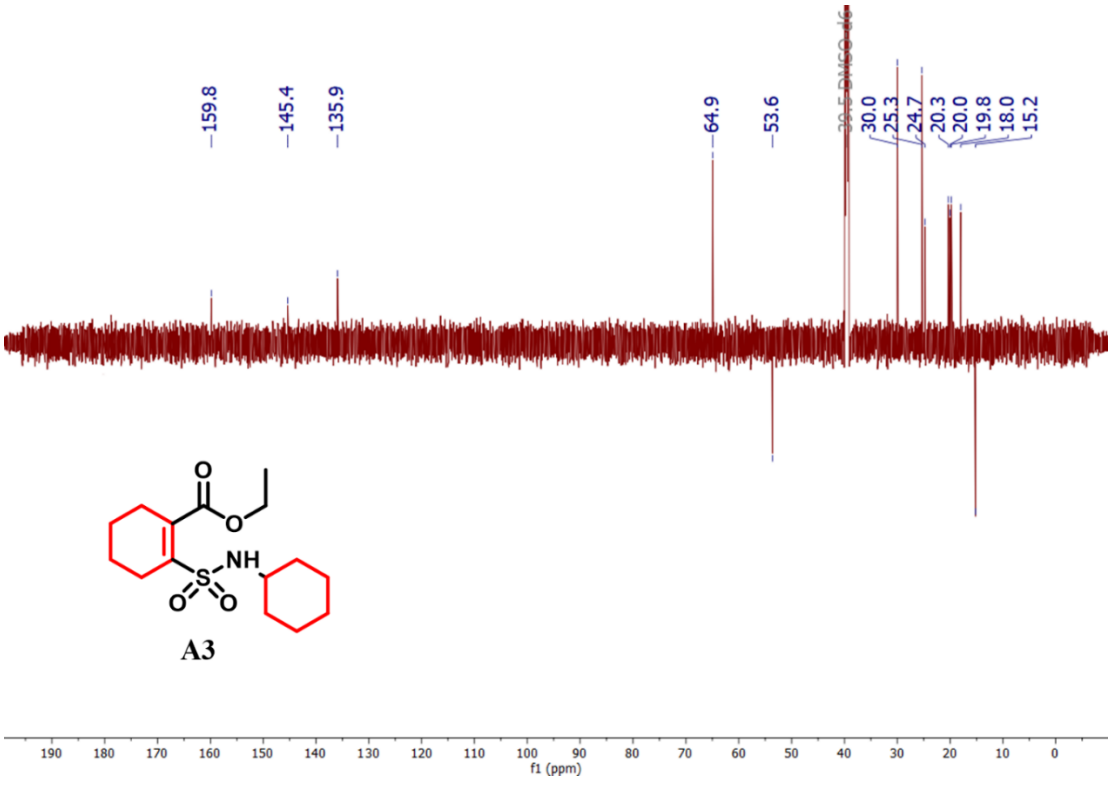
159.8
145.4
135.9
64.9
53.6
39.5 DMSO-d6
30.0
25.3
24.7
20.3
20.0
19.8
18.0
15.2
f1 (ppm)
A3

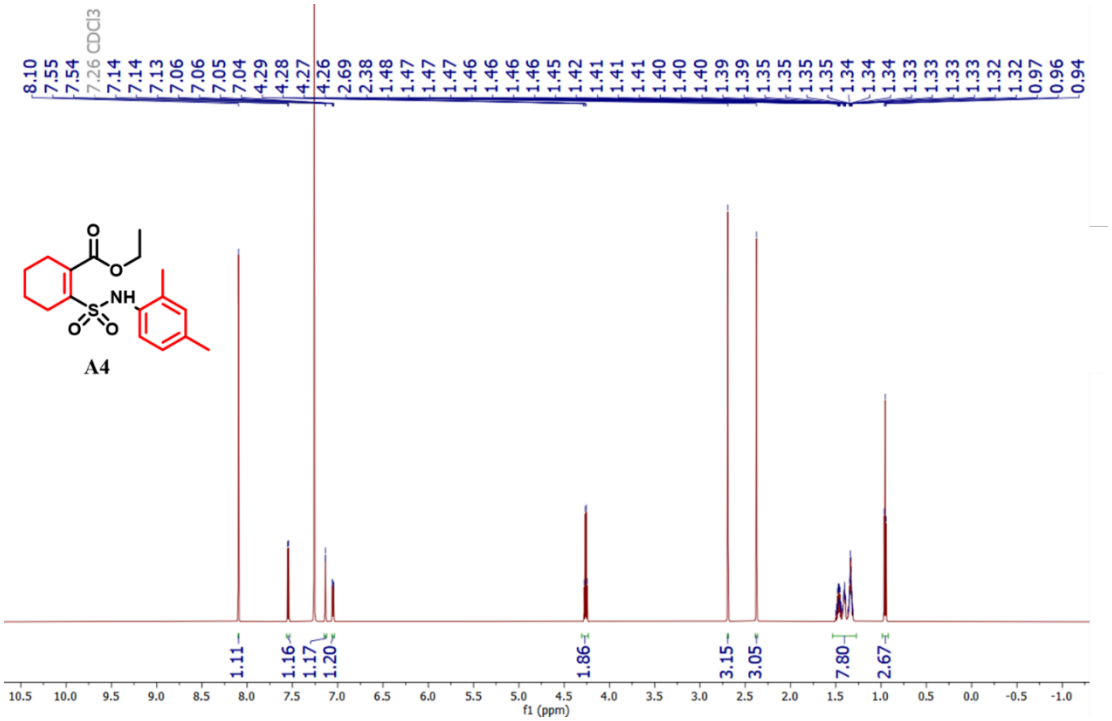
8.10
7.55
7.54
7.26 CDCl3
7.14
7.14
7.13
7.06
7.06
7.05
7.04
4.29
4.28
4.27
4.26
2.69
2.38
1.48
1.47
1.47
1.47
1.46
1.46
1.46
1.46
1.45
1.42
1.41
1.41
1.41
1.40
1.40
1.40
1.39
1.39
1.35
1.35
1.35
1.35
1.34
1.34
1.34
1.33
1.33
1.33
1.32
1.32
0.97
0.96
0.94
A4
1.11
1.16
1.17
1.20
1.86
3.15
3.05
7.80
2.67
f1 (ppm)

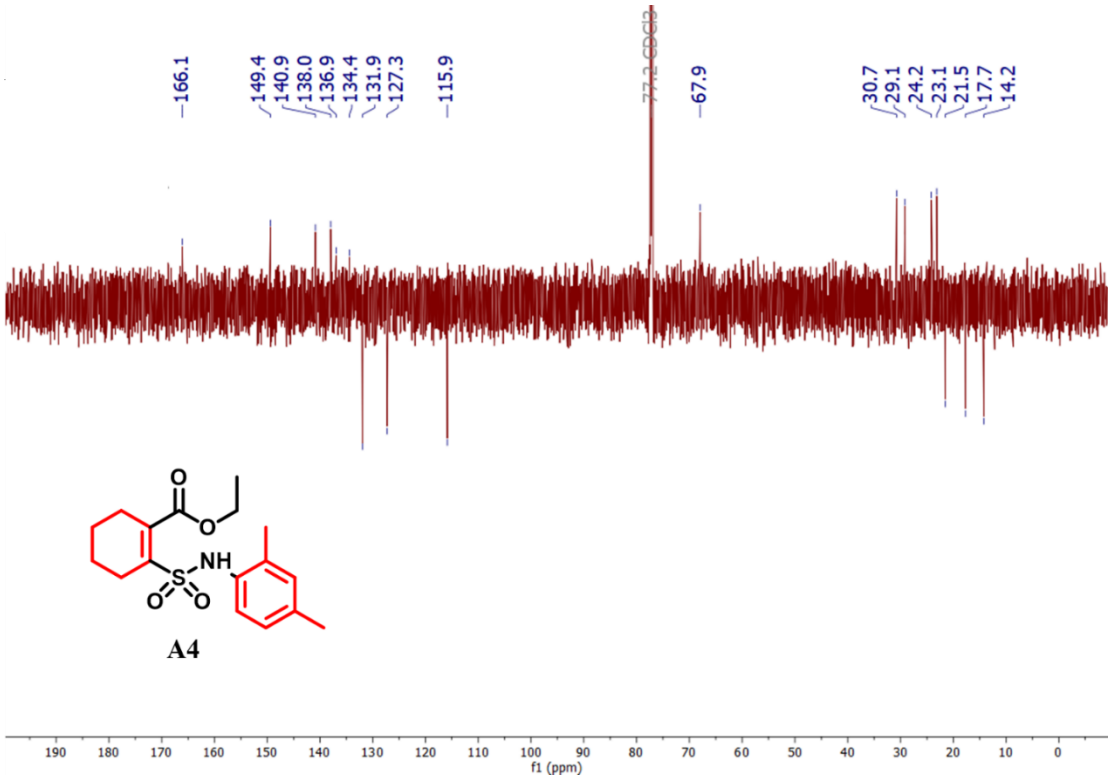
166.1
149.4
140.9
138.0
136.9
134.4
131.9
127.3
115.9
77.2 CDCl3
67.9
30.7
29.1
24.2
23.1
21.5
17.7
14.2
A4
f1 (ppm)

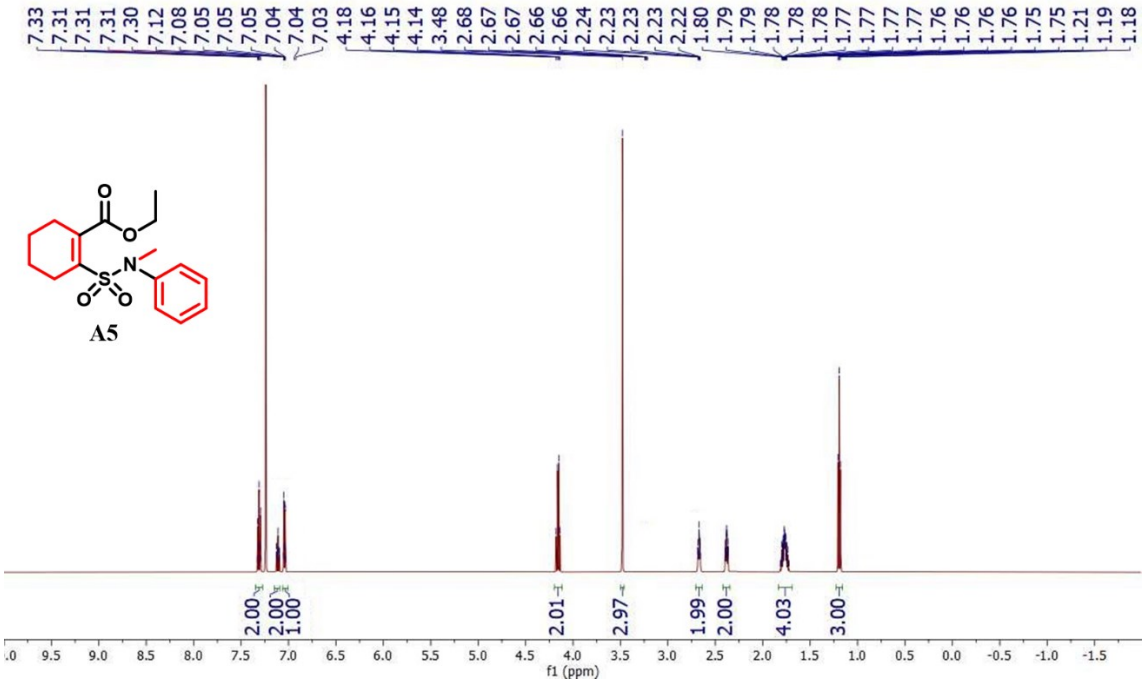
7.33 7.31 7.31 7.31 7.30 7.12 7.08 7.05 7.05 7.05 7.04 7.04 7.03 4.18 4.16 4.15 4.14 3.48 2.68 2.67 2.67 2.66 2.66 2.24 2.23 2.23 2.23 2.22 1.80 1.79 1.79 1.78 1.78 1.78 1.77 1.77 1.77 1.77 1.76 1.76 1.76 1.76 1.75 1.75 1.21 1.19 1.18
O
O
N
S
O
O
A5
2.00 2.00 1.00 2.01 2.97 1.99 2.00 4.03 3.00
f1 (ppm)

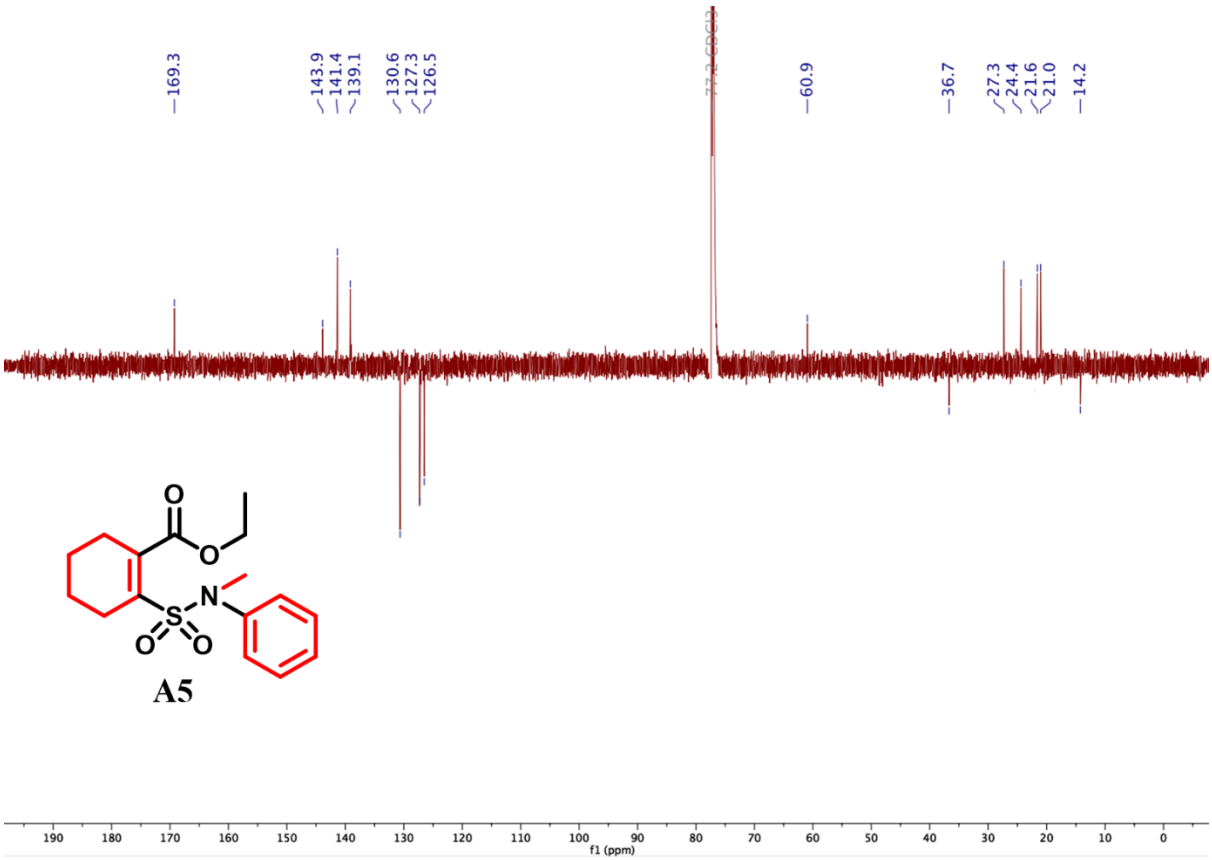
169.3
143.9
141.4
139.1
130.6
127.3
126.5
77.2 CDCl3
60.9
36.7
27.3
24.4
21.6
21.0
14.2
O
O
N
S
O
O
A5
f1 (ppm)

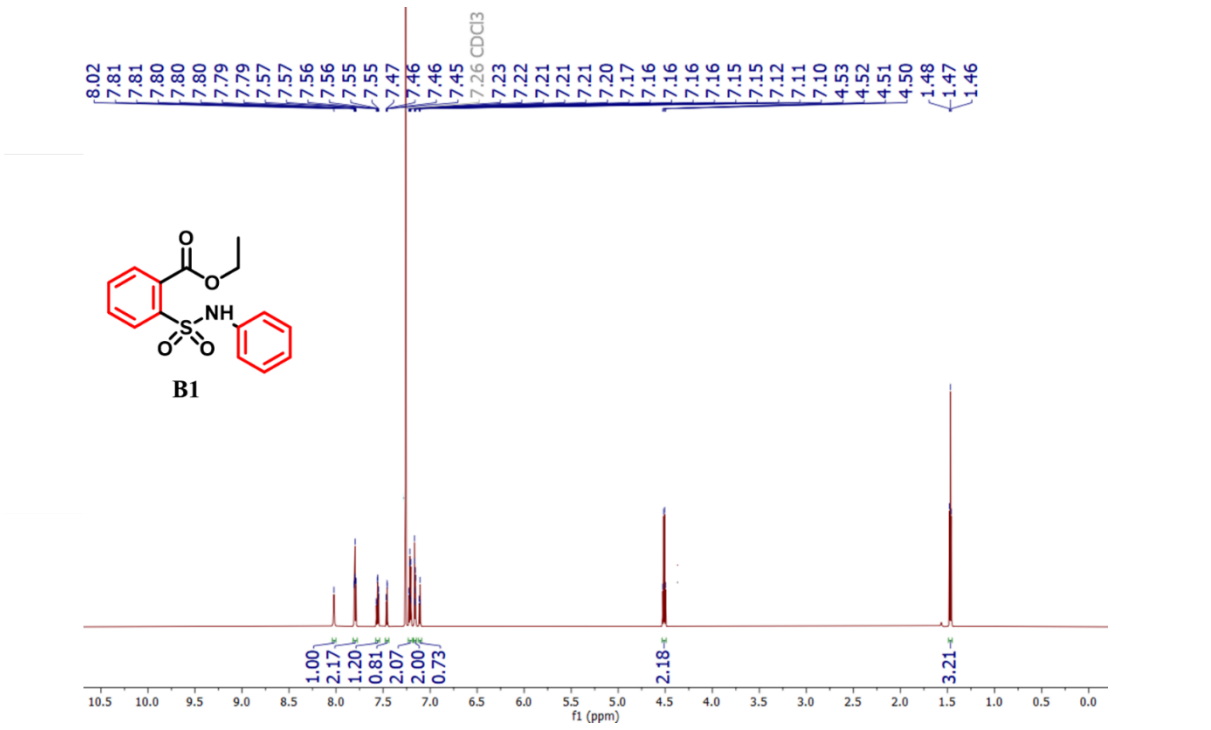
8.02
7.81
7.81
7.80
7.80
7.80
7.79
7.79
7.57
7.57
7.56
7.56
7.55
7.55
7.47
7.46
7.46
7.45
7.26 CDCl3
7.23
7.22
7.21
7.21
7.21
7.20
7.17
7.16
7.16
7.16
7.15
7.15
7.12
7.11
7.10
4.53
4.52
4.51
4.50
1.48
1.47
1.46
O
O
NH
S
O
O
B1
1.00
2.17
1.20
0.81
2.07
2.00
0.73
2.18
3.21
f1 (ppm)

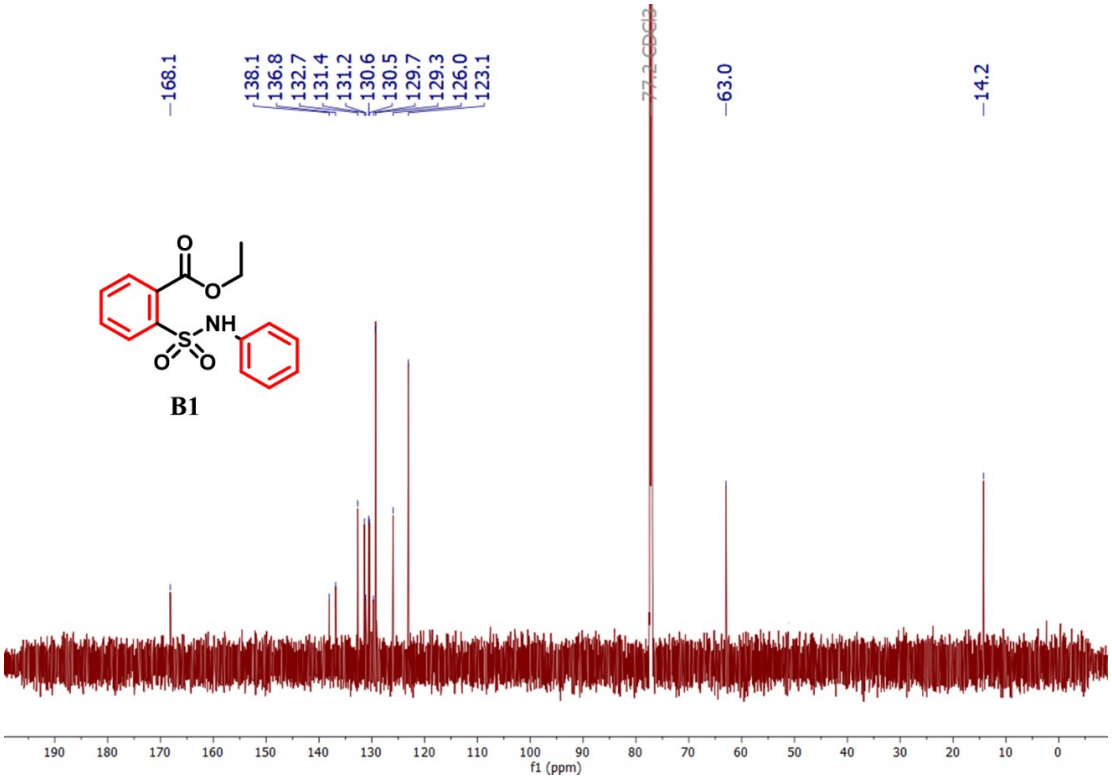
168.1
138.1
136.8
132.7
131.4
131.2
130.6
130.5
129.7
129.3
126.0
123.1
77.2 CDCl3
63.0
14.2
O
O
NH
S
O
O
B1
190 180 170 160 150 140 130 120 110 100 90 80 70 60 50 40 30 20 10 0
f1 (ppm)

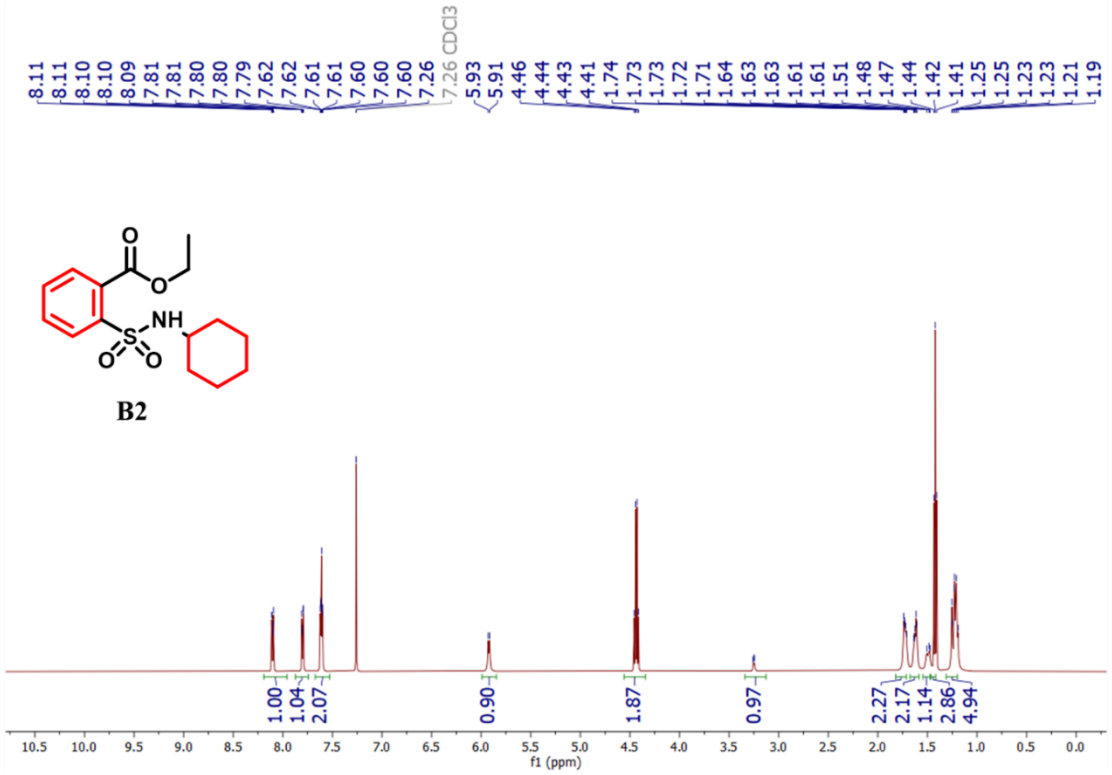
8.11
8.11
8.10
8.10
8.09
7.81
7.81
7.80
7.80
7.79
7.62
7.62
7.61
7.61
7.60
7.60
7.60
7.26
7.26 CDCl3
5.93
5.91
4.46
4.44
4.43
4.41
1.74
1.73
1.73
1.72
1.71
1.64
1.63
1.63
1.61
1.61
1.51
1.48
1.47
1.44
1.42
1.41
1.25
1.25
1.23
1.23
1.21
1.19
O
O
NH
S
O
O
B2
1.00
1.04
2.07
0.90
1.87
0.97
2.27
2.17
1.14
2.86
4.94
10.5 10.0 9.5 9.0 8.5 8.0 7.5 7.0 6.5 6.0 5.5 5.0 4.5 4.0 3.5 3.0 2.5 2.0 1.5 1.0 0.5 0.0
f1 (ppm)

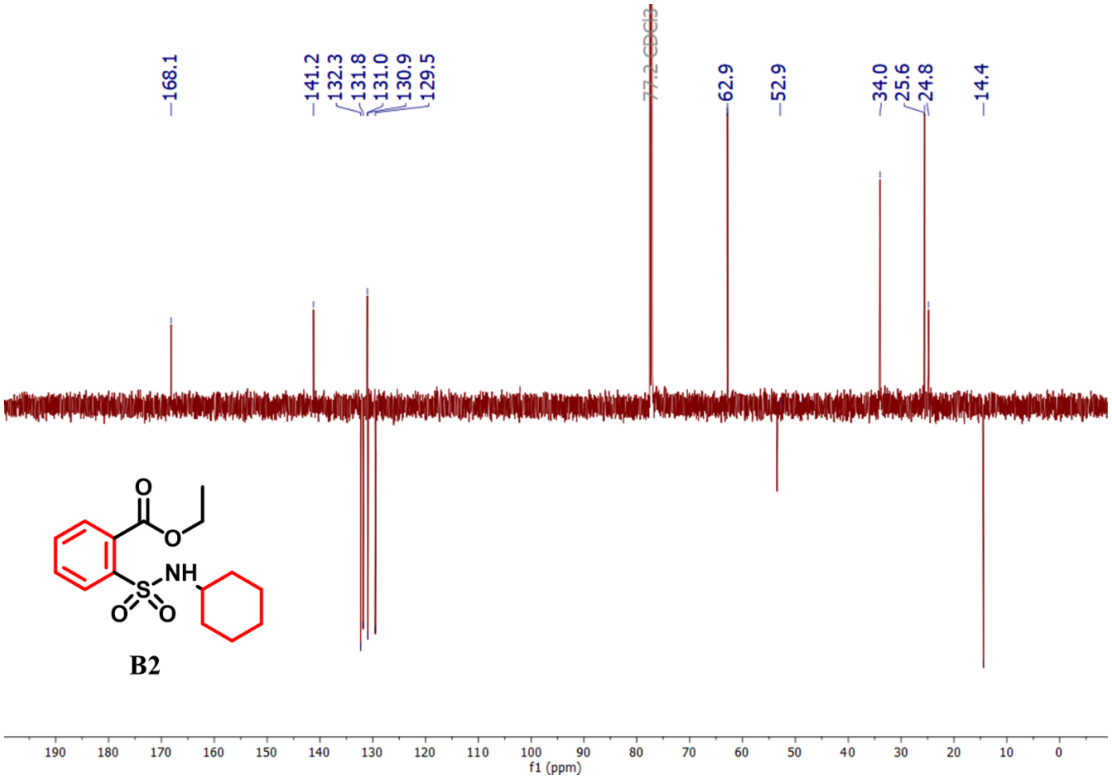
168.1
141.2
132.3
131.8
131.0
130.9
129.5
77.2 CDCl3
62.9
52.9
34.0
25.6
24.8
14.4
O
O
NH
S
O
O
B2
190 180 170 160 150 140 130 120 110 100 90 80 70 60 50 40 30 20 10 0
f1 (ppm)

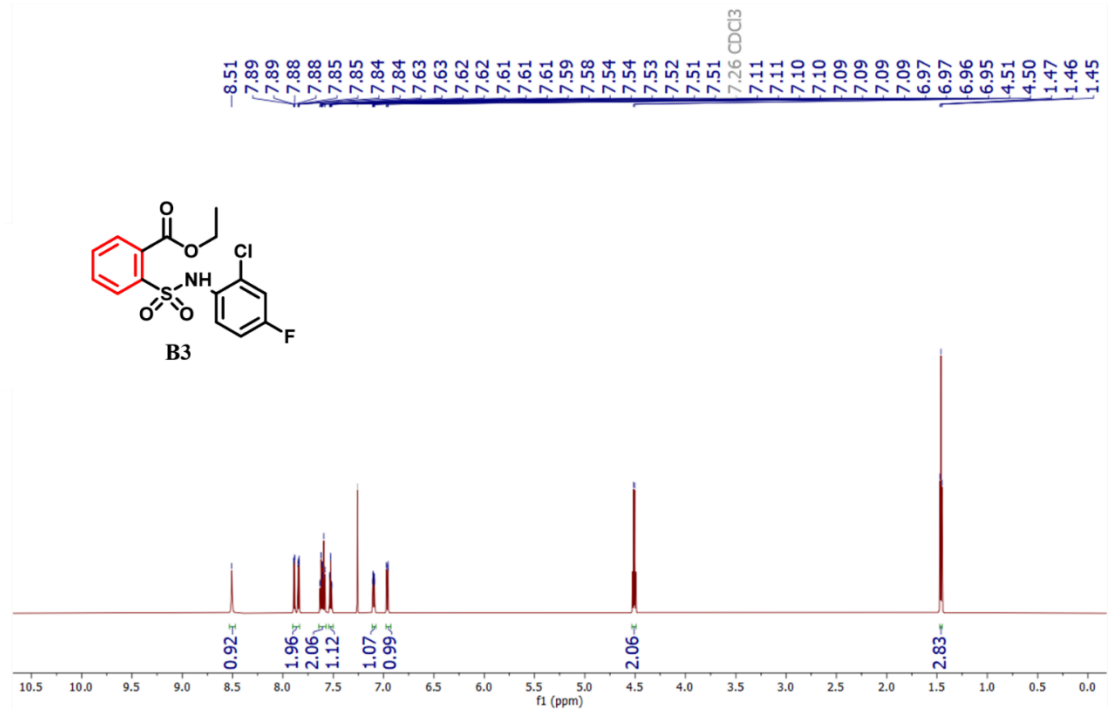
8.51
7.89
7.89
7.88
7.88
7.85
7.85
7.84
7.84
7.63
7.63
7.62
7.62
7.61
7.61
7.61
7.59
7.58
7.54
7.54
7.53
7.52
7.51
7.51
7.26 CDCl3
7.11
7.11
7.10
7.10
7.09
7.09
7.09
7.09
6.97
6.97
6.96
6.95
4.51
4.50
1.47
1.46
1.45
O
O
NH
Cl
S
O
O
F
B3
0.92
1.96
2.06
1.12
1.07
0.99
2.06
2.83
10.5 10.0 9.5 9.0 8.5 8.0 7.5 7.0 6.5 6.0 5.5 5.0 4.5 4.0 3.5 3.0 2.5 2.0 1.5 1.0 0.5 0.0
f1 (ppm)

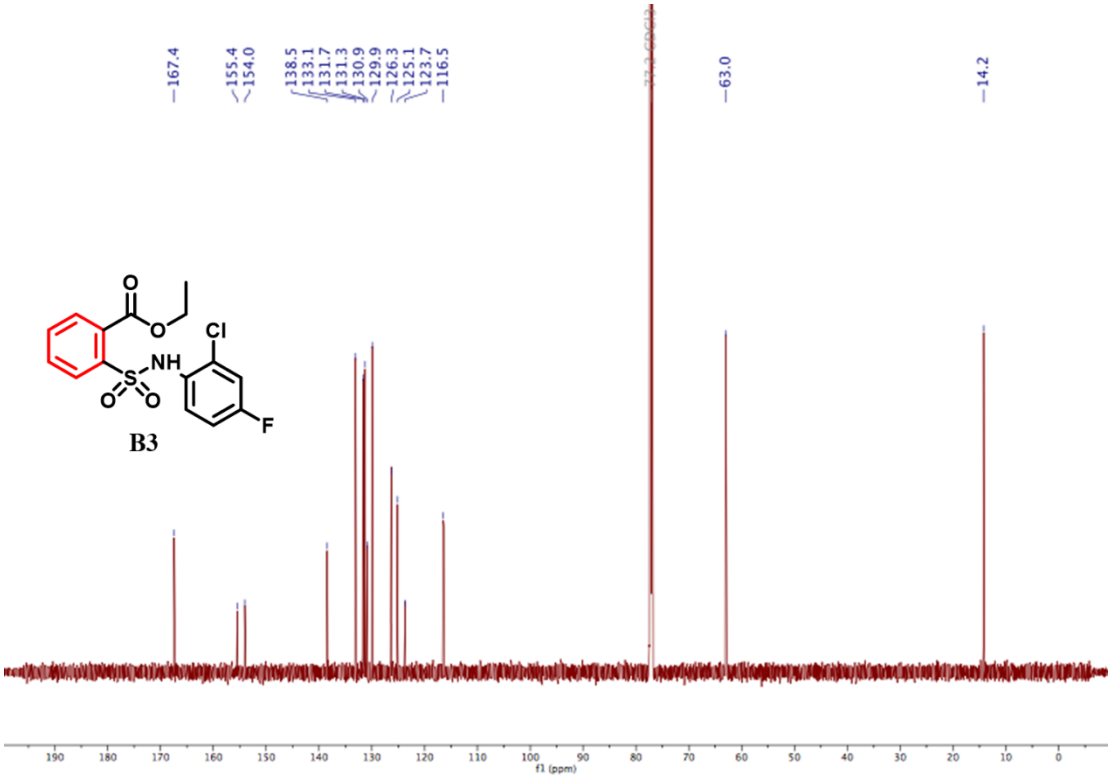
167.4
155.4
154.0
138.5
133.1
131.7
131.3
130.9
129.9
126.3
125.1
123.7
116.5
77.3 CDCl3
63.0
14.2
O
O
Cl
NH
S
O
O
F
B3
190
180
170
160
150
140
130
120
110
100
90
80
70
60
50
40
30
20
10
0
f1 (ppm)

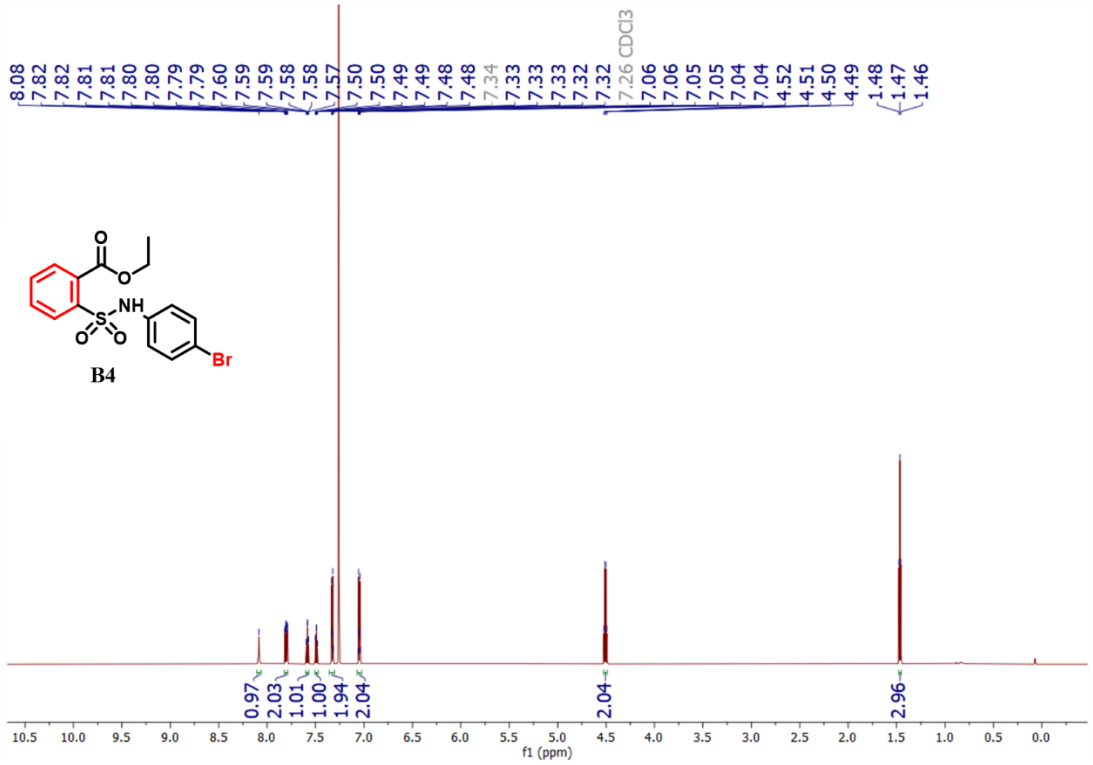
8.08
7.82
7.82
7.81
7.81
7.80
7.80
7.79
7.79
7.60
7.59
7.59
7.58
7.58
7.57
7.50
7.50
7.49
7.49
7.48
7.48
7.34
7.33
7.33
7.33
7.32
7.32
7.26 CDCl3
7.06
7.06
7.05
7.05
7.04
7.04
4.52
4.51
4.50
4.49
1.48
1.47
1.46
O
O
NH
S
O
O
Br
B4
0.97
2.03
1.01
1.00
1.94
2.04
2.04
2.96
10.5
10.0
9.5
9.0
8.5
8.0
7.5
7.0
6.5
6.0
5.5
5.0
4.5
4.0
3.5
3.0
2.5
2.0
1.5
1.0
0.5
0.0
f1 (ppm)

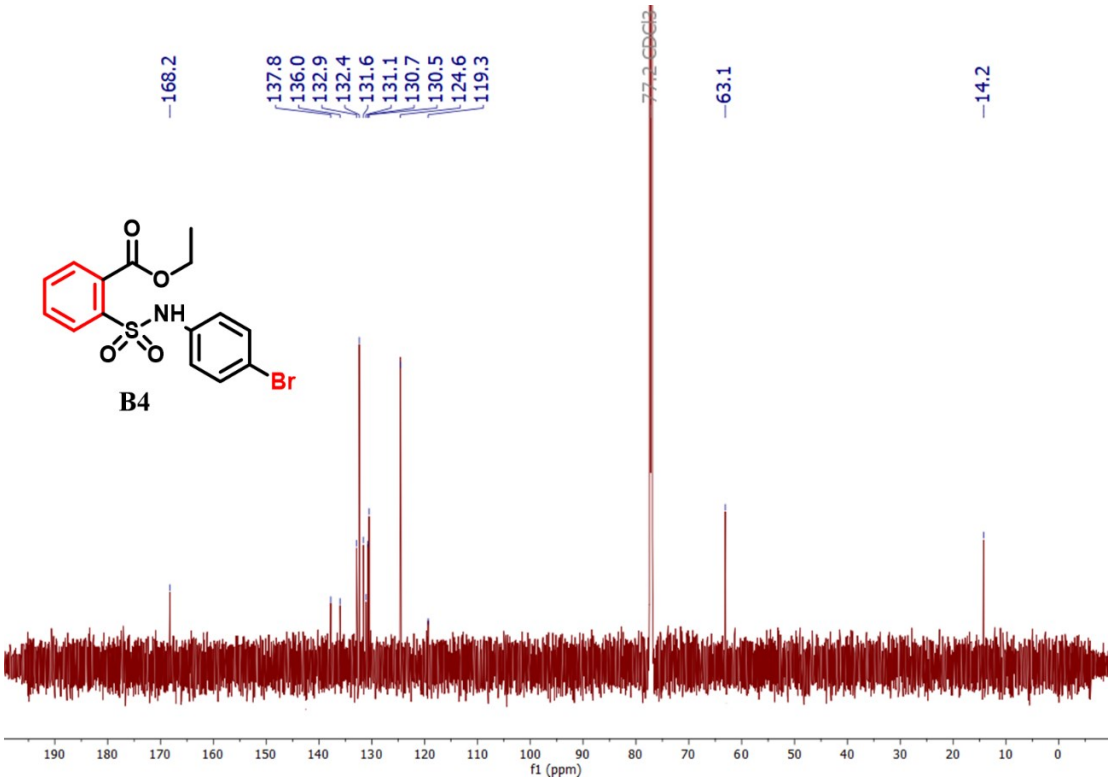
168.2
137.8
136.0
132.9
132.4
131.6
131.1
130.7
130.5
124.6
119.3
77.2 CDCl3
63.1
14.2
O
O
NH
S
O
O
Br
B4
190
180
170
160
150
140
130
120
110
100
90
80
70
60
50
40
30
20
10
0
f1 (ppm)

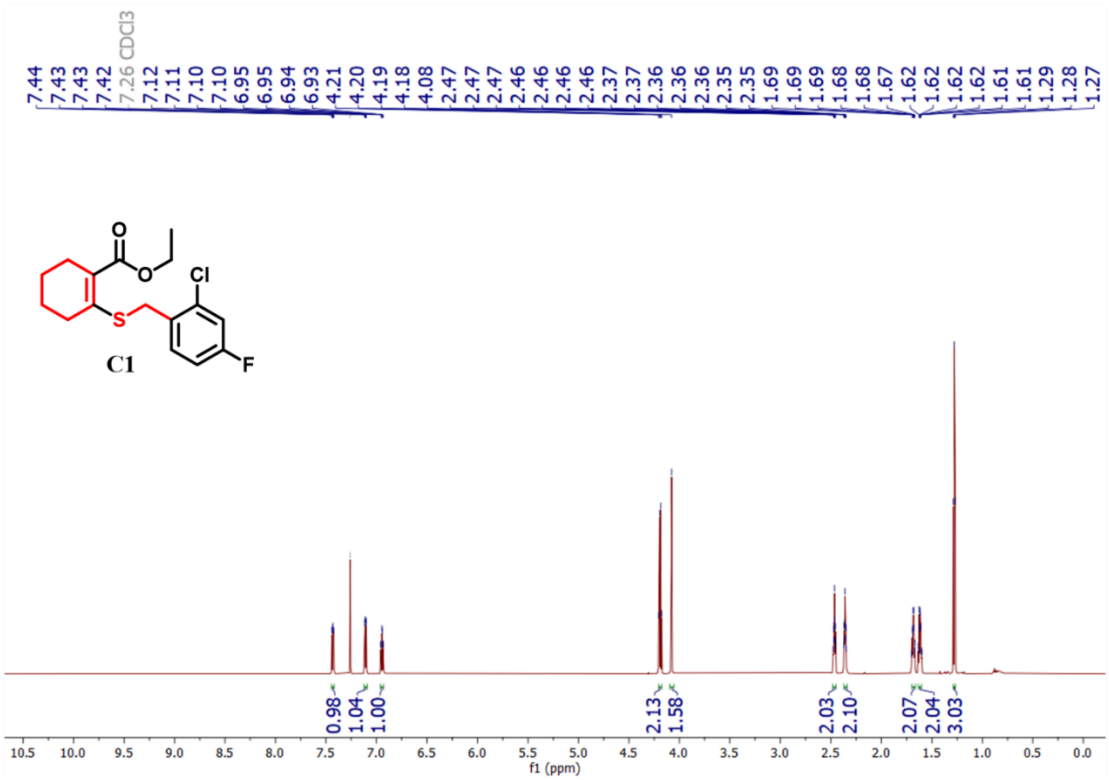
7.44 7.43 7.43 7.42 7.26 CDCl3 7.12 7.11 7.10 7.10 6.95 6.94 6.93 4.21 4.20 4.19 4.18 4.08 2.47 2.47 2.47 2.46 2.46 2.46 2.46 2.37 2.37 2.36 2.36 2.36 2.35 2.35 1.69 1.69 1.69 1.68 1.68 1.67 1.62 1.62 1.62 1.62 1.61 1.61 1.29 1.28 1.27
O
O
Cl
S
F
C1
0.98 1.04 1.00 2.13 1.58 2.03 2.10 2.07 2.04 3.03
10.5 10.0 9.5 9.0 8.5 8.0 7.5 7.0 6.5 6.0 5.5 5.0 4.5 4.0 3.5 3.0 2.5 2.0 1.5 1.0 0.5 0.0
f1 (ppm)

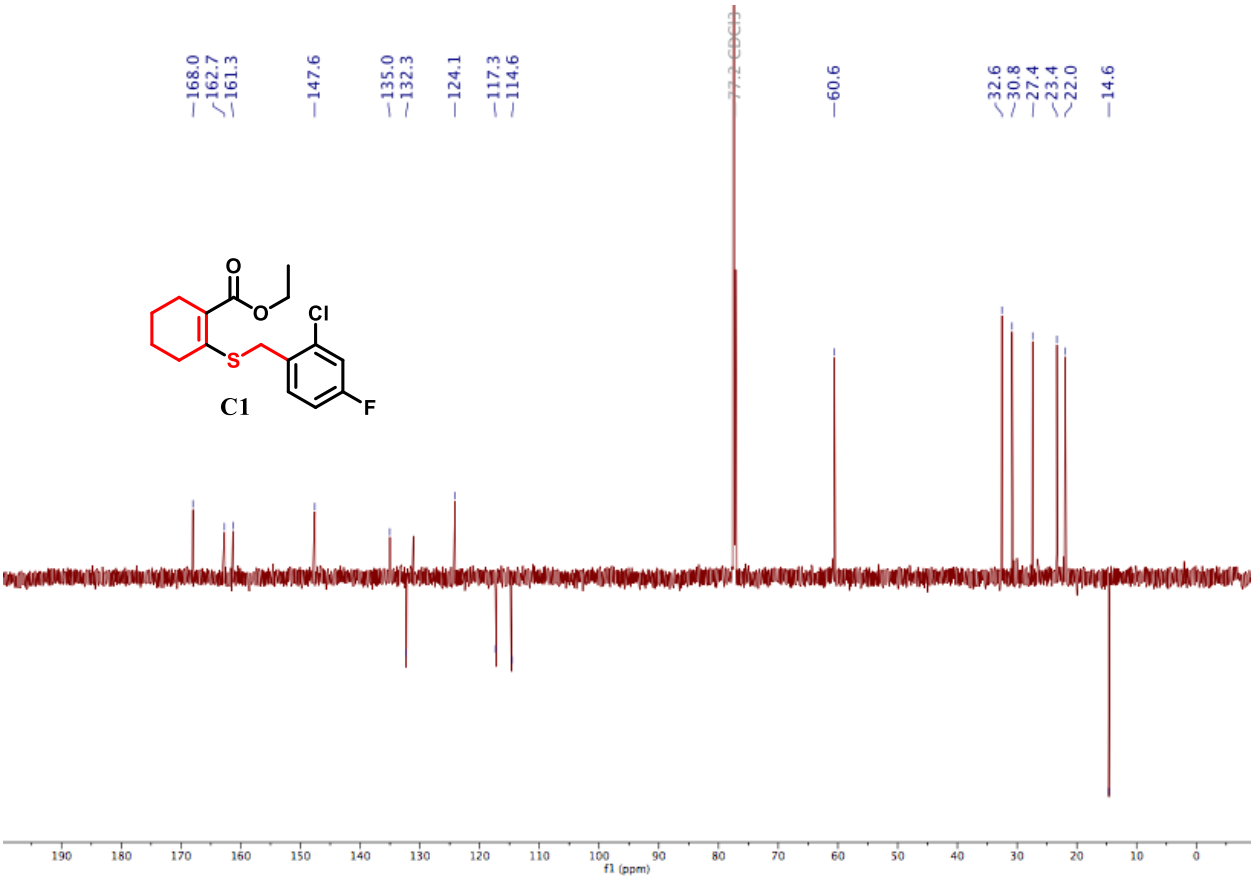
168.0 162.7 161.3 147.6 135.0 132.3 124.1 117.3 114.6 77.2 CDCl3 60.6 32.6 30.8 27.4 23.4 22.0 14.6
O
O
Cl
S
F
C1
190 180 170 160 150 140 130 120 110 100 90 80 70 60 50 40 30 20 10 0
f1 (ppm)

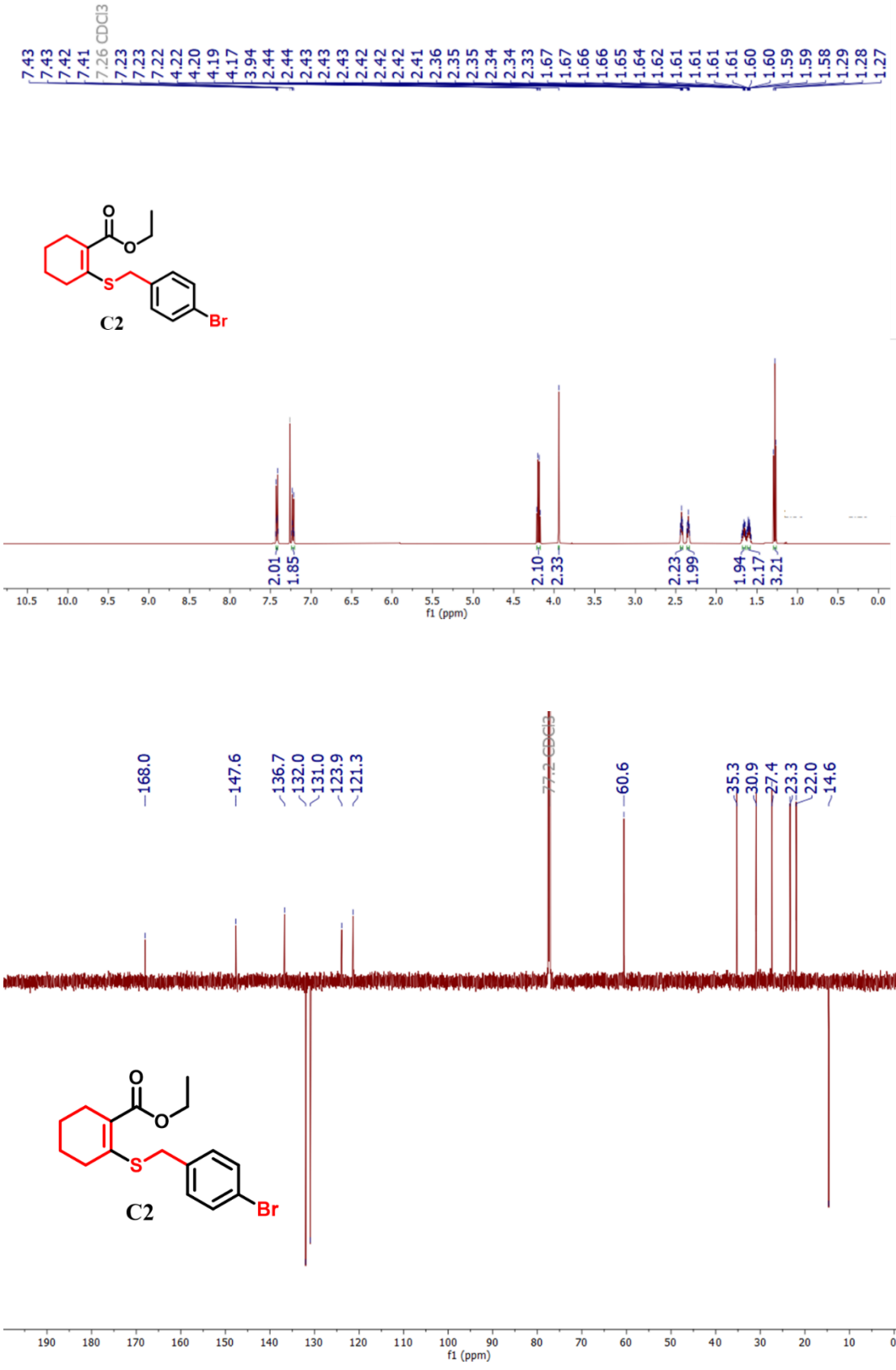
7.43
7.43
7.42
7.41
7.26 CDCl3
7.23
7.23
7.22
4.22
4.20
4.19
4.17
3.94
2.44
2.44
2.43
2.43
2.43
2.42
2.42
2.42
2.41
2.36
2.35
2.35
2.34
2.34
2.33
1.67
1.67
1.66
1.66
1.65
1.64
1.62
1.61
1.61
1.61
1.61
1.60
1.60
1.59
1.59
1.58
1.29
1.28
1.27
O
O
S
Br
C2
2.01
1.85
2.10
2.33
2.23
1.99
1.94
2.17
3.21
f1 (ppm)
168.0
147.6
136.7
132.0
131.0
123.9
121.3
77.2 CDCl3
60.6
35.3
30.9
27.4
23.3
22.0
14.6
f1 (ppm)

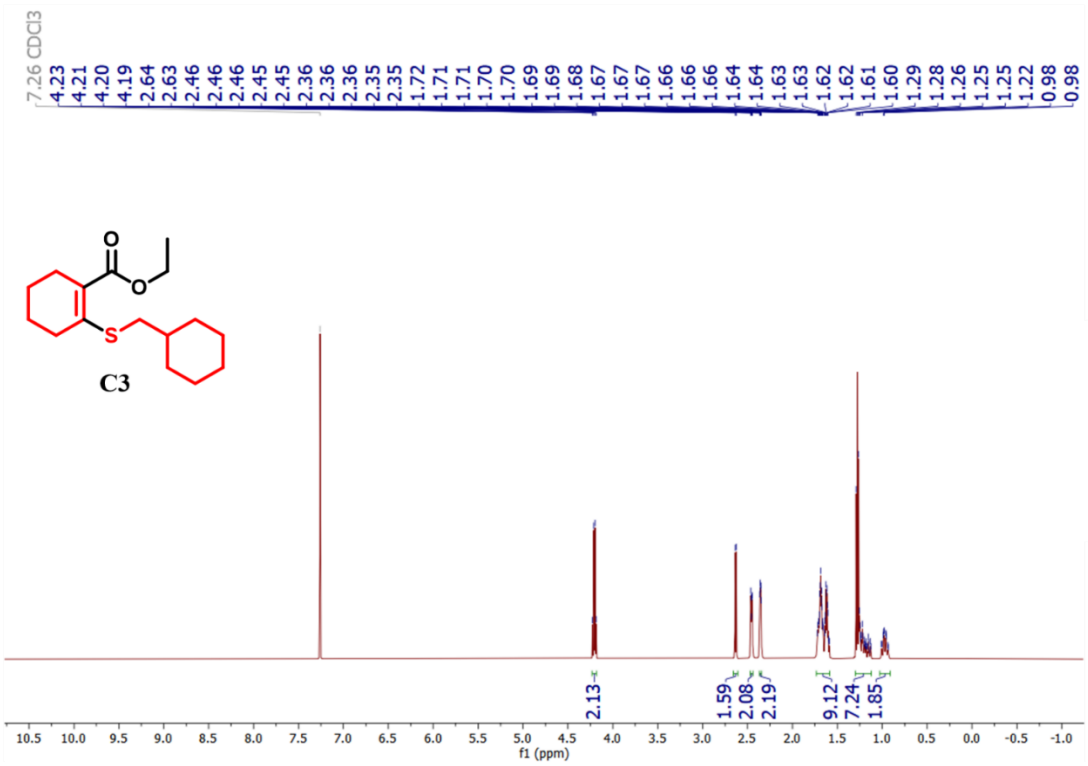
7.26 CDCl3
4.23 4.21 4.20 4.19 2.64 2.63 2.46 2.46 2.46 2.45 2.45 2.36 2.36 2.36 2.35 2.35 1.72 1.71 1.71 1.70 1.70 1.69 1.69 1.68 1.67 1.67 1.67 1.66 1.66 1.66 1.64 1.64 1.63 1.63 1.62 1.62 1.61 1.60 1.29 1.28 1.26 1.25 1.25 1.22 0.98 0.98
C3
2.13
1.59
2.08
2.19
9.12
7.24
1.85
f1 (ppm)

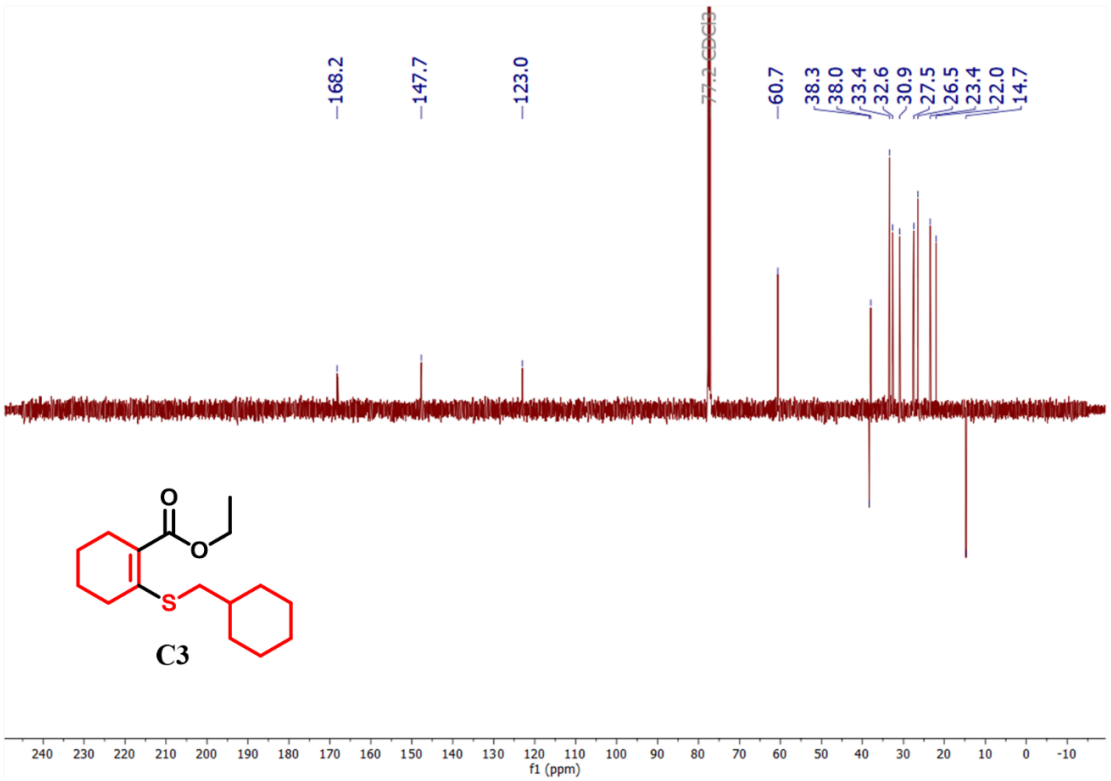
168.2
147.7
123.0
77.2 CDCl3
60.7
38.3
38.0
33.4
32.6
30.9
27.5
26.5
23.4
22.0
14.7
C3
f1 (ppm)

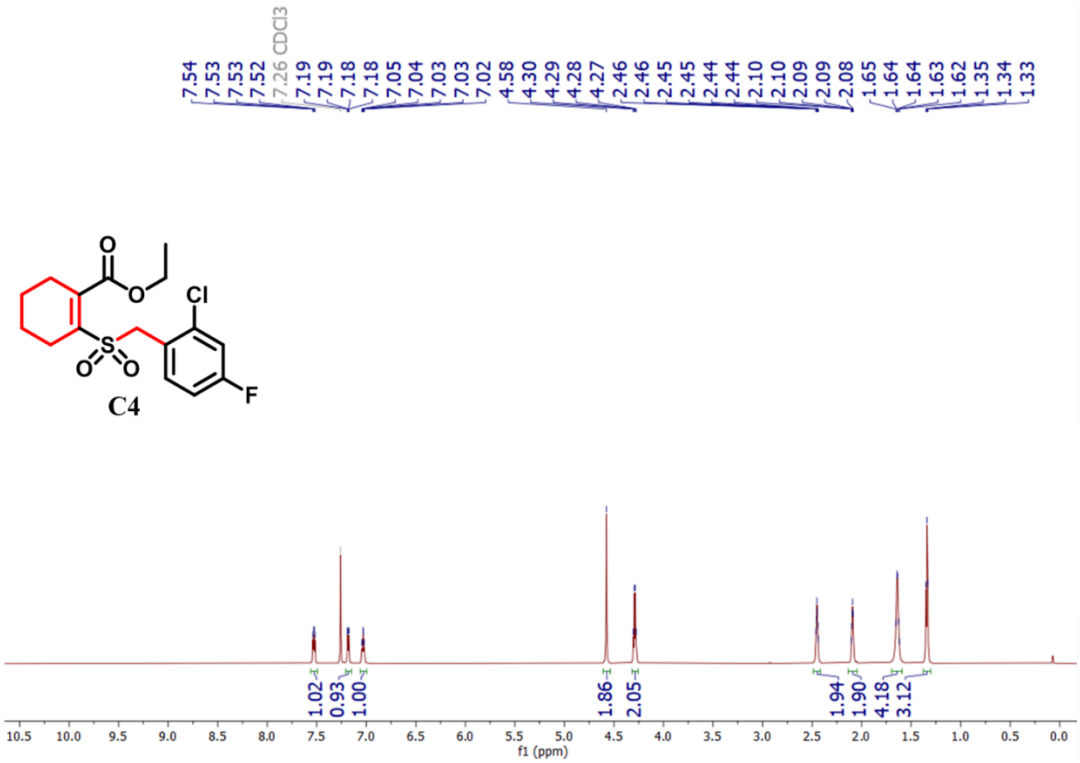
7.54
7.53
7.53
7.52
7.26 CDCl3
7.19
7.19
7.18
7.18
7.05
7.04
7.03
7.03
7.02
4.58
4.30
4.29
4.28
4.27
2.46
2.46
2.45
2.45
2.44
2.44
2.10
2.10
2.09
2.09
2.08
1.65
1.64
1.64
1.63
1.62
1.35
1.34
1.33
O
O
Cl
S
O
O
F
C4
1.02
0.93
1.00
1.86
2.05
1.94
1.90
4.18
3.12
f1 (ppm)

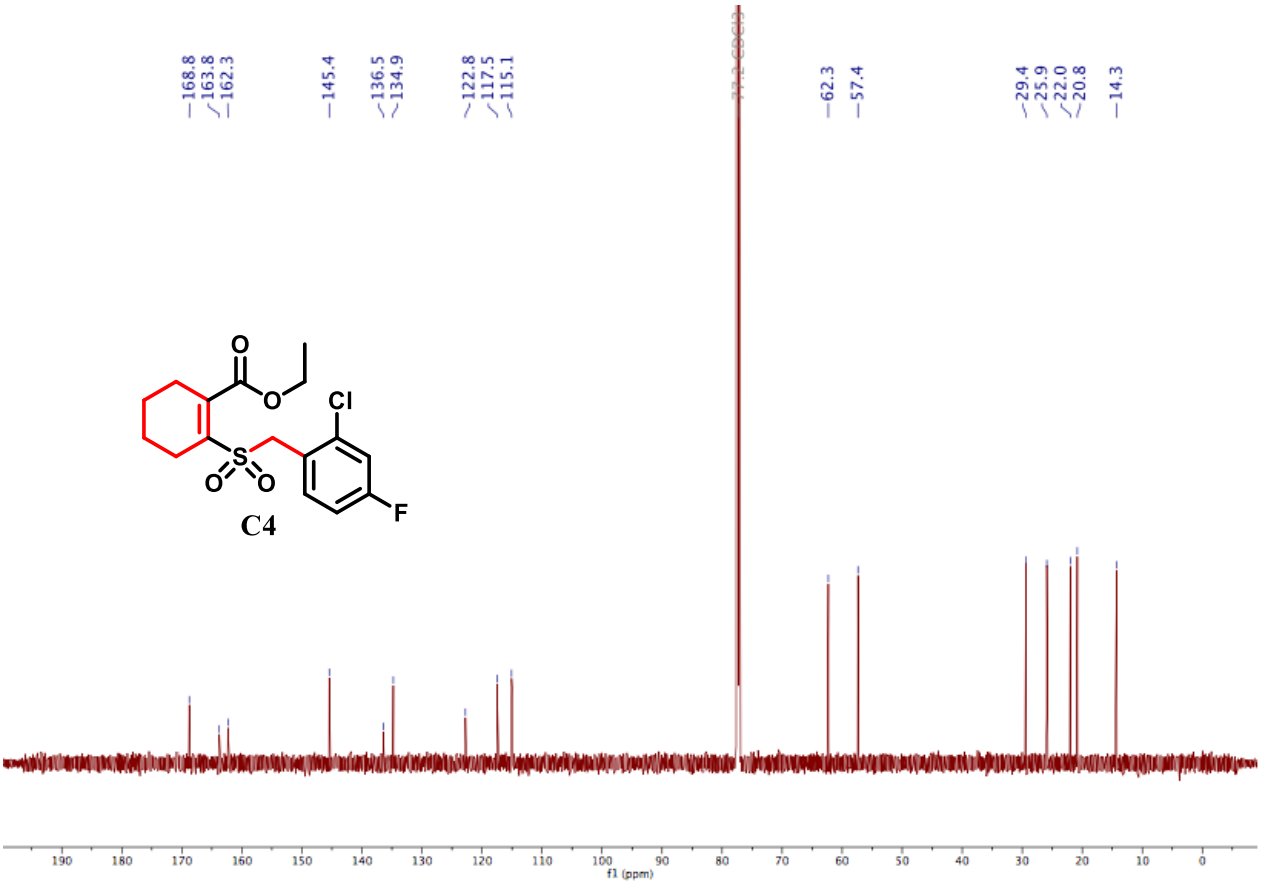
168.8
163.8
162.3
145.4
136.5
134.9
122.8
117.5
115.1
77.2 CDCl3
62.3
57.4
29.4
25.9
22.0
20.8
14.3
O
O
Cl
S
O
O
F
C4
f1 (ppm)

Appendix II: NMR Spectra
(Chapter 4)

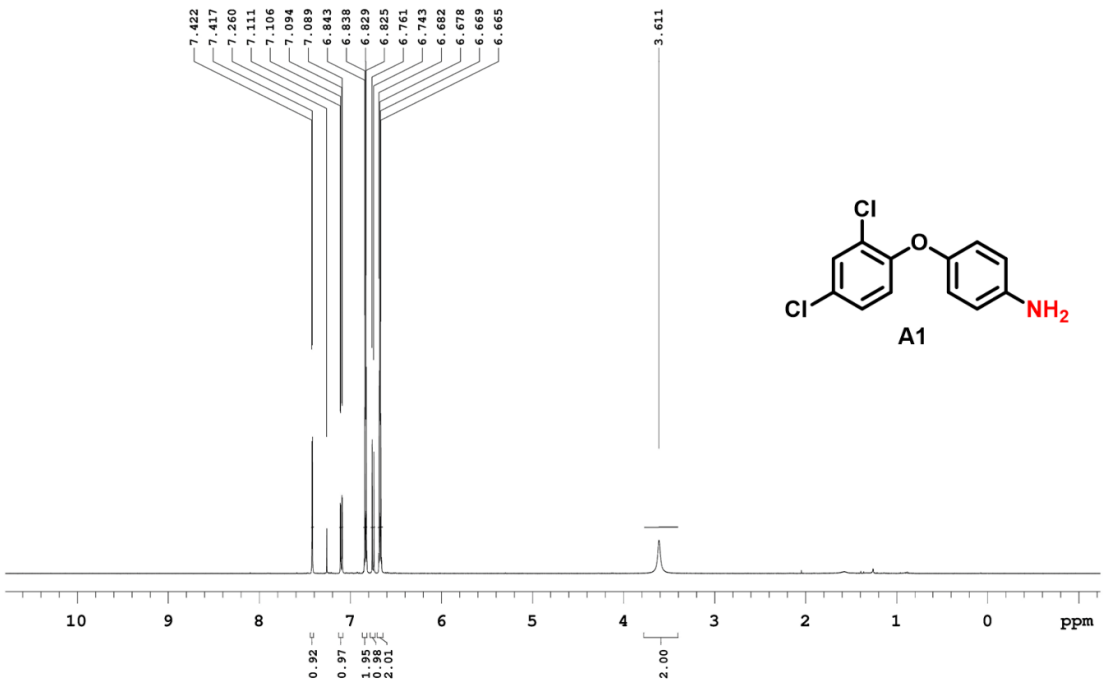
7.422
7.417
7.260
7.111
7.106
7.094
7.089
6.843
6.838
6.829
6.825
6.761
6.743
6.682
6.678
6.669
6.665
3.611
Cl
O
Cl
NH2
A1
10
9
8
7
6
5
4
3
2
1
0
ppm
0.92
0.97
1.95
0.98
2.01
2.00

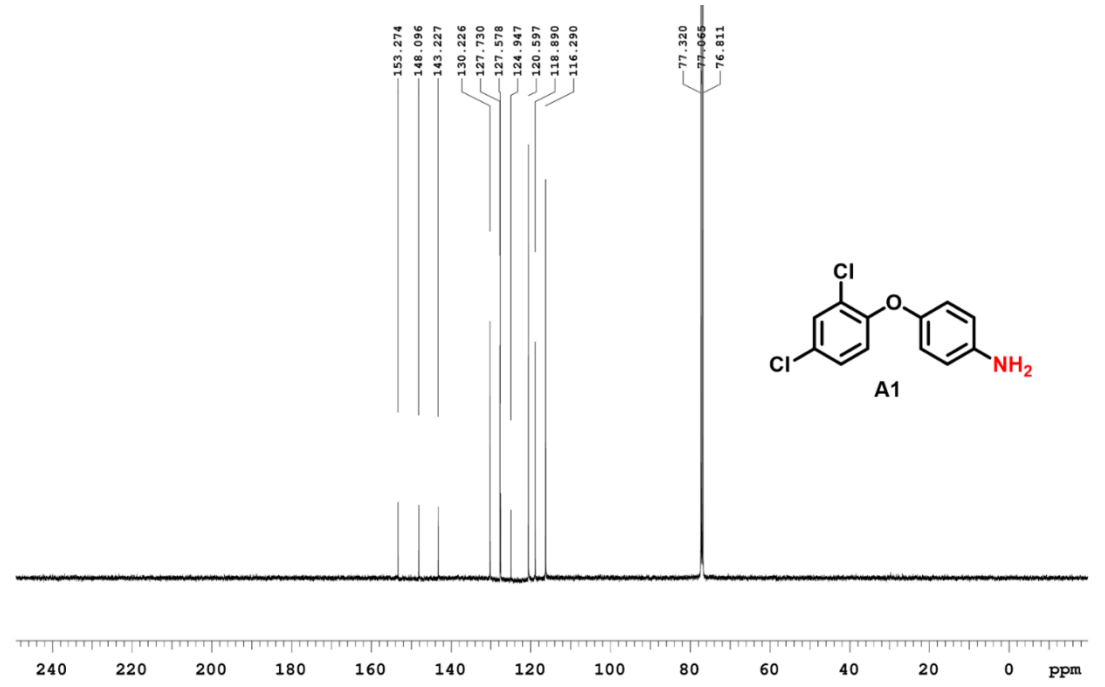
153.274
148.096
143.227
130.226
127.730
127.578
124.947
120.597
118.890
116.290
77.320
77.065
76.811
Cl
O
Cl
NH2
A1
240
220
200
180
160
140
120
100
80
60
40
20
0
ppm

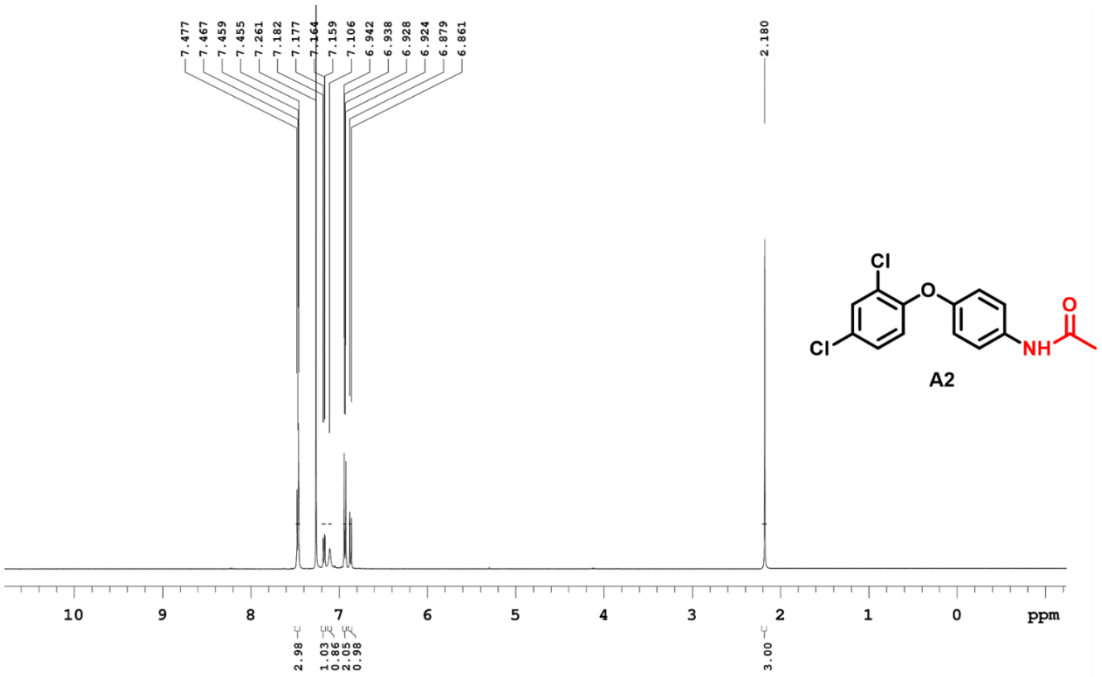
7.477
7.467
7.459
7.455
7.261
7.182
7.177
7.164
7.159
7.106
6.942
6.938
6.928
6.924
6.879
6.861
2.180
Cl
O
Cl
NH
O
A2
10
9
8
7
6
5
4
3
2
1
0
ppm
2.98
1.03
0.86
2.05
0.98
3.00

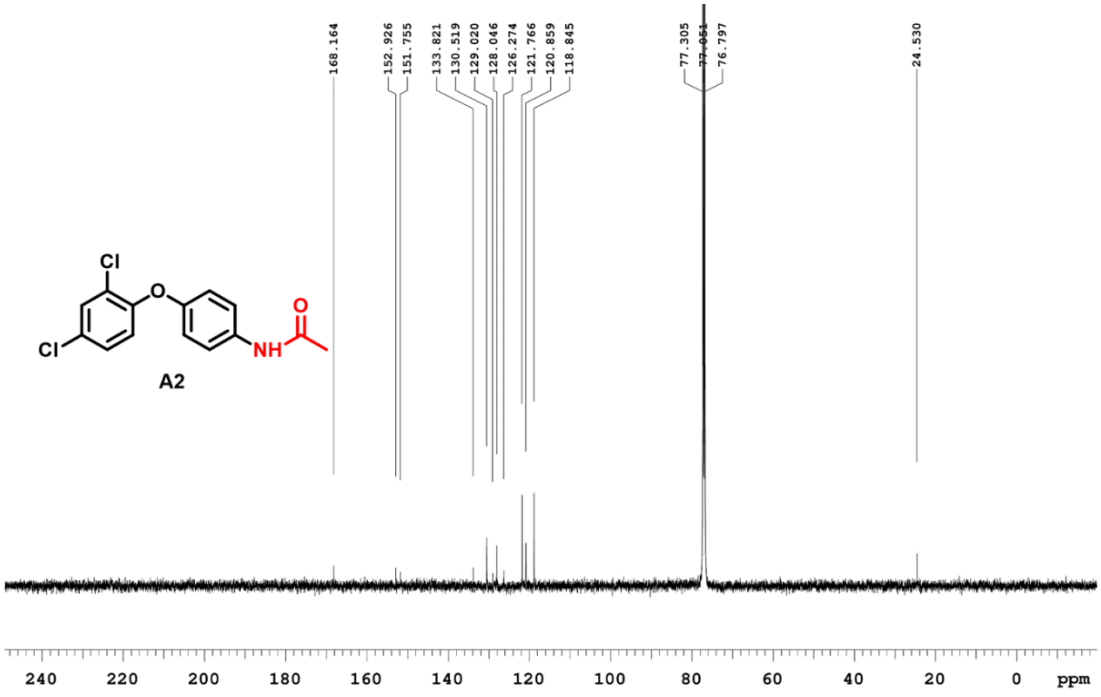
168.164
152.926
151.755
133.821
130.519
129.020
128.046
126.274
121.766
120.859
118.845
77.305
77.054
76.797
24.530
Cl
O
Cl
NH
O
A2
240
220
200
180
160
140
120
100
80
60
40
20
0
ppm

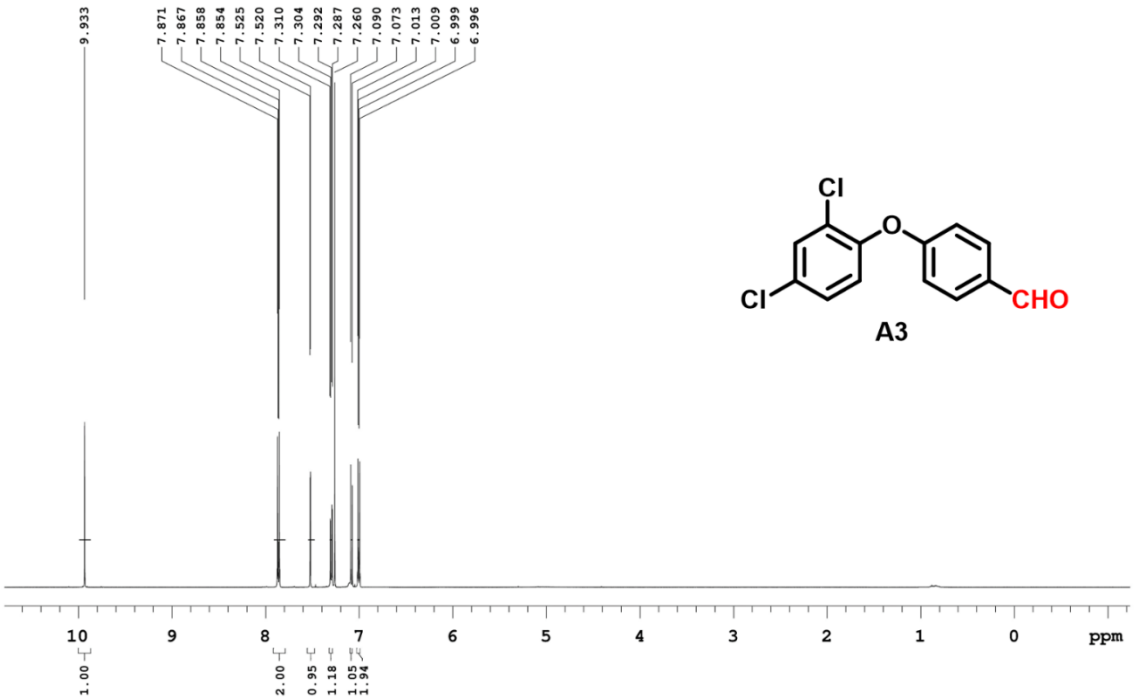
9.933
7.871
7.867
7.858
7.854
7.525
7.520
7.310
7.304
7.292
7.287
7.260
7.090
7.073
7.013
7.009
6.999
6.996
1.00
2.00
0.95
1.18
1.05
1.94
10
9
8
7
6
5
4
3
2
1
0
ppm
Cl
O
Cl
CHO
A3

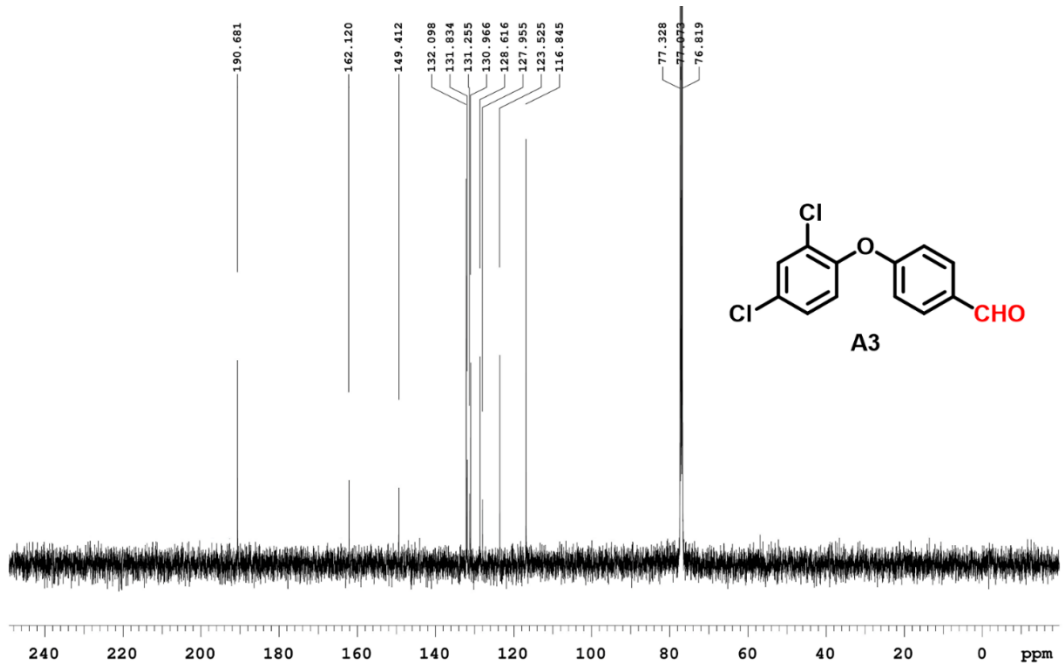
190.681
162.120
149.412
132.098
131.834
131.255
130.966
128.616
127.955
123.525
116.845
77.328
77.073
76.819
240
220
200
180
160
140
120
100
80
60
40
20
0
ppm
Cl
O
Cl
CHO
A3

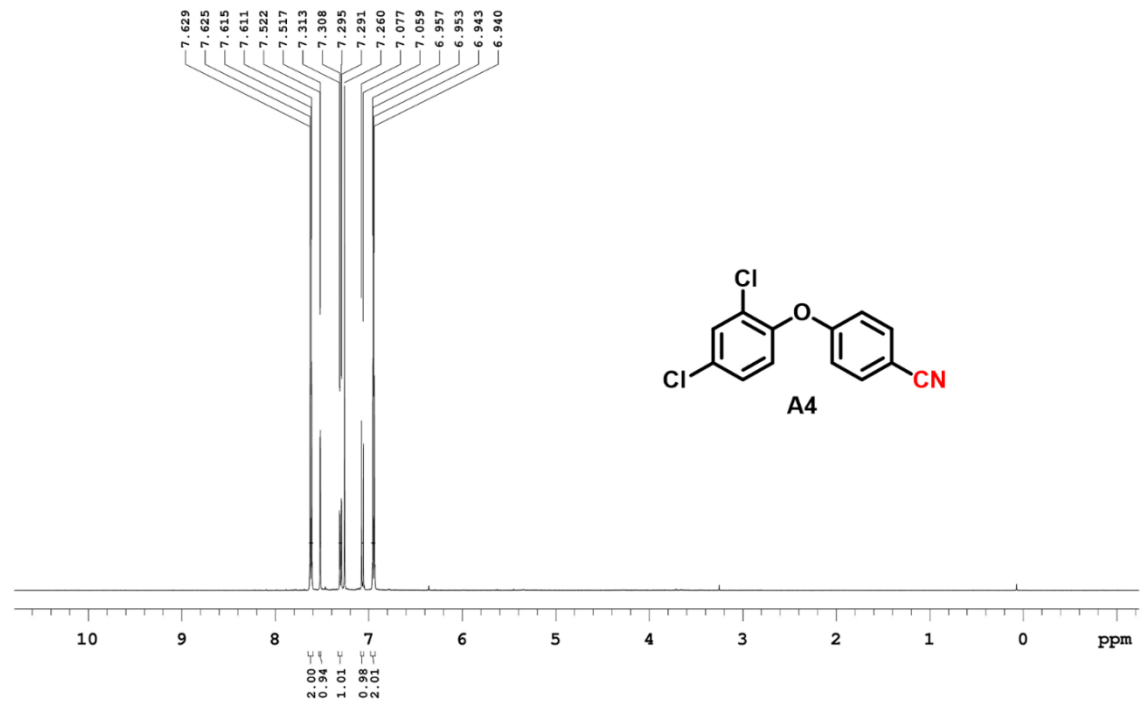
7.629
7.625
7.615
7.611
7.522
7.517
7.313
7.308
7.295
7.291
7.260
7.077
7.059
6.957
6.953
6.943
6.940
Cl
O
Cl
CN
A4
10
9
8
7
6
5
4
3
2
1
0
ppm
2.00
0.94
1.01
0.98
2.01

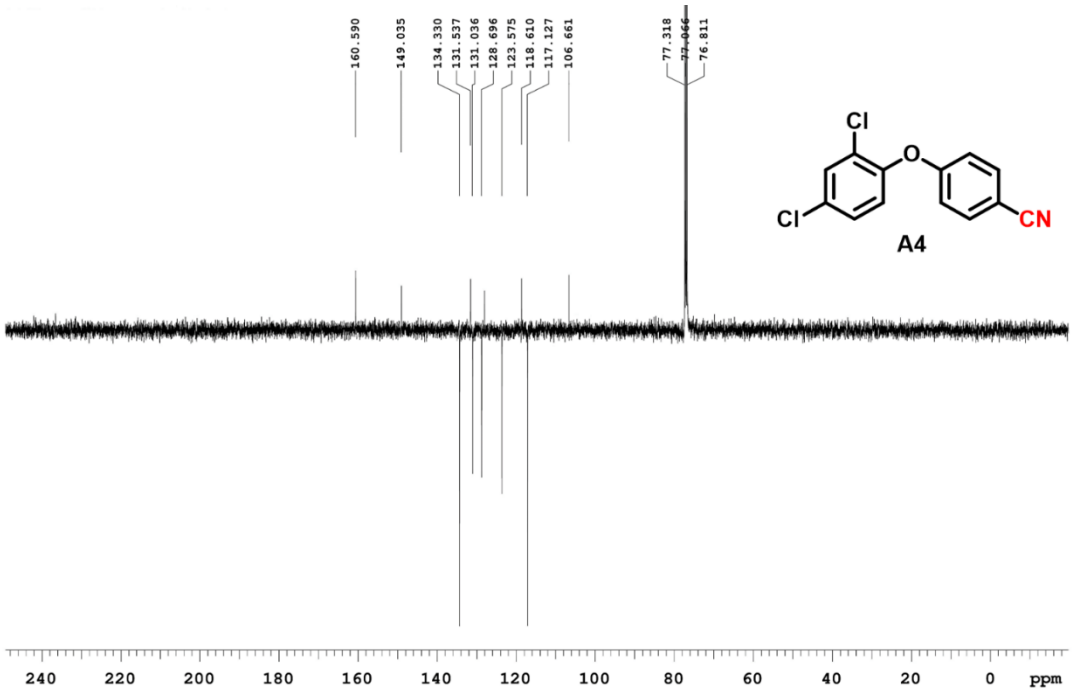
160.590
149.035
134.330
131.537
131.036
128.696
123.575
118.610
117.127
106.661
77.318
77.066
76.811
Cl
O
Cl
CN
A4
240
220
200
180
160
140
120
100
80
60
40
20
0
ppm

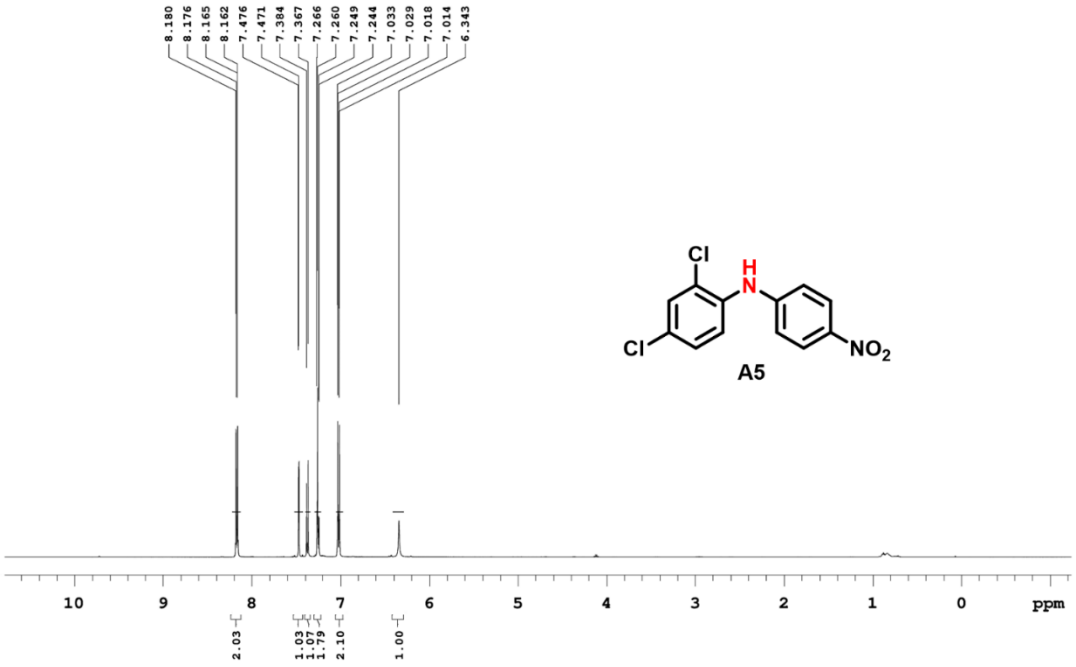
8.180
8.176
8.165
8.162
7.476
7.471
7.384
7.367
7.266
7.260
7.249
7.244
7.033
7.029
7.018
7.014
6.343
Cl
H
N
Cl
NO2
A5
10
9
8
7
6
5
4
3
2
1
0
ppm
2.03
1.03
1.07
1.79
2.10
1.00

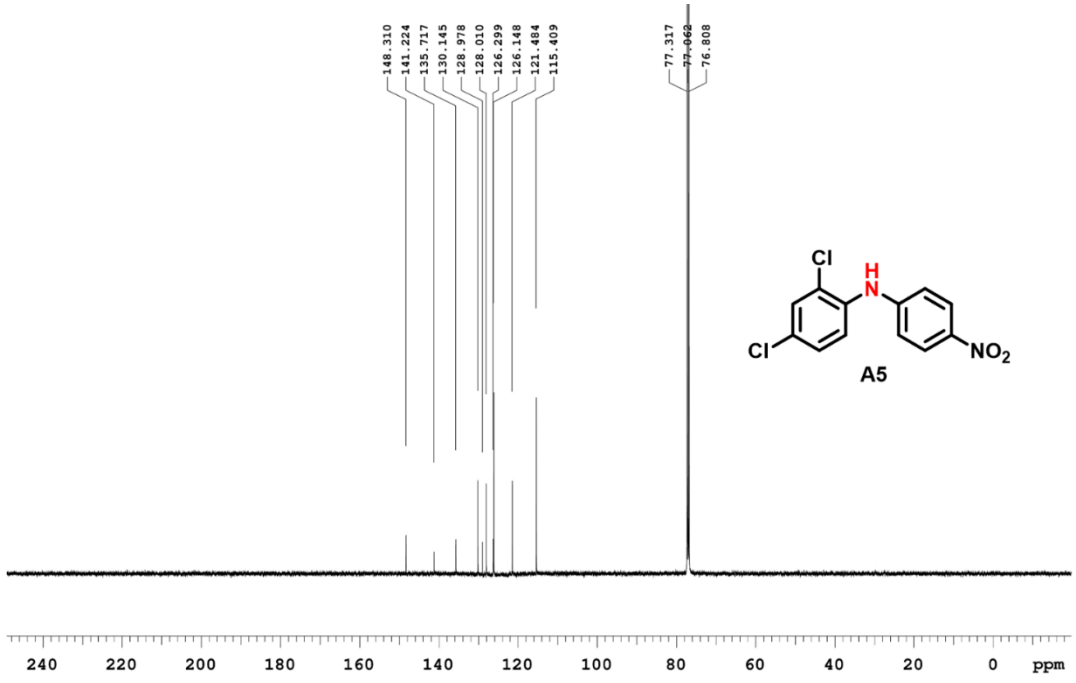
148.310
141.224
135.717
130.145
128.978
128.010
126.299
126.148
121.484
115.409
77.317
77.060
76.808
Cl
H
N
Cl
NO2
A5
240
220
200
180
160
140
120
100
80
60
40
20
0
ppm

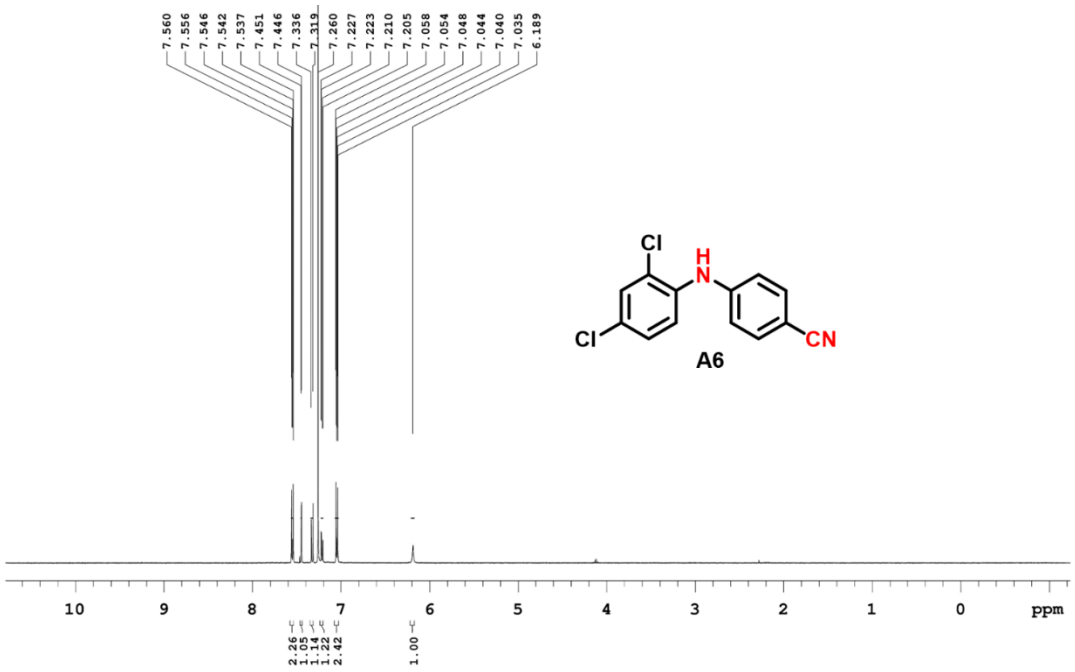
7.560
7.556
7.546
7.542
7.537
7.451
7.446
7.336
7.319
7.260
7.227
7.223
7.210
7.205
7.058
7.054
7.048
7.044
7.040
7.035
6.189
Cl
H
N
Cl
CN
A6
10
9
8
7
6
5
4
3
2
1
0
ppm
2.26
2.05
1.14
1.22
2.42
1.00

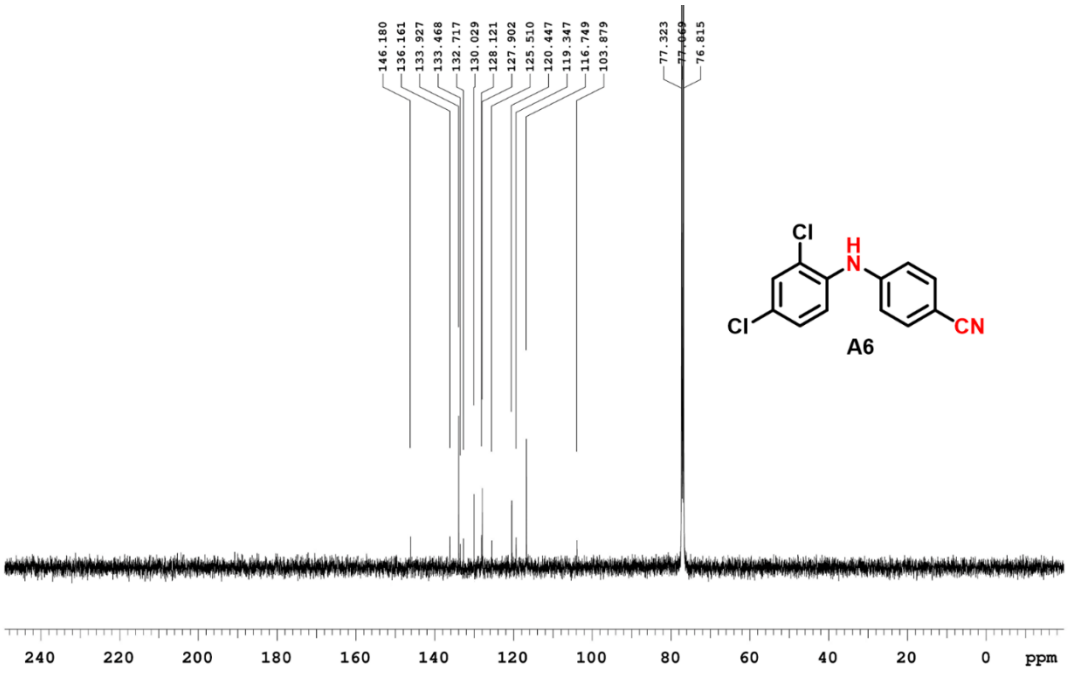
146.180
136.161
133.927
133.468
132.717
130.029
128.121
127.902
125.510
120.447
119.347
116.749
103.879
77.323
77.069
76.815
Cl
H
N
Cl
CN
A6
240
220
200
180
160
140
120
100
80
60
40
20
0
ppm

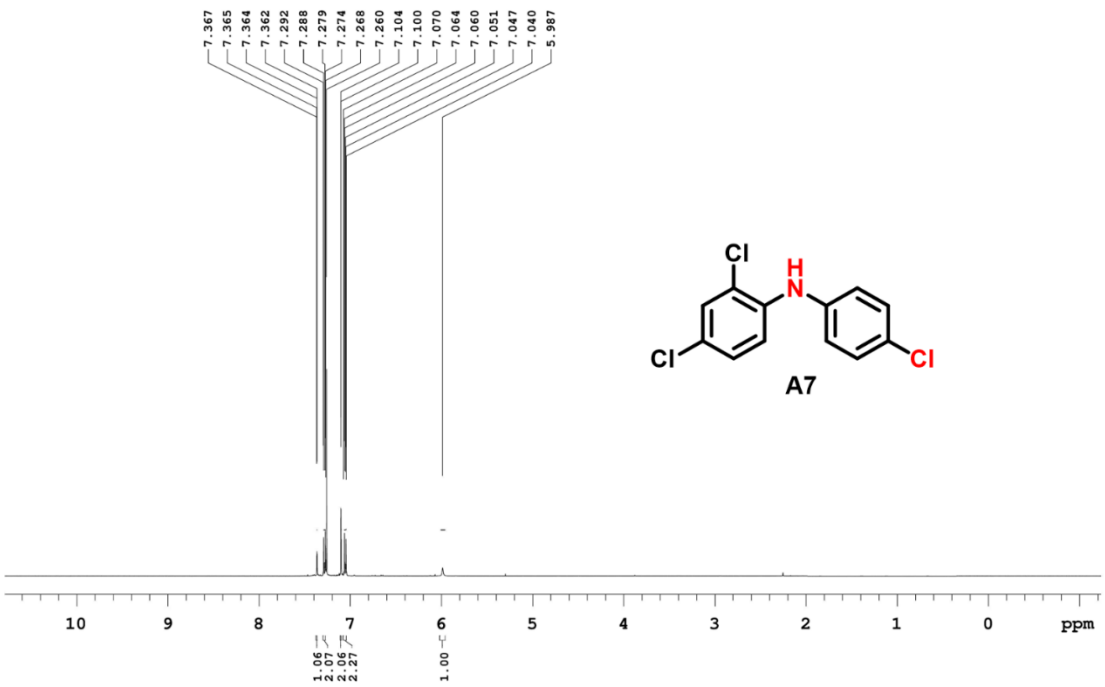
7.367
7.365
7.364
7.362
7.292
7.288
7.279
7.274
7.268
7.260
7.104
7.100
7.070
7.064
7.060
7.051
7.047
7.040
5.987
Cl
H
N
Cl
Cl
A7
10
9
8
7
6
5
4
3
2
1
0
ppm
1.06
2.07
2.06
2.27
1.00

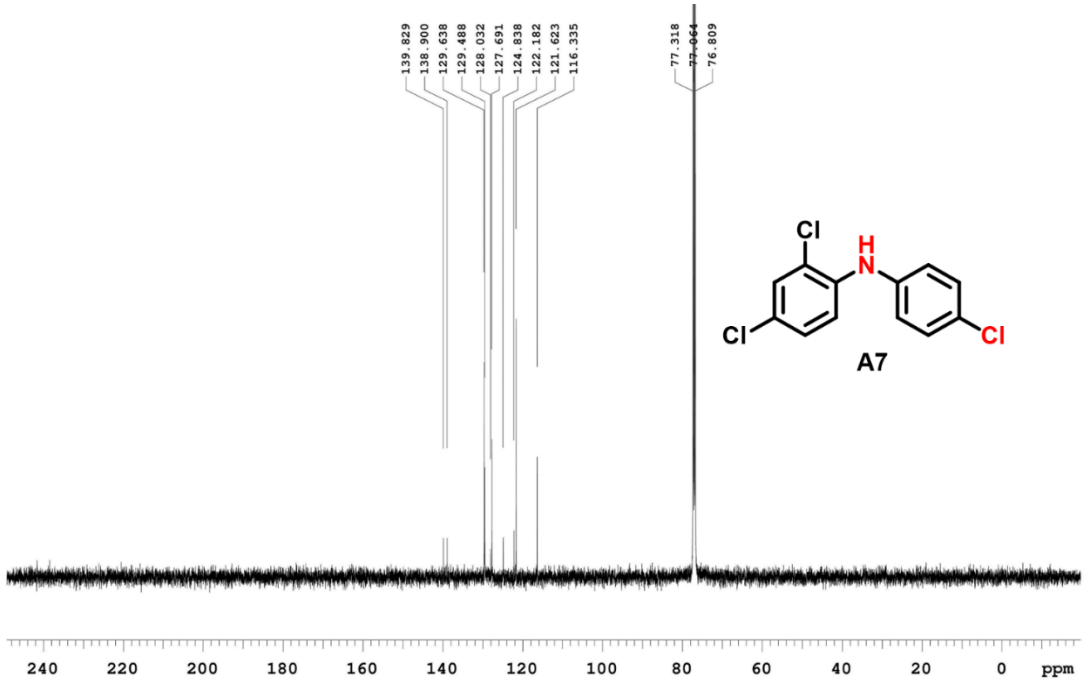
139.829
138.900
129.638
129.488
128.032
127.691
124.838
122.182
121.623
116.335
77.318
77.064
76.809
Cl
H
N
Cl
Cl
A7
240
220
200
180
160
140
120
100
80
60
40
20
0
ppm

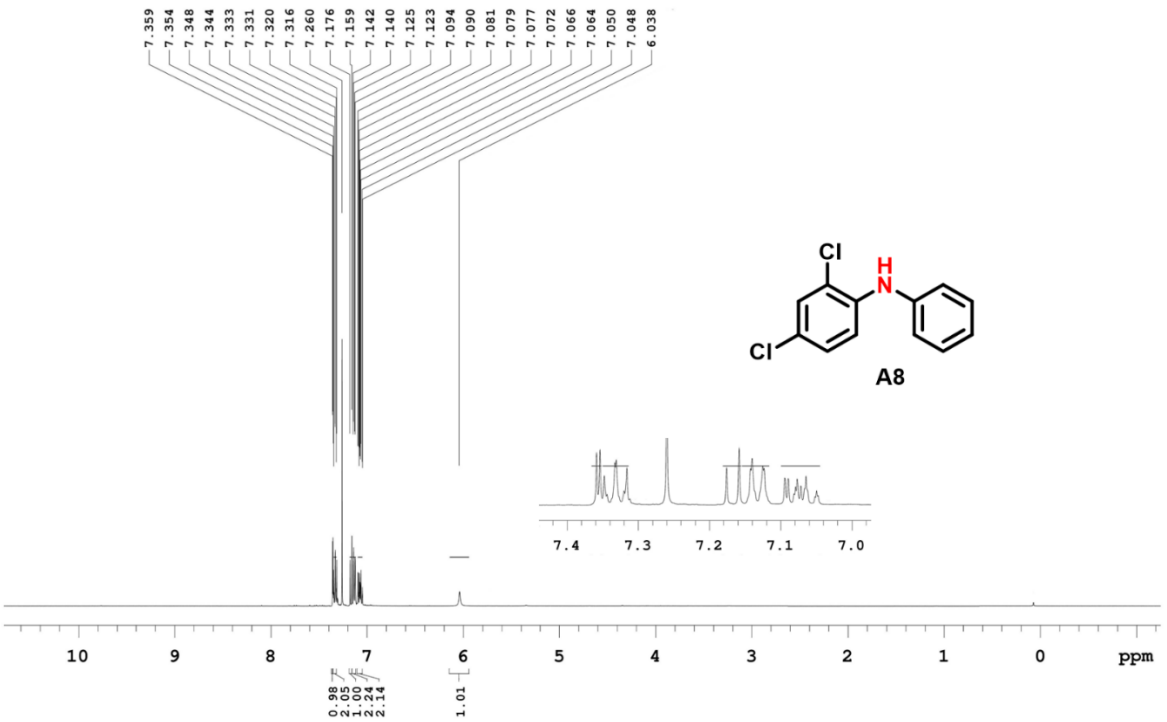
7.359
7.354
7.348
7.344
7.333
7.331
7.320
7.316
7.260
7.176
7.159
7.142
7.140
7.125
7.123
7.094
7.090
7.081
7.079
7.077
7.072
7.066
7.064
7.050
7.048
6.038
Cl
H
N
Cl
A8
7.4
7.3
7.2
7.1
7.0
10
9
8
7
6
5
4
3
2
1
0
ppm
0.98
2.05
1.00
2.24
2.14
1.01

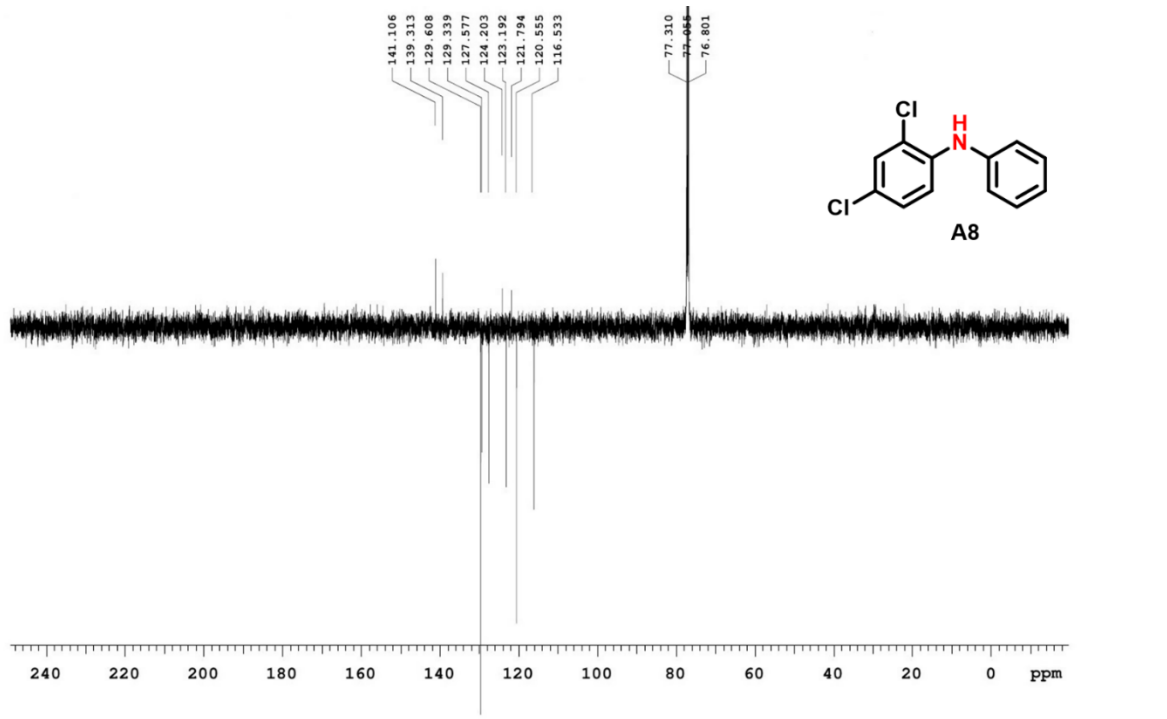
141.106
139.313
129.608
129.339
127.577
124.203
123.192
121.794
120.555
116.533
77.310
76.801
Cl
H
N
Cl
A8
240
220
200
180
160
140
120
100
80
60
40
20
0
ppm